Zeolitic imidazolate frameworks (ZIFs) and their derivatives: synthesis and energy related applications

Submitted by Binling Chen

to the University of Exeter as a thesis for the degree of

Doctor of Philosophy in Engineering

In April 2016

I certify that all material in this thesis which is not my own work has been identified and that no material has previously been submitted and approved for the award of a degree by this or any other University

Signature: ……..

Abstract

Zeolitic imidazolate frameworks (ZIFs) represent a new and special class of metal organic frameworks comprised of imidazolate linkers and metal ions, with structures similar to conventional aluminosilicate zeolites. Their intrinsic porous characteristics, abundant functionalities as well as exceptional thermal and chemical stabilities, have led to a wide range of potential applications for various ZIF materials. Explosive research activities ranging from synthesis approaches to attractive applications of ZIFs have emerged in this rapidly developing field in the past 5 years. Moreover, ZIF materials act as outstanding templates or precursors to produce porous carbons and related nanostructured functional materials based on their high surface area, controllable structures and rich metal/organic species in their scaffolds.

In this thesis, the synthesis and applications of ZIFs and their related nanostructured functional derivatives are demonstrated with special emphases on the applications in energy storage and conversion areas. In brief, this thesis presents the following research findings:

1). A cost-effective and facile preparation method for the synthesis of zeolitic imidazolate framework-8 (ZIF-8) material has been developed. ZIF-8 can be obtained from stoichiometric precursors in aqueous ammonia solution without any other additives at room temperature. The structures, particle sizes and textural properties of the resulting ZIF-8 materials can be controlled by the concentration of aqueous ammonia. In addition, the formation of ZIF-8 can be remarkably affected by different types of anions. The anion effect capacity is revealed to be $SO_4^{2-} > CH_3COO^- > Cl^- > Br^- > NO_3^-$, which follows the classic Hofmeister anion sequence.

2). Composites containing ZIF-8 and various contents of graphene oxide (GO) have been successfully prepared for the first time by using an *in-situ* method in aqueous ammonia solution. Different material characterization techniques confirm the formation of strong interactions between ZIF-8 and GO in the resulting composites. The crystal sizes and the textural properties of the synthesized composites can be modulated by control of the added amount of GO. Interestingly, the *in-situ* synthesized composites exhibit enhanced CO_2 adsorption energy and significant CO_2

storage capacity. A mechanism has been proposed accordingly to the strong interactions and the synergistic effect between ZIF-8 and GO.

3). Apart from the investigation of ZIFs themselves, exploration of ZIF derivatives has been carried out in this thesis. Homogeneously-dispersed ZnO nano-particles embedded within N-doped porous carbon matrix using ZIF-8 as a template and precursor have been successfully synthesized by a simple one-step water steam carbonization route. The as-synthesized ZnO/C-S-*S* and ZnO/C-S-*L* exhibit high CO_2 uptake capacities, CO_2 selectivity, and CO_2 adsorption energy. The mechanism of enhanced CO_2 adsorption energy has been proposed and discussed. Moreover, because of excellent adsorption and degradation abilities, these ZnO/C-S-*S* and ZnO/C-S-*L* composites are highly efficient for methylene blue (MB) removal from wastewater under visible-light irradiation. Kinetics studies of MB removal show that the adsorption process is dominated by a pseudo-second-order adsorption model.

4). In addition, ZIF-67 derivatives ranging from cobalt-embedded porous N-doped carbon/carbon nanotubes to hollow carbon nano-onions under different carbonization temperatures have been prepared. The carbonization temperature effects on the morphology and electrocatalytic properties of resultants are well studied. An optimum carbonization temperature at 800 ^{o}C for electrocatalytic performance was proposed within the range 600-2000 ^{o}C. Due to the hierarchical porous carbon structure, N-doping effect and the homogeneous cobalt dispersion, the as-synthesized sample Co@C-800 nanocomposite exhibits excellent catalytic activities for both Oxygen reduction reaction (ORR) and Oxygen evolution reaction (OER) with good stability.

5). Further development of the other ZIF-67 derivatives has been investigated. Homogeneously dispersed cobalt sulfide/N, S co-doped porous carbon nanocomposites and nickel promoted cobalt sulfides/N, S co-doped porous carbon have been successfully prepared by a simple and efficient method via the simultaneous carbonization and sulfurization using ZIF-67 and Ni-substituted ZIF-67 as a precursor and template, respectively. Due to the hierarchical porous carbon structure, N, S co-doping effect and the homogeneous nanoparticle dispersion, the as-synthesized nanocomposites exhibit excellent catalytic activities for both ORR and Oxygen evolution reaction OER with good stability.

Presentations and Publications

- **Chen, B.**, Li, R., Ma, G., Guo, X., Zhu, Y., Xia, Y. (2015). Cobalt Sulfide/N, S Co-doped porous carbon core-shell nanocomposites as superior bifunctional electrocatalysts for oxygen reduction and evolution reactions. ***Nanoscale***, **7**, 20674-20684.

- **Chen, B.**, Ma, G., Kong, D., Zhu, Y., Xia, Y. (2015). Atomically homogeneous dispersed ZnO/N-doped nanoporous carbon composites with enhanced CO2 uptake capacities and high efficient organic pollutants removal from water. ***Carbon*****,** 95, 113-124.

- **Chen, B.**, Zhu, Y., Xia, Y. (2015). Controlled in situ synthesis of graphene oxide/zeolitic imidazolate framework composites with enhanced CO2 uptake capacity. ***RSC Advances*****,** 5 (39), 30464-30471.

- **Chen, B.**, Bai, F., Zhu, Y., Xia, Y. (2014). Hofmeister anion effect on the formation of ZIF-8 with tuneable morphologies and textural properties from stoichiometric precursors in aqueous ammonia solution. ***RSC Advances***, 4(88), 47421-47428.

- **Chen, B.**, Yang, Z., Zhu, Y., Xia, Y. (2014). Zeolitic imidazolate framework materials: recent progress in synthesis and applications (Review). ***Journal of Materials Chemistry A***, 2(40), 168811-16831.

- **Chen, B.**, Bai, F., Zhu, Y., Xia, Y. (2014). A cost-effective method for the synthesis of zeolitic imidazolate framework-8 materials from stoichiometric precursors via aqueous ammonia modulation at room temperature. ***Microporous and Mesoporous Materials***, 193, 7-14.

- Bai, F., Xia, Y., **Chen, B**., Su, H., Zhu, Y. (2014). Preparation and carbon dioxide uptake capacity of N-doped porous carbon materials derived from direct carbonization of zeolitic imidazolate framework. ***Carbon***, 79, 213-226.

- **Chen, B.**, Ma, G., Zhu, Y., Xia, Y. (2016) Metal-organic-framework-derived bi-metallic sulfide on N, S-codoped porous carbon nanocomposites as superior

electrocatalysts for oxygen evolution reaction. ***Journal of Power Sources***, Submitted

- **Chen, B.**, Ma, G., Zhu, Y., Xia, Y. (2016) Cobalt-embedded in various carbon structures derived from metal-organic-frameworks as bifunctional electrocatalysts for oxygen reduction and evolution reactions. ***ACS Applied Materials & Interfaces,*** Submitted
- **Chen, B.**, Ma, G., Zhu, Y., Xia, Y. (2016). Study of ZIF-8 derived ZnO/N-doped nanoporous carbon composites for CO_2 uptake and organic pollutants removal from water. In preparation
- **Chen, B.**, Ma, G., Zhu, Y., Xia, Y. (2016). A simple method for the production of functional porous carbon materials diverted from ZIFs with enhanced carbon dioxide uptake capacities and excellent methylene blue adsorption. In preparation
- A cost-effective approach to the synthesis of zeolitic imidazolate framework-8 (ZIF-8) materials and anion effect on its formation. The 22nd Annual CSCST-SCI (Chinese Society of Chemical Science and Technology-Society of Chemical Industry) Conference. Birmingham, UK. 19 September 2015.

Table of Contents

List of Figures and Tables

Acknowledgments

I would like to express my deepest gratitude to Dr Yongde Xia for his continuous support, daily guidance and encouragement during my PhD studies. His attitude, enthusiasm and insight into the research are appreciable and will always be source of inspiration and motivations. His patience and encouragement regarding my education and personal development are greatly appreciated. I would also like to appreciate the guidance, valuable suggestions and advices from Prof. Yanqiu Zhu.

I would like to appreciate the friendship and constant help from our functional materials group members Dr. Zhuxian Yang, Dr. Fang Xu, Dr. Chunze Yan, Dr. Guiping Ma, Dr. Fenghua Bai, Dr. Lei Yu, Dr. Sakineh Chabi, Dr. Liangxu Lin, Dr. Juntong Hunang, Dr. Yan Wen, Dr. Zhoutian Xi, Dr. Bahareh Yazdani, Mrs Ke Bao, Mr Yuta Hino, Mr Mohamed Nasrul, Mr Nannan Wang and many others. Thanks also go to Dr. Dali Kong for his friendship and help with mathematical curve fitting.

I would like to thank Mr Peter Gerry and Mr Matthew Wears from Harrison workshop and Mr David Gregory from Physics workshop for their help with machining parts. Thanks to Mr David Weightman and Dr. Judith Bannerman from Harrison store for their help with products ordering and delivery.

I wish to give thanks to the technical support from Image Suit and X-AT group. Special thanks to Dr. Lesley Wears, Dr. Hong Chang, and Dr Yat-Tarng (Tommy) Shyng. Thanks to Mr Peter Splatt from Bioscience for help with SEM; Dr. Ellen Green from Physics for Raman characterisation; Dr. Lesley Wears and Dr. Hong Chang for XRD, SEM, and TEM; Dr Yat-Tarng (Tommy) Shyng for FTIR characterisation; Dr. Guiping Ma from Beijing University of Chemical Technology for XPS characterisation; Dr. Rong Li and Dr. Xinglong Gou from China West Normal University for electrocatalysis characterisation.

I would like to take the opportunity to thank my motherland-China. Thanks also go to the University of Exeter for the provision of scholarship.

Last but not least, my deepest gratitude goes to my parents and my wife for their love, caring, understanding and moral support.

List of abbreviations

Å	Angstrom, 10^{-10} m
Ar	Argon
BET	Brunauer, Emmett and Teller method
Br^-	Bromide ion
C	Carbon
Co	Cobalt
CO_2	Carbon dioxide
℃	Temperature in degree Celsius
CH_3COO^-	Acetate ion
Cl^-	Chloride ion
DTA	Differential thermal analysis
et al.	*et alia*; And others
eV	Electron volts
EDX	Energy dispersive x-ray spectroscopy
FTIR	Fourier transformation infrared spectroscopy
g	Grams
GO	Graphene oxide
HER	Hydrogen evolution reaction

H_2S	Hydrogen sulphide
H_2O	Water
H_2O_2	Hydrogen peroxide
Ir	Iridium
IrO_2	Iridium oxide
$KMnO_4$	Potassium permanganate
L	Liters
MB	Methylene blue
MIm	2-methylimidazole
MS	Mass spectrometry
mL	Milliliters, 10^{-3} L
µ L	Microliters, 10^{-6} L
MOF	Metal organic frameworks
mmol	Millimols
MMMs	Mixed matrix membranes
nm	Nanometers, 10^{-9} m
N	Nitrogen atom
N_2	Nitrogen gas
NH_3	Ammonia
Ni	Nickle
NO_3^-	Nitrate ion
$NaNO_3$	Sodium nitrate

Na_2SO_4	Sodium sulfate
NaCl	Sodium chloride
NaBr	Sodium bromide
NaOAc	Sodium acetate
OER	Oxygen evolution reaction
ORR	Oxygen reduction reaction
PL	Photoluminescence
Pt	Platinum
S	Sulfur atom
SO_4^{2-}	Sulfate ion
SAED	Selected area electron diffraction
SEM	Scanning electron microscope
STEM	Scanning transmission electron microscopy
XPS	X-ray photoelectron spectroscopy
XRD	X-ray diffraction
rpm	Rounds per minutes
TEM	Transmission electron microscope
TGA	Thermal gravimetric analysis
UV-Vis spectroscopy	Ultraviolet–visible spectroscopy

wt%	Weight percent
ZIF(s)	Zeolitic imidazolate framework
ZnO	Zinc oxide
Zn^{2+}	Zinc ion
$Zn(NO_3)_2 \cdot 6H_2O$	Zinc nitrate hexahydrate
$ZnSO_4$	Zinc sulfate
$ZnCl_2$	Zinc chloride
$ZnBr_2$	Zinc bromide
$Zn(OAc)_2$	Zinc acetate

1. Chapter 1: Introduction

Porous materials are significantly important for fundamental research and practical applications including gas adsorption, separation, catalysis, and sensing.[1-3] Because of their intrinsic properties such as high surface areas, large pore volumes and tuneable pore sizes, porous materials have attracted a large amount of research interest over last five decades and the study will be continuing to strengthen in the future. As the foundation of porous materials, they are defined as any solid containing pores and voids.[4] Porous materials traditionally are categorised into three types - microporous, mesoporous and macroporous materials. Microporous materials contain micropores, which have diameters or dimensions < 2 nm. Mesoporous materials contain mesopores, which have diameters in the range of 2 - 50 nm, and macroporous materials have pores > 50 nm.[4] Recently, the term "nanoporous" has become popular. Following the definition of nanoscale as referring to a size range of approximately 1 - 100 nm, this terminology refers to the materials which have pores < 100 nm in dimension. Traditionally, zeolite-type porous materials such as aluminosilicate zeolites are one of the most important nanoporous inorganic materials which have been widely researched and applied in the industry.

Metal organic frameworks (MOFs), a class of nanoporous materials assembled from metal ions and organic ligands,[5-7] exhibit tuneable structures, versatile functionalities and fascinating properties. Recently, zeolitic imidazolate frameworks (ZIFs) represent a new and special class of MOFs comprised of imidazolate linkers and metal ions. Similar to traditional aluminosilicate zeolites, ZIFs possess diverse structures, where typically M^{2+} ions play the role of silicon while the imidazolate anions form bridges that mimic the role of oxygen in zeolite frameworks, with the M-Im-M angle around 145^{o}. Their intrinsic porous characteristics, abundant functionalities as well as exceptional thermal and chemical stabilities, have led to a wide range of potential applications for various ZIF materials. In addition, owing to the molecular-like organic-inorganic crystal structure of ZIFs, ZIFs have emerged as excellent precursors or sacrificial templates for the preparation of porous carbon based nanocomposites.

Recent advance in porous materials have emerged along with new nanostructured porous materials possessing extraordinary structures and excellent properties.

Structurally well-ordered porous materials with high textural properties are generally good hosts in storage of energy-related gases such as carbon dioxide, hydrogen with high capacity, selectivity and regenerability. They also have the potential to light up portable electronic devices for electrochemical energy storage and conversion. Therefore, to design and develop novel nanostructured materials with appropriate functionalities and evaluation of their applications in a wide variety of environmental and energy-related fields becomes the primary aim of this PhD project.

Traditionally, ZIFs are synthesised from organic solvents,[8-15] which obviously cause some environmental concerns since organic solvents are usually toxic and flammable. Even though many efforts have been devoted to reducing the environmental impact,[14-19] those synthesis approaches are still not cost-effective. Therefore, the generation of ZIFs via a green and low-cost method remains highly desirable. In addition, from the previous studies, different parameters, such as solvents,[20, 21] temperatures[22, 23] and deprotonating agents,[21, 22, 24-26] for the synthesis of ZIFs have been widely investigated. However, one particular parameter-the effect of anions, has not been explored yet. It will be interesting to investigate whether anions may have influence on the formation of ZIF materials.

A big challenge in ZIF based composites preparation is the homogeneous dispersion of the reinforcement. Literature only reports inhomogeneous composites [27] such as mechanical mixtures that may significantly decrease in the textural properties of the resulting composites. Thus, the previous work encourages us to explore a method to synthesize ZIF based composites that integrate the unique properties of both components.

Similarly, homogeneous dispersion of nanoparticles in the carbon matrix is also the leading challenge in carbon based nanocomposites, because nanoparticles always tend to agglomerate. Conventionally, the components in these porous carbon-metal/metal oxide nanocomposites usually cannot achieve homogeneous dispersion since they were frequently prepared by mechanical or physical mixing the nanoparticles with the porous carbon materials. Thanks to the inorganic-organic crystal structure of the parental ZIFs, the generated metal/metal oxide can be retained homogeneously within the nanoporous carbon matrix.[28] To date, only a few reports have been reported such a

method for the preparation of nanocomposites. A simple and effective process remains highly desirable for the preparation of nanomaterials.

In addition, electrocatalytic oxygen reduction reaction (ORR), oxygen evolution reaction (OER) and hydrogen evolution reaction (HER) play key roles in many important next-generation energy storage and conversion technologies, such as fuel cells, metal-air batteries and water splitting.[29-38] Nowadays, most efficient electrocatalysts contain precious metals including Pt or Ir; however, due to the prohibitive cost and poor stability of precious metals, it is highly desirable to discover highly efficient and cost-effective non-precious electroactive materials.[39-42]

Therefore, the objectives of this thesis can be listed as follows:

- To explore a green and low-cost way to synthesize ZIFs and study the fundamental synthesising parameters on the formation of ZIFs.
- To investigate an approach to synthesize ZIF based composites with homogeneously dispersed reinforcement and research on their CO_2 uptake performance.
- To design a simple and facile way to produce ZIF derived nanocomposites that homogeneously dispersed nanoparticles including metal, metal oxide, or sulfides, embedded in a porous carbon matrix.
- To evaluate the applications of ZIF derivatives in environmental and energy-related fields including CO_2 uptake, waste water treatment, and their electrocatalytic activities.

The thesis has been presented as 9 chapters. Chapter 1 introduces the motivation, objectives and organization of the thesis. Chapter 2 presents the research background and literature review for the development and recent progress towards the different synthesis strategies to generate ZIF and ZIF derivatives materials. Their attractive and potential applications in gas separation, catalysis, and electrochemical energy storage and conversion in the past years are discussed and reviewed. Chapter 3 describes the materials and synthesis methods for ZIF and ZIF derivatives materials, in addition to the structural and property characterisation techniques employed. Chapter 4 demonstrates a cost-effective and facile method for the preparation of zeolitic imidazolate framework-8 (ZIF-8) material in an aqueous ammonia system. The anion

effect on the formation of ZIF-8 is also discussed. Chapter 5 describes the preparation and characterisation of ZIF-8/graphene oxide nanocomposites by using an *in-situ* controlled synthesis method. The effect of GO content on the crystal sizes of ZIF-8 and the textural properties of composites have been investigated. The CO_2 uptake performance of the as-synthesized composites has also been presented in Chapter 5. Chapter 6 presents the synthesis of zinc oxide/nanoporous carbon composites derived from ZIF-8. The excellent performance in CO_2 uptake and removal of methyl blue (MB) of the as-synthesized composites have both been presented in Chapter 6. Chapter 7 describes the preparation process, structural, thermal and textural properties characterisations of cobalt/nanoporous carbon composites derived from ZIF-67. Furthermore, their applications in oxygen reduction reaction (ORR) and oxygen evolution reaction (OER) have both been presented. Chapter 8 shows a one-step generation of homogeneously dispersed cobalt sulfide/N,S Co-doped porous carbon nanocomposites derived from ZIF-67, and as well as cobalt-nickel sulfides/N, S co-doped porous carbon composites derived from Ni-substituted ZIF-67. Their applications in electrochemistry such as ORR and OER are all presented. Conclusions of the thesis are summarised in Chapter 9, as well as some suggestions for future development in related research areas.

2. Chapter 2: Literature Review

2. 1. Introduction

For a long time, porous materials have continuously been the research focus not only in fundamental investigations but also in practical applications due to their intrinsic properties such as high surface areas, large pore volumes and tuneable pore sizes.[1] Noticeably, zeolite-type porous materials are technologically one of the most important nanoporous inorganic materials which have been widely used in large numbers of industrial processes including separation, catalysis and sensing.[43, 44] In addition to the well-known aluminosilicate zeolites, many other zeolite-like inorganic materials such as the aluminophosphates and transition metal phosphates discovered in the 1980s and 90s,[45] further enriched the zeolite family. The econmic volume of zeolites used in industries is annually up to 350 billion dollars worldwide.[46]

During the last decade, much effort has been devoted to developing a new class of porous materials based on hybrid metal–organic frameworks (MOFs), which are also known as "hybrid organic inorganic frameworks" or "coordination polymers". The term MOFs was introduced by Yaghi and his co-workers in 1995,[47] although it is worth noting that the first synthesis of a coordination polymer can be dated back to 1965.[48] MOFs are rapidly developed by the prospect of finding new structures, enhancing their functionalities, exploring new gas sorption and catalytic properties and expanding pore sizes.[49-51] The modular nature of MOFs and the mild conditions for their synthesis have permitted the rational structural design of numerous MOFs and the incorporation of various functionalities by applying the concept of secondary building units (SBUs), which have well-defined geometrical shapes in the synthesis. MOFs consist of metal clusters that are joined over polytopic linkers to form finite SBUs. The different topologies of MOFs can be achieved by varying the arrangement of SBUs.[52]

A number of MOFs with zeolitic architectures have been successfully synthesised as hybrid frameworks. Among them, the advent of zeolitic imidazole frameworks (ZIFs) has recently gained considerable attention. ZIFs are a sub-family of MOFs which consist of M-Im-M (where M stands for Zn, Co cation and Im stands for imidazolate

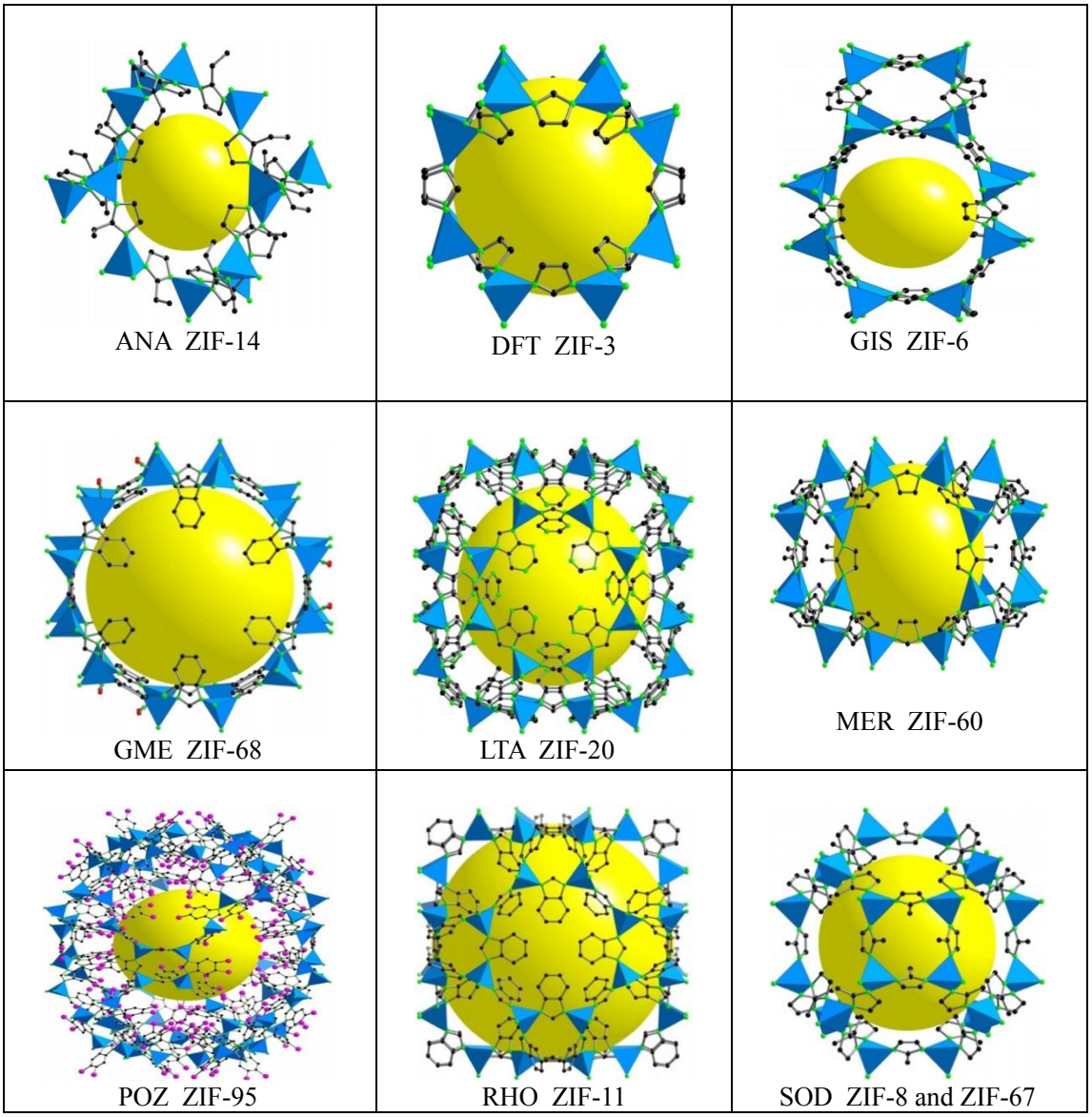

Figure 2.1 Representative crystal structures of ZIFs (the first three capital letters under each example stand for the zeolite stucture code).[46]

linker) formed by a self-assembly approach. The diverse structures of ZIFs are similar to conventional aluminosilicate zeolites, where typically Zn^{2+} ions play the role of silicon and the imidazolate anions form bridges that mimic the role of oxygen in zeolites, with metal-imidazole-metal (namely M-Im-M) angle ~145°.[53, 54] As a result, ZIFs tend to form zeolite-like topologies with structures similar to those observed in zeolites.[55, 56] However, structures that have not been known in traditional zeolites can be also formed in ZIFs.[6] The representative ZIFs with zeolitic structures are shown in Figure. 2.1.[46] Since these ZIFs simutaneously possess the characteristics of both MOFs and zeolites, it is not surprising that ZIFs generally display properties that combine the advantages of both zeolites and MOFs, such as ultrahigh surface areas,

unimodal micropores, high crystallinities, abundant functionalities and exceptional thermal and chemical stabilities,[53, 54, 57] which renders ZIFs holding great promise in many application fields including catalysis, separation and sensing. The unique characteristics of ZIFs make them different from conventional zeolites in many aspects, as shown in Table 2.1.

Since Yagi's seminal Account on the synthesis and structures of ZIFs published in 2010,[46] research in this field has developed rapidly and attracted increasing attention in the past 5 years. However, there have been no dedicated reports in the literature ever since to summarise this fast developed area on the synthesis and applications of ZIFs although some information of such kind has been dispatched in the reviews on MOFs.[58-64] A dedicated review focused on the state-of-the-art ZIF materials will provide scientists working in the relevant fields the full screen on the new developments of ZIFs, which is highly desirable.

Table 2.1 Comparison between the zeolites and zeolitic imidazolate frameworks.

Comparison content	Zeolites	Zeolitic imidazolate frameworks
Framework type	Inorganic	Inorganic-organic
Composition	Si; Al; O	Zn; Co; C; N; H and more
Secondary building unites	SiO_4 and AlO_4	$M(Im)_2$
Topology	Around 200	Found over 100; the number may increase exponentially
Stability	Depending on the Si/Al ratio, thermal and chemical stability are generally high	Thermal stability up to 500°C and high chemical stability in organic and aqueous media
Compatibility	Poor interaction with polymer	Relatively better compatibility with organic polymer
Functionality	Tuneable Si/Al ratio; generally difficult in functionalisation	Rich chemical functionalities with organic linkers
Development	Over 50 years	Around 10 years
Application prospect	Low-cost; large scale for industry applications	Expensive; potential for industry application

In addition, due to the highly ordered porous structures with abundant organic species, ZIF materials would be good candidates as templates and precursors to produce porous carbon materials under proper synthesis conditions.[65] Besides, due to the

regular arrangement of metal species in ZIF precursors, the carbon composites containing nanostructured metal/metal oxide species are prone to be formed in the in situ carbonization process. Moreover, the pure metal/metal oxide could also be formed from ZIF precursors under certain controlled synthesis conditions. These facile synthesis approaches will provide a new way to the preparation and application of nanomaterials in the future.

In this section, the recent research developments on the synthesis and applications of ZIF materials and their ZIF derivatives are analysed and summarised.

2.2 Synthesis of ZIF materials

ZIF-based materials have been traditionally prepared by hydrothermal or solvothermal synthesis routines in water or organic solvents respectively, with reaction temperatures varying from room temperature up to 200 ℃ and reaction duration from hours to days.[17] The fast development in this field has witnessed the emerging of new synthesis strategies of ZIFs in the past years. A variety of preparation methods including both solvent-based routines and solvent-free routines have been developed to generate ZIF-based materials, which are summarised in Figure 2.2. Undoubtedly, depending on the status of resulting ZIFs, different synthesis strategies must be adopted in order to generate power or film/ membrane-based ZIF materials.

2.2.1. Synthesis of powder-based ZIFs

Most of the ZIF materials, especially at the early research stage of ZIFs, dominantly formed as powders, which were separated from reaction mixture after removal of the solvents or other impurities. So far, both solvent-based and non-solvent-based synthesis approaches have been developed to produce powder-based ZIF materials.

2.2.1.1. Solvent-based synthesis

2.2.1.1.1. Solvothermal synthesis

ZIF materials are conventionally prepared through a solvothermal method where selected organic solvents acted as the reaction medium. In 2006, Yaghi et al pioneered the synthesis of twelve ZIF crystals, termed as ZIF-1 to-12, in organic solvent systems

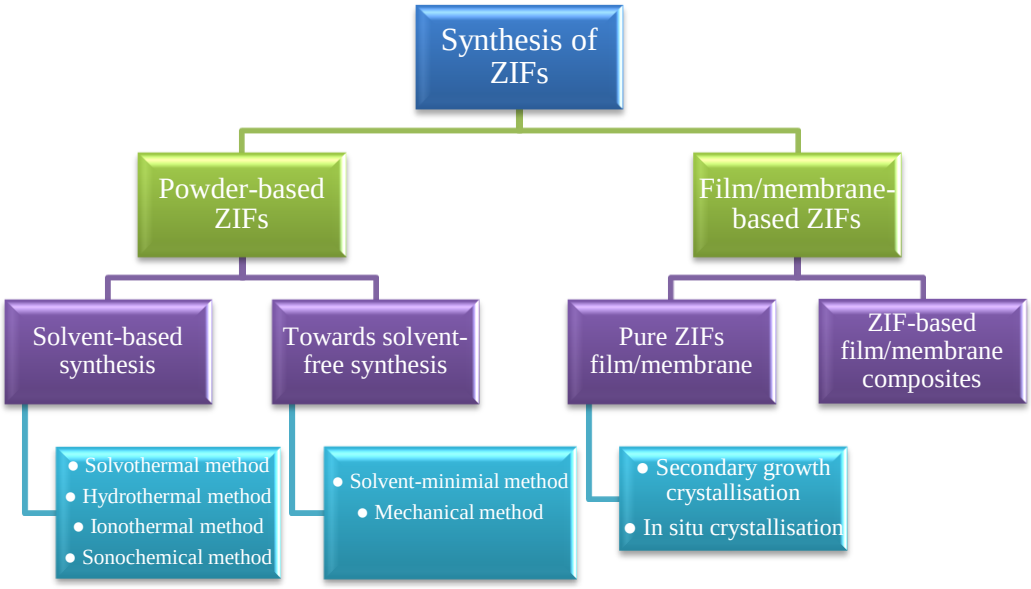

Figure 2.2 Summary of different synthesis methods for ZIF-based materials.

such as N,N-dimethylformamide (DMF), N,N-diethyformamide (DEF) and N-methylpyrrolidine (NMP).[55] The same group also used DMF/DEF/NMP as solvents to synthesise other ZIF materials including ZIF-60 to ZIF-77,[56] ZIF-78 to ZIF-82,[66] ZIF-90,[25] ZIF-95 and ZIF-100.[67] Later on, other researchers synthesised ZIFs using DMF or DEF as well to investigate the formation mechanism and relative properties.[68] Recently, modified recipes from Yaghi's method have been developed. Some organic amines such as pyridine and triethylamine (TEA) were added into the DMF or DEF solvent as a deprotonating agent to facilitate the material formation. For instance, micro-sized and hexagonal rod-shaped ZIF-78 crystal was prepared with the assistance of TEA,[69] while ZIF-90 was synthesised with the addition of pyridine in the DMF at room temperature.[70] In addition, NaOH was also applied as a base in the synthesis of ZIF-76 in the mixture of DMF and DEF to accelerate the crystal formation.[71]

Methanol was another important organic solvent widely used in the synthesis of ZIFs. In 2006, Chen's group first generated ZIF (it was named as MAF) crystals by using methanol as reaction medium, where 2-methylimidazole or 2-ethylimidazole-containing methanol solution was slowly and carefully layered onto the aqueous ammonia solution containing $Zn(OH)_2$ for one month.[72] Later, using a modified recipe,

they obtained ZIF-8 crystals in the mixture of 2-methylimidazole-containing methanol and aqueous ammonia (containing $Zn(NO_3)_2$ or $ZnO/Zn(OH)_2$) after 5 hours stirring at room temperature.[73, 74] In addition, nanoscaled ZIF-8 materials can be prepared in methanol,[75] where the methanol solution containing $Zn(NO_3)_2$ and 2-methylimidazole (MIm) were simply mixed with a Zn^{2+}/MIm molar ratio of 1:8 at room temperature.

The synthesis of ZIFs from methanol-based systems was promoted with the utilisation of additives. For examples, Nune et al found that the presence of high molecular weight poly(diallyldimethylammonium chloride) as a stabilizer in methanol can lead to the formation of hexagonally shaped and nanosized ZIF-8.[76] Wiebcke et al improved their previous method[75] to control the crystal size of ZIF-8 by employing modulating ligands such as sodium formate/1-methylimidazole and n-butylamine in methanol solution.[21] The crystal size of ZIF-8 could be tuneable between 10 and 65 nm for nanocrystals, or about 1 μm for microcrystals. The addition of modulating ligand sodium formate can also lead to a rapid, highly-yielding crystallisation of ZIF-8 in methanol at room temperature.[77] Moreover, other alcohols such as ethanol[78] and isopropyl alcohol[79] were also successfully used as organic solvents in ZIF synthesis.

2.2.1.1.2 Hydrothermal synthesis

Although the solvothermal synthesis method has dominated in the early stage of the ZIF research, undoubtedly, the organic solvents are expensive, flammable and not environmentally friendly. Recently, much effort has been devoted to the fabrication of ZIFs in green and facile ways via using less organic solvents or eventually avoiding the use of organic solvents. Pan et al first realised the generation of ZIF-8 in an aqueous system at room temperature via a simple procedure:[20] the zinc nitrate solution was mixed with the 2-methylimidazole (MIm) solution and the products were then collected by centrifugation after stirring for about 5 min. However, considering that the stoichiometric molar ratio of zinc ions and MIm in ZIF-8 is Zn^{2+}:MIm=1:2, it is obvious that excess amount of MIm (molar ratio of Zn^{2+}:MIm=1:70) in this method was wasted. Therefore, much effort has been devoted to synthesising ZIFs from stoichiometric molar ratios of metal ions and Im derivatives in aqueous systems. In particular, Miyake et al[80] succeeded in preparing pure ZIF-8 crystals in aqueous system at room temperature and the crystalline ZIF-8 could be produced from the molar ratio of Zn^{2+}:MIm=1:20.[81] In addition, Qian's group demonstrated that ZIF-67

nanocrystals could be generated from the molar ratio of Co^{2+}:MIm:H_2O=1:58:1100 in aqueous solutions at room temperature.[82]

Water-based systems for the synthesis of ZIFs were also modified by using additives. Both TEA[26] and ammonium hydroxide[83] were applied as deprotonation agents to reduce the use of ligand MIm and initiate the formation of ZIFs. Gross et al could prepare ZIF-8 and ZIF-67 in aqueous system with the addition of TEA at room temperature without the formation of by-products,[26] where the molar ratio of metal ion:MIm could be reduced to 1:4. Yao et al also reported that ZIF-8 could be prepared in the presence of ammonium hydroxide with the molar ratio of Zn^{2+}:MIm:NH_4^+:H_2O=1:4:16:547.[83] Interestingly, ZIFs could be obtained from stoichiometric metal ions and MIm ratio in the presence of other additives such as triblock copolymers poly(ethylene oxide)-poly(propylene oxide)-poly(ethylene oxide) (PEO-PPO-PEO)[83] and polyvinylpyrrodlidone (PVP)[84] in aqueous system. For example, both ZIF-8 and ZIF-67 were prepared from stoichiometric metal ions and MIm in aqueous ammonia systems in the presence of the triblock copolymer surfactant containing PEO groups,[83] where it was believed that this surfactant could promote the formation of porous ZIF-8 and ZIF-67 due to the electrostatic attraction to the metal ions. Shieh et al also found that micro-sized ZIF-90 crystals could be generated in an aqueous system in the presence of PVP (with molecular weight 40000).[84] PVP was hypothesised to control the morphology of crystals and prevent the aggregation of seed crystals.

Very recently, the synthesis of ZIFs from stoichiometric precursors via aqueous ammonia modulation has been successfully realised by us and other groups.[22, 85] Wang's group demonstrated the generation of ZIF-8 from stoichiometric precursors (Zn^{2+}:MIm =1:2) in concentrated ammonium hydroxide aqueous solutions at room temperature.[85] The addition of an appropriate amount of ammonium hydroxide was found to be essential to the formation and growth of ZIF-8 crystal through deprotonation and coordination reactions. Our group also found that ZIF-8 could be readily synthesised from stoichiometric precursors in aqueous ammonia solution without any other additives at room temperature.[22] The structures, particle sizes and textural properties of resulting ZIF-8 materials could be easily tuned by simply controlling the concentration of aqueous ammonia in the synthesis mixture.

Undoubtedly, these cost-effective synthesis strategies of ZIFs will greatly promote the large scale production of ZIFs for practical applications.

2.2.1.1.3 Ionothermal synthesis

Recently, a new synthesis strategy, ionothermal synthesis,[86-88] has been developed to generate ZIF materials, which involves the use of green solvents such as ionic liquids[89, 90] and eutectic mixtures[91] to produce ZIFs. Ionic liquids not only can simultaneously act as both solvents and templates to avoid the competition interactions between the solvent-framework and the template-framework that are present in hydrothermal preparations,[86] but also have negligible vapour pressure and non-flammability allowing the synthesis to be processed in an open system.[92-94] Moreover, ionic liquids can be recycled for further use.[88] The use of ionic liquid for the synthesis of ZIFs was first realised by Morris and co-workers.[89] They reported that four ZIFs, showing structures that were previously known or unknown, were generated under ionothermal conditions using the ionic liquid 1-ethyl-3-methylimidazolium bis-(trifluoromethyl)sulfonylimide.[89] In addition, it was reported that ZIF-8 could also be synthesised in the presence of ionic liquid 1-butyl-3-methyl-imidazolium tetrafluoroborate[90] or urea-choline chloride eutectic mixture.[91]

2.2.1.1.4 Sonochemical synthesis

ZIFs can also be produced by sonocrystallisation methods. Compared with the conventional oven heating for ZIFs preparations, sonochemical synthesis can not only promote the formation of nucleation, but also help to disperse the nucleation homogeneously.[95] During the sonochemical synthesis, bubbles are formed and collapsed in solutions, known as acoustic cavitation, generating high local temperature, pressure as well as remarkable heating and cooling rates.[96-98] According to Seoane's report, pure ZIF-7, ZIF-8, ZIF-11 and ZIF-20 crystals were obtained under ultrasound irradiation, with a power of 110 W and a frequency of 47 kHz, at lower temperature (45-60 ^{o}C) and shorter duration (6-9 h) in respect to the conventional solvothermal synthesis.[99] They also found that the crystals were smaller and had narrower particle size distribution than the conventional synthesised materials. Recently, Cho et al have realised the preparation of a high-yield ZIF-8 using a direct sonochemical route in DMF in the presence of NaOH and TEA.[100] In addition, they have successfully expanded to 1L-scale synthesis of ZIF-8 via this sonochemical method which can be potentially scaled up for industrial applications.

2.2.1.2 Towards solvent-free synthesis

2.2.1.2.1 Solvent-minimisation method

Although the synthesis of ZIFs in the aqueous-based system is environmental friendly and cost-effective compared with those in the organic solvents-based system, some problems such as the use of excessive imidazole sources and massive solvent washing still make the aqueous synthesis method inefficient. For this reason, solvent-minimisation methodologies have been developed recently.[59, 101] For example, Shi et al succeeded in fabricating porous ZIF-8 and ZIF-67 by a steam-assisted conversion method (or dry-gel conversion method).[23] Different from the common hydrothermal synthesis method, the solid phase containing metal salts and excess ligands was placed in a small Teflon cup surrounded by water vapour (or organic solvent steam such as DMF) under 120 ^{o}C for 24 h, and the small amount of water possibly acted as a structure-directing agent in the synthesis.[102] In addition, ZIF-8 samples were also generated by a vapor-assisted conversion method in nonpolar solvent n-heptane, where the transformation rate from the solid reagents to ZIF-8 was faster than that in methanol or DMF.[103]

Moreover, recent reports have demonstrated that ZIFs can be successfully produced through solvent-free methods. For example, Müller-Buschbaum et al have obtained $Co(IM)_2$ via a solvent-free synthesis procedure under heating.[104] Zhang et al have successfully generated porous ZIF-8 (it was sometimes also called MAF-5) from the oxide/hydroxide-based solvent-free reaction without any by-product.[105] The operating procedure is quite simple: a mixture of ZnO and MIm with molar ratio of 1:2, which had been ground uniformly, was heated at 180 ^{o}C for 12 hours, and ZIF-8 was then collected. The obtained ZIF-8 sample can be used for adsorptive applications without any further treatment. Beobide et al also have realised the preparation of ZIFs with a solvent-free method,[106] in which ZIFs were obtained under the acid-base reaction between ZnO/CoO/$Co(OH)_2$ and imidazolic ligands at temperature of 100-160 ^{o}C in a closed vessel. Moreover, by the addition of small amounts of structure directing agents, it is controllable to generate a zinc/cobalt-imidazolates network topology with a high yield (87–97%).

In addition, an "accelerated aging" method has also been developed for the preparation of ZIFs. Inspired by the geological biomineralisation and mineral

neogenesis, this mild and environmentally friendly novel method exploits the inherent mobility of molecules, which is different from solvent-based or other solvent-free synthesis methods.[107, 108] Friščić et al[107] firstly proposed the "accelerated aging" method and prepared close-packed ZIFs with imidazole, 2-methylimidazole, 2-ethylimidazole and benzimidazole by accelerated aging in a solvent-free and low-energy manner.[109-111] In detail, a stoichiometric molar ratio of zinc oxide and imidazole ligand were ground to form a mixture. Together with the catalyst ammonium sulfate, this mixture was placed in an open vial and aged at 45 ℃ and 98% relative humidity for several days, and closed-packed ZIFs were then obtained after washing and drying. In addition, the well-known open framework ZIF-8 can be obtained by the transformation of the closed-packed one under methanol vapours at room temperature. Recently, Friščić et al have developed the accelerated aging method for the one-step synthesis of scalable microporous ZIFs.[108] By changing different salt additives such as $KHSO_4$, $(IM)_2SO_4 \cdot H_2O$ and $(Hcaf)(HSO_4)$ (Hcaf = caffeine), accelerated aging can be optimised for the synthesis of microporous products. They claimed that microporous ZIF-8 and ZIF-67 can be assembled efficiently from metal oxide and MIm without any further activation, such as microwave and sonochemical treatment.

2.2.1.2.2 Mechanochemical synthesis

Mechanochemistry has shown significant potential as a green and efficient strategy for the construction of materials.[112] Therefore, the fabrication of ZIFs from the mechanochemical synthesis method (via ball milling) has been developed. In 2006, partial formation of the nonporous $Zn(IM)_2$ was first obtained by manual grinding ZnO with large excess amount of imidazole (IM).[113] The same nonporous $Zn(IM)_2$ products were also generated by Adams et al. using a two-step mechanochemical process starting from $ZnCl_2$.[114-116] Realising the limitation of oxide-based precursors for ZIF synthesis via neat grinding, Friščić et al. used modified mechanochemical methods called liquid-assisted grinding (LAG) or ion- and liquid-assisted grinding (ILAG) to produce ZIFs from a stoichiometric molar ratio (1:2) of ZnO and ligand such as imidazole, 2-methylimidazole and 2-ethylimidazole at room temperature.[117] It was found that the addition of a small amount of a liquid phase could enhance the mobility,[118, 119] and salt additives could facilitate the formation of ZIFs.[120] In addition, the topology of synthesised ZIFs could be controlled by choosing different grinding

liquids (such as DMF, DEF and ethanol) and salt additives (such as NH_4NO_3, $(NH_4)_2SO_4$ and $NH_4CH_3SO_3$). Furthermore, Friščić et al. could directly monitor the ball milling reaction, the formation of intermediates and the interconversion of ZIF topologies by in situ diffraction of high-energy synchrotron X-rays.[121] Recently, Tanka et al have claimed a truly solventless mechanical dry conversion of ZnO to ZIF-8 without adding any other additives.[122] Nano-sized ZnO powders (average particle size of 24 nm) and MIm were added into a ball mill under a rotation of 100 rpm. They found that the obtained nanoparticles of larger size contained untransformed ZnO, while the smaller nanoparticles had no ZnO. Thus, ZnO crystals were more likely to be converted into ZIF-8 due to the use of nano-sized ZnO particles. The proposed mechanism is shown below in Figure 2.3. Apart from the crystalline ZIFs, Cheetham et al found that the amorphous ZIFs can be synthesised by ball milling too.[79, 123, 124] Various amorphous products including ZIF-1,[123] ZIF-3,[123] ZIF-4,[123] ZIF-8[123, 124] and ZIF-69 [79] can be obtained under grinding.

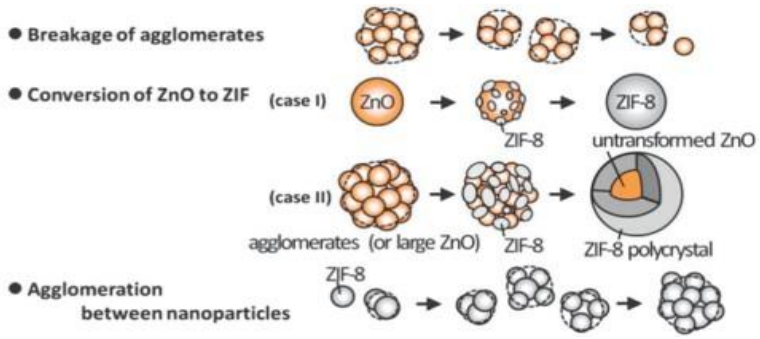

Figure 2.3 Proposed mechanism of mechanochemical synthesis dry conversion of ZnO to ZIF-8. The three main processes take place at the same time.[122]

2.2.2 Synthesis of ZIF-based films and membranes

Shortly after the synthesis of powder ZIF crystals, it is recognised that the formation of ZIFs film/membrane is very important in many applications such as gas separation and chemical sensors, due to their intrinsic properties especially the molecule-sized porosity and easy handling.

2.2.2.1 Pure ZIFs film

So far, diverse synthesis strategies on the fabrication of ZIF films and membranes have been explored. Generally, the preparation of ZIF membranes can be classified into two basic categories: secondary growth crystallisation and in situ crystallisation.

2.2.2.1.1 Secondary growth crystallisation

The preparation of membrane via the secondary growth crystallisation usually involves two main steps. In the first step, the crystal seeds are deposited on the bare or chemically modified support through selected strategies such as rubbing, dip-coating, thermal seeding and reactive seeding by repeated growth; in the second step, a continuous polycrystalline layer grows under solvothermal or hydrothermal conditions. Internal gaps among seeds can be closed-up by the growth of seeds, and finally a continuous membrane is formed. The notable advantage of the seeded growth method is that the membrane orientation can be systematically controlled. Other membrane properties such as membrane thickness and grain boundary structure can also be modulated by this method, which can lead to better membrane performance.[125] Secondary growth crystallisation can be normally realised via two different routes: (1) Depositing the crystal seeds via rubbing, dip-coating, thermal seeding or by repeated growth; (2) Pre-treating the support by using reactive seeding or organic functional groups. For example, Carreon et al prepared ZIF-8 membrane by secondary growth crystallisation method,[126] where an alumina support was seeded with ZIF-8 crystals by rubbing, followed by secondary growth to form a ZIF-8 layer on the support. ZIF-8 thin layers were also prepared on the seed rubbed vertically-aligned carbon nanotubes.[127] Moreover, high optical quality ZIF-8 films were prepared by dip-coating a colloidal solution of ZIF-8 nanoparticles on a polished silicon wafer,[128] while a ZIF-69 membrane was fabricated by dip-coating a colloidal solution on a porous α-alumina substrate.[125] In addition, a ZIF-8 membrane was prepared by secondary growth methods in an aqueous system at near room temperature.[129-131] Particularly, hollow fiber supported and continuous ZIF-8 membranes were generated from a diluted aqueous solutions.[132]

For secondary growth crystallisation methods, seeding on the support is regarded as the key factor to obtain high quality ZIF membranes. Thus, it is important to enthance the interaction between ZIF crystals and the support. Apart from the traditional seeding approaches such as dip-coating, slip-coating and rubbing seeding, many advanced seeding approaches including reactive seeding,[133-135] pre-coating polymer or organosilane binder,[136-141] infiltrating precursors[142] and microwave-assisted seeding[143] have been explored. These advanced seeding approaches are addressed as follows one by one.

Reactive seeding was proposed to eliminate the cracks and intercrystalline defects.[134] A ZIF-78 membrane was prepared by reactive seeding on a porous zinc oxide support,[134] where the ZnO supports were first seeded by hydrothermal synthesis, and secondary seeded growth was then carried out to crystallize a ZIF-78 layer on the support by hydrothermal synthesis.[134] A similar method was utilised to produce a ZIF-71 membrane using reactive seeded ZnO supports by solvothermal synthesis.[133] In addition, Tao et al successfully fabricated a continuous and well-intergrown ZIF-8 membrane on hollow ceramic fibre tube.[135] In this method (as shown in Figure 2.4), loosely packed crystals were first deposited on the support by in situ crystallisation, followed by the formation of a compact seed layer by rubbing seeding, and the secondary growth method was then applied to form the continuous and defect free ZIF-8 membrane on the seed loaded hollow ceramic fiber tube.

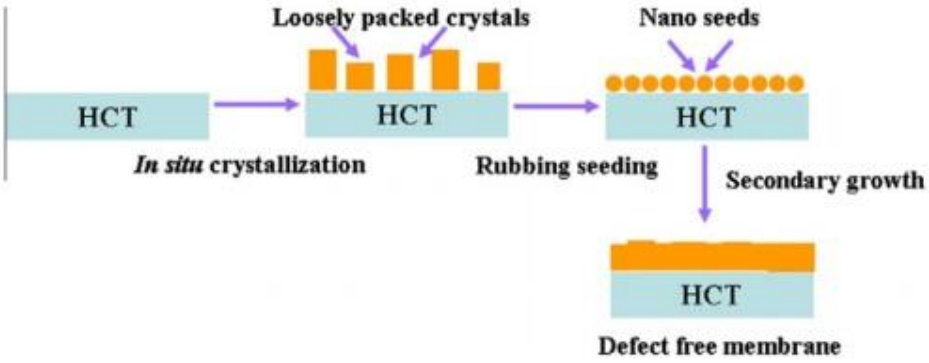

Figure 2.4 Schematic representation of ZIF-8 membrane fabrication by reactive seeding (crystallizing-rubbing seeding) approach followed by secondary growth (HCT: hollow ceramic fiber tube).[135]

Pre-coating polyethyleneimine (PEI) solution containing ZIF-7 seeds has been successfully used in the preparation of ZIF-7 membranes.[136-138] Although ZIF-7 cannot be dispersed in the aqueous phase due to its hydrophobic property, it can be homogeneously dispersed in an aqueous PEI solution because PEI can coordinate with the zinc ions at the surface of the nanoseeds, thereby making them compatible with the aqueous solution.[144] Moreover, PEI can effectively enhance the linkage between the seeds and the support through hydrogen bonding interactions. For instance, ZIF-8 membranes were prepared by pre-coating PEI solution containing ZIF-8 seeds[139, 140] and ZIF-8 films were fabricated on the 3-(2-imidazolin-1-yl)propyltriethoxysilane modified substrates at room temperature in aqueous system.[141]

Infiltrating precursors as a seed-and-nutrient layer was explored to produce dense and mechanically stable ZIF-8 membranes on a porous alumina support.[142] In this method, the alumina support was first infiltrated with MIm and zinc nitrate, then the infiltrated alumina discs were dipped into the solution of ZIF precursors, and finally the alumina discs saturated with ZIF precursors were subject to heat treatment at different temperatures.

Microwave-assisted seeding has been reported recently as a new approach to rapidly prepare supports strongly attached to seed crystals by Kwon et al.[143] With the assistance of microwaves, the strong absorption of microwave energy by precursors increased the temperature of the supports quickly, resulting in the rapid heterogeneous nucleation and growth of ZIF-8 nanocrystals (as shown in Figure 2.5). Thus, the seeded supports with a high packing density were quickly generated in a couple of minutes. Consequently, continuous and well-intergrown ZIF-8 membranes were formed after subsequent secondary growth on the seeded supports.

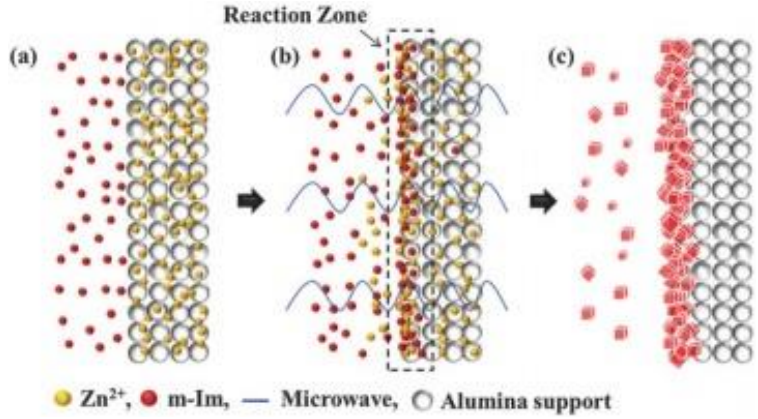

Figure 2.5 Scheme of microwave-assisted seeding; (a) a support saturated with a metal solution in a ligand solution, (b) formation of a reaction zone at the interface and microwave irradiation, and (c) heterogeneous nucleation near the support surface.[143]

An alternative way to improve the bonding between ZIF crystals and the support is to make use of an appropriate polymeric support because of the high affinity between ZIF and polymer. In this regard, continuous ZIF-90 membrane was fabricated on polymeric hollow fiber which is poly(amide–imide)Torlon.[145] Continuous and dense ZIF-8 thin layers were also synthesised on the porous polyethersulfone (PES) support via secondary seeded growth,[146] in which ZIF-8 has good affinity with the PES

support due to the trapping of ZIF-8 crystals into the surface pores of polymer and the favorable interactions between the organic ligands of ZIF-8 and PES.

However, on the other side, secondary growth crystallisation methods require the seeding step ahead of the solvothermal growth step. As a result, potential reproducibility issues may occur due to the increased number of steps in the process.[147] In addition, it is not easy to control the membrane thickness on the submicron scale by this method.[141]

2.2.2.1.2 In situ crystallisation

ZIF films or membranes can also be prepared by in situ crystallisation methods, where the polycrystalline layer is grown on the plain or chemically modified support through a one-step or one-pot solvothermal or hydrothermal synthesis without any seeding growth process.

In situ crystallisation methods for the generation of ZIF membranes have been widely explored by many researchers. A ZIF-8 membrane was prepared by Bux et al in a microwave assisted solvothermal reaction through an in situ crystallisation method.[148] [149] In brief, the solution mixture with porous titania support was charged into an autoclave and heated in a microwave oven, then a compact ZIF-8 layer was formed on the porous titania support. Meanwhile, continuous and compact ZIF-8 membrane was produced on the outer surface of porous hollow fibres by in situ crystallisation too.[150] It is worth noting that the direct growth of ZIF-8 membrane from zinc foil was reported by Zhu et al.[151] It is believed that the nucleation of ZIF-8 crystals took place heterogeneously from the grain boundaries at the zinc foil surface, which acted as both the substrate and the reagent. In addition, ZIF-69 membrane was also fabricated on the porous α-alumina discs by solvothermal in situ synthesis.[152]

In order to prepare ZIF films and membranes efficiently via in situ crystallisation methods, several advanced approaches, including substrate modification before in situ crystallisation, counter-diffusion-based in situ crystallisation and solvent evaporation-based in situ crystallisation, have been developed.

Substrate modification before the in situ crystallisation process is a widespread strategy to obtain continuous ZIF membranes. As shown in Figure 2.6a, a simple

support modification by heating and fast evaporation before rapid solvothermal in situ synthesis resulted in the preparation of ZIF-7 and ZIF-8 membranes easily.[153]

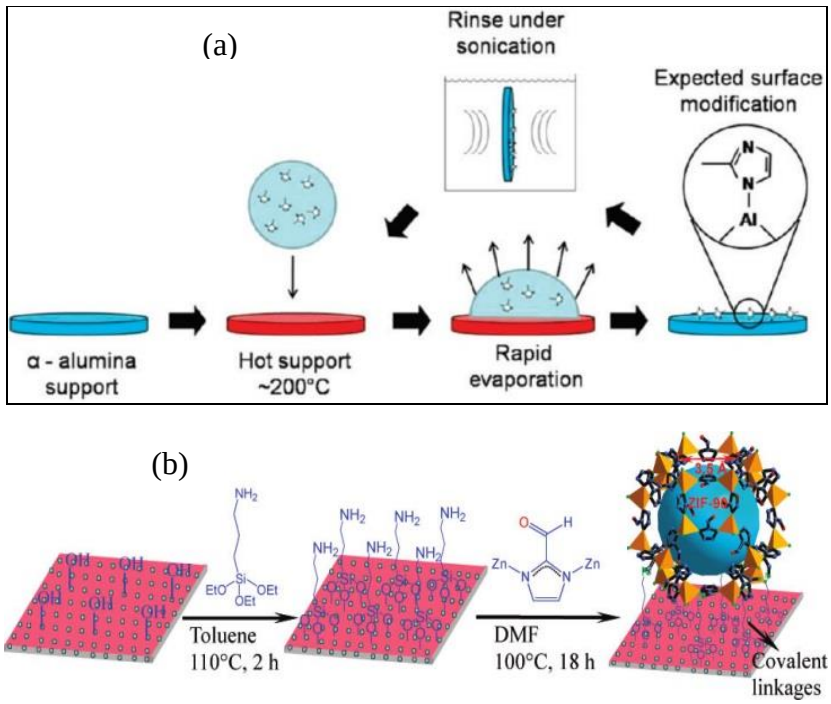

Figure 2.6 (a) Illustration of the substrate modification process[153] and (b) the preparation of ZIF-90 membranes using APTES as a covalent linker between membrane and alumina support.[154]

On the other hand, 3-aminopropyltriethoxysilane (APTES) was used as covalent linkers to promote the heterogeneous nucleation and membrane growth for in situ crystallisations.[142] A compact layer of ZIF-22, ZIF-90 and ZIF-95 was successfully formed on the APTES-modified support after the solvothermal synthesis.[154-157] The scheme of preparation of ZIF-90 membranes using APTES as a covalent linker is shown in Figure 2.6b. In addition, a ZIF-9-67 hybrid membrane was prepared on vinyltrimethoxysilane modified α-alumina support by a solvothermal synthesis method.[158]

Recently, a one step in situ synthesis of ZIF-8 membranes on unmodified porous α-alumina supports in the presence of sodium formate has been reported by Shah et al,[159] where the sodium formate has been found to enhance the heterogeneous nucleation of ZIF-8 crystals on alumina support as well as to promote the intergrowth of ZIF-8 crystals for the formation of continuous ZIF-8 membranes. Other continuous

ZIF membranes such as ZIF-7, ZIF-90, ZIF-61 and SIM-1 can also be prepared using the same one step in situ crystallisation method.

In addition, ZIF membranes can be prepared by a counter-diffusion-based in situ crystallisation method where the supports physically separate the metal ions from the ligand molecules. The counter-diffusion concept enables the synthesised membranes to be healed readily without completely disassembling the membrane capacity.[160] This unique feature of the counter-diffusion concept made the poorly intergrown membranes to be healed. Furthermore, the costly precursor solutions can be recycled multiple times for in situ synthesis.[160] Yao's group first reported the preparation of ZIF-8 membrane using a counter-diffusion-based (or contra-diffusion) in situ crystallisation synthesis method.[161] Two different synthesis precursor solutions were separated by the nylon membrane, and the ZIF-8 films were then grown on the surface of the nylon membrane (shown in Figure 2.7). Recently, they have claimed that ZIF-8 membrane was prepared in aqueous system using a stoichiometric ratio of Zn^{2+} and MIm (1:2) through a similar method.[162] Moreover, Xie et al generated ZIF-8 membrane by contra-diffusion synthesis where two precursor solutions were separately filled in the inner and outer volume of the APTES-modified tubular support.[163] In addition, Kwon et al successfully prepared continuous and well-intergrown ZIF-7, ZIF-8 and SIM-1 membranes with enhanced microstructure on precursor-soaked alumina supports,[160] where the porous alumina support was first saturated with a metal precursor solution, which was then placed in the ligand solution to initiate the reaction, and the ZIF-8 membrane was finally formed by counter-diffusion-based in situ crystallisation method.

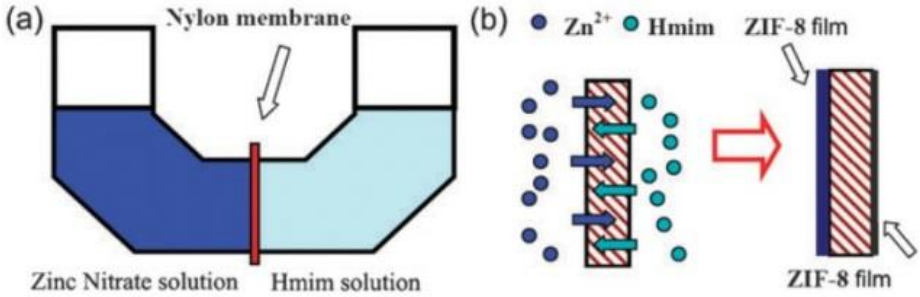

Figure 2.7 (a) Diffusion cell for the preparation of ZIF-8 film and (b) the schematic formation of ZIF-8 films on both sides of the nylon support via contra-diffusion of Zn^{2+} and MIm through the pores of the nylon support.[161]

Based on the concept of evaporation-induced crystallisation as reported by Ameloot et al,[13] Shah et al came up with the solvent evaporation-based in situ crystallisation (rapid thermal deposition).[164] They successfully prepared well-intergrown ZIF-8 membrane on a α-alumina support. In this rapid thermal deposition approach, the porous supports were soaked with a precursor solution and then subjected to elevated temperature. Rapid solvent evaporation from the supports drived the flow of the precursor solution from inside to outside of the supports, consequently, crystallisation was realised both inside and outside the supports simultaneously to form ZIF-8 membrane (as shown in Figure 2.8).

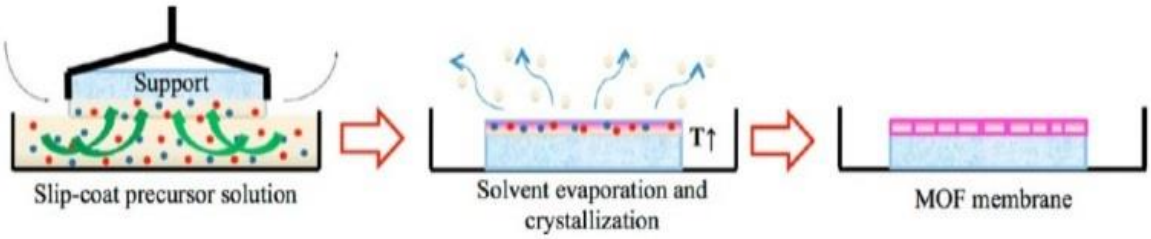

Figure 2.8 Scheme of the rapid thermal deposition approach.[164]

Compared with the secondary growth crystallisation method, the in situ crystallisation method is relatively simple and, therefore, it is the popular synthesis approach for the preparation of ZIF membranes. However, it is worth noting that in situ crystallisation method has its intrinsic disadvantage that it critically relies on the high rates of heterogeneous nucleation on the support surface to successfully obtain continuous and well-intergrown ZIF layers. Whether a high surface nucleation rate can occur or not depends on various factors, e.g., the surface chemistry of the support material. On the contrary, in the secondary growth crystallisation method, nucleation and crystal growth are decoupled, hence, high nucleation rates and chemical interactions with the support material are less crucial.[139]

2.2.2.2 ZIF based film/membrane composites

ZIFs have gained great attention as fillers for the generation of ZIF based film/membrane composites, namely, mixed matrix membranes (MMMs), due to their molecular sieving effect, facile synthesis and good compatibility with polymers. A desirable MMM usually consists of well-dispersed particles at as high loading as possible.[165] Although polymers are frequently used in the commercial gas separation, they often confront a significant problem of the compatibility between the polymeric phases and inorganic phases for optimum dispersion and interfacial contact that leads

to moderate loading of inorganic materials.[166, 167] Superior MMM permeability and performance selectivity can be achieved by matching the properties of the polymer and ZIF. Generally, several main issues, such as the tuneable synthesis of the sub-micrometer ZIF nanoparticles, the defect-free interface between the polymers and ZIFs and the controllable dispersion of ZIFs within the polymer, should be considered during the fabrication of ZIF/polymer MMMs.[168]

Traditionally, the supported MMMs are prepared through several steps including solution-blending, dip-coating and solution-casting. Briefly, the polymer and ZIF with specific permeability and performance selectivity are selected, and the amount of ZIF with a desired concentration which is necessary for the preparation of MMM is added to an organic polymer solution of known composition under stirring. The resulting mixture is sonicated or stirred for some time until an apparently homogeneous suspension was obtained. The suspension is cast or coated onto a substrate to form membranes, followed by heating and drying under vacuum. Finally, the membrane is cooled down to room temperature under vacuum (shown in Figure 2.9).

Figure 2.9 Basic procedures for the preparation of mixed matrix membranes.

The preparation of ZIF-8/polydimethylsiloxane (PDMS) MMMs for solvent resistant nanofiltration was reported by Basu et al.[169] It was found that the introduction of ZIF-8 as filler into PDMS-based MMMs was not successful due to the poor adhesion between PDMS and ZIF-8; however, it was successful after surface modification of ZIF-8 with trimethylsilyl which resulted in a strongly improved adhesion. In addition, ZIF-8/polymethylphenylsiloxane (PMPS) MMMs were also successfully fabricated by incorporating ZIF-8 nanoparticles into silicone rubber (PMPS) membranes.[170] The resulting MMM showed very promising performance in recovering bio-alcohols from dilute aqueous solution and offered significant potential for the construction of a membrane reactor for in situ product recovery applications.[170]

A variety of polyimides have been used in the production of ZIF/polyimide MMMs. So far ZIF-8,-90/Matrimid® polyimide[165, 168, 171-173] ZIF-8,-90/6FDA-DAM polyimide[173, 174] and ZIF-8/6FDA-based polyimide[175] MMMs have been successfully prepared using the conventional ZIF/polyimides fabrication method. In addition, sulfone-based polymers have been used in the generation of ZIF/polymer MMMs. For example, the preparation of ZIF-8/poly(1,4-phenylenether-ether-sulfone)[176] and ZIF-20,-8/polysulfone MMMs[68, 177, 178] were reported. Moverover, polybenzimidazole (PBI) is another major polymer that has been widely used in the fabrication of ZIF/polymer MMMs, and PBI has remarkable resistance to high temperatures (up to 500 ^{o}C)[179] with superior compression strength.[180] The preparation of ZIF-7/PBI nano-composite membranes was reported by Yang et al.[181] ZIF-8,-90/PBI MMMs were also prepared by the dip-coating or solution-casting method.[70, 182-184] Besides, other MMMs such as ZIF-90/P84,[185] ZIF-8/PIM-1,[186] ZIF-7/poly (amide-b-ethylene oxide) (Pebaxs1657)[187] and ZIF-7/chitosan[188] MMMs have been prepared too.

Apart from the traditional method used for the preparation of MMMs, recently advanced MMMs fabrication approaches have been developed.[189-191] The first successful production of mixed matrix asymmetric hollow fibre membranes containing ZIF-8 fillers was reported by Dai et al.[189] They incorporated ZIF-8 into a polyetherimide matrix and produced dual layer asymmetric hollow fibre membranes via the dry jet-wet quench method. SEM images of pure polyetherimide and ZIF-8/polyetherimide mixed matrix hollow fibre membranes are displayed in Figure 2.10. The dual-layer fibres incorporating the ZIF-8 show a noticeable interface indicating good adhesion between the two layers.

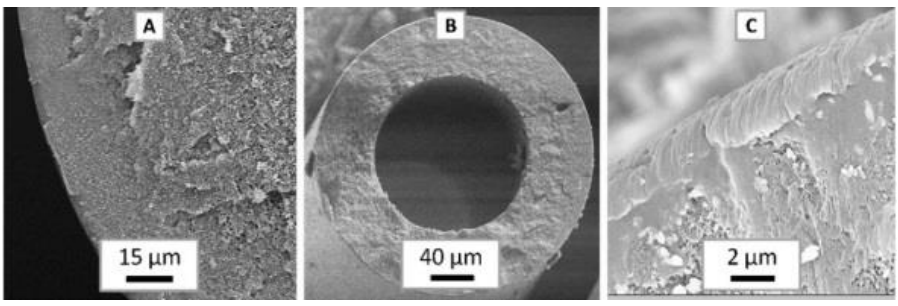

Figure 2.10 SEM images of pure polyetherimide (A) and ZIF-8/polyetherimide mixed matrix hollow fiber membranes (B and C).[189]

Liu et al successfully prepared a homogeneous ZIF-8/silicone rubber (PMPS) nanocomposite membrane with high particle loading and excellent stability on a hierarchically ordered stainless-steel-mesh (HOSSM) via a novel ‘‘plugging–filling’’ method.[191] In this synthesis strategy, the use of HOSSM can effectively avoid the problems such as the poor dispersion of the ZIF-8 nanoparticles at high particle loading and the deterioration of membrane performance during long-term operation, therefore remarkably improve the separation index and selectivity of ZIF-8. As shown in Figure 2.11, the holes were plugged in the top layer of the HOSSM with ZIF-8 nanoparticles, and silicone rubber was then filled the spaces between the ZIF-8 nanoparticles and the mesh wires. A homogeneous ZIF-8/silicone rubber (PMPS) membrane was finally obtained after repeated dip-coating and evaporation.

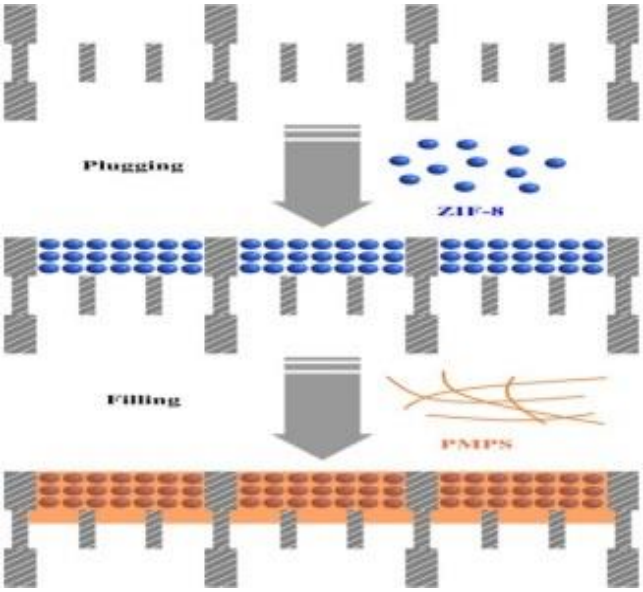

Figure 2.11 Schematic illustration of the fabrication procedure of the HOSSM-ZIF-8/silicon rubber membrane by the ‘‘plugging–filling’’ method.[191]

Although numerous research groups have studied ZIF/polymer MMMs, only a few reports on cross-linked MMMs have been published. Recently, Wijenayake et al[190] have reported the cross-linked ZIF-8/6FDA-durene. The surfaces of the synthesised MMMs were cross-linked by reacting with the ethylenediamine (EDA) vapour to improve gas selectivity. In brief, annealed ZIF-8/6FDA-durene MMM was first suspended in the chamber containing EDA vapour; the MMM was then reacted with EDA vapour inside the chamber for 40 min at about 35 ℃, the cross-linked MMM was finally obtained after washing and drying. The chemical reaction taking place is

the ring-opening reaction of the imide group in the 6FDA-durene to an amide group followed by cross-linking during EDA vapour reaction.[190]

2.2.3 Conclusions

In conclusion, undoubtedly there are a variety of synthesis methods available for the generation of ZIFs and ZIF-based composites. For the powder-based ZIF materials, the conventional synthesis methods such as solvothermal and hydrothermal methods, have been widely applied and developed with modifications (such as the ionothermal method and sonothermal method). Meanwhile, other synthesis methods like solvent-free synthesis and mechanical methods have been developed quickly too. While for the film/membrane-based ZIF materials, apart from the conventional secondary growth and in-situ method, novel ZIF membrane fabrication methods such as the electrospray deposition technique has recently been developed.[192, 193] The remaining challenge in the field is to produce ZIFs in large scales to meet the potential commercial application needs. Nevertheless, there is no doubt that novel synthesis approaches for ZIF materials which can offer reproducibility, scalability and cost-effectiveness will emerge with the effort of scientists in the future.

2.3. Applications of ZIF materials

Owing to their high level of porosity, adjustable compositions and controllable structures, applications of ZIF materials are emerging. Both pure ZIFs and ZIF-based films/membranes have been developed as multifunctional materials to show versatile excellent performances beyond the traditional uses as adsorbents and catalysts, and even contribute to the developments in the fields ranging from sensing and electrical devices to drug delivery. In this section, the typical and emerging applications of ZIF materials are highlighted and discussed.

2.3.1 Gas separation

Gas separation is becoming a more and more important research topic with the increasing of the global issues such as natural gas purification and carbon dioxide capture. Therefore, it is urgent and desirable to develop green and energy-efficient ways to realise gas separations effectively. As a novel class of highly porous materials with similar structures to zeolites, ZIF materials possess tuneable pore sizes, variable structures and multiple chemical functionalities. As a result, they hold great potential in gas separation applications. Both pure ZIFs and ZIF-based polymer mixed matrix

membranes (MMMs) have been widely explored in various gas separations, which are summarised in Figure 2.12.

The pure ZIF membranes have been explored in various gas separations showing very promising separation performance. Some gas separation results on pure ZIF membranes are summarised in Table 2.2. Obviously, most of the investigations are focused on hydrogen separation and carbon dioxide separation, due to the great potential in practical applications of ZIF membranes in these fields. Moreover, the reported ideal selectivity of pure ZIF membranes is variable and dependant on the properties of the gases involved. Generally, the nature and content of the target gas, the ZIF types and the operation conditions such as temperature and pressure, can all alter the separation efficiency. For example, due to the fact that the pore size of ZIF-7

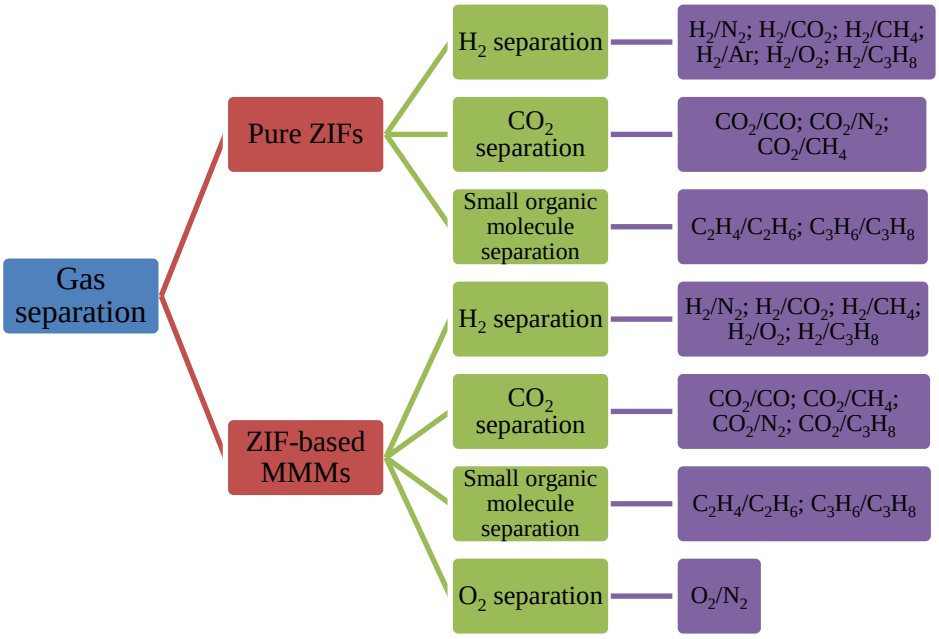

Figure 2.12 Summary of gas separation on both pure ZIFs and ZIF-based MMMs.

with sodalite (SOD) topology is about 0.3 nm,[55] which is just between the molecule sizes of H_2 (0.29 nm) and CO_2 (0.33 nm), a ZIF-7 membrane was applied in the H_2 mixed gas separations, such as H_2/CO_2, H_2/N_2 and H_2/CH_4. ZIF-7 membranes prepared by Li's group exhibited high H_2 permeance.[136, 137] Moreover, the high H_2/CO_2 ideal selectivity and separation factor exceeded the Knudsen separation factor

and the latest Robeson's "upper-bound" line.[194] ZIF-8 material is another promising porous membrane. Thanks to its pore size (~ 0.34 nm) and hydrophobic nature, ZIF-8 membranes have advantages to separate H_2 from other large gas molecules.[62] For instance, the ZIF-8 membrane prepared by Bux et al showed a high H_2/CH_4 separation factor (11.2), which significantly exceeded the Knudsen separation factor for H_2/CH_4 (~ 2.8).[148] ZIF-8 membranes also exhibited excellent separation performance for C_2-C_3 hydrocarbon mixtures. The high quality ZIF-8 membranes prepared by Pan et al showed that the separation factors for mixtures of ethane/propane, ethylene/propylene and ethylene/propane are 80, 10 and 167, respectively.[129] In addition, ZIF-69 membranes were reported for CO_2/gas mixtures separations, such as CO_2/CO, CO_2/N_2 and CO_2/CH_4. The continuous ZIF-69 membrane presented a high separation factor of CO_2/CO (3.5) with CO_2 permeance of 3.6 x 10^{-8} mol m^{-2} s^{-1} Pa^{-1} at room temperature.[152]

Table 2.2 Gas separation performance of pure ZIF membranes

Materials	Gases	Separation performance	Ref.
ZIF-7	H_2/CO_2	Ideal selectivity 6.7; separation factor 6.5	136
ZIF-7	H_2/CO_2; H_2/N_2; H_2/CH_4;	Separation factor 13.6; 18.0; 14.0 (H_2 permeance of 4.5x10^{-8} mol m^{-2} s^{-1} Pa^{-1}; at 220 ^oC)	137
ZIF-7	H_2/CO_2	Separation factor 9.6 (H_2 permeance of 4.61x10^{-7} mol m^{-2} s^{-1} Pa^{-1}; at 25 ^oC)	192
ZIF-78	H_2/CO_2	Ideal selectivity 11.0; separation factor 9.5	134
ZIF-8	H_2/CH_4	Separation factor 11.2 (298 K) (1 bar)	148
ZIF-8	H_2/N_2; H_2/CH_4	Ideal selectivity 11.6; 13	153
ZIF-8	H_2/C_3H_8	Separation factor above 300	139
ZIF-8	H_2/CO_2	Ideal selectivity 32.2; (7.1 for a H_2/CO_2 binary mixture (45% H_2))	150
ZIF-8	H_2/N_2; H_2/CO_2	Ideal selectivity 15.4 (H_2 permeance 5.73 x 10^{-5} mol m^{-2} s^{-1} Pa^{-1}); 17.0	163
ZIF-8	H_2/N_2	Ideal selectivity 5.7 (H_2 permeance 1.7 x 10^{-7} mol m^{-2} s^{-1} Pa^{-1})	142
ZIF-8	H_2/CO_2; H_2/Ar; H_2/O_2; H_2/N_2; H_2/CH_4	Ideal separation factor 4.9; 7.0; 13.6; 15.1 and 9.8.	195
ZIF-8	H_2/C_3H_8	Ideal selectivity more than 1000 (H_2 permeance 15x10^{-7} mol m^{-2} s^{-1} Pa^{-1}; room temperature)	131
ZIF-8	H_2/Ar; H_2/O_2; H_2/N_2; H_2/CH_4	Ideal separation factor 9.7; 10.8; 9.9; 10.7 (H_2 permeance 4x10^{-7} mol m^{-2} s^{-1} Pa^{-1}; 333K)	146
ZIF-8	H_2/CO_2; H_2/N_2; H_2/CH_4	Ideal separation factor 5.2; 7.3; 6.8 (H_2 permeance 1.1 x 10^{-6} mol m^{-2} s^{-1} Pa^{-1})	135

ZIF-8	H_2/N_2	Ideal selectivity 4.6	[162]
ZIF-8	H_2/N_2; H_2/CH_4	Ideal selectivity 10.3; 10.4 (H_2 permeance 20.8 x 10^{-8} mol m^{-2} s^{-1} Pa^{-1})	[196]
ZIF-8	H_2/CO_2; H_2/N_2; H_2/CH_4	Ideal selectivity 5.8; 11.1; 12.8 (303 K and 0.1 MPa)	[197]
ZIF-95	H_2/CO_2; H_2/N_2; H_2/CH_4; H_2/C_3H_8	Mixture separation factor 25.7; 10.2; 11.0; 59.7 (325 ^oC; 1 bar) (H_2 permeance 1.9 x 10^{-6} mol m^{-2} s^{-1} Pa^{-1})	[157]
ZIF-9 and ZIF-67 hybrid	H_2/CO_2	Ideal separation factor 8.89 (room temperature).	[158]
ZIF-69	CO_2/CO	Permselectivity 3.5 (3.6 x 10^{-8} mol m^{-2} s^{-1} Pa^{-1}; at room temperature)	[152]
ZIF-69	CO_2/N_2; CO_2/CO; CO_2/CH_4	Separation factor 6.3; 5.0; 4.6. (1 x 10^{-7} mol m^{-2} s^{-1} Pa^{-1}; at room temperature; 1 atm)	[125]
ZIF-7	CO_2/CH_4	Selectivity 12.22 (298K)	[198]
ZIF-8	C_2H_6/C_3H_8; C_2H_4/C_3H_6; C_2H_4/C_3H_8	Separation factors 80; 10 and 167	[129]
ZIF-8	C_3H_6/C_3H_8	Separation factor up to 50	[130]
ZIF-8	C_2H_4/C_2H_6	Selectivity 2.8 (1 bar); 2.4 (6 bar)	[127]
ZIF-8	H_2/C_3H_8; C_3H_6/C_3H_8	The ideal separation factors 2000 and 59 (298K)	[199]
ZIF-8	C_3H_6/C_3H_8	Selectivity about 30 (C_3H_6 permeance 1.1 x 10^{-8} mol m^{-2} s^{-1} Pa^{-1})	[200]

In addition, the presence of organic linkers in ZIFs offers better compatibility with organic polymers compared with other additives. Therefore, there has been growing interest in MMMs containing ZIF fillers, and a number of ZIF-polymer MMMs have been developed. Polymers that have been frequently explored include polysulfones, polyimides, polyetherimide, poly(1,4-phenylen ether-ether-sulfone) and polybenzimidazole. The MMMs can not only potentially extend the separation performance of traditional polymers, but also maintain the processing convenience of polymers. Generally, the permeability and diffusion properties of gases increase with the increase of ZIF loading. For this reason, a desirable MMM consists of well-dispersed ZIF particles with loadings as high as possible. For instance, polyimides and polyimides were frequently applied with the combination of ZIFs for gas separations due to their high gas selectivity and high stability. With the increased amount of ZIF-8, ZIF-8/Matrimid® MMMs exhibited increasing gas selectivity of CO_2/CH_4, as evidenced by the reported ideal selectivity of CO_2/CH_4 to be around 124.89 (~ 50% ZIF-8),[165] 35.8 (~ 20% ZIF-8)[168] and 39 (~ 25% ZIF-8)[172] respectively. Other

polyimides, such as 6FDA-based polyimides, 6FDA-durene and 6FDA-durene/DABA,[175] and 6FDA-DAM,[173, 174] were used in MMMs for gas separation. The ideal selectivity for C_3H_6/C_3H_8 was 27.38 by using 6FDA-durene/DABA (9/1), which increased up to 31 by using 6FDA-DMA. In addition, polybenzimidazole (PBI) was also applied in the incorporation of ZIF particles. Yang et al put ZIF-7 into PBI as ZIF-7/PBI MMMs, which exhibited high ideal H_2/CO_2 selectivity up to 12.3.[181, 201] ZIF-8/PBI MMMs also demonstrated good separation properties, where the ideal selectivity of H_2/CO_2 was 12.3 at 230 ^oC,[184] and the separation factor of CO_2/CH_4 was 32.[201]

2.3.2 Catalysts

Since ZIFs are analogous to another typical kind of porous materials, aluminosilicate zeolites, one of the most important and commercially available catalytic materials,[202] ZIFs and ZIF-based materials have been considered as efficient catalysts for a number of reactions, although much development is still required. Generally, pure ZIF materials can be active catalysts for many reactions including transesterification,[203] the Knoevenagel reaction,[204, 205] the Friedel-Crafts acylation,[206] the monoglyceride synthesis,[207] the synthesis of carbonates,[208-210] oxidation and epoxidation,[211-213] and the hydrogen production,[214, 215] as shown in Figure 2.13.

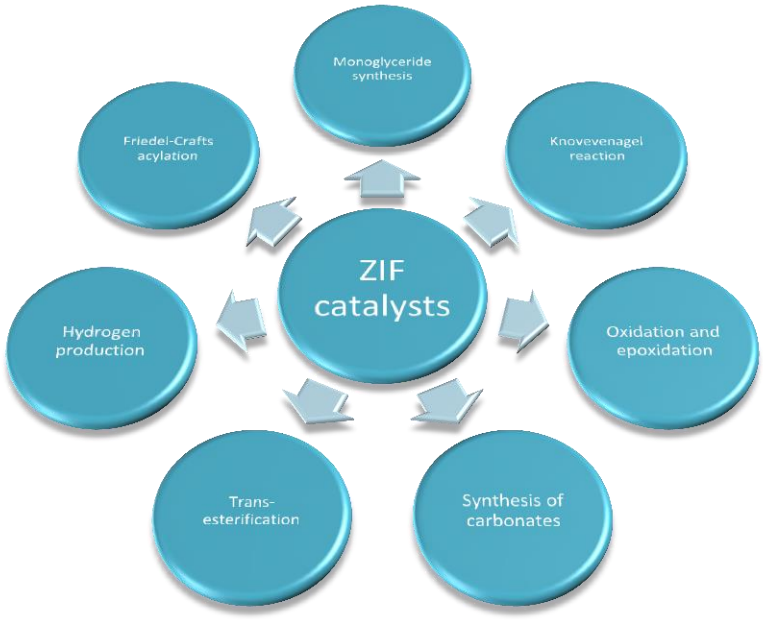

Figure 2.13 Summary of ZIFs as catalysts in various reactions.

ZIFs including ZIF-8,[204] ZIF-9 and ZIF-10 [205] have been demonstrated as efficient heterogeneous catalysts for the Knoevenagel reaction between the condensation of benzaldehyde and malononitrile to form benzylidene malononitrile. In addition, it has been reported that ZIF catalysts can be facilely separated from the reaction mixture and re-used without significant degradation in catalytic activity.[204, 205]

ZIF-8 was reported as an effective heterogeneous catalyst not only for transesterification reaction of vegetable oil with significant reactivity,[203] but also for Friedel-Crafts acylation reactions between benzoyl chloride and anisole without the requirement of an inert atmosphere, where high reaction conversion was achieved with small amounts of ZIF-8 (2-6 mol%).[206] Moreover, hierarchical nanosized ZIF-8 was explored as a re-usable catalyst for monoglyceride synthesis by Wee et al.[207] They found that the hierarchical ZIF-8 with mesopores which was transformed from the ZIF-8 nanoparticles through reaction with a fatty acid, was a promising heterogeneous catalyst for selective monoglyceride formation through esterification of oleic acid with glycerol under mild reaction conditions. Furthermore, ZIF-8 was demonstrated as an active catalyst for the formation of carbonates. For example, ZIF-8 performed as an efficient and reusable heterogeneous catalyst for the synthesis of ethyl methyl carbonate from the dimethyl carbonate and diethyl carbonate.[208] Carreon et al[209] found that ZIF-8 and amine-functionalised ZIF-8 exhibited high epoxide conversions and moderate to high selectivities at reaction temperatures as low as 70 ^{o}C in the synthesis of chloropropene carbonate from carbon dioxide and epichlorohydrin. In addition, they also reported the catalytic performance of ZIF-8 in the reaction between carbon dioxide and styrene oxide.[210] The reusable ZIF-8 catalyst showed significant catalytic activity at temperature as low as 50 ^{o}C. It is believed that Lewis acid Zn^{2+} sites and the nitrogen basic moieties from the imidazole linker in the frameworks of ZIF-8 can promote the adsorption of carbon dioxide, which can boost the further conversion to the carbonates.

Moreover, ZIFs have also exhibited catalytic activity in both oxidation and epoxidation reactions. For instance, ZIF-9 has been successfully used for the aerobic oxidation of tetralin with good reusability.[211] Meanwhile, ZIF-9 catalyst has also demonstrated catalytic activity in the oxidation of small aromatic molecules including phthalan, vanillyl alcohol, guaiacol, syringol, veratryl alcohol, and cinnamyl alcohol

in the presence of molecular oxygen.[212] It has been reported that ZIF is catalytically active in the aerobic epoxidation of olefins by using isobutyraldehyde under facile conditions.[213]

In addition, ZIFs have been demonstrated as catalysts for the hydrogen production. Fischer et al [214] reported the heterogeneous ZIF-8 catalyst for the dehydrogenation of dimethylamine borane (DMAB) shown in Figure. 2.14. The reaction could be carried out at room temperature due to the strong caging effect, probably combined with the polar and Lewis acid/base properties of the framework. In addition, ZIF-9 was also reported to be an efficient catalyst for $NaBH_4$ hydrolysis with relatively high stability.[215]

Apart from the pure ZIFs being active catalysts for a number of reactions, due to the large surface area and tuneable pore size, ZIFs can also act as promising supports for the incorporation of various metal or oxide nanoparticles to form novel catalysts with novel physical and chemical properties. Some typical catalytic applications of metal or metal oxide particles supported on ZIF materials are summarised in Table 2.3.

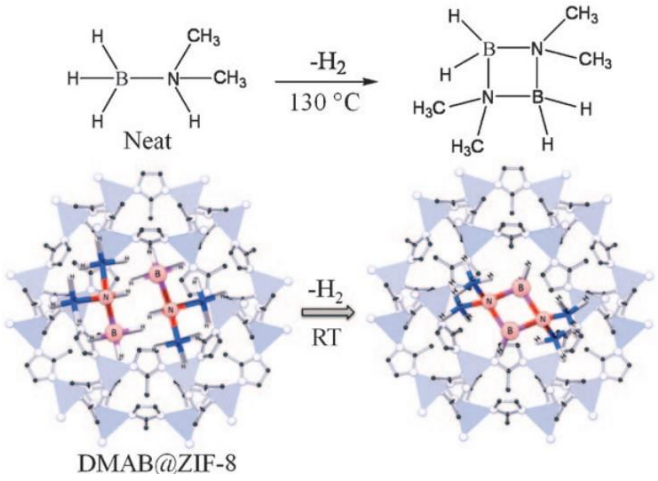

Figure 2.14 Conceptual representation of the catalytic dehydrogenation and cyclisation of DMAB inside ZIF-8.[214]

Recently, the immobilisation of noble metal nanoparticles on the surface of ZIF materials as catalytically active catalysts has been widely explored. For instance, Au nanoparticles have been introduced into ZIF-8 to form a nanocomposite which was

applied as an active catalyst in the gas phase CO oxidation.[216] In another example, the encapsulation of Au nanoparticles into the ZIF-8 and ZIF-90 matrixes results in the formation of Au@ZIF-8 and Au@ZIF-90 nanocomposites respectively, which exhibited high catalytic activity in the aerobic oxidation of benzyl alcohol in methanol and benzene. It is claimed that the functional groups of ZIF-90 can promote the stabilisation and monodispersion of those size-matched Au nanoparticles.[217] Various nanoparticles including Au, Ag and Pt have been incorporated into ZIF-8 via an encapsulation strategy by Guang et al,[218] and the resulting supported catalysts have demonstrated good catalytic activity in CO oxidation and excellent selectivity for catalytic hydrogen of n-hexene versus cis-cyclooctene. Other noble metal nanoparticles such as Ir,[219] Pd,[220] Ru [221] and Pt [222], were also incorporated into ZIF-8 as efficient catalysts.

Table 2.3 Summary of the catalytic applications of metal or metal oxide particles supported on ZIF materials

ZIF material	Additional materials	Reaction(s) catalysed	Ref.
ZIF-8	Au nanoparticles	Oxidation of CO	216
ZIF-8 ZIF-90	Au nanoparticles	Oxidation of the aldehyde groups	217
ZIF-8	Au@Ag core-shell nanoparticles	Reduction of 4-nitrophenol	223
ZIF-8	Au, Ag and Pt nanoparticles	Oxidation of CO, hydrogen of n-hexene	218
ZIF-8	Pt nanoparticles	Hydrogen of alkene	222
ZIF-8	Pt and TiO_2 nanotubes	Degradation of phenol	224
ZIF-8	Pd nanoparticles	Amincarbonylation	220
ZIF-8	Ir nanoparticles	Hydrogenation of cyclohexene and phenylacetylene	219
ZIF-8	Ru nanoparticles	Asymmetric hydrogenation of acetphenone	221
ZIF-8	Fe_3O_4 micropheres	Knovenenagel condensation	225
ZIF-8	Zn_2GeO_4 nanorods	Conversion of CO_2	226
ZIF-65	Molybdenum oxide	Degradation of methyl orange and orange II dyes	227

Moreover, it has also been reported that the core-shell structured bimetallic Au@Ag nanoparticles can be stabilised on ZIF-8, and synergistically improve the catalytic reduction reaction activity compared with the monometallic and alloy metal nanoparticles.[223] In particular, yolk-shell nanocrystal/ZIF-8 nanocomposites were

produced using Cu_2O as a sacrificial template and the resulting yolk-shell nanostructures showed high activity and selectivity for gas-phase hydrogenation catalysis, where the measured activation energy of the yolk−shell nanostructure was different from that of the core−shell nanostructure, demonstrating the influence of the cavity structure on catalytic performance.[228] Additionally, core-shell magnetic microspheres Fe_3O_4/ZIF-8 were successfully prepared and exhibited excellent catalytic activity for Knoevenagel condensation reaction of benzaldehyde and ethyl cyanoacetate.[225]

In addition, other nanostructured materials such as nanotubes[224] and nanorods[226] have also been incorporated into ZIFs for photocatalytic activities. For example, Tayirjan et al loaded TiO_2 nanotubes with Pt/ZIF-8 and found that Pt/ZIF-8-TiO_2 nanotubes had remarkably improved the performance in the photodegradation of phenol,[224] which could be served as a potential photocatalyst for water purification. Moreover, ZIF-8/Zn_2GeO_4 nanorods composite exhibited enhanced photocatalytic conversion of CO_2 into liquid CH_3OH fuel,[226] and Molybdenum oxide incorporated into ZIF-65 deomonstrated the photocatalytic property of degradation methyl orange and orange II dye under visible light.[227]

2.3.3 Sensing and Electronic devices

The intrinsic properties of ZIF materials such as high textural properties, tuneable pore diameters and easy functionalisation enable them to be used in sensors and electronic devices. Particularly, the excellent selective adsorption properties of ZIFs render them good candidates for chemical sensing while the large microporosity and hydrophobicity of ZIFs are attractive for low dielectric constant applications.

Hupp and co-workers first demonstrated the use of ZIF-8 as a sensing material by constructing a ZIF-8-based Fabry−Pérot device as a selective sensor for chemical vapors and gases.[229] The ZIF-8 sensor exhibited some chemical selectivity when it was exposed to the vapor of ethanol-water mixtures with varied ethanol contents, and the sensor also showed ethanol-concentration-dependence responses.

In addition, ZIFs are attractive matrices for the biosensor constructions. For instance, ZIFs based electrochemical biosensors for in vivo electrochemical measurement such

as glucose have been successfully prepared.[230] ZIF materials including ZIF-7, ZIF-8, ZIF-67, ZIF-68 and ZIF-70 served as a matrix respectively for co-immobilising electrocatalysts methylene green and glucose dehydrogenase on the electrode surface, and the as-fabricated ZIF-based biosensors demonstrated a high selectivity and sensitivity to the glucose in the cerebral system.

Based on the luminescence intensity, ZIF-8 has been studied as luminescent probes with multi-function sensitivity to detect metal ions and small molecules.[231] The luminescence intensity of ZIF-8 is highly sensitive to Cu^{2+} and Cd^{2+} ions and small molecules such as acetone due to the imidazole nitrogen site within the porous frameworks. Meanwhile, ZIF-8 nanoparticles can be used as a sensing platform for fluorescence-enhanced detection of nucleic acids with a high selectivity down to single-base mismatch.[232] The DNA detection is shown in Figure 2.15. In detail, the ZIF-8 nanoparticles combine closely with dye-labeled ssDNA after quenching the dye fluorescence; dsDNA, which detaches from the ZIF-8 nanoparticles, can be measured by the fluorescence recovery of the ZIF-8/ssDNA complex with the target. In addition, another ZIF material, $Zn_2(IM)_4$ (DMF), where IM represents imidazolate and DMF stands for dimethyl formamide, exhibits broad range near-UV excitation and broadened photoluminescence emission, which makes this material potentially useful in sensing near-UV or UV white light.[233]

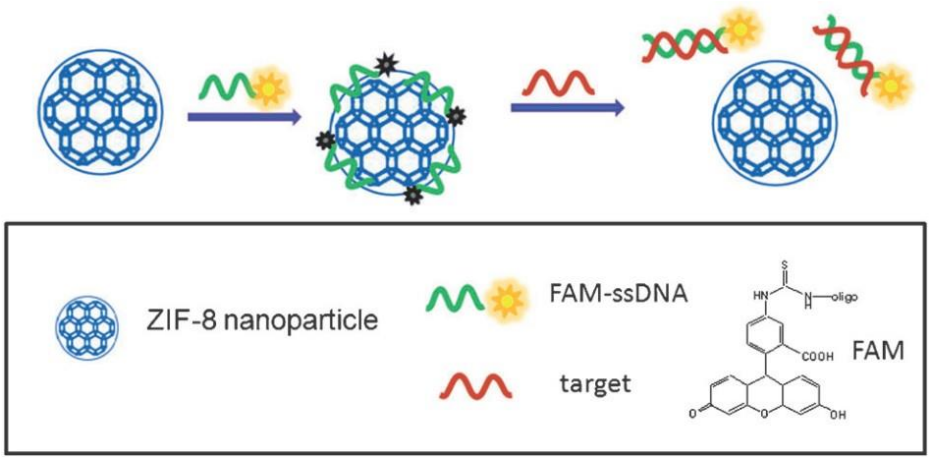

Figure 2.15 A schematic illustration of fluorescence-enhanced nucleic acid detection using ZIF-8 nanoparticles as a sensing platform.[232]

Recently, branched polyethylenimine-capped carbon quantum dots (BPEI-CQDs)/ZIF-8 nanocomposites have been successfully developed for the detection of

Cu^{2+} ions in environmental water, and the results showed that it can be used as an ultrasensitive and highly selective sensor for Cu^{2+} ion.[234] It is also recognised that BPEI-CQDs/ZIF-8 composites not only exhibit excellent fluorescent activity and sensing selectivity due to the addition of CQD, but also show strongly and selectively accumulate target analytes because of the adsorption property of ZIF-8.[234]

ZIF materials have been used in electronic devices as well.[235, 236] For example, ZIF-8 was claimed to be a promising candidate to substitute future low-κ dielectrics in microelectronics by Salvador et al who found that the ZIF-8 films that were deposited on silicon wafers, had the effective κ value necessary for the chip devices and good mechanical properties too.[235] On the other hand, ZnO@ZIF-8 heterostructures have shown great potential in electronic devices such as sensors. In particular, Zhang et al developed ZnO@ZIF-8 core-shell heterostructures which exhibited selective photoelectrochemistry responses to various hole scavengers because of ZIF-8 could successfully detect H_2O_2 in the presence of a series of buffer solutions (shown in Figure 2.16).[236] In addition, the ZnO@ZIF-8 core-shell heterostructures, where ZnO forms the core and ZIF-8 forms the shell, have exhibited not only excellent semiconducting properties because of the addition of ZnO,[237, 238] but also molecule-size-selective abilities due to the adsorption property of ZIF-8.

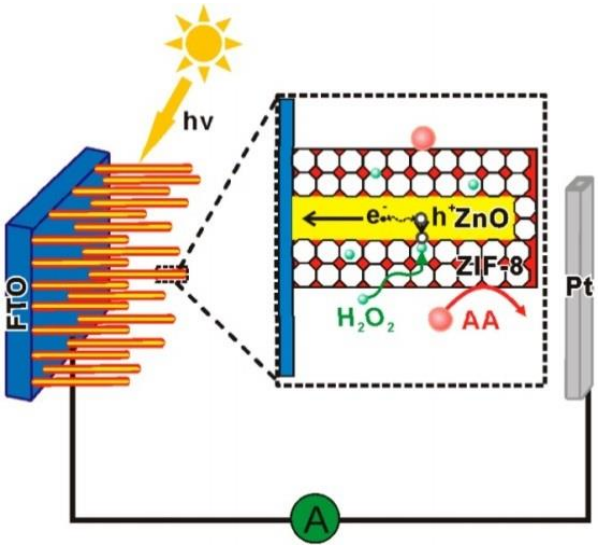

Figure 2.16 Scheme of the photoelectrochemistry sensor with selectivity to H_2O_2 (where AA is ascorbic acid, FTO is fluorine-doped tin oxide).[236]

2.3.4 Drug delivery

Thanks to the excellent porous structures, exceptional thermal and chemical stabilities, tuneable multifunctionalities in the frameworks and pH-sensitive release properties, ZIF materials are emerging as a powerful platform for drug deliveries and/or controlled release of drug molecules.[239]

ZIF-8 has been treated as a valuable candidate for the delivery of anticancer agents. Inspired by the fact that ZIF-8 is stable in water and sodium hydroxide aqueous solution[55] but quickly decomposable in acid solution, Sun et al first found that ZIF-8 could be used as a drug delivery vehicle due to its pH-sensitive property.[240] ZIF-8 has also exhibited a significant loading capacity for the anticancer drug 5-fluorouracil due to its highly porous structures and excellent textural properties. By responding to the physio-pathological pH signals, two different approaches for the release of the encapsulated 5-fluorouracil from ZIF-8 are illustrated as shown in Figure 2.17. The anticancer drug doxorubicin (DOX) was readily incorporated into ZIF-8 matrix.[241] The DOX incorporated ZIF-8 not only exhibited a high-loading (0.049 g DOX g^{-1}) and progressive release (66% of the drug released after 30 days), but also demonstrated a higher antitumoral potential and lower cytotoxicity towards the HL-60 and MCF-7 cell lines compared with the pure DOX. Recently, polyacrylic acid@ZIF-8 nanoparticles have been fabricated and employed as pH-dependent drug delivery vehicles in a facile and simple way.[242] The synthesised polyacrylic acid@ZIF-8 nanoparticles possessed ultrahigh loading capability for drug DOX (1.9 g DOX g^{-1}) with pH-sensitive drug release property and excellent biocompatibility. More recently, carbon nanodots@ZIF-8 nanoparticles with tuneable sizes and fluorescence intensity have been produced as a carrier for simultaneous pH-responsive drug delivery and fluorescence imaging of cancer cells.[243] Release experiments showed that the 5-fluorouracil loaded carbon nanodots@ZIF-8 nanoparticles exhibited a slow release at an early stage while a faster one at later stage.

Moreover, caffeine, an amphiphilic drug with remarkable lipolytic activity, has been encapsulated into the ZIF-8 cages.[244] In this case, ZIF-8 material could not only control the release of caffeine, but also provide thermal protection for the drug molecules in the cages during the high temperature process.

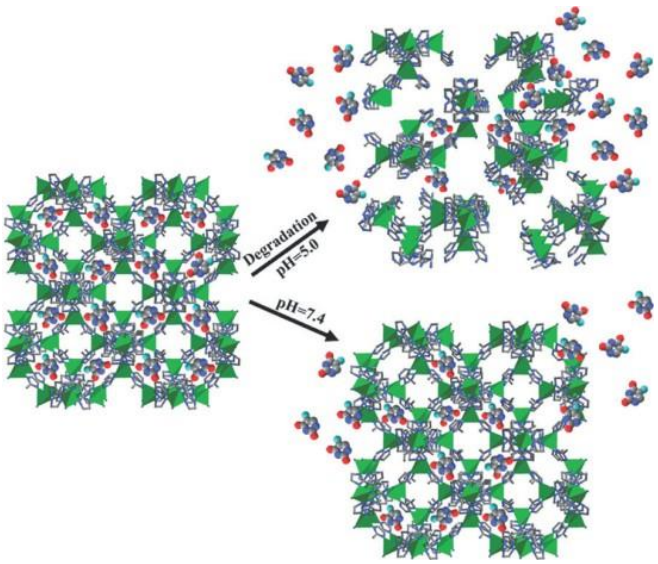

Figure 2.17 Schematic illustration of two ways to release the encapsulated 5-fluorouracil from ZIF-8.[240]

2.3.5 Conclusions

The intrinsic nature of ZIFs, such as diverse structures mimicking zeolites, adjustable components and functionalities and excellent textural properties, enables ZIF materials to be a truly versatile class of crystalline porous materials with great potential for numerous applications, ranging from conventional applications including adsorption, gas separation and catalysis to beyond traditional ones like sensing and electronic devices, and drug delivery. Both pure ZIFs and ZIF-based films/membranes or composites have been developed as multifunctional materials with versatile performances in many application fields. The combinations of ZIFs with other nanostructured components to form novel nanocomposites may further facilitate the wide applications due to the advantages of both components. Other novel applications of ZIFs such as in the areas of electrochemical and mechanical applications are to be developed. More exploiting of ZIFs in clean energy and/or environmentally sustainable energy resources will emerge soon.

2.4 Synthesis of ZIF derivatives

As discussed above, ZIF materials have received a lot of attention because of their diverse structures, tuneable properties and various applications such as gas storage and catalysis. Recently, ZIF materials acting as outstanding templates and precursors open a new way to generate porous carbons and their related nanostructured functional materials based on their high specific surface areas, controllable structures

and abundant metal and organic species. The ZIF materials consist of metal ions and organic units, which can be transformed to porous carbons, nanostructured metals/metal oxides or their hybrid materials under various synthesis conditions. The formation of different materials depends on the synthesis conditions, such as types of gas atmosphere, temperatures, post-treatment conditions, and so on.[245] In this section, recent developments of ZIFs with open frameworks for the preparations of porous carbons and related nanostructured functional materials derived from ZIFs are reviewed.

2.4.1 From ZIFs to carbons

Recently, the use of ZIFs as templates or precursors to produce porous carbon materials has been developed.[246] Thanks to the high surface area and pore volumes of ZIFs, these porous structures are beneficial to generate the porous carbon materials. For example, ZIF-8 is a typical template or precursor to fabricate porous carbon. An additional element N in ZIF-8 could effectively functionalize the carbon structure. Qiang's group first used ZIF-8 as a template or precursors and furfuryl alcohol as the second carbon source to prepare the nanoporous carbon materials by carbonization.[247] More recently, Yamauchi's [248, 249] and Xia's [246] group reported the direct carbonization of ZIF-8 without additional carbon sources. Generally, ZIF-8 was placed a flow-through tube furnace, and heated to the targeted temperature (from 600 to 1000 ^{o}C) under the inert atmosphere (argon or nitrogen) with flow rate of 50 ml/min, and then maintained at target temperature for 3 h, followed by cooling down to room temperature in inert atmosphere. The resulting products were then washed with 1 mol L^{-1} hydrochloric acid three times to remove inorganic compounds, followed by further wash with distilled water.[246] The different pyrolysis temperatures (600-1000 ^{o}C) could lead to the different BET surface areas.

Furthermore, other ZIF materials such as ZIF-67,[250] ZIF-68,[251] ZIF-69,[251] ZIF-7 [252] have been investigated as good candidates for the preparation of porous carbon materials. Their synthesis approaches are similar to that of ZIF-8. These ZIF materials were firstly heated at high temperature under the inert gas atmosphere, and cooled down to the room temperature with the inert gas protection. The resulting powders were then washed by acid to remove inorganic pieces. After water washing, the porous carbons were finally obtained.

2.4.2 From ZIFs to metal oxides

Synthesis of nanostructured metal oxides with controllable size, shape, porosity and surface area has been developed these years. Since the ZIF structure contains metal centres coordinated with organic complexes. Controlling heating under various conditions can produce unique metal oxide structures.[253] For example, zinc oxide nano particles can be obtained by the direct one-step air calcination.[254] Yamauchi's group reported a uniform 3D nanoporous cobalt oxide (Co_3O_4) can be prepared from ZIF-67.[255] ZIF-67 was firstly heated in nitrogen atmosphere at 500 ^oC for 30 min, which prevents collapse of the porous structure. Otherwise, only a very bulky structure was formed. These powders were then cooled at room temperature. Furthermore, the nitrogen was then turned off, and the sample exposed in air atmosphere at 350 ^oC for 2 h, leading to the conversion of these powders to cobalt oxide.

Comparing with other existing metal oxide synthesis methods, there are two main advantages of using ZIFs: (1) the processing method is relatively simple, which gives potential for the large-scale production; (2) the morphologies and particle sizes of metal oxides can be well controlled.[253]

2.4.3 From ZIFs to carbon-metal/metal oxide composites

The homogeneous dispersion of metal nodes in ZIF scaffolds makes it possible to generate metal or metal oxide nanoparticles that disperse into the carbon matrix under controlled thermolysis conditions.[253]

Our group first utilized ZIF-8 to synthesize ZnO/porous carbon composites by direct carbonization in argon atmosphere, but no XRD peaks related to either ZnO or Zn can be observed in these composites.[256] [257] Later, we designed a new synthesis strategy to create efficient porous carbon-metal oxide composites. We came up with a facile and green one-step oxidation method using water steam at high temperatures with the utilisation of ZIF-8 as a precursor to generate atomically homogeneous dispersed ZnO/nanoporous N-doped carbon composites.[254]

Furthermore, Yamauchi's group demonstrated the generation of nanoporous carbon–Co_2O_3 hybrid materials using a two-step thermal conversion of ZIF-9 [258]. In the first step, ZIF-9 powders were heated to the targeted carbonization temperature under nitrogen atmosphere. After reaching the targeted temperature, the powders were held

for 5 h and then cooled to room temperature naturally. In the second step, the obtained black powder was thermally treated under ambient air in a muffle oven. The powders were heated at the desired temperatures (250 or 300 ℃) for 90 min with a slow heating rate (1 ℃ min^{-1}) (shown in Figure 2.18).

In addition, ZIF-67 is another typical ZIF material used as a precursor to produce carbon-cobalt/cobalt oxide composites. Recent research works show that the porous carbon-cobalt nanocomposites could be obtained by the thermal pyrolysis of ZIF-67. In details, ZIF-67 was heated to the target temperature (600-1000 ^{o}C) at a rate of 5 ^{o}C min^{-1} in a tubular furnace under the inert gas (nitrogen or argon) flow (60 mL min^{-1}). The targeted temperature was maintained for 2 h and then cooled down to room temperature naturally.[259-261] The synthesis method for the preparation of porous carbon-cobalt oxide nanocomposites is a little complicated. Similarly to carbon-cobalt composites, ZIF-67 was firstly pyrolysed under Argon atmosphere. The resulting product was then dispersed in 2 M H_2SO_4 solution for 12 h to remove metallic cobalt with large particle size. After that, the as-collected black product was then heated at 350 ^{o}C with a rate of 5 ^{o}C min^{-1} and maintained at 350 ^{o}C for 2 h under air flow to finally to obtain carbon-cobalt oxide nanocomposites.[262]

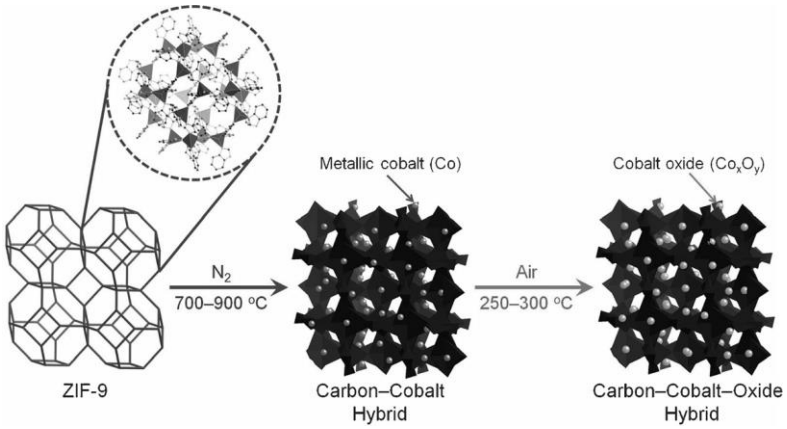

Figure 2.18 Schematic representation of the formation of carbon-cobalt-oxide hybrid materials through the twostep thermal treatment of ZIF-9.[258]

2.4.4 Conclusions

From the above literature survey, it is obvious that ZIF-derived materials have attracted much attention in recent years. Compared with other methods for the synthesis of carbons, metal oxides, and their nanocomposites, such an *in situ* generation approach makes the materials structure controllable. For the

nanocomposites, the nano-particles could be highly dispersed into the carbon matrix with less aggregation. One of the main challenges for this material generation method is, however, how to precisely control the particle size.

2.5 Applications of ZIF derivatives

2.5.1 Supercapacitors

Carbon materials have been shown to have a high surface area and tailorable porosity which makes them very attractive candidates for electrochemical energy storage.[263, 264] Recently, carbonaceous nanostructures of ZIF derivatives have been widely explored in supercapacitor applications. For example, derivation of N-doped carbons from ZIF-67 has been reported. This as-synthesized graphitic carbon could improve overall conductivity and capacitance.[250] It exhibited a high capacitance value of 238 F g^{-1} at 20 mV s^{-1} comparing with other ZIF derived carbon materials. Table 2.4 summarizes the different types of carbon from ZIFs with their respective surface areas and capacitance performance. Apart from the porous carbon products, layered double hydroxide nanocages derived from ZIF-67 also exhibited a very high capacitance of 1203 F g^{-1} at the current density of 1 A g^{-1}.[265]

Table 2.4 Surface area and capacitance performance of carbon derived from different types of ZIFs

Precursor	T (^{o}C)	S (m^2 g^{-1})	V (cm^3 g^{-1})	C (F g^{-1})	Ref.
ZIF-8	900	1215	0.57	214 at 5 mV s^{-1}	[248]
ZIF-8	800	2972	2.56	211 at 10 mV s^{-1}	[266]
ZIF-67	800	943	0.84	238 at 20 mV s^{-1}	[250]
ZIF-69	1000	2264	2.16	168 at 5 mV s^{-1}	[251]
ZIF-7	950	783	0.56	185 at 25 mV s^{-1}	[267]

2.5.2 Fuel cells

2.5.2.1 Oxygen reduction reaction (ORR) catalysts

As a typical ZIF material, ZIF-8 was designed as a microporous host in a catalyst system. In addition, the rich nitrogen contents in ZIF-8 could be converted to

nitrogen-doped in carbon which is beneficial for ORR.[268, 269] After a simple heat treatment of ZIF-8 loaded with phenanthroline and ferrous acetate, the result electrocatalysts exhibited a volumetric activity of 230 A cm^{-3} at 0.8 $V_{iR\text{-}free}$, which is best among the non-precious metal catalysts.[270]

Another ZIF material, ZIF-67, was used as a template to convert to cobalt/porous carbon composites. Through precise control of the particle size of the catalysts, small particle with more catalytic surface and active sites were produced.[259] The smallest ZIF-67 crystal derived catalyst exhibited a good ORR performance in acidic solution with an onset potential of 0.86 V and a half-wave potential of 0.71 V. The cobalt cations coordinated by the aromatic nitrogen ligands in ZIF-67 may be beneficial to the formation of ORR active sites in the as-synthesized composites.[260] In addition, other groups also reported that the cobalt/porous carbon composites derived from ZIF-67 precursors exhibited excellent ORR performance.[261, 271, 272] The electron transfer mechanism revealed a four-electron transfer process in ORR.

A novel $Co@Co_3O_4@C$ core@bishell nanoparticles into porous carbon matrix derived from ZIF-9 showed excellent ORR activity.[273] It exhibited a high ORR onset potential of 0.93 V and a half-wave potential of 0.81 V, of which performance is among the best performing non-precious metal electrocatalysts. It also showed superior stability to that of the commercial Pt/C catalyst, and good tolerance to methanol cross-over effect. The large surface area, high ratio of micropores, and favourable nanostructure enabled the rapid transportation of oxygen and proton.

2.5.2.2 Oxygen evolution reaction (OER) catalysts

In most cases, the synthesized OER catalysts were produced in the form of particle agglomerates which were then transferred into a thin film coated on electrodes such as glassy carbon. ZIF-67 is one of the most studied ZIF materials as a precursor for OER catalysts.[262, 274] For example, Co_3O_4 nanoparticles embedded in nitrogen-doped porous carbon dodecahedron which was derived from ZIF-67, exhibited superior OER electrochemical performance. The OER performance test of this composite showed an onset potential of 1.52 V, which is very close to that if the commercial Ir/C noble metal catalyst (1.45 V). Notably, the current density of commercial Ir/C even drops below that of this composite at potentials higher than 1.64 V, indicating this composite is a highly active OER catalyst. The resultant catalyst also possesses

superior durability.[262] Only little decay (4.4%) was shown in OER activity of the as-synthesized nanocomposite up to 6000 s of continuous operation at 1.7 V. This high durability result is probably due to the fact that the protective layers of carbon stabilize the Co_3O_4 nanoparticles.

In addition, another example is the nitrogen-doped graphene/cobalt-embedded porous carbon polyhedron hybrid derived from graphene oxide/ZIF-67 composites. This hybrid exhibited a good OER performance. The current density of 10 mA cm^{-2} can be achieved at a small overpotential of 1.66 V for the hybrid. The introduction of cobalt and nitrogen dopants was proposed to render the adjacent carbon atoms charged positively. The charged carbon atoms can facilitate the adsorption of OH ions, and then promote the electron transfer. As a result, the OER overpotential of this hybrid was comparable to those of other reported OER catalysts.[274] Furthermore, the chronoamperometric test of the hybrid also showed a small current density change after 6000 s, indicating the high OER stability.

2.5.3 Conclusions

Based on the above literature survey, it is clear that ZIF derivatives exhibited excellent electrochemical catalytic performance. ZIF derivatives have developed in these directions in recent years, but most recent research has been focused on developing nanoporous materials for energy storage and conversion such as supercapacitors and fuel cells. Therefore, potential applications in other fields need to be further explored.

2.6 Summary

In summary, the development and recent progress towards the different synthesis strategies to generate ZIF and ZIF derivatives materials are analysed and summarised. Recent years have witnessed explosive researches and development in ZIFs and ZIF derivatives, from synthesis to applications. The intrinsic porous nature of ZIFs combined with structures analogous to conventional aluminosilicate zeolites render a wide range of synthesis approaches available for efficient generation of ZIFs. The abundant functionalities in their framework coupled with the high textural properties enable ZIF materials to be a class of versatile crystalline porous materials. Thanks to the various molecular-like organic-inorganic structures of ZIFs, porous carbon based nanocomposites can be produced by using ZIFs as excellent precursors or sacrificial templates. To further develop new synthesis strategies and explore the potential

applications of ZIFs and ZIF derivatives, it is vital to take advantages of the knowledge and experiences gained from other research fields such as those in zeolites. Given the strong interest in ZIFs and ZIF derivatives by various research communities, we believe that new concepts and techniques for the synthesis of ZIFs and ZIF derivatives materials, new applications of the fast-growing unique materials for further exploring ZIFs and ZIF derivatives will continue to emerge in the future.

3. Chapter 3: Experimental methodology

3.1 Introduction

The generic experimental methodology and procedures applied for this research work will be presented in this chapter. For clarification, in this thesis, the uncertainties to numbers in tables and the error bars to graphs is less than 5%.

3.2 Synthesis of ZIF materials and ZIF based composites

3.2.1 Materials

2-methylimidazole (99%, MIm), $Zn(NO_3)_2•6H_2O$ (99%), $ZnSO_4$, $ZnCl_2$, $ZnBr_2$, $Zn(OAc)_2$, $NaNO_3$, Na_2SO_4, NaCl, NaBr, NaOAc, 35 wt% ammonia aqueous solution, graphite power, $KMnO_4$ and 30% H_2O_2 were obtained from Sigma-Aldrich and used without further purification.

3.2.2 Sample preparation

3.2.2.1 Preparation of ZIF-8

ZIF-8 was synthesized by rapid pouring an aqueous solution of $Zn(NO_3)_2•6H_2O$ into an aqueous ammonia solution of 2-methylimidazole and the mixture was stirred at room temperature for 24 h. In a typical synthesis, zinc nitrate dissolved in distilled water was added into a solution of 2-methylimidazole in distilled water, where 35 wt% ammonia solution was added in the water beforehand. After aging for 24 hours at room temperature or elevated temperatures, the product was collected by repeated centrifugation (6000 rpm, 10 min). The resulting powders were then air dried in a fume cupboard for five days before subject to further characterizations. For the research of Hofmeister anion effect on the formation of ZIF-8, ZIF-8 was synthesized by rapid pouring an aqueous solution of zinc salts into an aqueous ammonia solution of 2-methylimidazole and the mixture was stirred at room temperature for 24 h. In a typical synthesis, zinc salt and corresponding sodium salt dissolved in distilled water was added into a solution of MIm in distilled water, where 35 wt% ammonia solution was added in the water beforehand. After aging for 24 hours at room temperature, the product was collected by repeated centrifugation (6000 rpm, 10 min). The resulting powders were then air dried in a fume cupboard for five days before subject to further characterizations.

3.2.2.2 Preparation of ZIF-67

ZIF-67 was synthesized from cobalt nitrate hexahydrate and 2-methylimidazole in water, following a modified procedure.[275] . In a typical synthesis, 0.9 g $Co(NO_3)_2 \cdot 6H_2O$ was dissolved in 6 mL of distilled water; then 11 g 2-methylimidazole was dissolved in 40 mL of distilled water. These two solutions were mixed and stirred for 24 h at room temperature, then the resulting purple precipitates were collected by centrifuging (6000 rpm, 10 min), washed with water and methanol subsequently for 3 times, and the resulting powders were then air dried in a fume cupboard for several days before subject to further characterizations.

3.2.2.3 Preparation of Ni-substituted ZIF-67

Ni-substituted ZIF-67 crystals were solvothermally synthesized using requisite amount (1, 2, and 4 mmol) of $Ni(NO_3)_2 \cdot 6H_2O$ together with 4 mmol $Co(NO_3)_2 \cdot 6H_2O$ and 300 mmol 2-methylimidazole dissolved in 100 mL distilled water, then stirred continuously at room temperature for 24 hours. Followed washing with 15 mL water for three times, solid powders were collected and the obtained product was designed as Ni_xCo_y-ZIF-67, where x and y stand for the molar ratio of n(Ni)/n(Co) in the Ni-substituted ZIF-67 sample.

3.2.2.4 Preparation of GO/ZIF-8 composites

Firstly, GO was prepared using a modified Hummers method.[276] Briefly, graphite powder (10 g) was mixed with concentrated H_2SO_4 (230 mL) under stirring and the temperature was controlled by an ice/water bath at 0 ^oC, followed by the addition of $KMnO_4$ (30 g) slowly to the suspension and the reaction mixture was maintained at 2 ^oC under continuously stirring. After removal of the ice bath, the mixture was further stirred at room temperature for 0.5 hour. Oxidation of graphite occurred and very viscous dark brown product formed after 0.5 hour. Distilled water (230 mL) was slowly added into the reaction vessel and the temperature was controlled at 98 ^oC. The diluted suspension was stirred for an additional 15 minutes and further diluted with distilled water (1.4 L), before the addition of H_2O_2 (30%, 100 mL). The mixture was left overnight. GO particles, settled at the bottom, were separated from the excess liquid by decantation followed by centrifugation. The product was washed with plenty of distilled water for many cycles and separated by centrifugation untill neutral pH is achieved. The solid product was transferred to a petri dish and dried in air for further applications.

Pure ZIF-8 was prepared from aqueous ammonia solution via a slightly modified approach which was recently developed by our group.[277, 278] GO/ZIF-8 composites were also synthesized via the same method with slight modification. Briefly, requisite amount of GO was dispersed in dilute aqueous ammonia solution and sonicated for 1 hour, followed by the addition of requisite amount of 2-methylimidazole (MIm) under stirring. This solution was then combined with a requisite amount of $Zn(NO_3)_2$ aqueous solution and was further stirred at room temperature for 24 hours. The molar ratio of synthesis mixture is Zn^{2+} : MIm : NH_3 = 1 : 8 : 100. The product was collected after several water wash and centrifugation (6000 rpm for 10 minutes) cycles. Finally the power was air dried in a fume cupboard at room temperature. The resulting solid composites with variable GO content were denoted as xGO-ZIF, where x stands for the weight percentage of GO in comparison with ZIF-8. Therefore 3GO-ZIF, 10GO-ZIF, 15GO-ZIF, and 30GO-ZIF corresponds to the sample with weight ratio of GO to ZIF-8 in the composite is 3, 10, 15 and 30 wt%, respectively. A mechanic mixing of GO and ZIF-8 with 10 wt% GO content, labelled as 10GO-ZIF-M, was also prepared for comparison.

3.2.3 Characterisation techniques

3.2.3.1 Structural characterisation techniques

3.2.3.1.1 XRD

XRD technique was applied to identify the crystallographic structure and crystallite size of the materials. X-rays can produce constructive interference after reflection from atomic planes within the crystalline materials. The relationship between the incident and reflected X-rays can be expressed by Bragg's formula:[279, 280]

$$n\lambda = 2d \sin\theta \qquad (3.1)$$

where n is an integer, λ is the wavelength of X-rays, d is the inter-lattice spacing, and θ is the incident angle. Samples were examined by plotting the angular position and the intensities of the resultant diffracted peaks.

Crystalline size can be assessed by measuring the peak breadth in an X-ray diffraction pattern, which can be explained by Debye-Scherrer equation:[280]

$$t = \frac{K\lambda}{B\cos\theta} \qquad (3.2)$$

where *t* is the crystallite size and *K* is the crystalline shape factor, λ is the wavelength of incident X-rays, *B* is the breath of the peak at half maximum intensity of a specific plane (hkl) in radians. For the materials testing, fine powders of samples were flatly pressed onto a glass slide. XRD investigations were performed using Bruker D8 Advanced X-ray diffractometer. XRD patterns were recorded with Cu Kα radiation (40 kV-40 mA) at step time of 1 s and step size of 0.02 ^{o}. Crystalline phase features were identified with the computer software of Bruker Advanced X-ray Solutions.

3.2.3.1.2 SEM

Scanning Electron Microscopy (SEM) is a powerful tool to characterize the surface morphology under high magnification. For a standard SEM instrument, an electron stream produced by a filament is directed towards the sample, using a positive electron potential. As demonstrated in Figure 3.1, this stream is confined and focused by metal apertures and magnetic lenses into a thin and focused monochromatic beam. Electrons from the electron source can scatter elastically and produce back scattered electrons (BSE). They can also interact with the specimen resulting in the generation of X-rays and new electrons which are called secondary electrons (SE). The secondary electron images can provide the topography of the specimen surface because the secondary electrons are emitted from the very top layer (10 nm) of the specimen.[281]

In our work, SEM images of the samples were recorded using a Philips XL-30 scanning electron microscope in a high vacuum mode and at an acceleration voltage of 20 kV. Samples were mounted using a conductive carbon double-sided sticky tape. A thin (*ca.* 10 nm) coating of gold was sputtered onto the samples to reduce the effects of charging.

3.2.3.1.3 TEM

Transmission Electron Microscopy (TEM) is a powerful tool that enables detailed crystal structure, crystal quality, grain size and crystal orientation study inside materials. The resolution of TEM can approach atomic scale. The electron beams of TEM are similar with that of SEM. However, for TEM, the electron beam is transmitted through an ultra-thin specimen. An image is then formed from the interaction of the electrons transmitted through the specimen. As shown in Figure 3.2, the electron beams are normally generated by thermionic emission of a filament or by field emission of a single tungsten crystal. It is accelerated through an electromagnetic

field that also narrowly focuses the beam. The beam then will pass through the ultra-thin sample, producing transmitted electrons, elastically and inelastically scattered electrons. The prepared thin specimen is inserted onto a plane and located close to the focal plane of the objective lens. The objective aperture is located on the back focal plane of the objective lens, transmitted electrons with a large scattering angle will be blocked, thus enhancing the contrast of the projected image. The image is projected onto a florescent screen or camera by the projector lens.[281] High-resolution transmission electron microscopy (HRTEM) can image the crystallographic structure of a sample, and also can reveal lattices with atomic resolution. During TEM investigation, selected area electron diffraction (SAED) could be used to identify the crystal structural, measure lattice parameters, study crystal orientation of the sample and image based on diffraction contrast.

In our work, TEM images were obtained on a JOEL 2100 at an acceleration voltage of 100 kV. The samples were dispersed in absolute ethanol by moderate sonication at a concentration of 1 wt% solid for 30 minutes. The specimen was dispersed on a copper-supported carbon film.

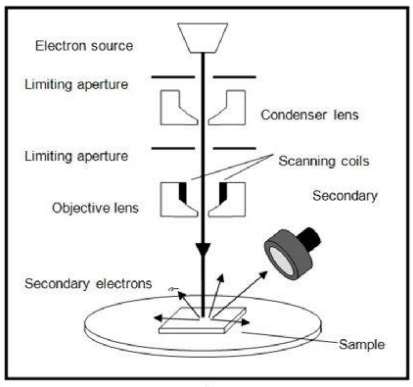

Figure 3.1 Schematic demonstration of SEM.[281]

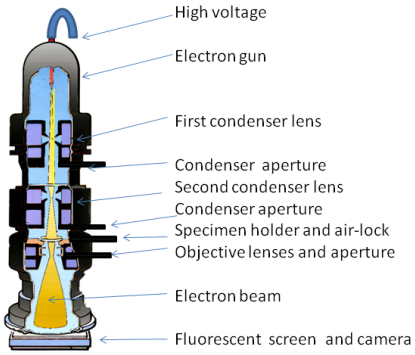

Figure 3.2 Schematic diagram of the basic components of TEM

3.2.3.1.4 FTIR

Fourier transform infrared spectroscopy (FTIR) is a powerful technique which is used to obtain an infrared spectrum by absorption or transmission through a solid, liquid or gas. When IR (infra-red) radiation passes through a sample, some part of the electromagnetic radiation are absorbed and some are transmitted. The resulting spectrum shows the characteristics of the sample and also shows the unique molecular finger-print of the sample.[282] FTIR can measure all infrared frequencies and subsequently decodes them with the assistance of computer software, and the spectral information of the sample is then generated. In our experiment, FTIR spectra were obtained using an Alpha Bruker system. The samples were measured in the wavenumber range of 4000–450 cm^{-1}.

3.2.3.1.5 UV-Vis spectrum

Ultraviolet–visible spectroscopy (UV-Vis) refers to absorption spectroscopy or reflectance spectroscopy in the ultraviolet-visible spectral region. The instrument used in ultraviolet-visible spectroscopy is called a UV/Vis spectrophotometer. It measures the intensity of light passing through a sample (I), and compares it to the intensity of light before it passes through the sample (I_o) by using the light in the visible and adjacent (near-UV and near-infrared) ranges.[283] Molecules containing π-electrons or non-bonding electrons (n-electrons) can absorb the energy from the ultraviolet or visible light to excite these electrons to higher anti-bonding molecular orbitals and thus changes the intensity of light.[283]

In this experiment, powder samples were first dispersed into water, the sample solutions were then measured by the means of a Jenway 6715 UV/Vis spectrophotometer under absorption mode in the wavelength range of 280-700 nm.

3.2.3.2 Thermal investigation and mass spectroscopy

3.2.3.2.1 DTA-TGA

For the thermal investigation of materials, thermal analysis is usually carried out to study the differences of material properties with the temperature change. Differential thermal analysis (DTA) measures the difference in temperature between the actual sample and the reference sample when they are both measured under the same heat whereas thermogravimetric analysis (TGA) determinates the changes in weight of the sample in relation to the change of temperature.

DTA/TGA was performed on a TA SDT Q600 instrument from room temperature to 800 ^{o}C with a heating rate of 10 ^{o}C min^{-1} under a continuous air flow of 100 mL min^{-1}. The obtained thermal data were then analysed using Universal Analysis 2000 computer software provided by TA Instruments, USA.

3.2.3.2.2 MS

Mass spectrometry (MS) is a technique to determine the molecular composition, during which the charged molecules are generated by ionizing the chemicals and the composition is measured by determining their mass to charge ratio.[284] It can be used for the compositional analysis of gases produced from the heated samples. In our study, a Hiden QGA gas analysis mass spectrometer (MS) was coupled with the TA SDT Q600 instrument to monitor and detect the gaseous compositions in the exhaust emission.

3.2.3.3 Textural investigation and gas adsorption

3.2.3.3.1 BET

The Brunauer-Emmett-Teller method (BET) is used to determine the physical adsorption of gas molecules in solid materials with complicated shapes, such as porous materials. In BET method, adsorption and desorption isotherms are used to identify the number of gas molecules adsorbed on the material.[285] The BET equation describes an adsorption where the adsorbate contains multilayer. Its main assumptions includes: (1) The adsorbed molecules are fixe; (2) The enthalpy of adsorption for the layers is the same; (3) The energy of adsorption for the layers is the same except the first one; (4) A new layer can start before another is finished.

In this experiment, N_2 gas sorption isotherms and textural properties of samples were carried out on a Quantachrome Autosorb-iQ gas sorptometer via conventional volumetric technique. Before gas analysis, the sample was evacuated for 4 h at 120 ℃ under vacuum. The textural properties were determined via nitrogen sorption at -196 ℃. The surface area was calculated using the BET method based on adsorption data in the partial pressure (P/Po) range of 0.02-0.22. The total pore volume was determined from the amount of nitrogen adsorbed at P/Po of ca. 0.99.

Generally, the classical macroscopic theories such as Dubinin-Radushkevich (DR), Barrett, Joyner, and Halenda (BJH), and Horvath-Kawazoe (HK) methods can not provide a realistic description of the filling of micropores and narrow mesopores. But

Non-Local Density Functional Theory (NLDFT) model can provide a much more accurate approach for pore size analysis and bridge the gap between the molecular level and macroscopic approaches. Therefore, in our experiment, the pore size distribution (PSD) of the synthesized materials was analysed using the NLDFT model based on N_2 adsorption branch data. In addition, because all our PSD results were analysed by using NLDFT model, the systemic error can be reduced and the PSD results of different samples become comparable.

3.2.3.3.2 CO_2 uptake measurement

CO_2 gas adsorption capacities were carried out on a Quantachrome Autosorb-iQ gas sorptometer via conventional static volumetric technique. Prior to the gas adsorption analysis, the samples were evacuated for 5 h at 120 ℃ under vacuum. The CO_2 uptake capacities were performed at 0 and 25 ℃. The CO_2 adsorption energy (i.e., isosteric heat of adsorption, Q_{st}), which indicates the strength of interaction between CO_2 molecules and the adsorbents, was calculated using the CO_2 sorption isotherms measured at 0 and 25 ^{o}C based on the Clausius-Clapeyron equation.

3.3 Synthesis of ZIF derivatives

3.3.1 Materials

ZIF-8, ZIF-67, and Ni-substituted ZIF-67 (the synthesis methods were shown in Section 3.2.2 Sample preparation).

3.3.2 Sample preparation

3.3.2.1 Zinc oxide/nanoporous carbon composites derived from ZIF-8

ZIF-8 was synthesized from zinc nitrate hexahydrate and 2-methylimidazole in methanol solution, following an established procedure.[286] The porous composites were prepared by a one-step direct carbonization process in the presence of water steam. In a typical synthesis, an alumina boat with 0.25 g of dried ZIF-8 was placed in the centre of a flow-through quartz tube sitting in a tube furnace. The furnace was heated at 10 ^{o}C /min to the target temperature (typically 800 ℃) under pure argon; when the furnace temperature reached 800 ^{o}C, a 20 ml/min of argon flow saturated with water vapour was introduced in and maintained at the target temperature for 3 h. The gas flow was then switched to argon only while the furnace cooled to room temperature. The final product was collected from the quartz tube and labelled as ZnO/C-S-*S*. Another sample was also obtained via the similar one-step direct

carbonization process where a 20 ml/min of argon flow saturated with water vapour is constantly presented during the heating up step, the maintaining at the target temperature for 3 h and the cooling down to room temperature. This sample was designed as ZnO/C-S-*L*. For comparison, the one-step process was also applied to the annealing of ZIF-8 at 800 ^{o}C for 3 h under argon atmosphere with a flow rate of 20 ml/min,[257] and the collected samples was named as ZnO/C-A. A pure ZnO was also obtained via annealing of ZIF-8 in air at 800 ^{o}C for 3 h.

3.3.2.2 Cobalt/nanoporous carbon composites derived from ZIF-67

The composites were prepared by temperature programmed pyrolysis of the ZIF-67 in the argon atmosphere. Typically, 0.25 g ZIF-67 was heated to 600-2000 ^{o}C at 10 ^{o}C min^{-1} under Ar stream in a tube furnace, then kept at the peak temperature for 3 h and allowed to cool down to room temperature. The composites were designated as Co@C-T, where T is the carbonization temperature.

3.3.2.3 Cobalt sulfides/N, S co-doped porous carbon composites and relevant nickel promoted cobalt sulfides/N, S co-doped porous carbon composites derived from ZIF-67

3.3.2.3.1 Cobalt sulfides/N, S co-doped porous carbon composites derived from ZIF-67

ZIF-67 was synthesized from cobalt nitrate hexahydrate and 2-methylimidazole in water, following a modified procedure [82]. The porous nanocomposites were prepared by a one-step direct carbonization and sulfurization process in the presence of hydrogen sulfide. In a typical synthesis, an alumina boat loaded with 0.25 g of dried ZIF-67 was placed in a flow-through quartz tube sitting in the centre of a tube furnace. In order to focus on the specific temperature, the furnace was first heated to the target temperature (typically 600 – 1000 ℃) with ramp rate 10 ^{o}C/min under pure argon atmosphere; when the furnace temperature reached the target temperatures, a 20 mL/min of hydrogen sulfide was then introduced in and maintained at the target temperature for 1 hour. The gas flow was then switched to argon only as the furnace cooled down to room temperature. The final product was collected from the quartz tube and labelled as Co_xS_y@C-z, where z stands for the sulfurization and carbonization temperature. Therefore the sample obtained from sulfurization temperature of 600, 800 and 1000 ^{o}C was labelled as Co_xS_y@C-600, Co_xS_y@C-800 and Co_xS_y@C-1000 respectively.

3.3.2.3.2 Nickel promoted cobalt sulfides/N, S co-doped porous carbon composites derived from Ni-substituted ZIF-67

The porous nanocomposites were prepared via a one-step direct carbonization and sulfurization process in the presence of hydrogen sulfide. In a typical synthesis, an alumina boat loaded with 0.25 g of dried Ni-substituted ZIF-67 was placed in a flow-through quartz tube sitting in the centre of a tube furnace. The furnace was first heated to the target temperature (typically 600 – 1000 ℃) with ramp rate 10 ^{o}C/min under pure argon atmosphere; when the furnace temperature reached the target temperatures, a 20 mL/min of hydrogen sulfide was then introduced in and maintained at the target temperature for 1 hour. The gas flow was then switched to argon only as the furnace cooled down to room temperature. The final product was collected from the quartz tube and labelled as Ni_xCo_yS@C-z, where x and y stand for the molar ratio n(Ni)/n(Co) in the parental Ni-substituted ZIF-67, and z stands for the sulfurization and carbonization temperature. Therefore, the samples obtained at sulfurization temperature of 600, 800 and 1000 ^{o}C from the parental Ni-substituted ZIF-67 with molar ratio n(Ni)/n(Co)=1/4, were labelled as Ni_1Co_4S@C-600, Ni_1Co_4S@C-800 and Ni_1Co_4S@C-1000 respectively.

3.3.3 Characterisation techniques

The crystalline phase structures of ZIF derivatives were identified by XRD. The morphologies of ZIF derivatives were measured by SEM and TEM. Thermal properties of ZIF derivatives were investigated by DTA-TGA, and MS. The textural properties and CO_2 uptake of ZIF derivatives were measured by BET. Details regarding XRD, SEM, TEM, DTA-TGA, MS, and BET are available in Section 3.2.3.

3.3.3.1 Structural characterisation techniques

3.3.3.1.1 EDX

Energy dispersive X-ray analysis (EDX) is normally used for local elemental identification, using an SEM or TEM. When the electron beams interact with the specimen, intense bombardment of high energy electrons on the inner most electron shell of an atom results in the escape of high energy electrons and an escape vacancy is generated. As a result, emitting energy in the form of an X-ray can be generated when an electron from the outer orbit shell then jumps into the empty electron shell. The energy of the X-rays which emits arise from the difference in energy between the two shells, is characteristic to the atomic structure of the element. The number and energy of the X-rays emitted from a specimen can be measured by an energy-

dispersive spectrometer. The element-specific spectral lines are identified to provide the elemental composition of the selective area.[281]

In this work, EDX analysis was performed using the energy dispersive system for detailed compositional analysis combined with SEM or TEM observation. Qualitative and quantitative chemical analysis of the samples down to the atomic number 5 (boron) can be determined.

3.3.3.1.2 XPS

X-ray Photoelectron Spectroscopy (XPS) is a widely used surface-sensitive spectroscopic analysis technique because it can be applied to a broad range of materials and provides valuable quantitative and chemical state information from the surface of the materials. XPS is normally accomplished by exciting a sample surface with mono-energetic Al Kα x-rays causing photoelectrons to be emitted from the sample surface (from the top 0 to 10 nm). An electron energy analyzer is applied to measure the energy of the emitted photoelectrons. The elemental identity, chemical state, and quantity of a detected element can be determined from the binding energy and intensity of a photoelectron peak.[287, 288]

In our experiment, XPS was performed using a Kratos AXIS ULTRA spectrometer with a mono-chromated Al Kα X-ray source (1486.6 eV) operated at 10 mA emission current and 15 kV anode potential. The analysis chamber pressure was better than $1.3x10^{-12}$ bar. The take-off angle for the photoelectron analyser was 90^{o}, and the acceptance angle was 30^{o} (in magnetic lens modes).

3.3.3.1.3 Raman spectroscopy

Raman spectroscopy is a spectroscopic technique providing information about molecular vibrations that can be used for sample identification and quantification. The technique involves shining a laser light source on a sample and detecting the scattered light. The majority of the scattered light is of the same frequency as the excitation source, which is known as elastic scattering. However, a very small amount of the scattered light is shifted in energy from the laser frequency due to interactions between the incident electromagnetic waves and the vibrational energy levels of the molecules in the sample. Plotting the intensity of this "shifted" light versus frequency results in a Raman spectrum of the sample. In a Raman spectrum, the band positions correspond to the energy levels of different functional group vibrations.[289] In addition,

Raman spectroscopy is a powerful technique to investigate carbonaceous materials. In the Raman spectra, the bond stretching of all pairs of sp^2 atoms in both rings and chains and the breathing modes of sp^2 atoms in rings.[290, 291] The G band at around 1590 cm^{-1} supports the presence of some nanocrystalline carbon and a high content of sp^2-hybridized carbon atoms caused by the carbonization of the samples. The D band at around 1340 cm^{-1} is an indication of less disordered carbon.

In this work, Raman spectra were recorded by using Renishaw RM1000 Raman microscope (Wooton-Under-Edge, UK) equipped with a 1200-line/mm grating providing a spectral resolution of 1 cm^{-1}, a diode laser providing excitation at 532 nm/785 nm with up to 300 mW power, and a 40× microscope objective lens was used to focus light onto the substrate. For our powder samples, the powders were pressed flatly onto a Si wafer substrate, and then were placed under the microscope. The system was calibrated using the Raman band of a silicon wafer at 520 cm^{-1}. The Raman spectra of the samples were recorded in the backscattering arrangement, using a 532 nm laser excitation under laser power of 6 mW. Spectral data was acquired using Renishaw v.1.2 WiRE software.

3.3.3.2 Adsorption and photodegradation evaluation

For the samples of zinc oxide/nanoporous carbon composites derived from ZIF-8, adsorption capacity on the removal of methylene blue (MB) in water solution for the as-prepared ZnO/C composites was evaluated in a dark box. In details, 20 mg of as-prepared sample was added to 100 mL of 20 ppm MB solution, and the suspension was immediately kept in the dark box under stirring. At predetermined time intervals, a small amount of suspension was taken out and the concentration of MB in the solution was monitored by the UV-vis spectrophotometry. Similarly, the synergistic effect of adsorption and photocatalytic activities of the ZnO/C samples under the irradiation of visible light was also evaluated. 20 mg of sample dispersed in 100 mL of 20 ppm MB solution was immediately subjected to visible light and the concentration of MB in the solution was monitored at designed time intervals. The visible light (cutoff filter applied, $l > 420$ nm) was provided by 10 lamps of 20W (PerfectLight, wavelength range: 320 nm $\leq \lambda \leq$ 780 nm, light intensity: 160 mW/cm^2).

3.3.3.3 Electrocatalysis measurements

The electrocatalytic performance of the catalysts was evaluated by cyclic voltammograms (CV), linear sweep voltammograms (LSV) and chronoamperometry

in a three-electrode electrochemical cell which was connected to a computer controlled electrochemical workstation CHI 760D, coupled with a rotating disk electrode (RDE) system. The diagram of this electrochemical set up is shown in Figure 3.3. A platinum wire and a Ag/AgCl/KCl (saturated solution) were used as the counter electrode and the reference electrode, respectively. A 3 mm in diameter bare glassy carbon electrode (GCE) or modified GCE with the studied material was used as the working electrode. Prior to use, GCE was hand-polished with chamois leather containing 0.05 μm alumina slurry to obtain a mirror-like surface, washed with ethanol and distilled water by sonication for 5 min and allowed to dry. The modified GCE was prepared by casting a 5 μL aliquot of the catalyst ink, which was obtained by ultrasonically dispersing 1 mg of the catalyst into 0.5 mL 0.05 wt% in alcohol Nafion solution, onto the fresh surface of the pretreated GCE electrode and dried naturally to form a uniform thin film. The loading amount of each catalyst was kept to be 141.5 μg cm^{-2}. For ORR and OER (Oxygen Reduction Reaction and Oxygen Evolution Reaction), the experiments were carried out at room temperature in 0.1 M KOH solution, which was purged with high purity argon or oxygen with a flow rate of 20 mL min^{-1} for at least 30 min prior to each measurement. For HER (Hydrogen Evolution Reaction), the experiments were carried out at room temperature in 0.5 M H_2SO_4 solution. The electrode potential reported in this paper is relative to the reversible hydrogen electrode (RHE) potential, which can be converted by using the basis of Nernst equation as follows:

$$E_{RHE} = E_{Ag/AgCl} + 0.059(pH) + 0.197(V) \qquad (3.3)$$

The kinetics parameters can be analyzed with the K-L equations as following:[292, 293]

$$\frac{1}{J} = \frac{1}{J_K} + \frac{1}{B\omega^{1/2}} \qquad (3.4)$$

$$B = 0.62nFC_0D_0^{2/3}\upsilon^{-1/6} \qquad (3.5)$$

Where J is the measured current density, J_K is the kinetic current density, ω is the angular velocity of the rotating electrode, B is the Levich constant, n is the overall number of electron transferred in the ORR process, F is the Faraday constant (96485 C mol^{-1}), C_0 is the bulk concentration of O_2 (1.2×10^{-6} mol cm^{-3}), D_0 is the diffusion

coefficient of O_2 (1.9×10^{-5} cm^2 s^{-1}) and υ is the kinematic viscosity (0.01 cm^2 s^{-1}) of the electrolyte.

The electron transfer number and the peroxide percentage can be calculated by the equations as following:[292, 293]

$$H_2O_2(\%) = 200 \times \frac{I_r/N}{I_d + I_r/N} \tag{3.6}$$

$$n = 4 \times \frac{I_d}{I_d + I_r/N} \tag{3.7}$$

Where I_d is disk current, I_r is ring current and N is the current collection efficiency (0.37) of the Pt ring.

Tafel plot shows the dependence of steady-state current densities on a variety of potentials. Generally, the potential (Z) is logarithmically related to the current density (j) and the linear portion of the Tafel plot is fit to the Tafel equation:

$$Z = a + b\ logj \tag{3.8}$$

Where b is the Tafel slope.

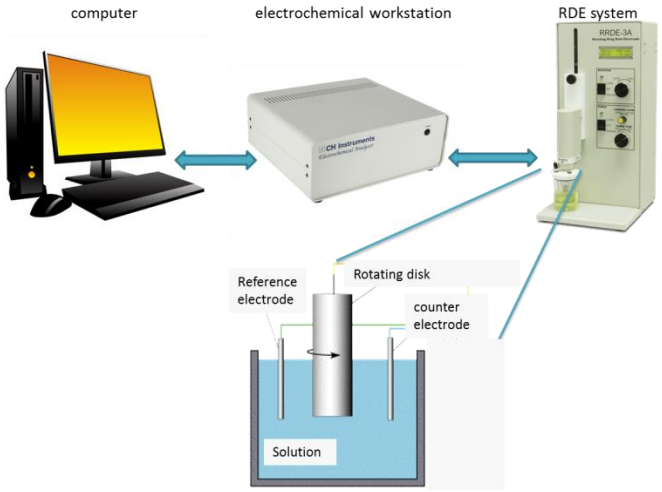

Figure 3.3 Schematic diagram of the electrochemical set up

4. Chapter 4: Synthesis of ZIF-8 *via* aqueous ammonia modulation and the anion effect

4.1 Introduction

Zeolitic imidazolate frameworks (ZIFs) are a new sub-family of porous metal-organic frameworks (MOFs) which usually consist of M-Im-M (M=Zn, Co and Im=imidazolate linker) formed by a self-assembly approach. The diverse structures of ZIFs are similar to some aluminosilicate zeolites due to the fact that the bridging angle in the M-Im-M fragment is coincident with that of the Si-O-Si preferred angle of 145 °in zeolites.[294] As a result, a large number of ZIFs with zeolite-type tetrahedral topologies have been synthesized and the ZIFs materials generally possess properties similar to those of zeolites, such as ultrahigh surface area, unimodal micropore and high crystallinity,[56, 294] which has attracted increasing attention in the fields of gas storages,[56, 294, 295] separations,[296-298] catalysis[299-301] and sensings,[302, 303] as well as other potential applications.[304-306] ZIF-8, which consists of zinc ions and 2-methylimidazolate (MIm), is a typical representative of ZIF materials and has been the research focus for many investigations.[296-302]

Traditionally, most of ZIFs are synthesised from organic solvents such as N,N-dimethylformamide (DMF), N,N-diethyformamide (DEF), N-methylpyrrolidinone, methanol and mixed solvents such as DMF/methanol.[8-15] The use of organic solvents as reaction medium obviously presents plenty of disadvantages, especially some environmental concerns since organic solvents are usually toxic and flammable. Although Chen and his co-workers were then able to successfully synthesised ZIF-8 from a stoichiometric molar ratio of zinc ions and 2-metlylimidazolate ligands (1:2) in methanol solution in the presence of ammonium hydroxide,[9, 307, 308] undoubtedly, a large amount of organic solvents, which are usually expensive, flammable and not environment friendly, were wasted by this synthesis method.

In the past several years, great effort has been devoted to develop green synthesis routes to generate ZIF-8 and therefore to reduce the environmental impact. In particular, water has been explored as a green solvent to replace organic solvents in the synthesis of ZIF-8 since water will not pose any environmental risks. Pan et al. could synthesize ZIF-8 in an aqueous system at room temperature.[309] However, a

highly excess amount of MIm (molar ratio of Zn^{2+}:MIm=1:70) was required to prepare ZIF-8. Recently, Tanaka and coworkers could generate ZIF-8 in a pure aqueous system at room temperature with molar ratio of Zn^{2+}:MIm as low as 20.[81] In addition, it is reported that organic amines such as n-butylamine,[14] polyamine,[15] triethylamine (TEA),[16-18] and pyridine,[19] can be added into the reaction mixtures as deprotonation agents to reduce the use of ligand MIm. For example, Gross et al. can prepare ZIF-8 in an aqueous system with the addition of TEA at room temperature.[18] The molar ratio of Zn^{2+}:MIm can be increased to 1:4.[18] More recently, Yao et al found ZIF-8 could be also produced from stoichiometric molar ratio of raw materials (namely molar ratio of Zn^{2+}:MIm=1:2) in aqueous solution at room temperature in the presence of non-ionic tri-block copolymer and ammonium hydroxide.[83] However, the recycling of these tri-block copolymer surfactants after the formation of ZIF-8 is difficult, which makes this synthesis approach not cost-effective. Therefore, the generation of ZIF-8 via a green and low-cost route is still remaining as a big challenge.

In addition, in the previous studies, a variety of approaches such as solvothermal method[24, 55, 72, 310-312] and hydrothermal method[20, 22, 81] for the synthesis of ZIFs have been extensively investigated, and the different parameters, such as solvents,[20, 21] temperatures[22, 23] and deprotonating agents,[21, 22, 24-26] that affect the ZIF formation, have also been widely discussed. However, one particular parameter that may affect the ZIFs formation – the effect of anions, has not been explored yet. Considering that dramatic salt effects on the formation mechanisms and the morphologies of supramolecular materials that have been observed,[313] it is of high interest to understand whether anions may potentially have significant influence on the formation of ZIF materials.

The Hofmeister series of anions were initially developed in the research of protein solubility,[313] and the orders of anions with decreasing Hofmeister effect are as follows: SO_4^{2-}, HPO_4^{2-}, OH^-, F^-, $HCOO^-$, CH_3COO^-, Cl^- , Br^- , NO_3^- ,I^- , SCN^- , ClO_4^-.[313] In the past, the effects of Hofmeister anions on the formation process of mesoporous silica have been examined and it was claimed that Hofmeister anions offer a wide range of possibilities to modulate the morphologies, stabilities and surface properties of mesoporous silicas.[313] For instance, Takashi and co-workers demonstrated that the effect of counter anion on the formation of mesoporous materials under the acidic synthesis process,[314] while Zhao's group studied the anion sequence in the phase

transformation of mesostructures.[315] Moreover, anion effects on the formation of metal based supramolecular complexes was also reported. It was found that the radius of anion played an important role in the formation of the structure and luminescent intensity of the Cd based coordination frameworks,[316] it is even claimed that Cd(II) coordination frameworks obtained from various anions can result in anion-induced structural transformation and anion-responsive photoluminescence.[317] In addition, reports of the anion effect on the formation of metal based supramolecular complexes , such as silver (I) complexes[318] and zinc (II) complexes,[319] can be also found in literature. These previous work encouraged us to explore the salt effect on the formation of ZIFs in this work.

In this chapter, we presented a facile, green and low-cost method for highly efficient preparation of ZIF-8 from stoichiometric molar ratios of zinc ions and 2-methylimidazolate precursor as the first part of this chapter. This synthesis approach of ZIF-8 can be facilitated in an aqueous ammonia solution without any other additives at room temperature and the effect of concentration of aqueous ammonia on the particle sizes and textural properties of the resulting ZIF-8 was clearly demonstrated. In addition, as the second part of this chapter, we reported our recent findings on the effect of anions on the formation of ZIF-8 materials. It is found that the introduction of anions (SO_4^{2-}, CH_3COO^-, Cl^-, Br^-, NO_3^-) into the reaction media of the aqueous ammonia system, accelerates the self-assembly of stoichiometric zinc ions with the 2-methylimidazole (MIm) linker (1:2) and results in the formation of pure ZIF-8 with tuneable morphologies and textural properties. Our findings indicated that: 1) the requirement of aqueous ammonia concentrations for the formation of pure ZIF-8 is modulated by the anion types; 2) the generation of pure ZIF-8 materials is promoted by the anion concentrations and the anion types, which follows the rule of the Hofmeister anion effect.

4.2 Synthesis of ZIF-8 *via* aqueous ammonia modulation

4.2.1 Synthesis of ZIF-8 in pure aqueous system

Presented in Figure 4.1a are the XRD patterns of the products generated from a pure aqueous system with variable molar ratios of Zn^{2+}/MIm ranging from 1/4 to 1/70. Clearly, while the molar ratio of Zn^{2+}/MIm is higher than 1:24 (such as in the range of 1:4 to 1:16), the XRD patterns of the resulting products display complicated diffraction peaks that can be indexed to $Zn(OH)_2$, $Zn(NO_3)_2$ and their hydrates

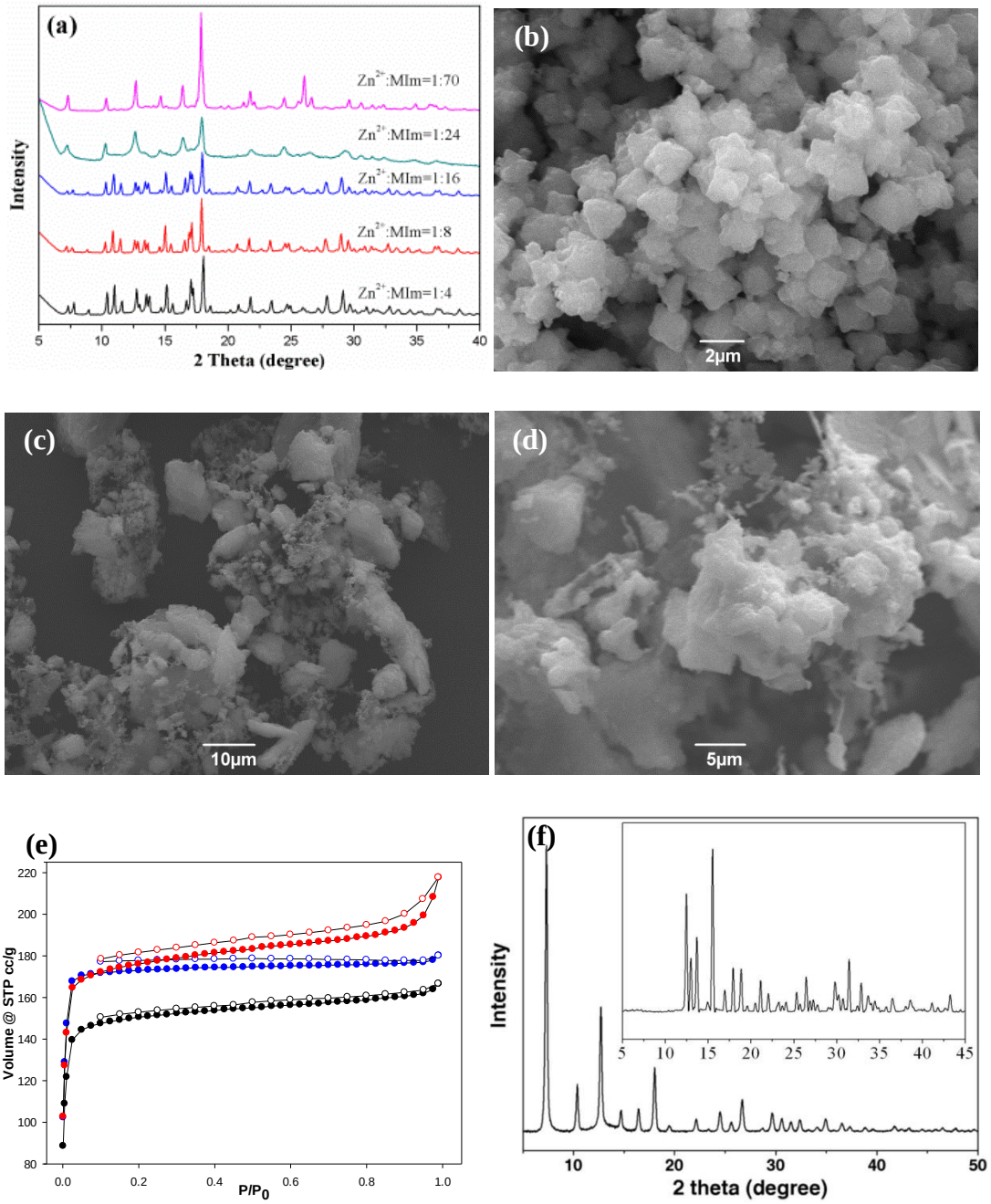

Figure 4.1 XRD patterns (a), representative SEM images (b-d) and nitrogen sorption isotherms (e) of the as-synthesised samples from pure aqueous system with different concentrations of MIm. The molar ratio of Zn^{2+}:MIm is (b) 1:16; (c) 1:24; (d) 1:70 respectively. Black, red and blue correspond to the sample synthesized from Zn^{2+}:MIm molar ratio of 1:24, 1:70 and 1:50 respectively. Solid and hollow data correspond to the adsorption and desorption branches, respectively. XRD patterns (f) of standard pure ZIF-8, inset is the standard pure *dia*(Zn).

together with some unknown phases, which is consistent with Tanaka and coworkers' observations.[81] It is interesting to note that no dense *dia*(Zn) structure was detected in our samples although a large excess of MIm was used in the synthesis mixture, which is different from other reports.[83, 304] The structure of *dia*(Zn) is the same as that of ZIF-8, but *dia*(Zn) has no pores. When the molar ratio of Zn^{2+}/MIm ranges from 1/24 to 1/70 in pure aqueous system, the synthesized products exhibit sodalite (SOD)-type structures in their XRD patterns (shown in Figure 4.1a), which is in agreement with previous observations.[81, 309] Moreover, increasing of synthesis temperatures can only help to improve the intensity of XRD diffraction peaks, but cannot promote the formation of any new phases (Figure 4.2). Clearly, synthesis temperatures have no obvious effect on the formation of ZIF-8 materials in pure aqueous system.

The morphology of the as-synthesised products in aqueous solution with different concentrations of MIm was detected via SEM and representative images were presented in Figure 4.1b-d. The products showed irregular particle morphologies, which is different from literature reports.[81, 309] This is maybe due to the fact that an excess amount of MIm could deprotonate other MIm in aqueous ZIF syntheses and the polar water may inhibit the conversion of the crystal shape to the rhombic dodecahedron shape. In addition, the nitrogen sorption isotherms for the as-synthesized ZIF-8 derived from pure aqueous system display type I isotherms with adsorption and desorption branches are largely reversible (as shown in Figure 4.1e), indicating that the resulting ZIF-8 samples are micropore dominated materials. The specific surface area and pore volume of ZIF-8 synthesized from pure aqueous solution with Zn^{2+}/MIm in the range of 1/24 to 1/70 increase slightly with the increase of the concentration of MIm, up to 600 m^2 g^{-1} and 0.34 cm^3 g^{-1} respectively (see Figure 4.3), which are much lower than those of prepared using methanol as solvent.[8] It is worth noting that the relative low surface area and pore volume for ZIF-8 derived from pure aqueous system may be due to the fact that the molar ratios of reaction components in the mixture system were not optimized for high texture properties and the amount of water was kept constant in all our synthesis runs including in ammonia aqueous solution, which enable us to compare the results obtained from different synthesis system and to identify the parameters that affect the material synthesis. ZIF-8 samples with high textural properties is achievable from pure water system if optimal molar ratio of reaction components is applied.[81]

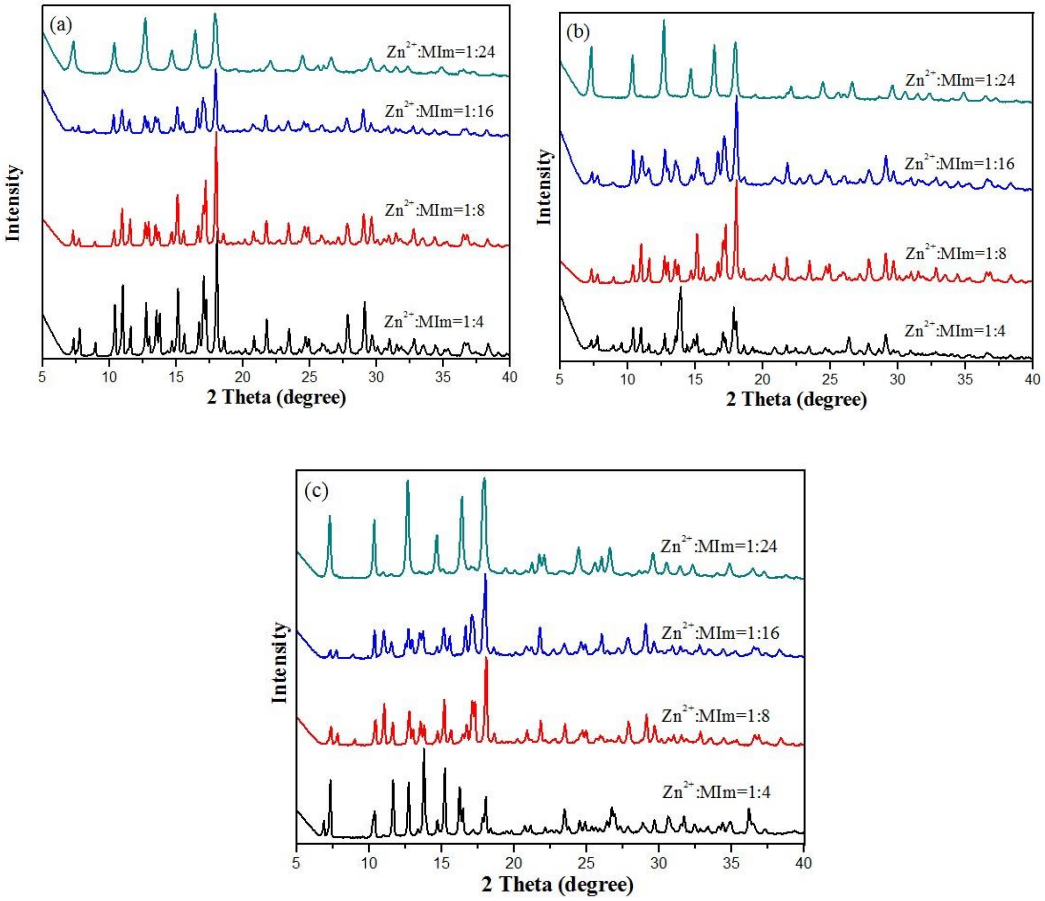

Figure 4.2 XRD patterns of the synthesized products prepared in aqueous solution at (a) 50°C; (b) 80°C; (c) 110°C for 24 h with different molar ratios of Zn^{2+}:MIm.

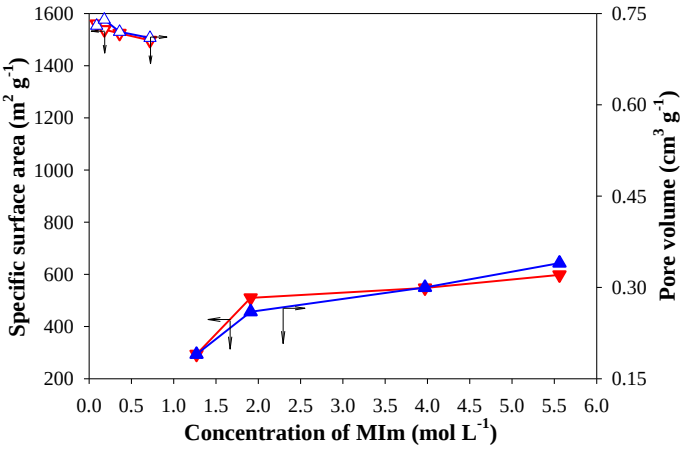

Figure 4.3 Specific surface area (triangle down) and pore volume (triangle up) of synthesised ZIF-8 as a function of concentration of MIm in pure aqueous system (solid) and concentrated ammonia solution (hollow).

4.2.2 Synthesis of ZIF-8 in concentrated ammonia aqueous solution

In the presence of concentrated ammonia aqueous solution (35 wt%), ZIF-8 can be readily generated as long as the molar ratio of Zn^{2+}/MIm is no less than the stoichiometric proportion of the reaction (Zn^{2+}/MIm =1/2) (see Figure 4.4). Namely, the amount of organic linker MIm in the synthesis mixture can be significantly reduced down to the stoichiometric proportion of the reaction under concentrated ammonia aqueous solution without forming unwanted by-products. We noticed that an unknown product was formed if the molar ratio of Zn^{2+}/MIm increased to 1:1, which is consistent with literature report.[304] The yield for ZIF-8 from concentrated ammonia aqueous solution is generally high (> 93%) based on Zn. Therefore, the synthesis efficiency, where Zn^{2+}:MIm molar ratio is 1:2, is much higher than those in the literature in amine solutions (where Zn^{2+}:MIm molar ratio is 1:4-1:16).[18] Moreover, the formation of ZIF-8 materials in concentrated aqueous ammonia system is not sensitive to the synthesis temperature since the increase of reaction temperature does not prompt the formation of any new phases (as shown in Figure 4.5).

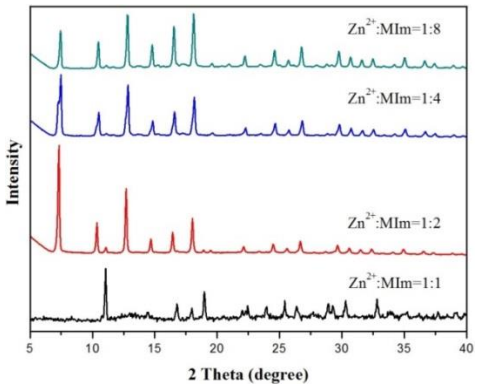

Figure 4.4 Powder XRD patterns of the as-synthesised samples from concentrated (35 wt%) aqueous ammonia solution.

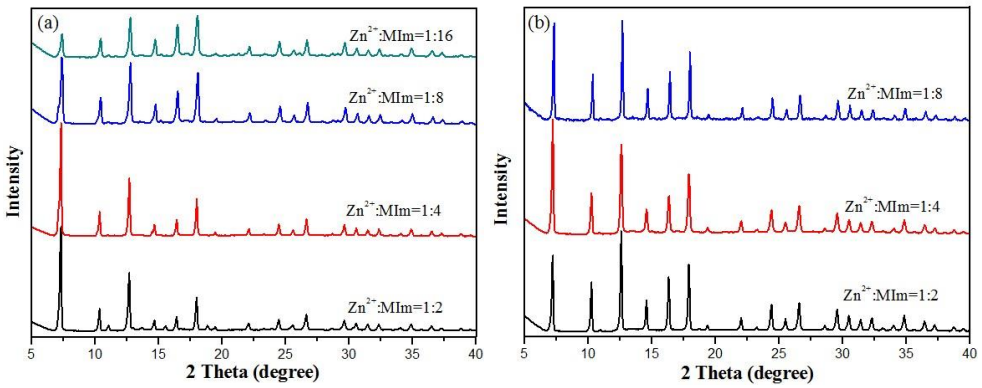

Figure 4.5 XRD patterns of the products prepared in concentrated ammonia solution at (a) 50°C; (b) 110°C for 24 h with different molar ratios of Zn^{2+}:MIm.

Different from the products derived from the pure aqueous system, the morphology of the ZIF-8 obtained from concentrated ammonia aqueous solution with variable Zn^{2+}/MIm molar ratios from 1/2 to 1/8 exhibited rhombic dodecahedron particle shapes (Figure 4.6) with the particle sizes exclusively around 2 μm, suggesting the concentration of MIm in the synthesis mixture in concentrated ammonia aqueous solution does not affect the particle shapes and sizes of ZIF-8. To determine the effect of aging time on the morphology of ZIF-8 materials, the evolvement of particle morphologies of as-synthesized ZIF-8 as a function of aging time in concentrated ammonia aqueous solution with Zn^{2+}:MIm:NH_3.H_2O molar ratio of 1:2:400 was checked by SEM. As shown in Figure 4.7, after 2 minutes reaction, the product displays slight round particles with hexagonal plate contour on which small nanoparticles were deposited. With increasing of the reaction time to 5 and 10 minutes, there are less small particles on the plates and the surface of the plates change gradually from rough to smooth with fewer defects. After long reaction time up to 24 h, the particle surface is very smooth without visible defects and the products exhibit rhombic dodecahedron shapes with particle size around 2 μm. It is likely that during the synthesis process, increase of the reaction time can effectively accelerate the deprotonation of MIm by the excess amount of ammonia molecules in the aqueous solution, hasten the sedimentation of small nanoparticles to form large crystal and therefore promote the conversion of the crystal morphology to the rhombic dodecahedron shape.

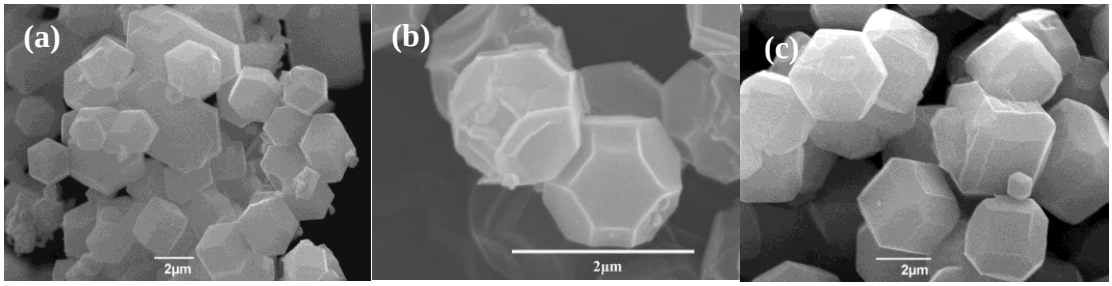

Figure 4.6 Representative SEM images of as-synthesised ZIF-8 from concentrated aqueous ammonia solution at different molar ratios of Zn^{2+}:MIm:NH_3•H_2O. (a)1:2:400; (b)1:4:400; (c) 1:8:400.

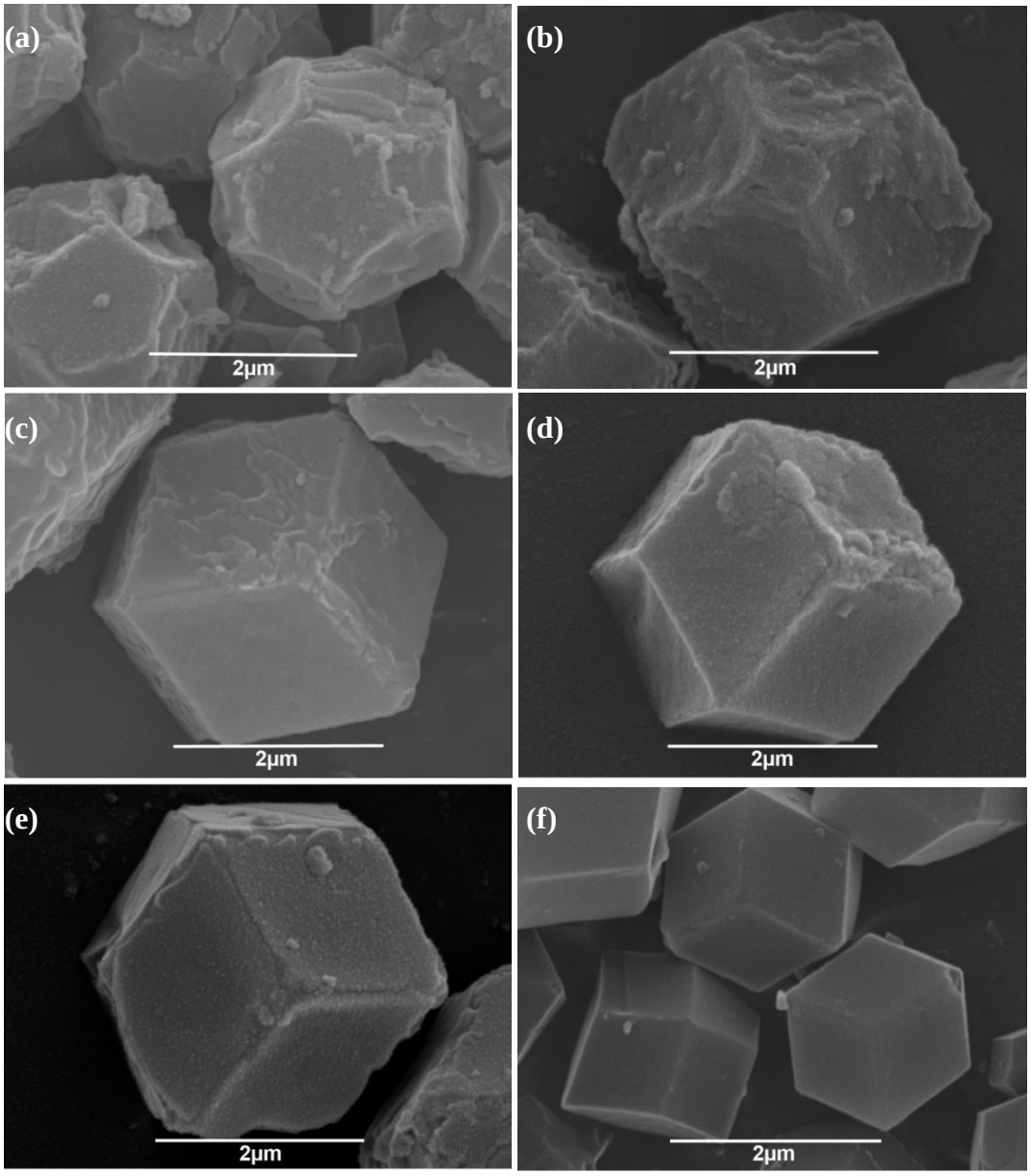

Figure 4.7 The evolution of particle morphologies of as-synthesized ZIF-8 as a function of aging time in concentrated ammonia aqueous solution with Zn^{2+}:MIm:NH_3.H_2O molar ratio of 1:2:400. (a) 2 min; (b) 5 min; (c) 10 min; (d) 1 h; (e) 6 h and (f) 24 h.

The textural properties of the as-synthesized ZIF-8 derived from concentrated ammonia aqueous solution were also measured by nitrogen adsorption at liquid nitrogen temperature. The nitrogen sorptions for all the resulting ZIF-8 samples exclusively show type I isotherms with adsorption and desorption branches are completely reversible (as shown in Figure 4.8), and all the samples exhibit high N_2 adsorption at low relative pressure, implying those ZIF-8 samples are micropore

dominated materials. The specific surface area and pore volume of ZIF-8 synthesized from concentrated ammonia aqueous solution are largely in the range of 1550 -1600 $m^2\ g^{-1}$ and 0.65 – 0.70 $cm^3\ g^{-1}$ respectively (see Figure 4.3), decreasing slightly with the increase of the concentration of MIm (namely change of the molar ratio of Zn^{2+}/MIm from 1/2 to 1/16, as shown in Figure 4.3). The extremely high textural properties (specific surface area and pore volume) for ZIF-8 derived from concentrated ammonia aqueous solution are very similar to those synthesised from organic solvents,[8, 10] indicating that high quality of ZIF-8 materials can be readily generated from stoichiometric precursors in concentrated ammonia aqueous solution at room temperature without compromising in their textural properties. Remarkably, the surface area and pore volume of ZIF-8 from concentrated ammonia solution are about 3 and 2 times of their counterparts prepared from pure aqueous system under the same conditions (Figure 4.3).

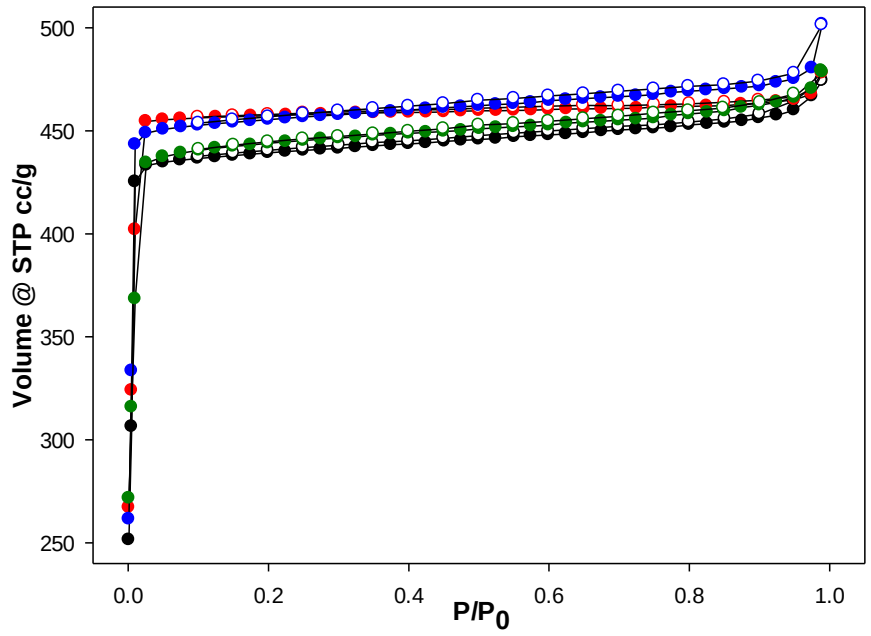

Figure 4.8 Nitrogen sorption isotherms of as-synthesized ZIF-8 from concentrated ammonia aqueous solution with different concentrations of MIm. Black, red, blue and green correspond to the sample synthesized in concentrated ammonia aqueous solution with Zn^{2+}:MIm molar ratio=1:2, 1:4, 1:8 and 1:16. Solid and hollow data correspond to the adsorption and desorption branches, respectively.

4.2.3 Effect of concentration of ammonia solution on the synthesis of ZIF-8

The effect of concentration of ammonia solution on the formation of ZIF-8 was then investigated. Figure 4.9a shows the XRD patterns of the products from Zn^{2+}/MIm =1/2 with variable ammonia concentrations. When the $Zn^{2+}/NH_3.H_2O$ molar ratio is 1/10, the product is a dense structure of *dia*(Zn).[304] However, with the decrease of Zn^{2+}/NH_3 molar ratio from 1/20 to 1/100, namely increase of the concentration of ammonia from 1.6 to 6.7 mol/L, ZIF-8 can be obtained with high yield (90%). The similar trend can be observed as well from the Zn^{2+}/MIm =1/4 system with variable ammonia concentrations (see Figure 4.9b) and the only difference is the XRD patterns of the products from $Zn^{2+}/NH_3 \cdot H_2O$ molar ratio of 1/10 display complicated diffraction peaks that can be indexed to $Zn(OH)_2$, $Zn(NO_3)_2$ and their hydrate complexes together with some unknown phases, which is consistent with Tanaka and coworkers' report.[81] Increasing of the concentration of ammonia (namely change the Zn^{2+}/ $NH_3.H_2O$ molar ratio from 1/20 to 1/100) in the Zn^{2+}/MIm =1/4 system will result in the formation of high quality of ZIF-8, except minor by-product was found in the Zn^{2+}/ $NH_3.H_2O$ = 1/20 system.

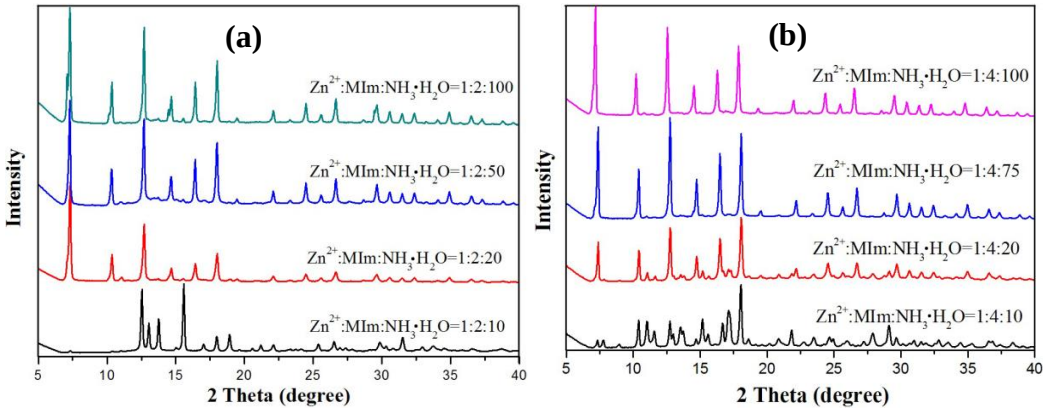

Figure 4.9 XRD patterns of the as-synthesised samples in different concentrations of ammonia solution for variable Zn^{2+}/MIm molar ratio of (a) 1:2 and (b) 1:4.

Obviously, the efficiency for the formation of ZIF-8 (with minimal molar ratio of Zn^{2+}:MIm: $NH_3.H_2O$ =1:2:20) is remarkably improved comparing with the work of Yao et al (where the molar ratio of Zn^{2+}:MIm: $NH_3.H_2O$ =1:4:16)[83]. Different from the synthesis of ZIF-8 from pure aqueous system and concentrated ammonia solution system, the synthesis temperature does affect the formation of ZIF-8 under lower concentration of ammonia solution. When the reaction temperature increased from

room temperature to 50, 80 or 110 ^{o}C, the products change from ZIF-8 to by-products only (shown in Figure 4.10). Figure 4.11 shows the particle morphologies of ZIF-8 derived from variable ammonia concentrations. Uniform rhombic dodecahedron particle shapes with SOD-type crystalline structure of ZIF-8 were formed from Zn^{2+}:MIm:$NH_3.H_2O$ molar ratios of 1:2:20, 1:2:50 and 1:2:100 and the average crystal size decreases from 10 to 2 μm with increase of the ammonia concentration from 1.6 to 6.7 mol/L, indicating that the particle sizes of resulting ZIF-8 can be readily tunable by simply control over the concentration of aqueous ammonia.

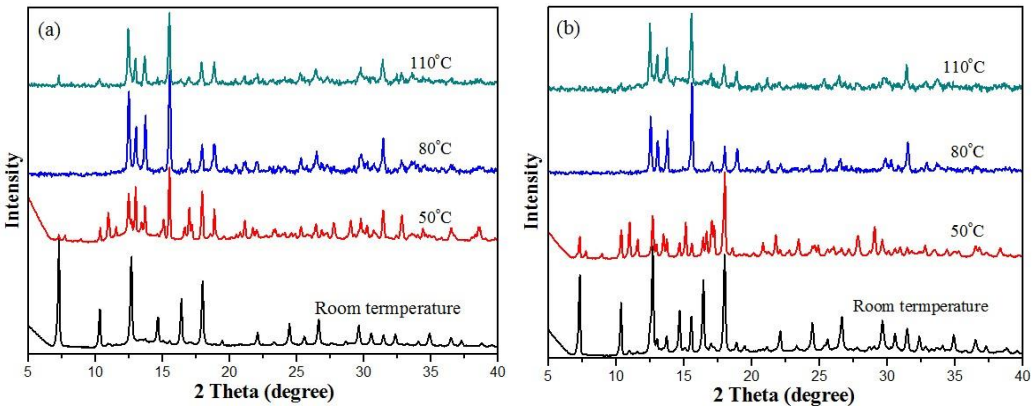

Figure 4.10 XRD of the products prepared in two concentrations of ammonia solutions (a) Zn^{2+}:MIm:NH_3•H_2O=1:2:50; (b) Zn^{2+}:MIm:NH_3•H_2O=1:4:50 at room temperature, 50^{o}C, 80^{o}C and 110^{o}C.

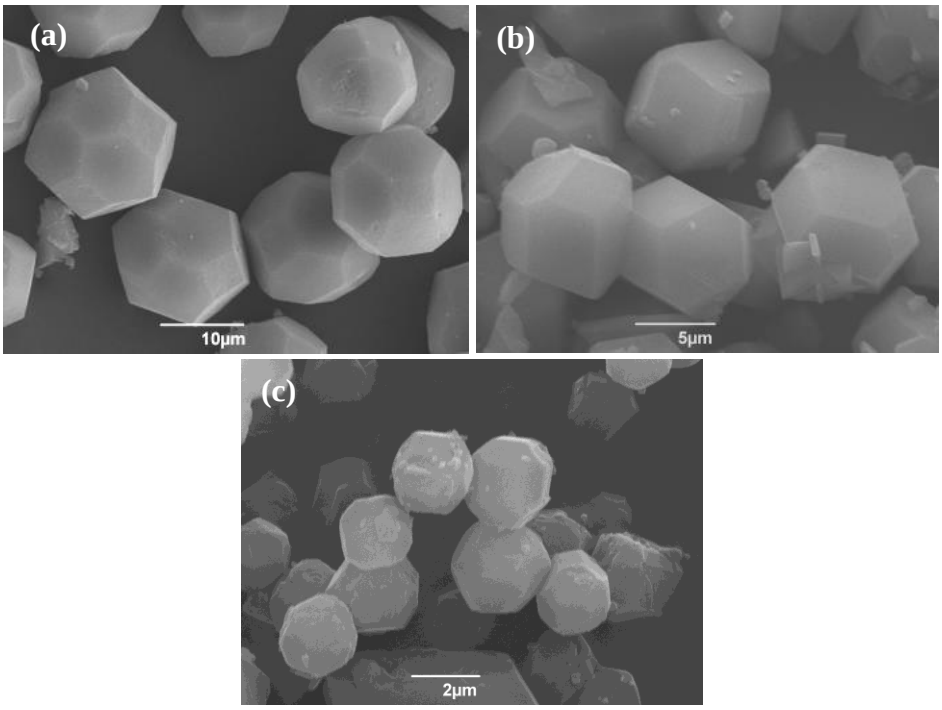

Figure 4.11 Representative SEM images of as-synthesised ZIF-8 in ammonia solution with Zn^{2+}:MIm:NH_3.H_2O molar ratios 1:2:20, 1:2:50 and 1:2:100, respectively.

In addition, the concentration of ammonia in the synthesis mixture can significantly affect the textural properties of resulting ZIF-8 products. All the materials exclusively exhibit type I nitrogen sorption isotherms with micropore dominating (see Figure 4.12). As presented in Figure 4.13, adjusting the concentration of ammonia from 1.6 mol L^{-1} up to concentrated ammonia (18.1 mol L^{-1}), the specific surface area for ZIF-8 is increased by 60% from 1000 to 1600 m^2 g^{-1}, accompanied with up to 40% increase of pore volume. This observed change trend of surface area and pore volume with the concentration of ammonia clearly demonstrates that the textural properties of ZIF-8 can be easily fine tunable via change of the concentration of ammonia in the synthesis mixture.

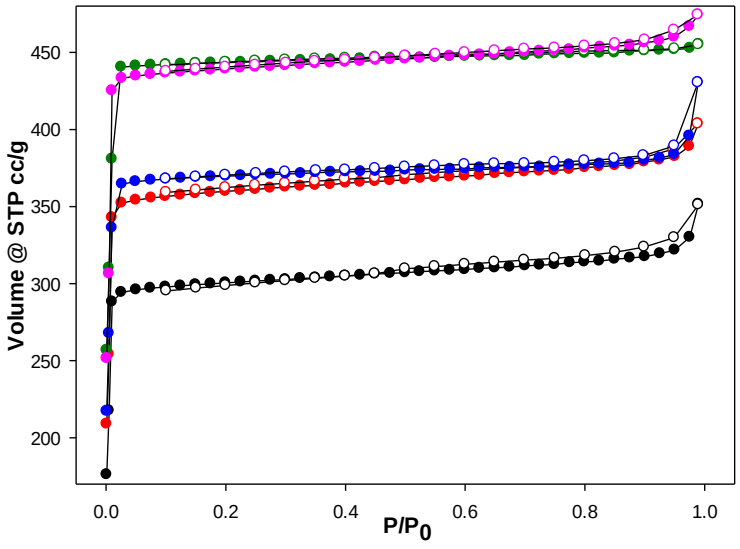

Figure 4.12 Nitrogen sorption isotherms of as-synthesized ZIF-8 from different concentrations of aqueous ammonia. Black, red, blue, green and pink correspond to the sample synthesized under Zn^{2+}:MIm:$NH_3 \cdot H_2O$ molar ratio=1:2:20; 1:2:50; 1:2:100; 1:2:200 and 1:2:400, respectively. Solid and hollow data correspond to the adsorption and desorption branches, respectively.

It is believed that $NH_3 \cdot H_2O$ can not only deprotonate the imidazole ligand but also coordinate the release of metal ions.[320] Therefore, we hypothesize that ammonia could deprotonate MIm ligands and initiate the formation of ZIF-8 like other amines, such as TEA.[18] MIm is firstly deprotonated by aqueous ammonia, ZIF-8 is then formed from the reaction between zinc ions and deprotonated MIm species. In addition, it has been found that the concentration of ammonia is very important to the crystal sizes of

resulting ZIF-8 materials. Since the crystal size decreases with the increase of the amount of MIm[81] and an excess of MIm is beneficial to a high nucleation density at the start of synthesis,[14] it is therefore reasonable to suppose that under higher concentration of ammonia, the excess amount of ammonia molecules increase the number of nuclei generated by the complex formation in the early stages of reaction, which leads to a decrease in the crystal particle size.

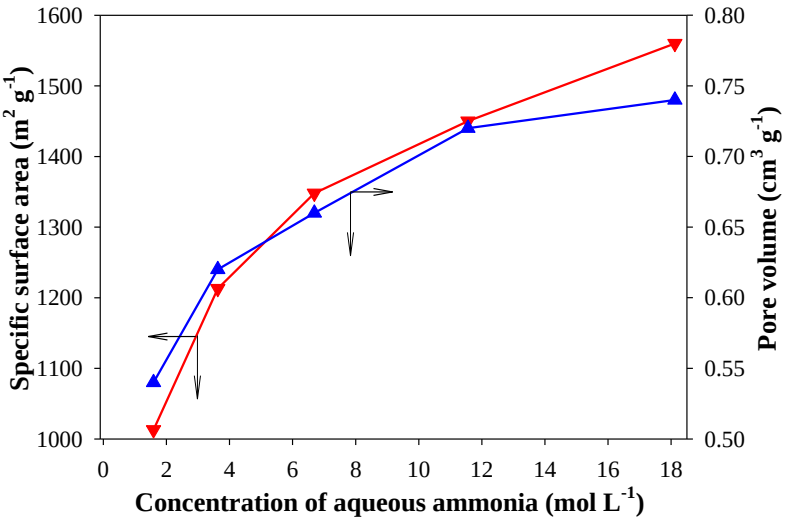

Figure 4.13 The changes of specific surface area (triangle down) and pore volume (triangle up) of synthesised ZIF-8 as a function of concentration of ammonia in the synthesis mixture.

4.2.4 Conclusions

A cost-effective and facile method for the preparation of zeolitic imidazolate framework-8 material was presented. ZIF-8 can be readily synthesized from stoichiometric precursors in aqueous ammonia solution without any other additives at room temperature, comparing that a large excess of organic ligand is required to form ZIF-8 under similar conditions in pure aqueous solution. The structures, particle sizes and textural properties of resulting ZIF-8 materials can be easily tunable by simple control over the concentration of aqueous ammonia in the synthesis mixture. This green, low-cost and efficient synthesis method has great potential for large scale production of ZIF-8 for practical applications.

4.3 Hofmeister anion effect on the formation of ZIF-8 in aqueous ammonia solution

4.3.1 Effect of ammonia concentrations on the formation of ZIF-8

The effect of ammonia concentrations on the formation of ZIF-8 was first investigated using different zinc salts in aqueous system, where stoichiometric molar ratio of 1:2 for Zn^{2+}/MIm was used. From the XRD patterns in Figure 4.14, it is clear that lower ammonia concentrations result in the impurity in the product, while higher ammonia concentrations can generate pure ZIF-8, which is in agreement with previous reports.[22, 85] Taking SO_4^{2-} as an example (Figure 4.14a), the products derived from the molar ratios of $Zn^{2+}/NH_3 < 1{:}75$ are mixture of ZIF-8 and a dense *dia*(Zn) impurity, but the products from molar ratios of $Zn^{2+}/NH_3 \geq 1{:}75$ exhibit pure sodalite (SOD)-type structures in their XRD patterns. While other different anion zinc salts such as CH_3COO^-, Cl^-, Br^- or NO_3^- were used, the XRD patterns of the products (shown in Figure 4.14b-e) revealed that the molar ratios of $Zn^{2+}/NH_3 \geq 1{:}100$, 1:200, 1:400 or 1:20 were required to form pure ZIF-8, respectively. These results also indicate that the requirement of ammonia concentrations for the formation of pure ZIF-8 phase is modulated by the anion types. The morphologies of pure ZIF-8, which were obtained from different anion zinc salts at high ammonia concentrations, exclusively exhibited equilibrium rhombic dodecahedral particle shapes (Figure 4.15).[321] In addition, the textural properties of the resulting ZIF-8 materials, as shown in Figure 4.16, are clearly different for samples from different anion zinc salts, implying that the anion types can affect the textural properties of the samples even if they are obtained under the same conditions.

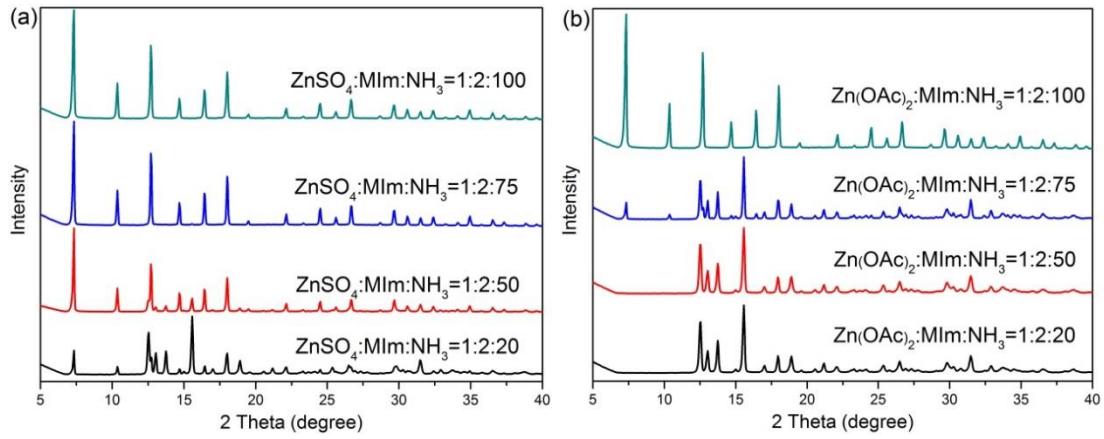

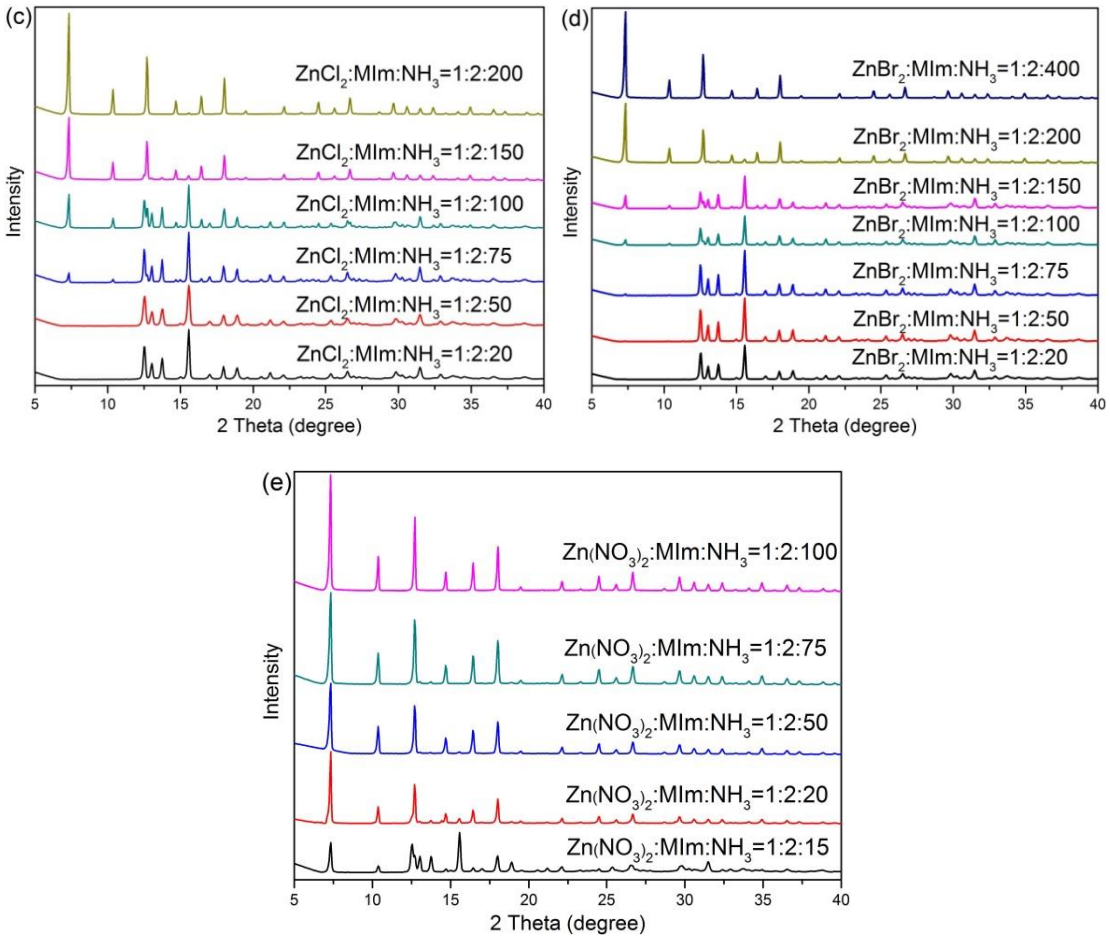

Figure 4.14 XRD patterns of the as-synthesised samples in different concentrations of ammonia solution for variable zinc salts: (a) $ZnSO_4$ (b) $Zn(OAc)_2$, (c) $ZnCl_2$, (d) $ZnBr_2$, and (e) $Zn(NO_3)_2$, representatively.

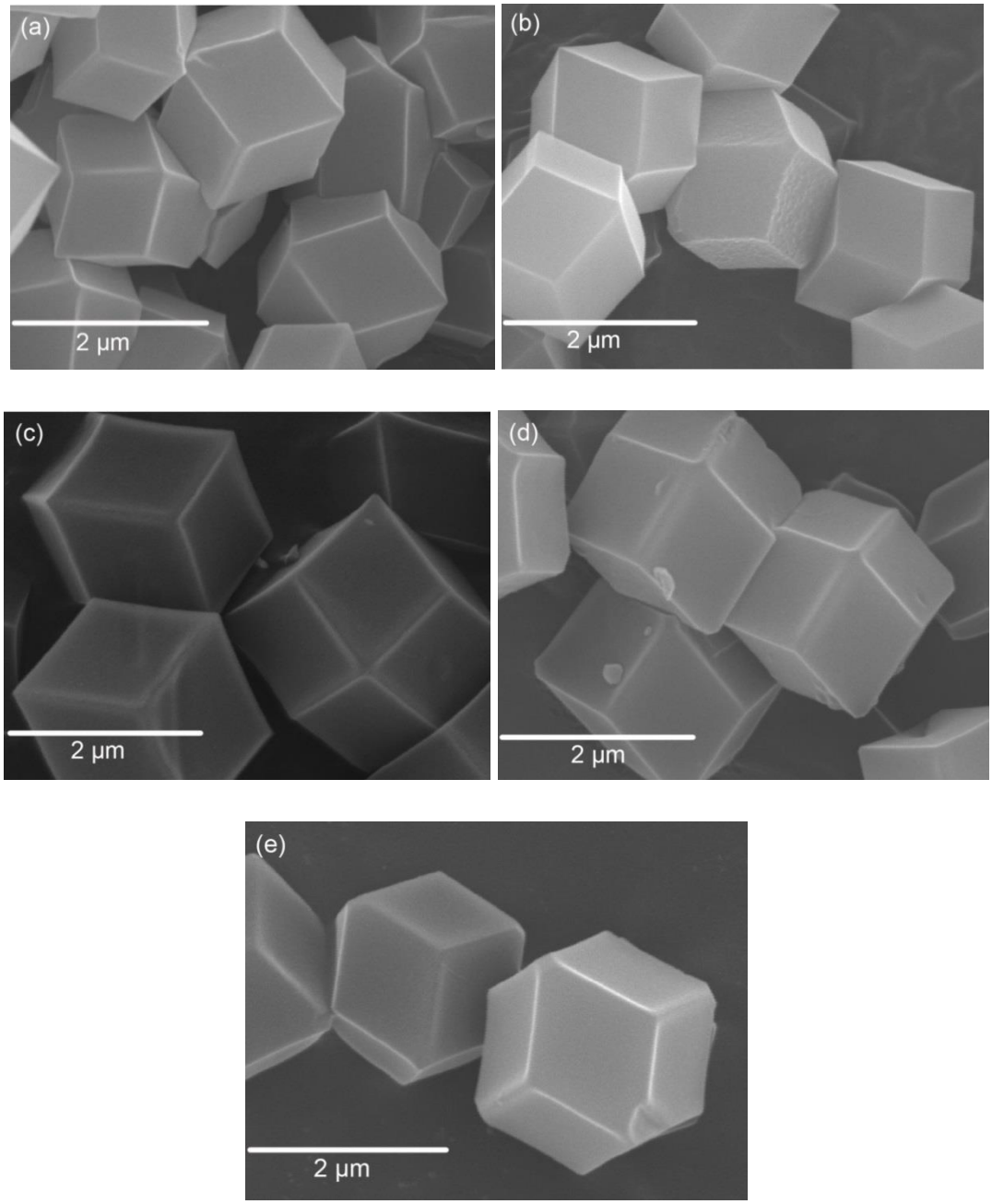

Figure 4.15 Representative SEM images of as-synthesised ZIF-8 in ammonia solution with various anions: (a) $ZnSO_4$:MIm:NH_3 =1:2:100; (b) $Zn(OAc)_2$:MIm:NH_3 = 1:2:100; (c) $ZnCl_2$:MIm:NH_3 =1:2:200; (d) $ZnBr_2$:MIm:NH_3 =1:2:400 and (e) $Zn(NO_3)_2$:MIm:NH_3 =1:2:100, respectively.

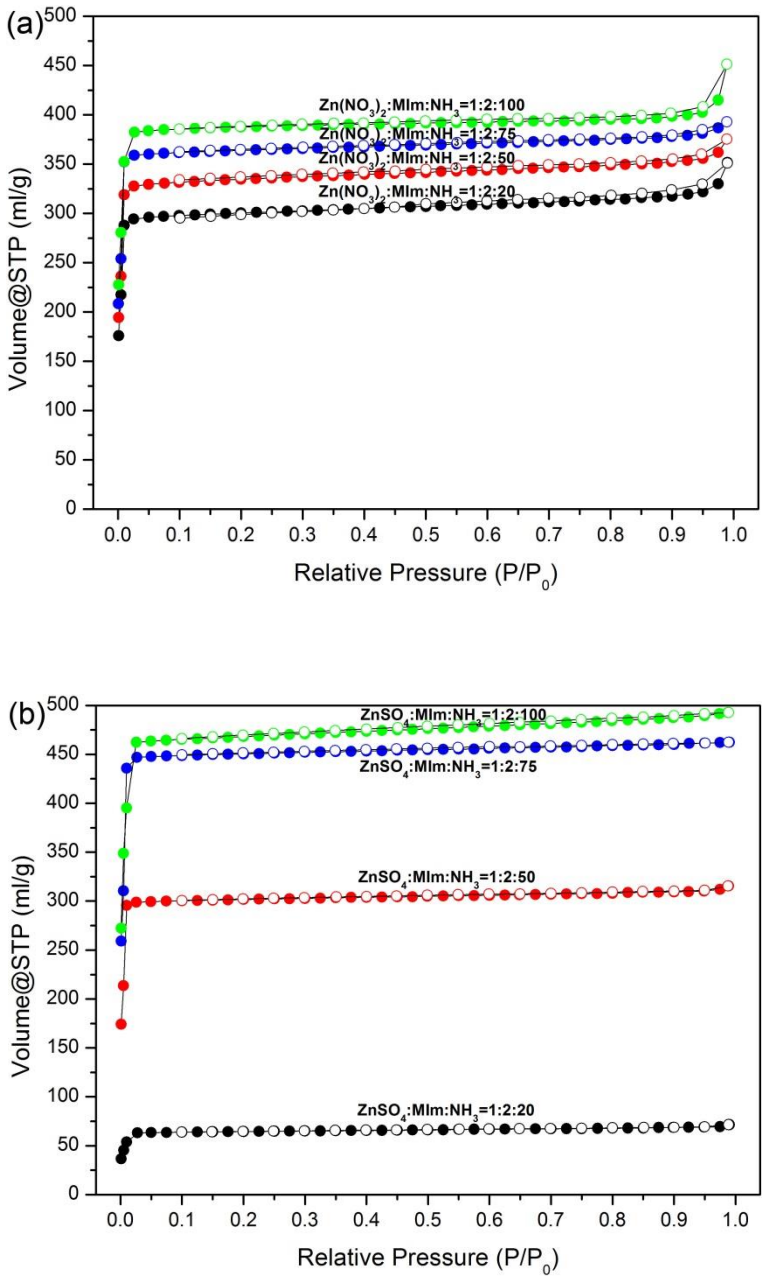

Figure 4.16 Nitrogen sorption isotherms of as-synthesised ZIF-8 derived from different anion zinc salt in various concentrations of aqueous ammonia solution. (a) $Zn(NO_3)_2$ and (b) $ZnSO_4$. Solid and hollow data correspond to the adsorption and desorption branches, respectively.

4.3.2 Effect of additional anions on the formation of ZIF-8

In order to determine whether the introduction of additional anions can influence on the formation of ZIF-8 phase, a variety of anion sodium salts including Na_2SO_4, CH_3COONa (NaOAc), NaCl, NaBr, and $NaNO_3$ were separately added as additional anion sources, to the reaction media containing zinc salts with the same anion for one batch synthesis. Based on the results in Figure 4.14, we chose the lowest ammonia concentration required for the formation of mixture of ZIF-8 and *dia*(Zn) phase to determine whether the presence of extra anions in the synthesis media can promote the transformation the formation of mixture to pure ZIF-8 phase. For example, the synthesis product from the molar ratio of $ZnSO_4$:MIm:NH_3=1:2:50 is a mixture. However, with the introducing of increased amount of Na_2SO_4 into the synthesis system, interestingly the impurity *dia*(Zn) in the product was gradually reduced and pure ZIF-8 was eventually formed with the molar ratio of $ZnSO_4$:Na_2SO_4 =1:15 (as shown in Figure 4.17a), suggesting that the additional SO_4^{2-} indeed accelerates the formation of pure ZIF-8 phase. Moreover, SEM images (Figure 4.17b-d) clearly show that with the introduction of increased additional SO_4^{2-} into the reaction media, the morphologies of the products changed significantly from irregular rough-surface particle shapes to regular smooth-surface ZIF-8 with rhombic dodecahedral particle shapes. In addition, as presented in Figure 4.18, with the increase in the concentrations of SO_4^{2-} in the synthesis system, all the products exclusively exhibit type I nitrogen sorption isotherms with micropore domination; however, compared with the sample without additional Na_2SO_4, the sample from $ZnSO_4$:Na_2SO_4 =1:20 exhibited up to 50% increase in both the specific surface area and total pore volume, remarkably changing from 1015 to 1576 $m^2\ g^{-1}$ and 0.49 to 0.74 $cm^3\ g^{-1}$ respectively. Obviously, the introduction of additional SO_4^{2-} anions effectively promotes the formation of pure ZIF-8 phase with variable particle morphologies and textural properties.

Other anion sodium salts such as NaOAc, NaCl and NaBr were also introduced into the synthesis system and it was found that the transformation from the mixture of ZIF-8 and dense *dia*(Zn) phase to pure ZIF-8 could be also readily realised when the molar ratio of zinc ion/sodium anion salt is higher than 1:20, 1:30 and 1:20 for NaOAc, NaCl and NaBr respectively (shown in Figure 4.19a-c). However, the addition of $NaNO_3$ into the synthesis media of Zn^{2+}:MIm:NH_3=1:2:15, which is the lowest

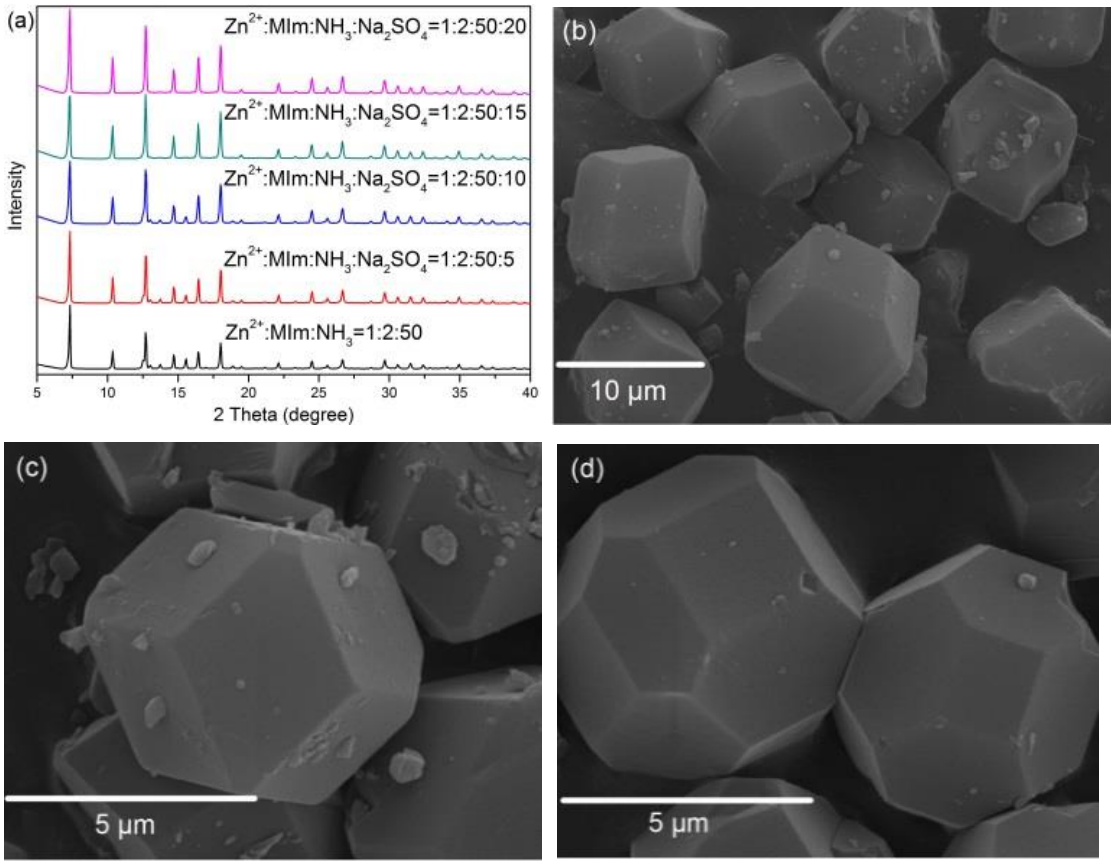

Figure 4.17 (a) XRD patterns of the as-synthesised samples in different concentrations of sodium sulfate, (b-d) SEM images of as-synthesised samples in ammonia solution with Zn^{2+}:MIm:NH_3: Na_2SO_4 molar ratios of 1:2:50, 1:2:50:5 and 1:2:50:20, respectively.

ammonia concentration for the formation of a mixture (as demonstrated in Figure 4.14e), has no observable effect on the formation of pure ZIF-8 and the XRD patterns were kept unchanged even if the molar ratio of $Zn(NO_3)_2$:$NaNO_3$ is up to 1:30 (shown in Figure 4.19d), indicating that NO_3^- has the weakest anion effect on the modulation of pure ZIF-8 generation among the studied anions. In addition, SEM images clearly show that the introduction of increased additional anions into the synthesis system results in the morphologies changes from irregular rough-surface particles to regular smooth-surface ZIF-8 particles with rhombic dodecahedral shape (seen Figure 4.20). Based on the results above, it is clear that except NO_3^-, the presence of anion sodium salts with appropriate anion concentrations in the synthesis solution can effectively accelerate the formation of pure ZIF-8 phase with adjustable particle morphologies.

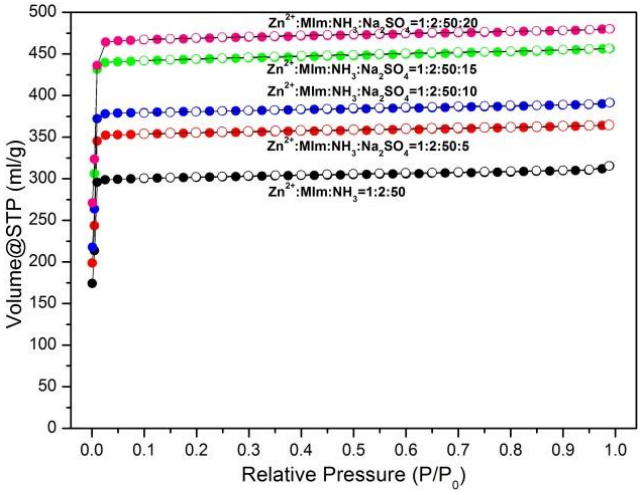

Figure 4.18 Nitrogen sorption isotherms of as-synthesised ZIF-8 under different concentrations of sodium sulfate. The solid and hollow cycle correspond to the adsorption and desorption branches, respectively.

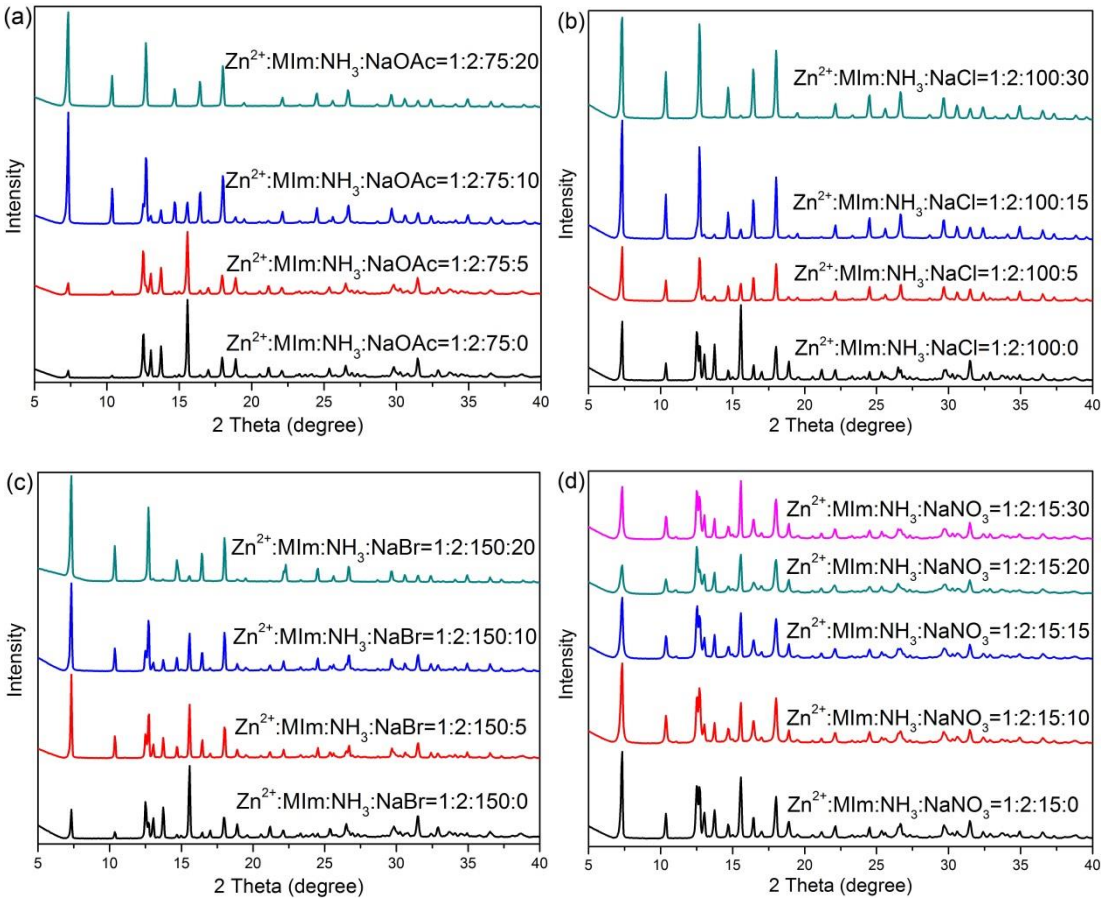

Figure 4.19 XRD patterns of the as-synthesised samples in different concentrations of ammonia solution for variable zinc salts with the additional anions: (a) NaOAc, (b) NaCl, (c) NaBr, and (d)$NaNO_3$, representatively.

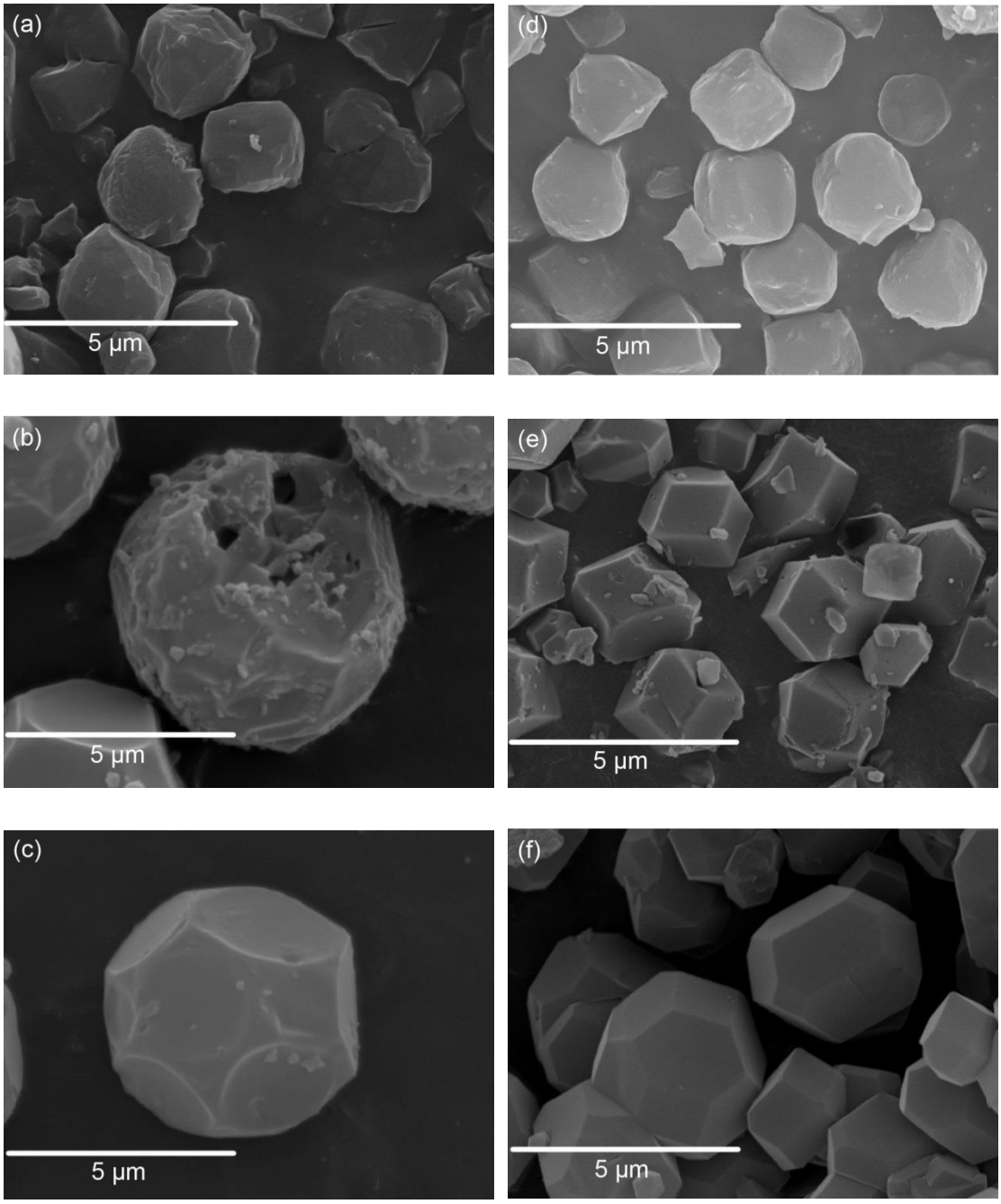

Figure 4.20 Representative SEM images of as-synthesised products in ammonia solution from different anion sodium salts (a, b and c) NaOAc and (d, c and e) NaCl with various additional anion concentrations: (a) Zn^{2+} : MIm : NH_3 = 1 : 2 : 75; (b) Zn^{2+} : MIm : NH_3 : NaOAc = 1 : 2 : 75 : 10; (c) Zn^{2+} : MIm : NH_3 : NaOAc = 1 : 2 : 75 : 20; (d) Zn^{2+} : MIm : NH_3 = 1 : 2 : 100; (e) Zn^{2+} : MIm : NH_3 : NaCl = 1 : 2 : 100 : 5; (f) Zn^{2+} : MIm : NH_3 : NaCl = 1 : 2 : 100 : 30, respectively.

4.3.3 Effect of anion capability on the formation of pure ZIF-8

To find out the anion effect capability on the formation of pure ZIF-8 phase, different anion sodium salts with various concentrations were introduced into a reaction solution with molar ratio of Zn^{2+}:MIm:NH_3=1:2:50 (namely a synthesis system with the same ammonia concentration). It is surprising to note that except $NaNO_3$, pure ZIF-8 can be readily formed because of the presence of additional anion sodium salts, as shown in Figure 4.21. Most strikingly, it can be summarised from the XRD results in Figure 4.17a and Figure 4.21 that the lowest molar ratio of Zn^{2+}:anion sodium salt, where the anions include SO_4^{2-}, CH_3COO^-, Cl^-, Br^- and NO_3^-, that leads to the formation of pure ZIF-8 phase is 1:15, 1:20, 1:40, 1:60 and nil, respectively. Combined the above observed NO_3^- has the weakest anion effect on the modulation of pure ZIF-8 formation, we can reasonable to conclude that the anion effect capacity on the formation of pure ZIF-8 phase from our experimental results is SO_4^{2-} > CH_3COO^- > Cl^- > Br^- > NO_3^-, which is in agreement with the classic Hofmeister anion sequence.[313]

Due to the fact that anions have negative charges, there could be interactions between zinc ions and the anions in the synthesis system. Anions could also interact with the protons that are deprotonated from the 2-methylimidazole ligand, which is hypothesised to initiate the formation of ZIF-8.[322] As various anions have different radii effect and dehydration effect in the aqueous system,[313] these effects lead to the different abilities to interact with zinc ions and protons, and also lead to the final observed orders which follows the classic Hofmeister anion sequence. Therefore, it is believed that additional anions can not only promote the formation of pure ZIF-8 phase, but also affect the properties of obtained ZIF-8 materials.

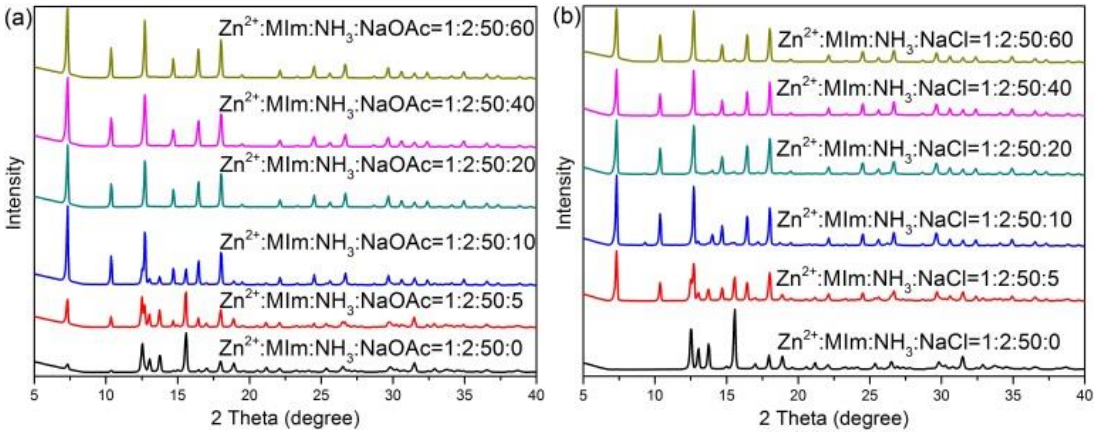

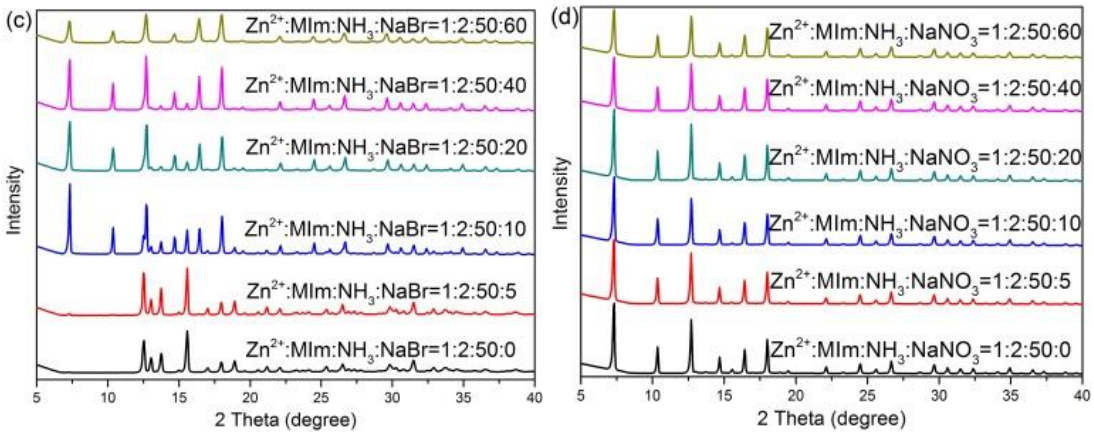

Figure 4.21 XRD patterns of the samples derived from a same concentration of aqueous ammonia solution with the introduction of additional of (a) NaOAc, (b) NaCl, (c) NaBr and (d) $NaNO_3$, respectively.

4.3.4 Conclusions

A series of anions were demonstrated to remarkably affect and promote the formation of ZIF-8 from stoichiometric molar ratio of precursors in aqueous ammonia solution at room temperature. The requirement of ammonia concentration for the formation of pure ZIF-8 phase can be readily modulated by the anion. In addition, the anion types and concentrations can effectively promote the formation of pure ZIF-8 phase with tuneable particle morphologies and textural properties. The anion effect capacity was revealed to be SO_4^{2-} > CH_3COO^- > Cl^- > Br^- > NO_3^-, which follows the classic Hofmeister anion sequence.

4.4 Summary

A cost-effective and facile method for the preparation of ZIF-8 materials from stoichiometric molar ratios of zinc ions and 2-methylimidale precursor in aqueous ammonia solution at room temperature with high efficiency was presented. Ammonia can promote the deprotonation of 2-methylimidazole ligand and accelerate the formation of ZIF-8. The concentration of ammonia is an important factor which can be readily adjusted to give control the structures, particle crystal sizes and textural properties. This green, low-cost and efficient synthesis method has great potential for large scale production of ZIF-8 for practical applications in the future.

In addition, a series of anions that affects the formation of ZIF-8 in aqueous ammonia systems has been demonstrated. The requirement of ammonia concentration for the

generation of pure ZIF-8 phase can be modulated by the anions. In addition, the anion types and concentration remarkably influence on the formation of pure ZIF-8 and the anion effect capacity follows the classic Hofmeister anion sequence. The Hofmeister anion effect is important to better understand the formation mechanism of ZIFs in different systems and is also useful in other research areas such as interface chemistry.

5. Chapter 5: ZIF-8/graphene oxide nanocomposites with their applications

5.1 Introduction

Recently ZIFs materials have triggered great interests on their promising and potential applications in gas separation, catalysis, sensing and electronic devices, and drug delivery.[294, 323, 324] In particular, the presence of basic imidazolate units as an integral part of the frameworks offers great potential to utilize ZIFs as CO_2 capture candidates.[294, 307] However, owing to the relative small accessible pore apertures and/or the weak interactions between the pore walls and small gas molecules, it is difficult to fully take advantage of the ZIFs pores for gas adsorption. It is, nevertheless, suggested that the combination of an inert CO_2 absorbent with an active one, can produce a novel material that can remarkably improve CO_2 uptake efficiency.[325]

On the other hand, the last few years have witnessed the great rise of interest in graphene and graphene-based materials.[326-328] Graphene oxide (GO), a very important precursor for graphene, has a layered structure with plenty of functional groups, which consist of hydroxyl and epoxy groups mostly in the graphene layers, and small amount of carboxy, carbonyl, phenol, lactone and quinone on the edges of the layers.[329-332] GO is usually produced by chemical treatment of graphite with strong oxidizing agents. Owing to its unique structure, GO has been widely explored and utilized in the preparation of composite materials with promising adsorptive and electronic properties.[333-335]

Actually, MOFs-based graphite oxide composites have been investigated for various applications. For instance, Bandosz and colleagues reported the synthesis of MOF-5 and graphite oxide hybrid composites for the adsorption of ammonia.[335, 336] Later they further explored the coordination chemistry of GO/MOF composites and their applications as adsorbents.[337] Recently, the same group found that the composites of copper-based MOF with aminated GO can enhance CO_2 adsorption.[338] Moreover, Jahan et al generated conducting nanowires consisting of MOF-5 and functionalized graphene,[339] and they also prepared copper-centered MOFs and GO composites as a tri-functional catalyst in three important electrocatalysis reactions,[340] partly due to the good synergistic interactions between MOFs and GO. There are, however, rare reports

on the ZIF/GO composites in literature. Recently, Rao and co-workers generated hybrid composites of GO with ZIF-8, which exhibited tunable nanoscale morphology and good CO_2 uptake at 195 K.[334] Unfortunately, the use of methanol as synthesis medium presents plenty of disadvantages, especially some environmental concerns since organic solvents are usually toxic and flammable. Moreover, the poor dispersion capacity of GO in methanol,[27] inevitably results in the formation of inhomogeneous samples such as mechanical mixtures that may remarkably decrease in the textural properties of the resulting materials. Therefore, these previous works encouraged us to explore a facile and green approach to generate graphene oxide/zeolitic imidazolate frameworks composites that integrate the unique properties of both components.

In this chapter, we present a simple and controllable *in-situ* synthesis method to produce GO/ZIF-8 composite materials in aqueous ammonia solution. These composites largely maintain the high textural properties, and the crystal sizes for ZIF-8 in the composites are tunable via control over the amount of GO in the synthesis medium during the generation. The resulting GO/ZIF composites exhibited enhanced CO_2 uptake capacity due to the increased interactions between CO_2 molecules and the composites.

5.2 Characterizations of the ZIF-8/graphene oxide nanocomposites

The X-ray diffraction patterns (XRD) of the controlled *in-situ* synthesized GO/ZIF-8 composites with different GO contents are presented in Figure 5.1. For comparison, the XRD for pristine GO, bare ZIF-8 and a mechanical mixed sample 10GO-ZIF-M are also included in Figure 5.1. The pristine GO shows a characteristic peak at 2θ of 12^o, representing the average interlayer spacing of 7.4 Å;[341] while bare ZIF-8 exhibits pure sodalite (SOD)-type structures in the XRD patterns. Moreover, the mechanical mixed sample 10GO-ZIF-M displays XRD peaks contributed from both ZIF-8 and GO, suggesting that there is no obvious interaction between ZIF-8 and GO in the mechanical mixing sample. However, the XRD results of the controlled *in-situ* synthesized GO-ZIF composites exclusively exhibit only peaks from the sodalite (SOD)-type ZIF-8 without other new peaks or peaks from GO, regardless of GO contents in the composites. Actually, even if the GO content is up to 30 wt%, the XRD patterns for the composite 30GO-ZIF (see Figure 5.2) are still similar to those for the ZIF-8 and other GO-ZIF composites with lower GO contents, indicating that GO sheets in the *in-situ* synthesized GO-ZIF composites may form strong interactions

with ZIF-8 in the aqueous ammonia system during the synthesis procedure. Considering that GO contains rich hydroxyl, carboxy and epoxy groups, while 2-methylimidazole possesses abundant N-H functional groups, it is highly likely that the presence of GO may facilitate the formation of hydrogen bonds between GO and the imidazolate unit that is an integral part of ZIF-8, resulting in the homogenous combination of the imidazolate unit and GO, which is consistent with previous reports.[334] It is, however, worth noting that the XRD results of composites with higher GO contents are different from the previous reports,[334, 336] likely due to the poor dispersion ability of GO in organic solvent synthesis media, which result in the formation of composites similar to mechanically mixed materials. In addition, the XRD peak for GO may shift in a wide range depending on the water content in the GO sheet layers, thus its peak may be overlapped with the XRD peaks of ZIF-8 although we cannot rule out the possibility that the low GO content in the in-situ synthesized GO-ZIF8 composites may be beyond the detection limit of XRD instrument.

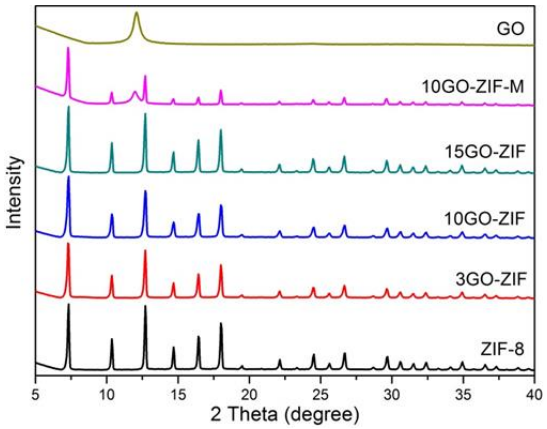

Figure 5.1 Powder XRD patterns of *in-situ* synthesized GO-ZIF composites, GO-ZIF-M, GO and ZIF-8.

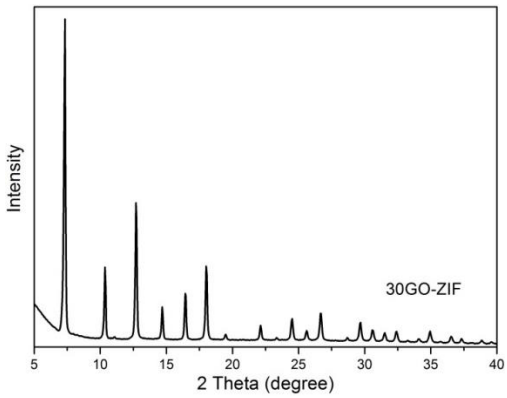

Figure 5.2 Powder XRD pattern of in-situ synthesized 30GO-ZIF composite.

The thermal gravimetric analysis (TGA) and corresponding mass spectroscopy (MS) signals of ZIF-8, 10GO-ZIF, 10GO-ZIF-M and pristine GO, performed under air flow are presented in Figure 5.3, which provides another evidence of the formation of strong interaction between GO and ZIF-8 in the controlled *in-situ* synthesized GO-ZIF composites. For pristine GO, besides the removal of adsorbed water at low temperature (see the weight loss in Figure 5.3a and H_2O signal in Figure 5.3d), it decomposes dramatically at 250 ^oC, accompanied by the release of CO_2 and H_2O (see Figure 5.3a, b and d). For sample ZIF-8, two weight loss events centred at 450 and 500 ^oC were observed, corresponding to the decomposition of organic imidazolate species and the burning off the formed carbon species with the emission of CO_2, NO_2 and H_2O, as demonstrated by MS signals in Figure 5.3b, c and d. For the mechanical mixed composite 10GO-ZIF-M, it exhibits not only the weight loss events in TGA but also the MS signals from degradation of both components GO and ZIF-8, implying that there is no obvious interaction between GO and ZIF-8 in this mechanically mixed sample. However, the TGA-MS results of the *in-situ* synthesized 10GO-ZIF composite exhibit similar decomposition temperatures, weight losses and gas releasing signals with the pristine ZIF-8, without any feature of pristine GO, indicating that the GO sheets in the *in-situ* synthesized composites may form strong interaction with ZIF-8, which is also in agreement with XRD results.

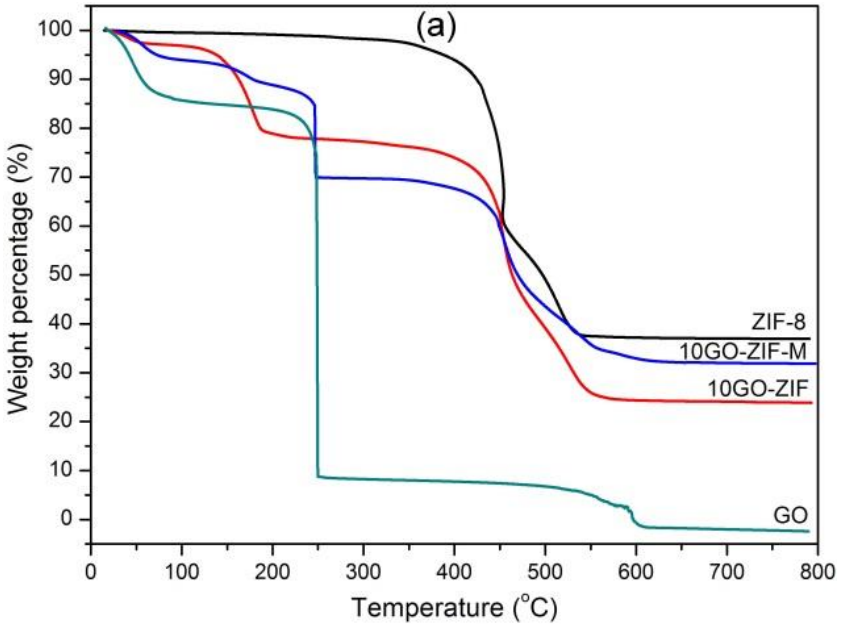

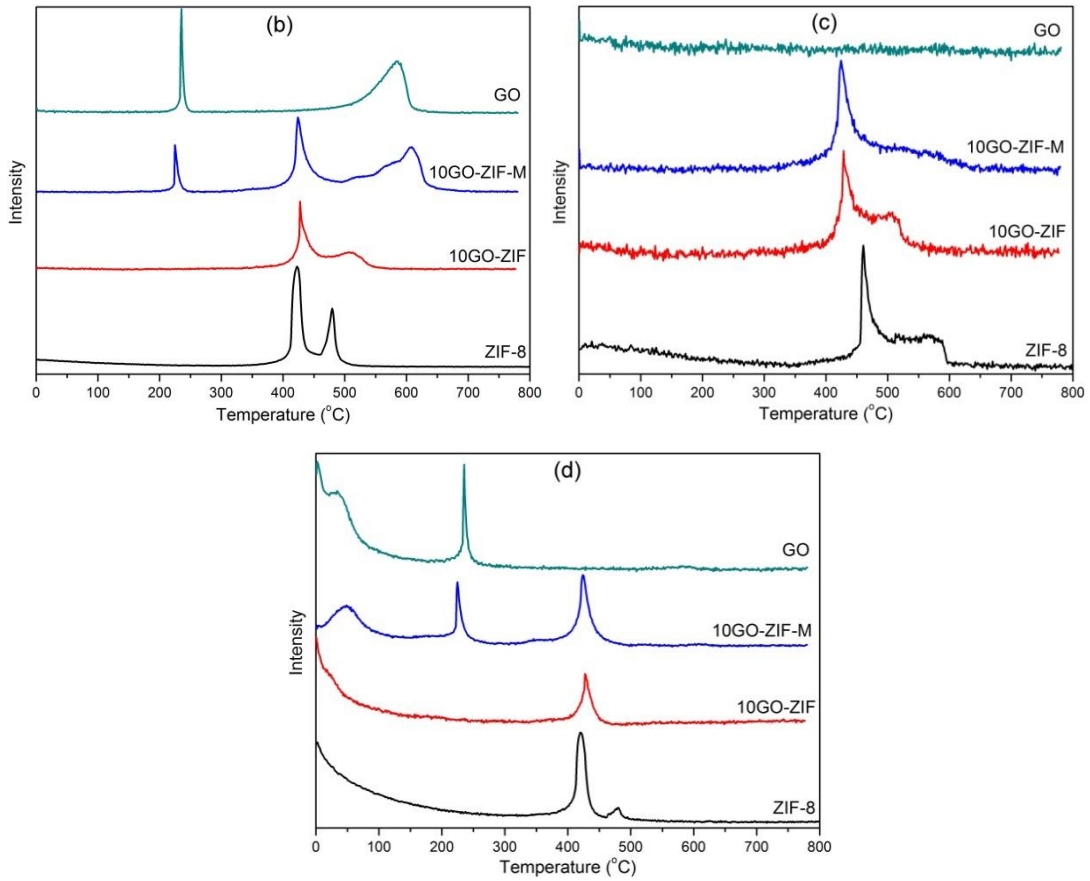

Figure 5.3 (a) TGA curves and MS signals of (b) CO_2, (c) NO_2 and (d) H_2O respectively for sample GO, ZIF-8, 10GO-ZIF and 10GO-ZIF-M.

Moreover, the FTIR spectra also confirm the formation of strong interactions between GO and ZIF-8 in the *in-situ* synthesized GO-ZIF composites. As shown in Figure 5.4a, all the *in-situ* synthesized GO-ZIF composites exclusively exhibit FTIR spectra similar to ZIF-8, but the mechanical mixed 10GO-ZIF-M sample displays spectrum contributing from both GO and ZIF-8. As presented in Figure 5.4b, most of the absorption bands for ZIF-8 and the *in-situ* synthesized GO/ZIF composites are associated with the vibrations of the imidazole units, such as the peak at 1584 cm^{-1} can be assigned as the C=N stretch mode, while the bands at 1350–1500 cm^{-1} are associated with the imidazole ring stretching. The bands in the spectral regions of 900–1350 cm^{-1} and those below 800 cm^{-1} are assigned as the in-plane bending and out-of-plane bending of the imidazole ring.[342] Particularly, the strong bands at 1150 and 995 cm^{-1} is due to the C-N stretching of the imidazole units. Clearly, no bands can be attributed to C-O bonds in the *in-situ* synthesized GO-ZIF composites. However, the mechanical mixed 10GO-ZIF-M sample displays absorption bands not only from

ZIF-8, but also the main bands from GO, such as C=O stretching vibrations at 1710 cm^{-1}, C-O stretching vibrations in epoxy or alkoxy groups at 1049 cm^{-1} and C=C skeletal vibration bands from unoxidized graphitic domains or the stretching deformation vibration of intercalated water at 1620 cm^{-1}, which are consistent with previous reports.[343] These observations clearly confirmed that strong interactions are formed between GO and ZIF-8 in the *in-situ* synthesized GO-ZIF composites, while no such interactions exist in the mechanical mixed 10GO-ZIF-M sample.

Figure 5.5 presents the UV-Vis absorption spectra of GO, ZIF-8 and 10GO-ZIF dispersed in water. The absorption peak of GO at 217 nm is due to the characteristic π -plasmon absorption and a shoulder peak at about 260 nm, which is assigned to n-π transitions of C=O bonds. The pristine ZIF-8 has an absorption band at 220 nm, while 10GO-ZIF composite shows a slight shift in absorption band at 222 nm compared to pristine ZIF-8. This red shift in the absorption band could be caused by charge or energy transfer interaction between the poly-aromatic scaffold in GO and ZIF-8,[340] further suggesting the formation of strong interaction between the GO and ZIF-8 species in the *in-situ* synthesized GO/ZIF composites.

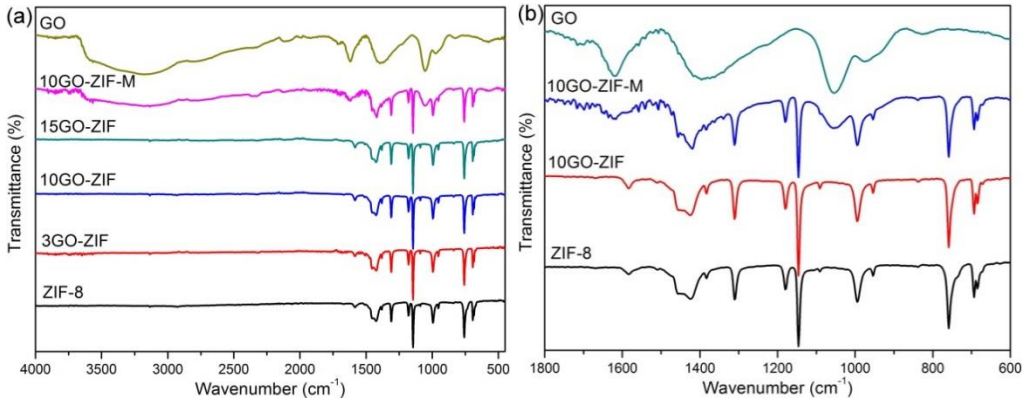

Figure 5.4 FTIR spectra of GO-ZIF composites, GO-ZIF-M, GO and ZIF-8.

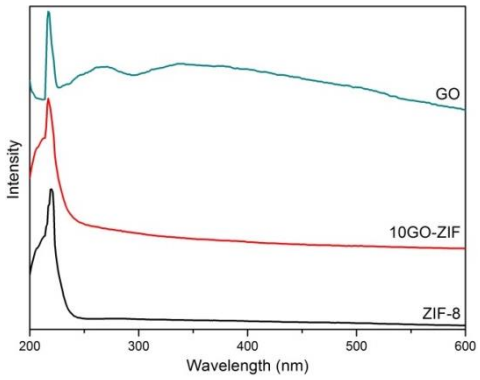

Figure 5.5 UV-Vis spectra of GO, ZIF-8 and representative GO-ZIF composite.

The morphologies of the studied samples were characterized using scanning electron microscopy (SEM) and transmission electron microscopy (TEM). SEM images in Figure 5.6a-d show that the pristine ZIF-8 crystals have the uniform micrometer-sized cubic shapes, which is consistent with previous reports.[344] Obviously, the crystal size of ZIF-8 can be adjustable by control over the amount of GO in the *in-situ* synthesized composites. The average crystal size for ZIF-8 particles decreases gradually from 5 μm for pristine ZIF-8 to 1.5 μm for the *in-situ* synthesized 15GO-ZIF sample with 15 wt% GO content. Actually, if the GO content in the *in-situ* synthesized composite further increases up to 30 wt%, the average crystal size for ZIF-8 particles in the resulting 30GO-ZIF sample can decrease to 0.7 μm (see Figure 5.7). The crystal sizes of ZIF-8 particles in the *in-situ* synthesized GO-ZIF composites are probably controlled by the functional groups of GO through coordination modulation which inhibits the growth of crystals,[334] in which the GO sheets could be performed as a structure-directing agent for the nucleation and growth of ZIF-8 crystals. In addition, Figure 5.6e and Figure 5.6f present the SEM images of 10GO-ZIF-M and GO, respectively. Obviously, the mechanical mixed sample 10GO-ZIF-M displays ZIF-8 crystals with size around 5 μm and the GO sheets are clearly separated from the ZIF-8 crystal without any interactions with GO due to mechanical mixing.

Representative TEM images of *in-situ* synthesized 10GO-ZIF composite were presented in Figure 5.8. It is found that the as-synthesized GO-ZIF composite exhibits the regular cubic-shape of ZIF-8 crystals, which is consistent with the SEM results. Furthermore, it can be clearly observed that some GO sheets are attached on the edges of the ZIF-8 crystals (Figure 5.8a) and some GO sheets are actually embedded in the ZIF-8 cubic particles (Figure 5.8b), suggesting the potential to form strong interaction between the ZIF-8 particle and GO sheets; Consequently, it is likely to generate homogenously ordered structures in the *in-situ* synthesized GO-ZIF composites.[336] However, it's worth noting that the particle sizes for GO in the in-situ synthesized GO-ZIF8 composites (Figure 5.8a) are much smaller than those for pristine GO (Figure 5.6f), which also further confirm that the GO in the *in-situ* synthesized GO-ZIF8 composites is different from the pristine GO particles due to the formation of new chemical bonds between GO and ZIFs crystals.

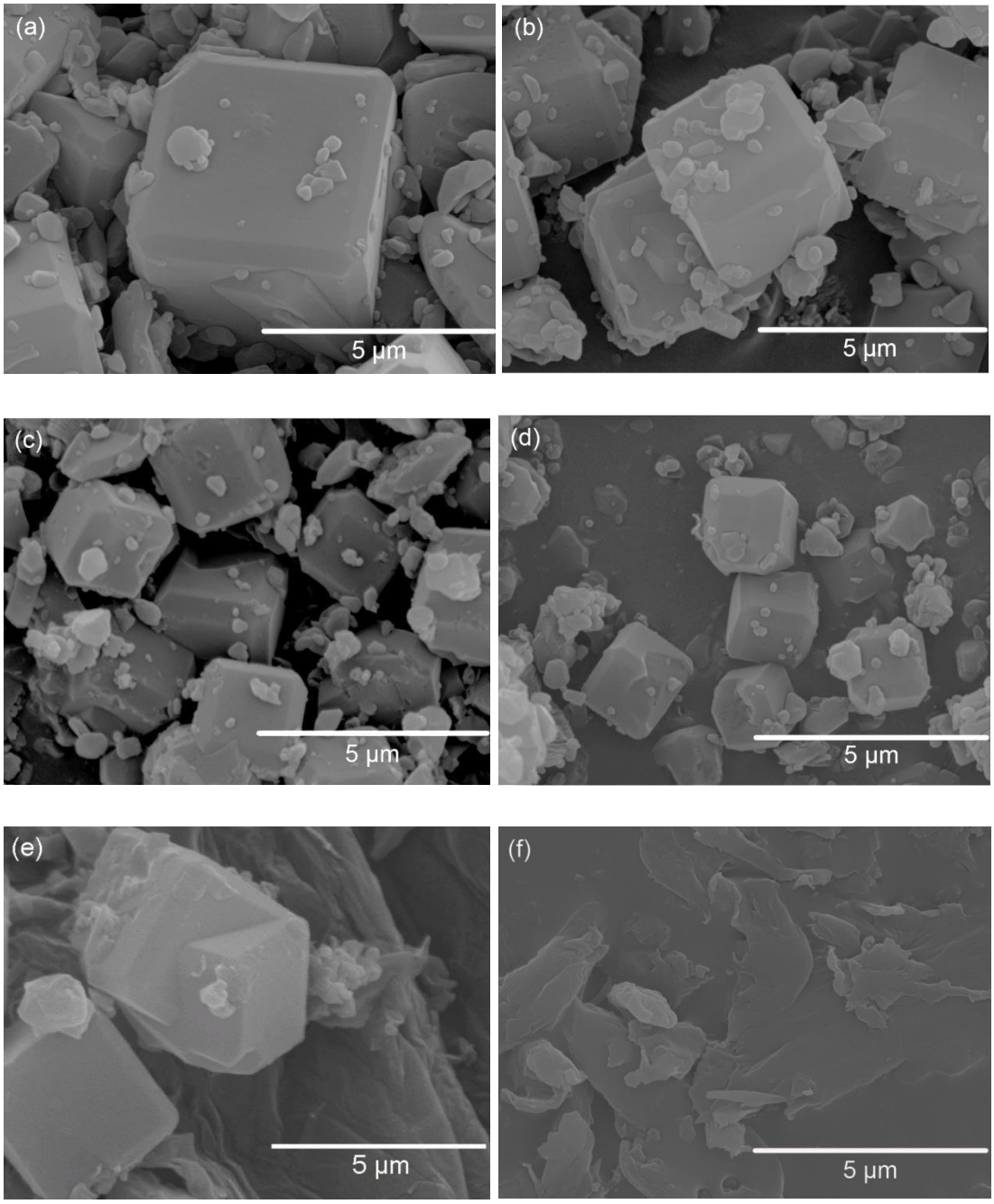

Figure 5.6 Representative SEM images of *in-situ* synthesized GO-ZIF composites and GO sample: (a) ZIF-8, (b) 3GO-ZIF, (c) 10GO-ZIF, (d) 15GO-ZIF, (e) 10GO-ZIF-M and (f) GO.

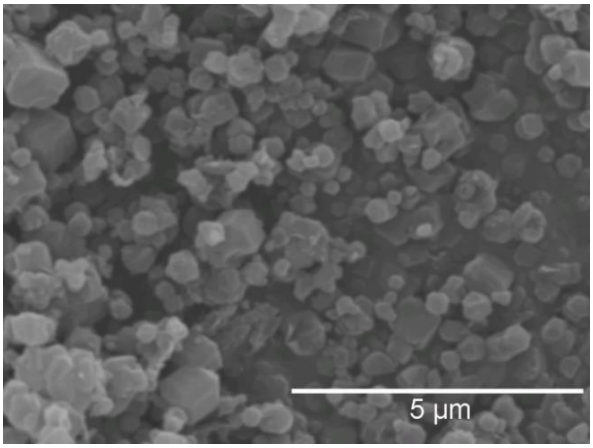

Figure 5.7 Representative SEM image of in-situ synthesized 30GO-ZIF composite.

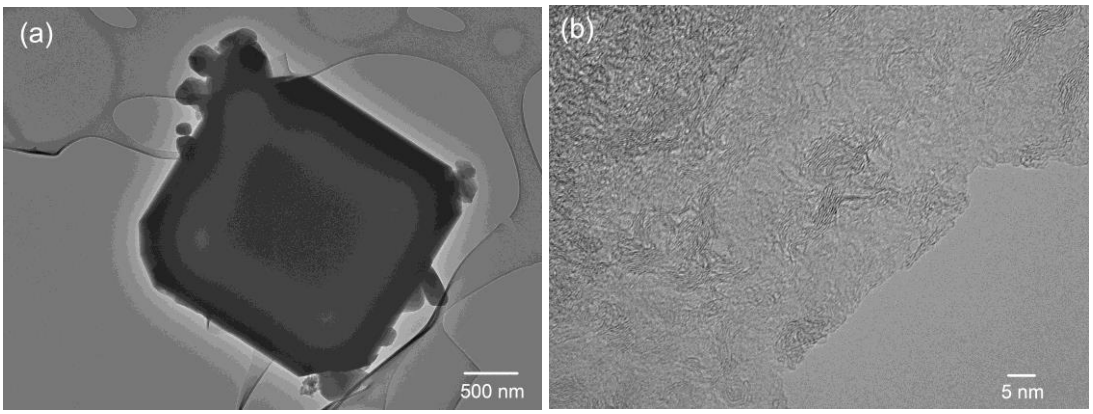

Figure 5.8 Representative TEM images of *in-situ* synthesized 10GO-ZIF composite.

The textural properties of the GO-ZIF composites can be obtained from N_2 adsorption–desorption measurements at liquid nitrogen temperature. As shown in Figure 5.9, the nitrogen sorption for GO is quite low because of its nonporous structure,[345] and all the *in-situ* as-synthesized GO-ZIF composites show type I isotherms with adsorption and desorption branches are completely reversible, indicating negligible mesopores existed in these composites. Moreover, all the *in-situ* synthesized GO-ZIF composites display significant adsorption of nitrogen under low relative pressure, implying those composites are micropore dominated materials, which are in agreement with the microporous nature of ZIF-8 material (as shown in Figure 5.9). The mechanical mixed sample 10GO-ZIF-M also exhibits large quantity of nitrogen adsorption under low relative pressure in its isotherms due to the

microporous nature of ZIF-8; however, it shows a large hysteresis loop between adsorption and desorption branches, suggesting the existence of mesoporous voids between the sample particles, which is obviously different from the *in-situ* synthesized GO-ZIF composites. In addition, as summarized in Table 5.1, the textual properties of the *in-situ* synthesized GO-ZIF composites are tuneable by control over the GO content in the composites. Generally, compared to the pristine ZIF-8, the surface area and pore volume for the *in-situ* synthesized GO-ZIF composites with lower GO content (such as sample 3GO-ZIF and 10GO-ZIF) increase slightly, but the surface area for GO-ZIF composite with higher GO content (such as sample 15GO-ZIF) decreases slightly. The increase in surface area for lower GO content composites (sample 3GO-ZIF and 10GO-ZIF) can arise from the synergistic effect,[338] which is the strong interactions between GO and ZIF-8 resulting in the formation of new developed porosities in the *in-situ* synthesized composites; while the decrease in surface area for 15GO-ZIF may due to an increasing proportion of nonporous GO in the composite, which may result in partially blocking the pore channels of ZIF-8. Compared to the pristine ZIF-8, the *in-situ* synthesized 15GO-ZIF composite with 15 wt% GO exhibits small level (around 5.6%) of decrease in surface area. On the contrary, a mechanical mixed sample 10GO-ZIF-M with 10 wt% GO, shows surface area of 1188 m^2 g^{-1}, which is 15.6% lower than that of the pristine ZIF-8 sample and 16.0% lower than that of *in-situ* synthesized 10GO-ZIF composite with the same amount of GO content. These observations clearly demonstrated that the *in-situ* synthesized composites are not just simply a physical mixture of GO and ZIF-8, but formed by a synergy effect between GO and ZIF-8. This synergistic effect may not only lead to form new porosity between GO and ZIF-8 units, but also may cause those "lace-like" structures where GO sheets could be embedded within ZIF-8 crystals.[338]

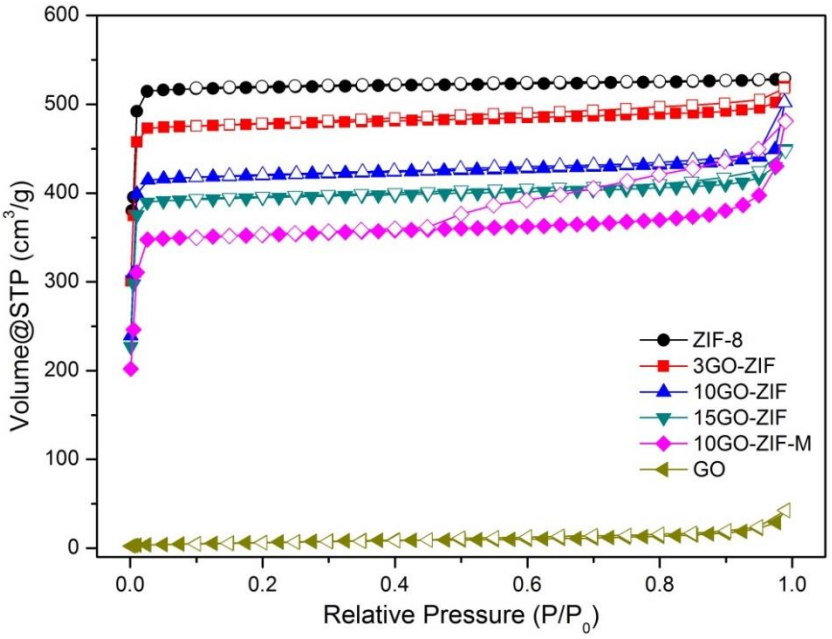

Figure 5.9 Nitrogen sorption isotherms measured at -196 ^{o}C for sample GO, ZIF-8, 10GO-ZIF-M and the as-synthesized composites (3GO-ZIF, 10GO-ZIF and 15GO-ZIF). For clarity, the isotherms for samples 3GO-ZIF and ZIF-8 are offset for 50 and 100 along y axis respectively.

Table 5.1 Textural properties and CO_2 uptake capacities of studied samples.

Sample	GO content (wt %)	Surface area (m^2 g^{-1})	Pore volume (cm^3 g^{-1})	CO_2 uptake at 1.0 bar (cm^3 g^{-1})
ZIF-8	0	1408	0.67	37
3GO-ZIF	3	1439	0.71	40
10GO-ZIF	10	1414	0.78	49
15GO-ZIF	15	1328	0.68	35
10GO-ZIF-M	10	1188	0.74	33
GO	100	25	0.07	6

5.3 CO_2 uptake performance

A variety of porous materials including zeolites, mesoporous silicas, MOFs and porous carbons can be used as solid adsorbents for CO_2 capture due to the increased environmental concerns.[346-349] The CO_2 adsorption capacities at 0 ^oC for GO, ZIF-8, 10GO-ZIF-M and the *in-situ* synthesized composites (3GO-ZIF, 10GO-ZIF and 15GO-ZIF) are presented in Figure 5.10a and their CO_2 uptake capacities are also summarized in Table 5.1. Generally, CO_2 uptake capacities of porous materials are related to sample surface area, which is consistent with our previous report.[350] GO is a weak CO_2 adsorbent with an uptake capacity of 6 $cm^3\ g^{-1}$ at 0 ^oC and 1.0 bar, while the pristine ZIF-8 shows a CO_2 uptake capacity of 37 $cm^3\ g^{-1}$ under the same conditions. Compared with the pristine ZIF-8, the *in-situ* synthesized composites with GO content up to 10 wt% (sample 3GO-ZIF and 10GO-ZIF) exhibit increased CO_2 uptake capacities, but the composite with higher GO content (sample 15GO-ZIF) then shows decreased CO_2 adsorption. As a result, both samples 3GO-ZIF and 10GO-ZIF display higher CO_2 uptake while sample 15GO-ZIF show slightly lower CO_2 sorption capacity than pristine ZIF-8. It is worth noting that compared with the pristine ZIF-8, the *in-situ* synthesized 10GO-ZIF composite exhibited up to 33% increase in the CO_2 uptake capacity at 0 ^oC and 1.0 bar. This unusual CO_2 uptake can also be attributed to the synergistic effect of GO and ZIF-8, where GO with different functional groups provides specific interaction sites for CO_2.[334] Moreover, the formation of hydrogen bonds between GO and imidazolate unit that is an integral part of ZIF-8 can increase not only the degree of interaction between graphene oxide layers and ZIF-8 crystals, but also the generation of new porosities. Consequently, the total porosities of the composites have been increased and therefore the CO_2 adsorption capacities have also been enhanced. This is supported by the data in Table 5.1 where the CO_2 uptake capacity of sample 10GO-ZIF is higher than that of pristine ZIF-8 and bare GO. In addition, as the composites were synthesized in aqueous ammonia solution medium, the synthesized composites may undergo N-doping treatment, which may benefit to CO_2 adsorption.[246] However, the mechanical mixed sample 10GO-ZIF-M shows CO_2 uptake capacity of 33 $cm^3\ g^{-1}$, which is 10.8% and 32.7% lower than that of pristine ZIF-8 and the *in-situ* synthesized 10GO-ZIF composite with the same amount of GO content respectively. Therefore, the introduction of GO into the composites via controlled *in-situ* synthesis method can effectively affect the textural properties and

consequently influence remarkably on the CO_2 uptake capacities of resulting composites.

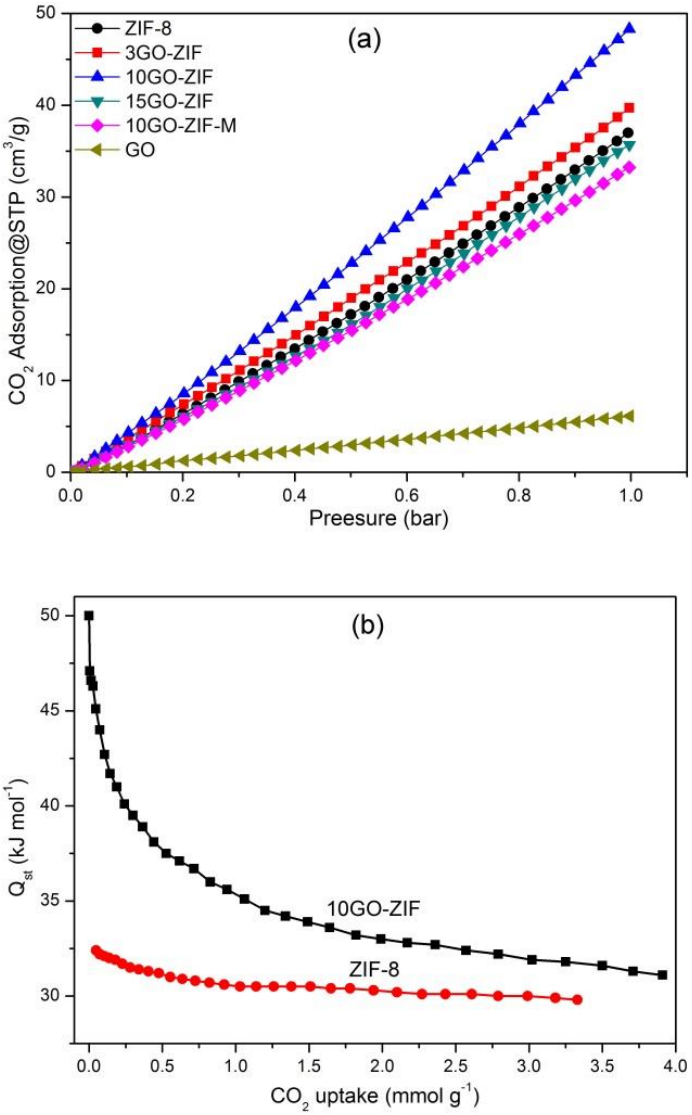

Figure 5.10 (a) CO_2 adsorption capacities at 0 ^oC for sample GO, ZIF-8, 10GO-ZIF-M and the *in-situ* synthesized composites (3GO-ZIF, 10GO-ZIF and 15GO-ZIF); (b) Isosteric heat of CO_2 adsorption (Q_{st}) for representative *in-situ* synthesized 10GO-ZIF composite and pure ZIF-8 as a function of the amount of CO_2 adsorbed.

The CO_2 adsorption energy (i.e., isosteric heat of adsorption, Q_{st}), which indicates the strength of interaction between CO_2 molecules and the adsorbents, was calculated using the CO_2 sorption isotherms measured at 0 and 25 ^oC based on the Clausius-Clapeyron equation. The plots of Q_{st} as a function of CO_2 uptake for ZIF-8 and 10GO-ZIF are presented in Figure 5.10b. The initial isosteric heat of the adsorption

Q_{st} for pristine ZIF-8 is 32 kJ mol^{-1} at low CO_2 uptake (low surface coverages), which gradually drops to an average Q_{st} of 29 kJ mol^{-1} at high CO_2 uptake (high surface coverages). The initial and average Q_{st} for ZIF-8 are generally higher than those values reported in literature[334, 351] These observed higher Q_{st} values for ZIF-8 are probably due to the use of the aqueous ammonia solution as synthesis system. Interestingly, the initial isosteric heat of the adsorption Q_{st} for the representative *in-situ* synthesized 10GO-ZIF composite displays a significantly high value of 50 kJ mol^{-1} at low CO_2 uptake, suggesting a strong interaction between CO_2 molecule and 10GO-ZIF composite. It indicated that under aqueous ammonia system, the synergistic effect of GO and ZIF-8 plays a predominant role in the initial interaction when CO_2 adsorbed on the surface of the composite, probably due to the formation of strong acid-base interaction between the acidic CO_2 molecules and the basic imidazolate units as an integral part of the composites. At higher CO_2 coverages, the Q_{st} value of 10GO-ZIF reduces to an average value of 31 kJ mol^{-1}, which is higher than that of ZIF-8, suggesting stronger interaction between CO_2 molecule and the *in-situ* synthesized 10GO-ZIF than that in ZIF-8 at higher CO_2 coverages, due to the synergistic effect between GO and ZIF in the *in-situ* synthesized 10GO-ZIF composite. The synergistic interactions of ZIFs and GO may offer a new approach to prepare other ZIFs/GO composites for different applications.

5.4 Summary

In summary, composites containing ZIF-8 and various contents of GO have been successfully prepared using an *in-situ* controlled synthesis method in an aqueous ammonia system. Different material characterization techniques including XRD, TGA-MS, FTIR and UV-Vis spectra confirm the formation of strong interactions between ZIF-8 and GO in the synthesized composites. The crystal sizes of ZIF-8 and the textural properties of composites can be modulated by the control over the amount of GO in the composites. GO may act as a potential structure-directing agent for the growth and stabilization of ZIF-8 crystals. In addition, the *in-situ* synthesized composites show enhanced CO_2 adsorption energy and significant CO_2 storage capacity, due to the strong interactions and the synergistic effect between GO and ZIF-8 facilitating the formation of new developed porosities in the *in-situ* synthesized composites. The synergistic interactions of ZIFs and GO may provide a new path to fabricate novel GO/ZIFs composites for a wide range of applications.

6. Chapter 6: Zinc oxide/nanoporous carbon composites derived from ZIF-8 and its applications

6.1 Introduction

Porous carbon materials with high specific surface area, large pore volume, narrow pore-size distribution, good chemical and thermal resistance, and affinity to organic contaminations are very promising for many applications,[352-355] particularly being widely used in air and water purification, gas storage, catalysts, and eletrochemical devices.[356-359] After enormous efforts have been devoted in recent years, the pore structures of carbon at micropore or mesopore levels can be controlled by various synthetic approaches.[360-362]

Recently, porous carbon–metal oxide composite materials have attracted huge interest due to their promising potential in environmental applications, such as gas sorption and contamination removal from water. Reducing CO_2 emission has become a key environmental challenge since CO_2, one of the main greenhouse gases and mainly generated from the combustion of fossil fuels, has been widely recognised to contribute to global warming. For instance, mesoporous carbon-MgO composites have showed high efficiency for CO_2 capture.[363, 364] In addition, removal of organic pollutants from industrial and household wastewater is also an important environment issue and carbon-semiconductor composites have been explored for organic pollutants removal from wastewater.[365-368] For example, porous carbon-TiO_2 composites act not only as a photocatalyst under visible light and show good photodegradation activity for organic pollutants, but also as an adsorbent to adsorb the pollutants through the pores of the matrix.[365-367] Similarly, a porous carbon-doped ZnO composite also exhibited a good photocatalytic performance in terms of the degradation of organic pollutants under visible light.[368, 369]

However, the components in these porous carbon-metal oxide composites usually cannot achieve homogeneous dispersion since they were frequently prepared by mechanical or physical mixing of the metal oxides with the porous carbon materials. More recently, metal organic frameworks (MOFs) (including Zeolitic Imidazolate Frameworks (ZIFs)), a new class of inorganic-organic crystalline nanoporous materials that assembled from metal ions coordinated to rigid organic ligands,[370, 371] have emerged as promising precursors or sacrificial templates for the preparation of

porous carbon based materials,[28, 372] due to their tuneable structures, vast functionalities and fascinating properties. The preparation procedure is simple, and porous carbon-based materials can be produced by the direct carbonization of MOFs in an inert atmosphere, without any additional carbon precursors. Thanks to the inorganic-organic crystal structure of the parental MOFs, the generated metal or metal oxide can be retained homogeneously within the nanoporous carbon matrix.[28] To date, only a few reports have adapted such a thermal treatment of MOFs route for the fabrication of composites. Das *et al* reported a generalized strategy for the synthesis of crystalline metal oxide nanoparticles embedded in a carbon matrix by a controlled thermolysis of MOFs.[373] Yamauchi *et al* demonstrated the creation of nanoporous carbon–Co_2O_3 hybrid materials using a two-step thermal conversion of ZIF-9,[258] while Guangju *et al* obtained N-doped carbon-Co_3O_4 composites using a one-step thermal conversion from a specific MOF, Co–I–MOF.[374] Most recently, we utilized a typical sodalite topology ZIF-8, which is built from corner-sharing tetrahedral ZnN_4 units and the coordination bonds between the Zn^{2+} ions and 2-methylimidazole anions that are amongst the most stable N-donor ligands,[256] to synthesize ZnO/porous carbon composites by the direct carbonization in argon atmosphere, but no XRD peaks related to either ZnO or Zn can be observed in these composites.[257] Therefore, designing new synthesis strategies to create efficient porous carbon-metal oxide composites is highly desirable.

Water is a natural green solvent and water steam has been widely considered as a weak oxidizing agent that can benefit to the slow oxidation rate. Therefore, such a mild and fine controllable oxidation process will not compromise the properties of target materials. This becomes particularly true when water steam is used as an oxidation agent during the generation of porous carbon-metal oxide composites since water steam can react with and oxidise carbons at high temperatures. Inspired by these facts, in this part of the work, a mild and green one-step oxidation approach using water steam at high temperatures has been developed and demonstrated its promising effectiveness in the utilisation of ZIF-8 as a single precursor to generate atomically homogeneous dispersed ZnO/nanoporous N-doped carbon composites, which exhibited excellent CO_2 uptake capacities, efficient adsorption and photodegradation performance in the removal of methylene blue (MB) from water under visible light irradiation.

6.2 Characterizations of the zinc oxide/nanoporous carbon composites

In a typical synthesis, an alumina boat with ZIF-8 was placed in the centre of a flow-through quartz tube sitting in a tube furnace. The furnace was heated at 10 ^{o}C /min to the target temperature under pure argon; when the furnace temperature reached 800 ^{o}C, a 20 ml/min of argon flow saturated with water vapour was introduced in and maintained at the target temperature for 3 h. The gas flow was then switched to argon only while the furnace cooled to room temperature. The final product was collected from the quartz tube and labelled as ZnO/C-S-*S*. Another sample was also obtained via the similar one-step direct carbonization process where a 20 ml/min of argon flow saturated with water vapour is constantly presented during the heating up step, the maintaining at the target temperature for 3 h and the cooling down to room temperature. This sample was designed as ZnO/C-S-*L*. For comparison, the one-step process was also applied to the annealing of ZIF-8 at 800 ^{o}C for 3 h under argon with a flow rate of 20 ml/min,[257] and the collected samples was named as ZnO/C-A. A pure ZnO was also obtained via annealing of ZIF-8 in air at 800 ^{o}C for 3 h.

The sodalite structure of precursor ZIF-8 was first confirmed by XRD in Figure 6.1a and the crystal structures of the as-synthesized ZnO/C composites were characterized by XRD and presented in Figure 6.1b. The sample ZnO/C-S-*S* which derived from water vapour carbonization of ZIF-8 for shorter period (3 h) shows XRD peaks at 2θ of 31.7 °, 34.3 °, 36.2 °, 47.4 °, 56.5 °, 62.7 °, 66.3 °, 67.9 ° and 69.0 °, which can be assigned to (100), (002), (101), (102), (110), (103), (200), (112) and (201) of ZnO with polycrystalline wurtzite structure (Zincite, JCPDS 5-0664). The ZnO/C composite derived from water vapour carbonization of ZIF-8 for longer duration (sample ZnO/C-S-*L*), exhibits the main XRD peaks from wurtzite ZnO with reduced peak intensities. However, the sample derived from the carbonization in argon (sample ZnO/C-A) displays no peaks from ZnO, which is consistent with our previous observation.[257] Clearly the carbonization atmosphere has significant effect on the resulting composites. In addition, all the ZnO/C composites exhibit a broad XRD peak centred at the 2θ of 25^{o} due to the (002) diffraction of carbon, indicating that the utilization of water vapour atmosphere does not damage the formation of porous carbon from ZIF-8 precursors.

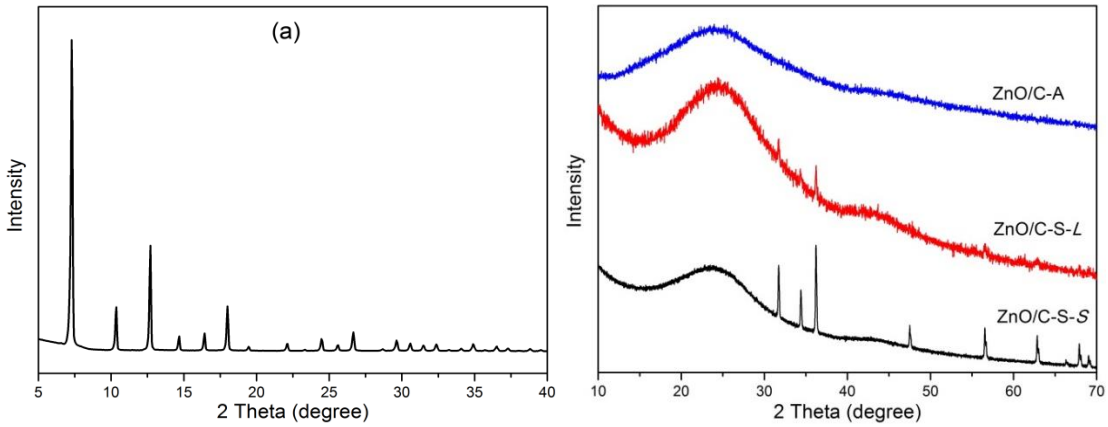

Figure 6.1 Powder XRD patterns of ZIF-8 (a); and the composites of ZnO/C-S-*S*, ZnO/C-S-*L* and ZnO/C-A (b).

FTIR is an excellent technique for monitoring the presence of different functionalities on the surface of the composites. As shown in Figure 6.2, sample ZnO/C-A derived from the carbonization in argon atmosphere displays broad peaks at 1210 cm^{-1} that can be assigned to C–C, C–N stretch while the 1580 cm^{-1} peak may come from aromatic C=C, C=N stretch of N-doped carbon. A shoulder peak at around 1057 cm^{-1} can be due to the Zn-N stretching. For the composites derived from steam carbonization, however, a strong asymmetric peak centred at 1205 cm^{-1} is the contribution from the C-O stretch as well as the C-C and C-N stretch. The peak at 1580 cm^{-1} is stronger than in sample ZnO/C-A owing to the bending vibration of Zn-O-H bonding coupled with the contribution of C=C and C=N stretch from carbon, and Zn-O stretching model is clearly observed at 555 cm^{-1}. Moreover, an asymmetric peak between 1650–1850 cm^{-1} was observed for the steam carbonized samples, likely corresponding to the stretching vibration of C=O from the –COOH. In addition, a peak located at 3600-3700 cm^{-1} is attributed to the stretching of O-H groups from the Zn-OH or adsorbed water.[375] These observations clearly demonstrate that steam carbonization of ZIF-8 results in the formation of ZnO crystals and N-doped carbons with –COOH and –OH functional groups.

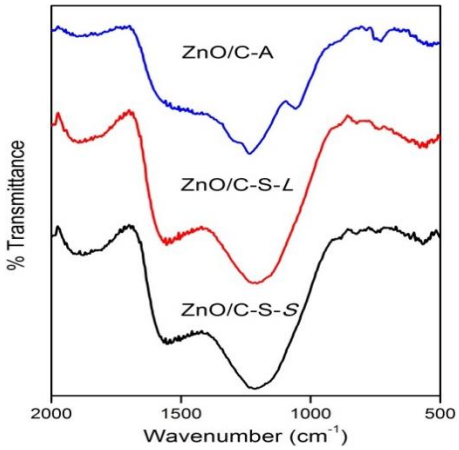

Figure 6.2 FTIR spectra of the composites of ZnO/C-S-*S*, ZnO/C-S-*L* and ZnO/C-A.

In the Raman spectra of the as-synthesized ZnO/C composites, the G band and D band are clearly seen as shown in Figure 6.3, due to the bond stretching of all pairs of sp^2 atoms in both rings and chains and the breathing modes of sp^2 atoms in rings, respectively.[376, 377] The G band at around 1590 cm^{-1} supports the presence of some nanocrystalline carbon and a high content of sp^2-hybridized carbon atoms caused by the carbonization of the samples. The D band at around 1350 cm^{-1} is an indication of less disordered carbon. Therefore, the relatively higher I_D/I_G values of 0.89 and 0.96 for sample ZnO/C-S-*S* and ZnO/C-S-*L* respectively than that of 0.82 for sample ZnO/C-A, not only indicates the formation of abundant defects and amorphous carbons during the annealing process under both water steam and argon atmosphere,[378] but also suggests that ZnO/C composites derived from water steam carbonization possess more defects than that derived from argon atmosphere due to the weak oxidation capacity of high temperature water steam.

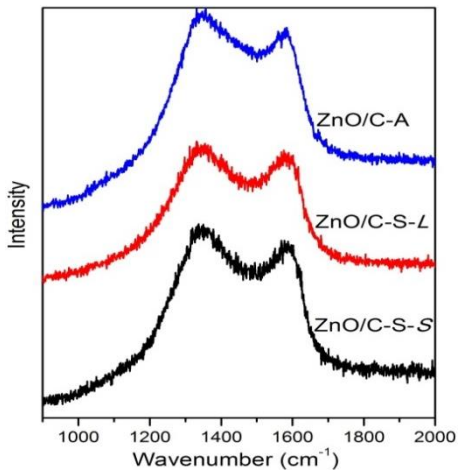

Figure 6.3 Raman spectra of the ZnO/C-S-*S*, ZnO/C-S-*L* and ZnO/C-A samples.

As presented in Figure 6.4a, the elemental survey by XPS of the as-synthesized composites confirms the presence of C, N, Zn and O in all the samples. The Zn 2p spectrum contains a doublet at binding energy of 1021.8 and 1044.5 eV (Figure 6.4b), assigned to Zn 2p3/2 and 2p1/2 lines, respectively. The binding energy distance between these two lines is 22.7 eV, indicating that the Zn ions in the composites are of a +2 state. As shown in Figure 6.4c, the O 1s spectrum exhibited the bonding energy peaked at 531.8 eV, which can be assigned to O^{2-} ions in the Zn–O bonding of the wurtzite ZnO structure.[379] Moreover, the main peak for the O 1s spectra can be deconvoluted into three peaks centred at 530.7, 532.1 and 533.2 eV, which can ascribe to the contribution from the functional groups HO-C=O, C=O and C-OH, respectively.[380, 381] It is worthwhile to note that the samples derived from water steam carbonization display higher O 1s peak intensity than sample derived from the carbonization in argon, indicating that water steam treatment successfully incorporates oxygen species into the resulting composites. The spectra for N species exhibit an intense peak at 398.7 eV and a less intense peak at about 400.6eV (see Figure 6.4e) , indicating the formation of highly coordinated quaternary 'pyrrolic' N atoms (400.6 eV) incorporated into graphene sheets, along with pyridine-like N atoms incorporated into graphene sheets (398.7 eV).[257] As shown in Figure 6.4d, the C 1s spectrum of the samples exhibits a main peak at 284.9 eV, consistent with sp^2 carbon. In addition, the C 1s spectrum can be further deconvoluted into peaks positioned at 284.8, 285.8 and 287.7 eV, which may attributed to C=C, C=N/C-O and C-N/C=O respectively.[375, 380, 381] Based on these XPS analysis and above-mentioned XRD results, we believe that the products derived from the carbonization of ZIF-8 under various conditions are basically N-doped carbon and ZnO composites.

The elemental analysis results of the composites based on EDX analysis are presented in Table 6.1. The N content for ZnO/C-S samples derived from carbonization under water steam is in the range of 11.6 to 8.1 wt%, remarkably lower than that for sample ZnO/C-A which produced via carbonization under argon atmosphere and exhibits the highest N content of 16.5 wt%, possibly due to the high volatility of N species under water steam atmosphere. Actually the N content in sample ZnO/C-S-*S* is only half of that in sample ZnO/C-A. In addition, the bulk N content is very close to its surface content obtained from XPS (i.e., 8.1 and 7.8 wt% for sample ZnO/C-S-*S* obtained via

EDX and XPS analysis, respectively), implying the homogenous dispersion of N species in the resulting composites.

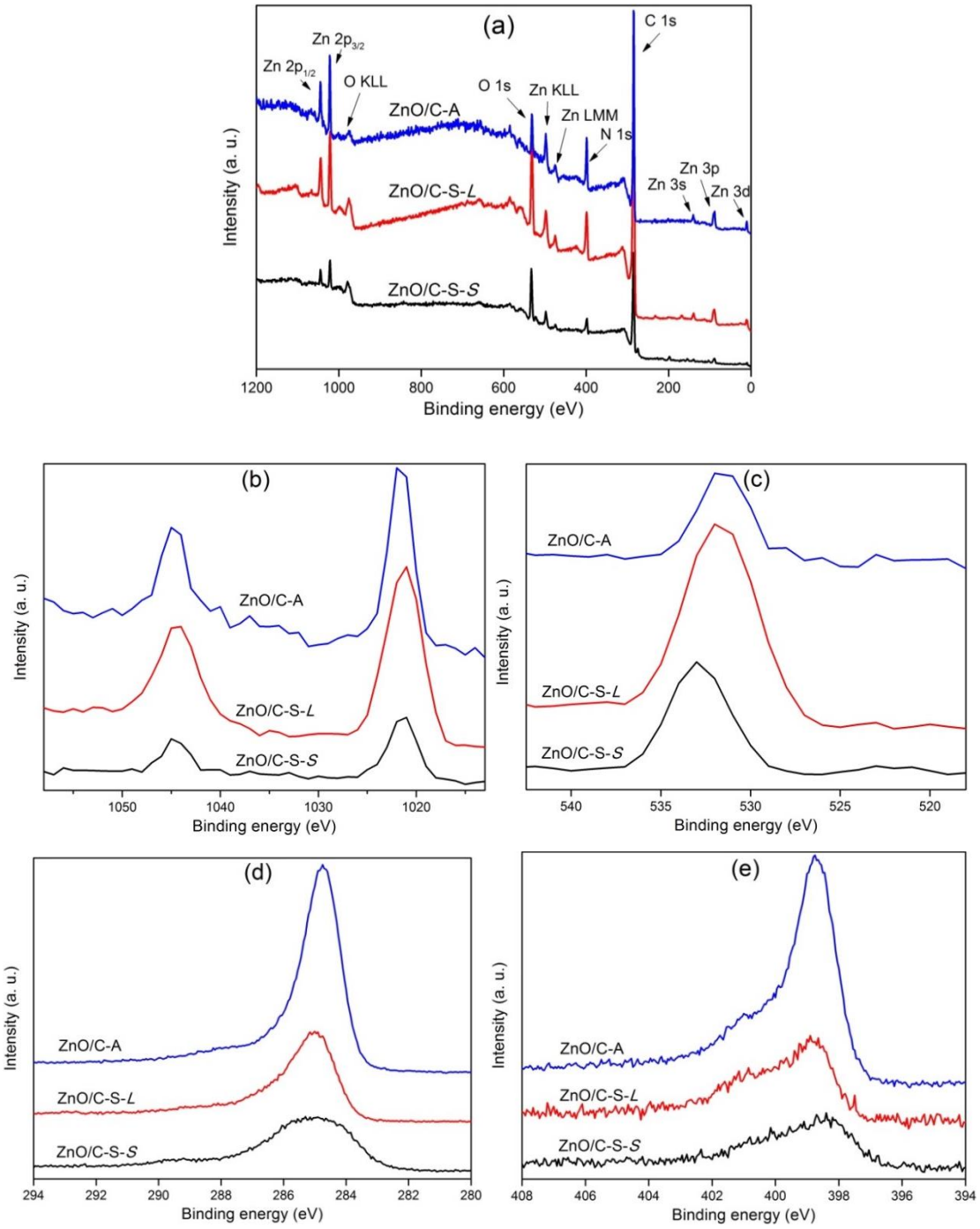

Figure 6.4 XPS results of (a) elemental survey, (b) Zn 2p, (c), O 1s, (d) C 1s and (e) N 1s for samples derived from carbonization of ZIF-8 at 800 ^{o}C under different conditions.

Table 6.1 Textural properties, composition contents and CO_2 uptake capacities of ZnO/C composites derived from the direct carbonization of ZIF-8 under different conditions.

Sample	Surface area[a] / $m^2 g^{-1}$	Pore volume[b] / $cm^3 g^{-1}$	N content[c] / wt%	CO_2 uptake[d] / mmol g^{-1}
ZnO/C-S-*S*	995 (895)	0.58 (0.41)	8.1 (7.8)	3.05 (5.32)
ZnO/C-S-*L*	1134 (986)	1.06 (0.45)	11.6 (10.4)	3.23 (6.08)
ZnO/C-A	771 (706)	0.41 (0.33)	16.5 (14.4)	2.85 (4.42)

[a] The data in parenthesis are microporous surface area; [b] The values in parenthesis are micropore volume.; [c] Data in parenthesis are obtained from XPS analysis; [d] Data obtained at 25 ^oC and 1 bar, while the values in parenthesis are measured at 0 ^oC and 1 bar.

In addition, the photoluminescence (PL) of ZnO/C-S-*S*, ZnO/C-S-*L*, ZnO/C-A and ZnO is shown in Figure 6.5. The PL intensity of ZnO obtained via annealing of ZIF-8 in air shows a peak around 520 nm which is caused by oxygen vacancies. However, the PL intensity of ZnO/C-S-*S*, ZnO/C-S-*L* and ZnO/C-A significantly decreased, suggesting that the excited electrons from ZnO can be transferred to the carbon phase [369]. This phenomenon, quenching in emission of ZnO/C-S-*S*, ZnO/C-S-*L* and ZnO/C-A, also indicates samples ZnO/C-S-*S*, ZnO/C-S-*L*, ZnO/C-A have a superior photo catalysis activity comparing with the pure ZnO.

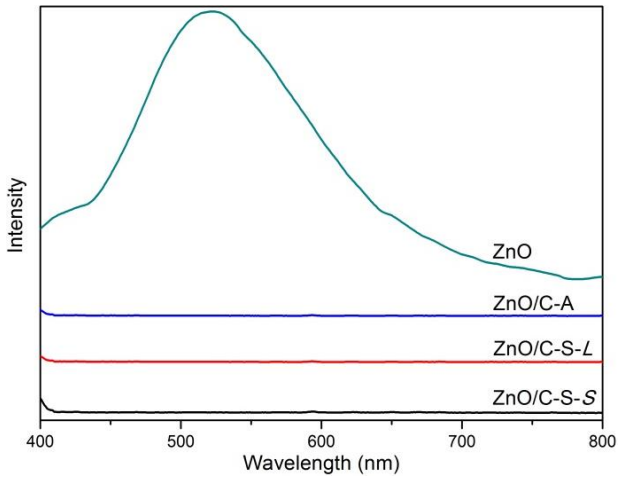

Figure 6.5 PL spectrum of ZnO/C-S-*S*, ZnO/C-S-*L*, ZnO/C-A and ZnO

The thermal stabilities of the composites in air were evaluated by TGA-MS. As shown in Figure 6.6a of the TGA profiles, all the composites exhibit a major weight loss event below 100 ^{o}C, corresponding to the removal of adsorbed water from the composites (Figure 6.6c). Moreover, composites ZnO/C-S-*S* and ZnO/C-S-*L* derived from the carbonization of ZIF-8 under water steam display a single weight loss event centred at 410–490 ^{o}C, which arises from the burn off the N-doped carbon species in air, as confirmed by the emission of CO_2, NO_2 and trace amount of H_2O in their MS signals (see Figure 6.6b and d). However, the composite ZnO/C-A derived from the carbonization of ZIF-8 under argon atmosphere exhibits two weight loss events centred at 400 and 510 ^{o}C, due to the burning off N-doped carbons. Obviously, composites ZnO/C-S-*S* and ZnO/C-S-*L* retain lower residual material than composite ZnO/C-A after TGA measurement in air and the residuals are dominated by ZnO.[257] The general lower residual ZnO content (in the range of 10-16%) may be attributed to the fact that ZnO was reduced to metallic Zn by the formed carbon during the carbonization, and the formed Zn would evaporate during the high temperature process since Zn has a relative low boiling point (907 ^{o}C).

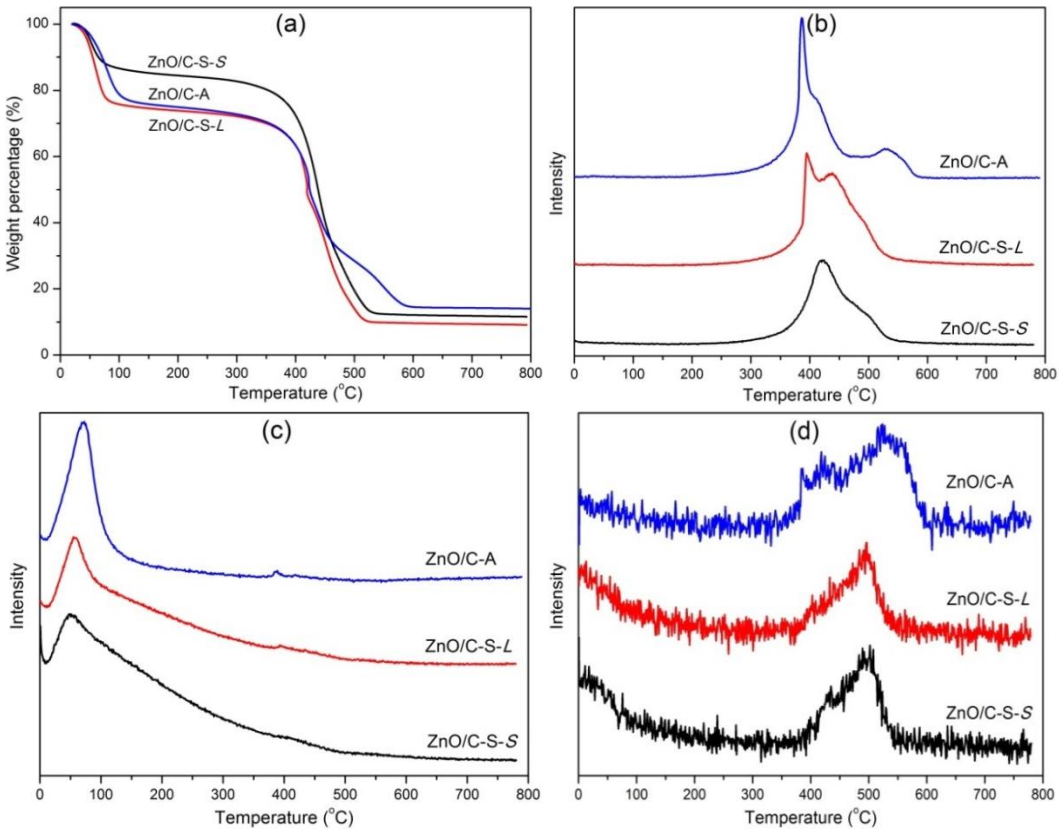

Figure 6.6 TGA (a) and their corresponding MS curves for CO_2 (b), H_2O (c) and NO_2 (d) for different composites.

The textural characteristics of the as-synthesized composites are analysed by N_2 sorption at -196 ^oC and the results are summarized in Table 6.1. As shown in Figure 6.7a, the N_2 sorption of the as-synthesized composites all exhibit type I isotherms with significant adsorption below the relative pressure (P/P_0) = 0.1, due to the capillary filling of micropores. The isotherms for all the composites are similar, and the adsorption–desorption isotherm branches are generally reversible, confirming their predominant microporous feature. Sample ZnO/C-S-*S*, ZnO/C-S-*L* and ZnO/C-A has a specific surface area of 995, 1134 and 771 $m^2 g^{-1}$ and pore volume of 0.58, 1.06 and 0.41 $cm^3 g^{-1}$, respectively, slightly lower than that of the precursor ZIF-8 (Figure 6.8a). It is worth noting that, compared with the composite derived from carbonization in Ar, the composites derived from water steam carbonization exhibit a 29-47% increase in specific surface area and up to 1.5 times improvment in pore volume, indicating water steam carbonization can remarkably improve the surface area and pore volume of the resulting ZnO/C-S composites. Moreover, all the composites display high micropore surface areas (706–986 $m^2 g^{-1}$) and micropore volumes (0.33–0.45 $cm^3 g^{-1}$), originating from the high level of zeolite-type pore ordering of ZIF-8 which acts as both the template and the carbon precursor. The proportion of micropore surface areas for all the composites is around 90%, but the proportion of micropore volumes varies from 42–80%. The pore size distribution (PSD) of the composites is further analysed using a Non-Local Density Functional Theory (NLDFT) model based on N_2 adsorption branch data, and the results show that all the as-synthesized composites possess a relative sharp PSD centred at 1.2 nm, without obvious mesopores (as shown in Figure 6.7b). In addition, the formation of supermicropores in the range of 1.3–2.0 nm is clearly observed for these composites and the level of the supermicropores increases with the introduction of water steam, and it seems longer steam carbonization can accelerate the formation of supermicropores, implying that steam atmosphere processing can affect not only the surface area and pore volume, but also the pore diameters of the composites. Compared with the previous report that the hierarchical porous carbon contains micropores, along with the mesopores and macropores synthesized by solvent evaporation during the carbonization of MOFs[382], our products mainly contain micropores, without obvious mesopores or macropores. Clearly, the introduction of the oxygen-containing functional groups via water steam process into the ZnO/C-S-*S*

and ZnO/C-S-*L* materials can effectively improve the textural properties of the composites[383].

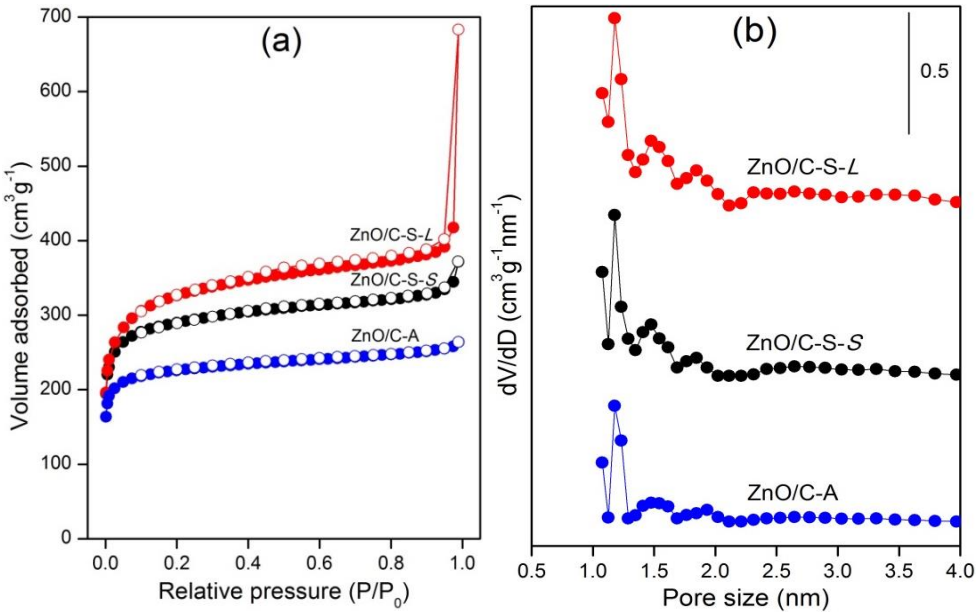

Figure 6.7 N_2 sorption isotherms (a) and the corresponding pore size distribution curves (b) of different porous composite samples.

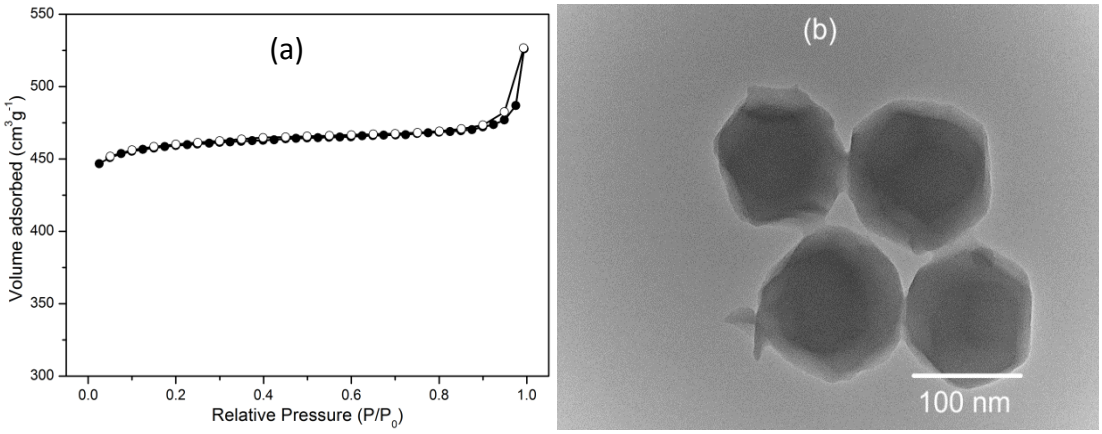

Figure 6.8 N_2 sorption isotherms (a), and TEM image (b)of ZIF-8 material.

TEM analysis is carried out to further investigate the morphologies and microstructures of the resulting porous composites. As shown in Figure 6.8b, the ZIF-8 precursor displays the typical rhombic dodecahedron morphology with an average particle size of 100-150 nm.[257] After carbonization process either in Ar or in steam

atmosphere, as presented in Figure 6.9, all the ZnO/C composites exhibit spherical-like particles with smaller sizes around 100-130 nm but the small particles tend to agglomerate to form larger particles. It is difficult to observe obvious ZnO particles in low resolution TEM analysis, maybe due to the small particle size of ZnO and confinement effects by the carbon. However, under high resolution TEM, ZnO particles with size in the range of 5-10 nm can be clearly identified (as shown in Figure 6.9b and Figure 6.10). This is maybe due to the fact that the use of ZIF-8 as both precursor and template, can result in ZnO nanoparticles formed locally surrounded or coated by carbon derived from the carbonization of 2-methylimidazole species in ZIF-8 with arrangement similar to the precursor ZIF-8 structures, leading to homogeneous embedded the ZnO nanoparticles in the porous carbon matrix.[384] In addition, as shown in Figure 6.9b, d and f, some pore channels in the carbon domains are distinguishable, with an estimated pore diameter of *ca*. 0.8–1.0 nm, which is consistent with the pore size obtained from N_2 sorption analysis. A selected area electron diffraction (SAED) pattern (inset in Figure 6.9b) confirms the formation of crystalline ZnO and amorphous carbon, which is in agreement with the XRD observation in Figure 6.1b**.**

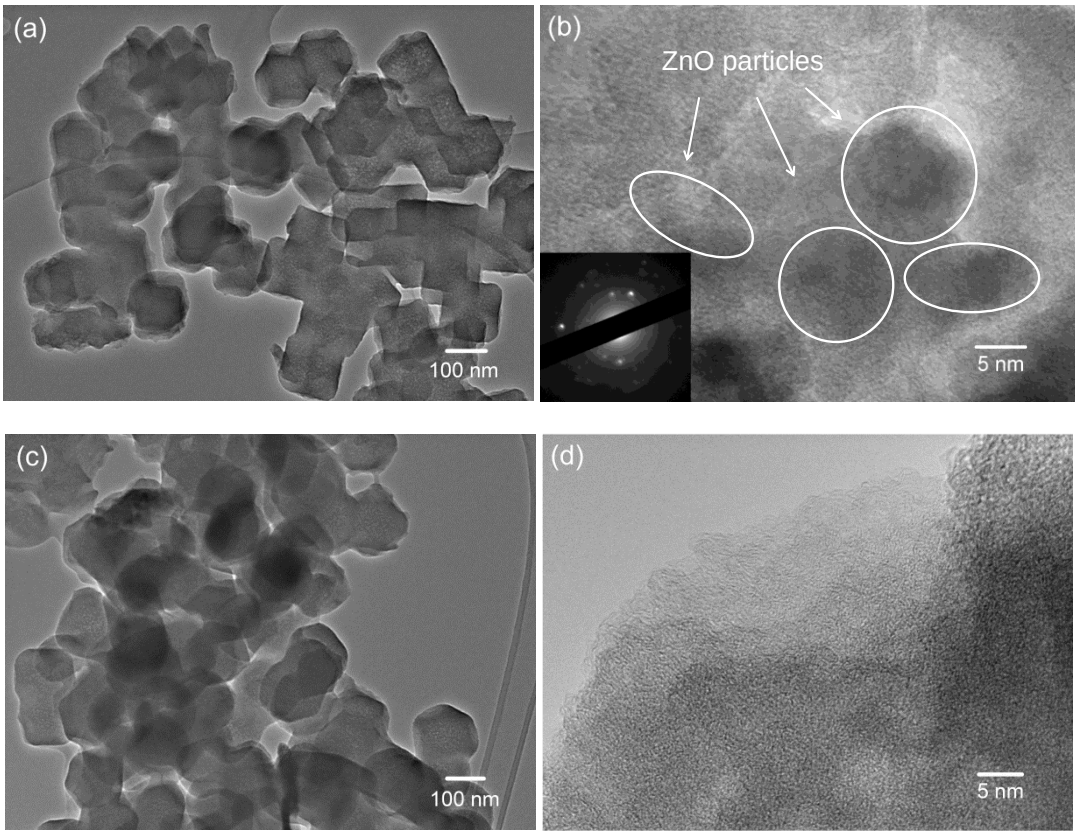

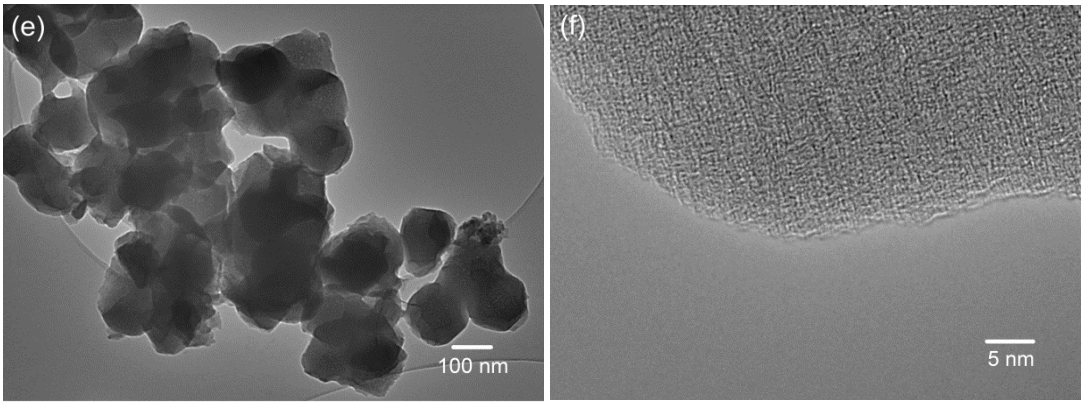

Figure 6.9 Representative TEM images for composite: (a) and (b) ZnO/C-S-*S*, inset showing selected area electronic diffraction pattern, (c) and (d) ZnO/C-S-*L*, and (e) and (f) ZnO/C-A.

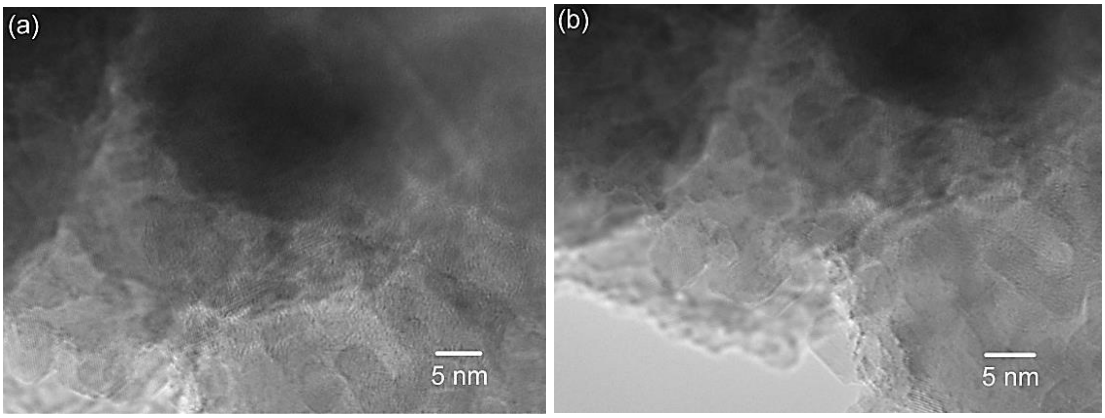

Figure 6.10 High-resolution TEM images of (a–b) ZnO/C-S-*S*

To ascertain the distribution of ZnO nanoparticles in the composite samples, scanning transmission electron microscope combined with elemental mapping technique were used. As shown in Figure 6.11, the elemental mapping for both element O and Zn exhibit similar patterns to their selected area of TEM image, indicating the uniform dispersion of ZnO in the carbon matrix. In addition, the elemental mapping for C and N are also similar to their patterns of selected area of TEM image, implying both C and N are uniformly distributed throughout the ZnO/C-S-*S* sample. These results clearly demonstrated that atomically homogeneous dispersed ZnO/N-doped nanoporous carbon composites can be obtained via carbonization of ZIF-8 under water steam carbonization. The reason for the uniform dispersion of ZnO and N-doped carbon is due to the use of a single molecular-like crystalline precursor ZIF-8,

whose homogeneously distributed Zn and N ensures their final thorough distribution on both the external and internal surfaces within the bulk after the carbonization process. In addition, as shown in Figure 6.12 and Figure 6.13, other composites, ZnO/C-S-*L* and ZnO/C-A, also demonstrate homogeneous elemental distribution throughout the samples, suggesting the formation of atomically and uniformly dispersed ZnO/N-doped carbon composites.

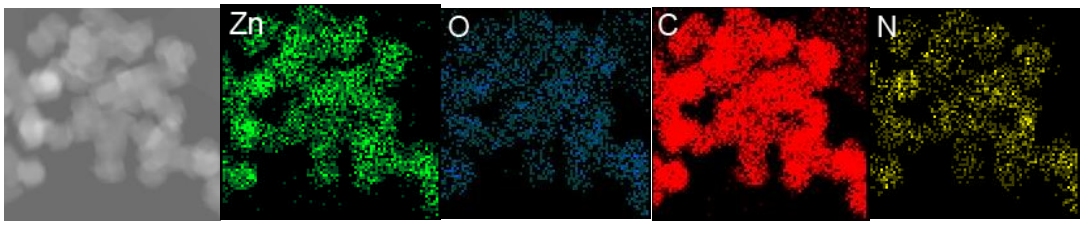

Figure 6.11 Scanning transmission electron microscope image and elemental mapping for sample ZnO/C-S-*S*.

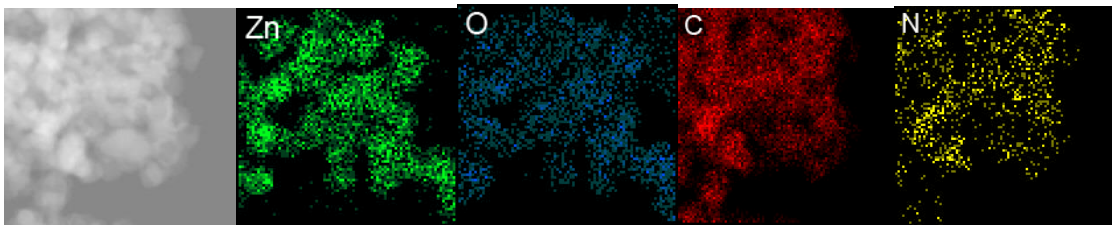

Figure 6.12 Scanning transmission electron microscope image and elemental mapping for sample ZnO/C-S-*L*.

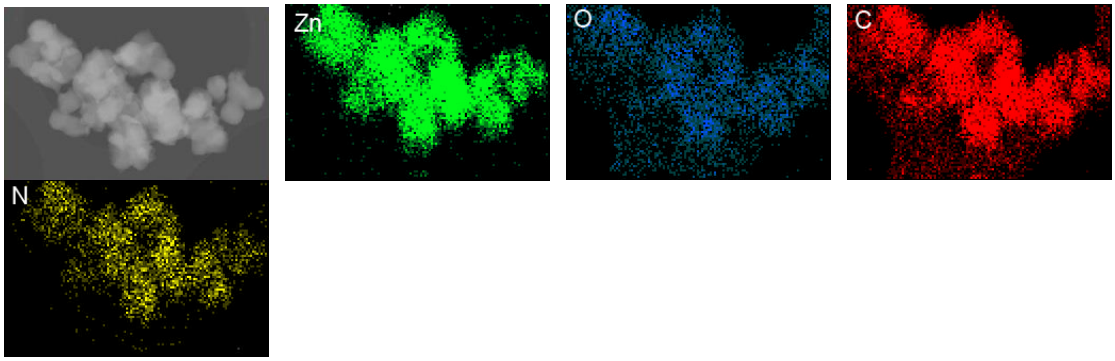

Figure 6.13 Scanning transmission electron microscope image and elemental mapping for sample ZnO/C-A.

6.3 Applications

6.3.1 CO_2 uptake performance

To evaluate the applications of the obtained ZnO/N-doped porous carbon composites, CO_2 adsorption capacities at 25 ^oC for all the samples are presented in Figure 6.14a and the CO_2 uptake capacities at 1 bar are summarized in Table 6.1. The CO_2 adsorption data is confirmed to be highly reproducible, almost identical over several runs, with variations usually lower than 1% in uptake capacity through the entire pressure range. At 25 ^oC and 1 bar, the CO_2 adsorption capacities for samples ZnO/C-A, ZnO/C-S-*S* and ZnO/C-S-*L* are 2.85, 3.05 and 3.23 mmol g^{-1}, which is generally consistent with the gradually increased specific surface areas of these composites. Therefore, sample ZnO/C-S-*L* derived from steam carbonization for longer time shows the highest CO_2 uptake at 1 bar amongst these composites. However, under low pressures, the ZnO/C-A sample with lower surface area but higher N content out-performs the samples ZnO/C-S-*S* and ZnO/C-S-*L* with higher specific surface area but lower N content in the CO_2 uptake, implying that both specific surface area and N content play important roles in the CO_2 adsorption process at 25 ^oC, which is consistent with previous reports.[257, 385] Moreover, as shown in Figure 6.15 and Table 6.1, the CO_2 adsorption capacities at 0 ^oC and 1 bar for composites ZnO/C-S-*L*, ZnO/C-S-*S* and ZnO/C-A, are 6.08, 5.32 and 4.42 mmol g^{-1} respectively, which is in agreement well with the observed change trends for CO_2 uptake at 25 ^oC. Obviously, the longer steam carbonised sample ZnO/C-S-*L* exhibits the highest CO_2 uptake at 1 bar and 0 ^oC amongst the three studied composites. It is, however, worthwhile to note that under low pressures, the CO_2 uptake capacity at 0 ^oC for sample ZnO/C-A out-performs that for samples ZnO/C-S-*S*, but lower than that for sample ZnO/C-S-*L*, indicating that textural properties as well as surface chemistry (with different functional groups) can remarkably affect CO_2 adsorption. Actually, surface modification is important for the CO_2 adsorption. When water steam was used during the carbonization process, hydrophilic oxygen-containing functional groups such as –OH and –COOH may be introduced onto the surface of ZnO/C-S-*S* and ZnO/C-S-*L* composites, which may benefit to the enhancement of the interaction between the adsorbents with CO_2 molecules.

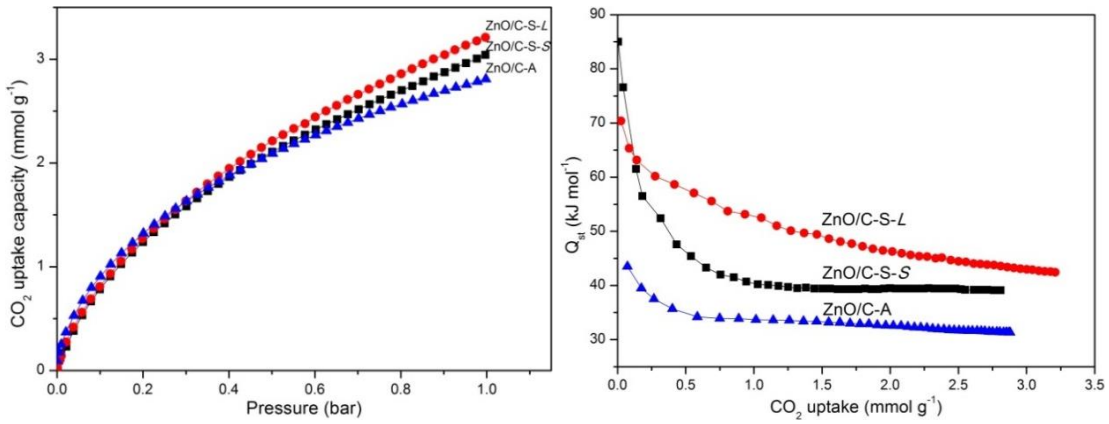

Figure 6.14 CO_2 adsorption capacities at 25 ^oC (a) and the CO_2 isosteric heat Q_{st} (b) for the composite ZnO/C-S-*S*, ZnO/C-S-*L*, and ZnO/C-A.

The CO_2 adsorption energy (i.e., isosteric heat of adsorption, Q_{st}), an indicator of the interaction strength between CO_2 molecules and the adsorbents, is calculated using the CO_2 sorption isotherms measured at 0 and 25 ^oC based on the Clausius-Clapeyron equation for all the samples, and the resulting curves of Q_{st} *vs* CO_2 uptake are presented in Figure 6.14b. The initial Q_{st} for the ZnO/C-A, ZnO/C-S-*S* and ZnO/C-S-*L* materials is 44, 85 and 70 kJ mol^{-1}, respectively, at lower CO_2 uptake (low surface coverages). The adsorption Q_{st} of ZnO/C-A is similar to previous observations on other typical N-doped porous carbon materials, but higher than those of most MOFs.[385, 386] This high initial Q_{st} values indicate a strong interaction between CO_2 molecules and the N-doped carbon.[257] Surprisingly, the CO_2 adsorption Q_{st} of ZnO/C-S-*S* and ZnO/C-S-*L* display significantly high values, suggesting much stronger interactions between CO_2 molecules and steam carbonised samples than Ar atmosphere carbonised sample ZnO/C-A. This is maybe due to the fact that when CO_2 was adsorbed by samples ZnO/C-S-*S* and ZnO/C-S-*L*, a strong acid-base interaction may have occurred between the hydrophilic oxygen-containing functional groups and the acidic CO_2 molecules. Furthermore, ZnO may also have played an important role in the initial interaction, by forming a strong chemical interaction between ZnO nanoparticles and CO_2 molecules when CO_2 was chemisorbed onto its surfaces.[387-389] Although the mechanism of the chemical interaction between them is yet to fully understood, it is believed the chemisorption of CO_2 on ZnO is resulting in the formation of CO_3^{2-} carbonate,[390] which increases the interactions between the adsorbents and CO_2.

At higher coverages, the Q_{st} of the ZnO/C-A, ZnO/C-S-*S* and ZnO/C-S-*L* materials reduce to an average of 32, 39, and 42 kJ mol^{-1}, respectively, which are much higher than previously reported values for pure carbon and N-doped carbon absorbents.[385, 391] Sample ZnO/C-S-*L* that has the intermediate N content, the highest textural properties and CO_2 uptake capacity, and the longest steam treatment time, exhibits the highest Q_{st} of 42 kJ mol^{-1} at higher coverages, which is actually the highest ever reported for any porous carbon based materials. Sample ZnO/C-S-*S*, possessing the intermediate specific surface area, the intermediate N content, and shorter steam treatment time, exhibits a Q_{st} of 39 kJ mol^{-1} at high coverages. However, sample ZnO/C-A, which has a higher N content and lower textural properties but without steam treatment, shows the lowest Q_{st} of 32 kJ mol^{-1} at high coverages. These results suggest that at higher CO_2 coverages, both the textural properties and water steam treatment determined the interactions between CO_2 and composites.

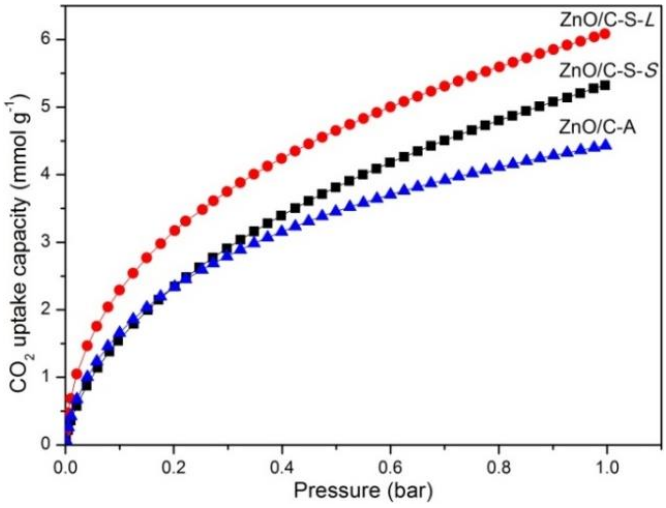

Figure 6.15 CO_2 adsorption capacities at 0 ^oC for composites ZnO/C-S-*S*, ZnO/C-S-*L* and ZnO/C-A.

To probe the selectivity of the materials, the CO_2 uptake at 298 K was compared to N_2 sorption (Figure 6.16). At ambient temperature and pressure, CO_2 adsorption capacity on sample ZnO/C-S-*S* (3.05 mmol g^{-1}) is far higher than that of N_2, which only reaches 0.18 mmol g^{-1}. Therefore the CO_2/ N_2 adsorption ratio on sample ZnO/C-S-*S* is 16.9. Similarly, the CO_2/ N_2 adsorption ratio on sample ZnO/C-S-*L* and ZnO/C-A is 17.7 and 15.7, respectively, implying excellent selectivity for CO_2 uptake for the synthesized nanocomposites. This high CO_2 uptake capacity and good selectivity for CO_2 show the potential for next generation CO_2 absorbents.

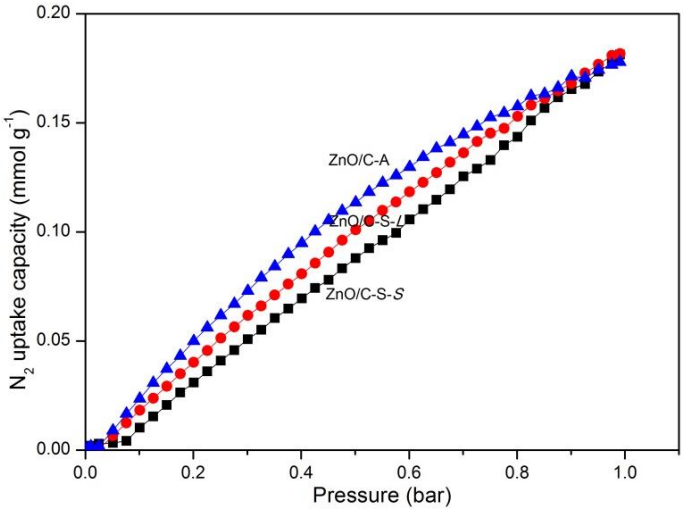

Figure 6.16 N_2 sorption profiles at room temperature on sample ZnO/C-S-*S*, ZnO/C-S-*L* and ZnO/C-A.

6.3.2 Removal of methyl blue from water

The porous carbons embedded with ZnO nanoparticles are frequently considered as efficient materials in adsorption and photodegradation of a toxic model substance, methylene blue (MB), under visible-light irradiation.[368, 369] To evaluate the capability to removal MB pollutant from water, the adsorption performance of different samples were first carried out in a dark room. As shown in Figure 6.17a, the time dependence of the percentage of the adsorbed MB amounts on ZnO/C-S-*S*, ZnO/C-S-*L*, ZnO/C-A and pure ZnO is presented. All the as-synthesized composite samples adsorb MB with time in dark, but not for pure ZnO, which indicates the carbon matrix plays the key role in the adsorption of MB in the dark. After 4 h, the composites ZnO/C-A, ZnO/C-S-*S* and ZnO/C-S-*L* can adsorb 46, 67 and 64% MB from water solution respectively. Moreover, both samples ZnO/C-S-*S* and ZnO/C-S-*L* showed a similar uptake curve with higher adsorption capacities than sample ZnO/C-A. In addition, all the composites ZnO/C-S-*S*, ZnO/C-S-*L* and ZnO/C-A exhibited rapid adsorption performance in the first 1 h, then the adsorption gradually slowed down till approaching their adsorption/desorption equilibrium. The inset Figure 6.17a showed the time-dependent adsorption capacities of ZnO/C-S-*S* and ZnO/C-S-*L*, where ZnO/C-S-*S* and ZnO/C-S-*L* present impressive equilibrium MB dye adsorption capacity of 99 and 97 mg g^{-1}, respectively.

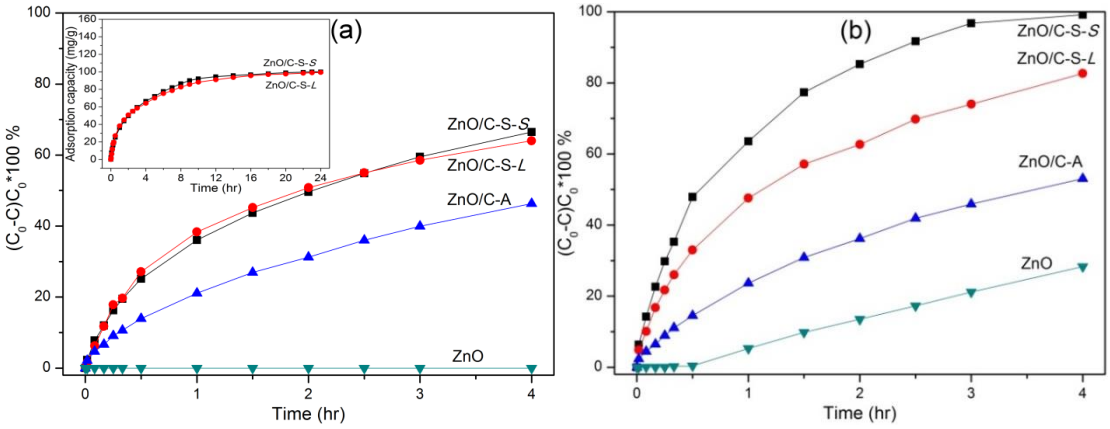

Figure 6.17 The adsorption/photodegradation performances of the samples for the removal of methylene blue from water in dark room (inset: adsorption capacity) (a) and under visible light irradiation (b).

The good adsorption performance of the composites can be accounted for by several factors, including the surface charge, hydrophilicity/hydrophobicity, and textural properties of the composite substrates. The high nanoporosity and open pore network of the carbon matrix can facilitate fast molecular diffusion, improving the accessibility to the entire pore surface. MB has a dimensional size of 1.43 nm × 0.61 nm × 0.4 nm, which is compatible with the pore ranges of 1.2 to 2.0 nm for the ZnO/C composites obtained via the NLDFT method from N_2 gas sorption analysis (Figure 6.7). Thus, the matched pore diameters can easily facilitate the diffusion of MB molecules into the carbon matrices. Moreover, the MB dye can interact effectively with the carbon surface, due to the π–π interactions between the MB molecule and the sp^2 graphitic carbon in the ZnO/C composites (as confirmed by Raman analysis in Figure 6.3).[392] In addition, the -COOH groups formed on the pore surfaces of the ZnO/C-S-*S* and ZnO/C-S-*L*, which were introduced by water steam carbonization, may also increase the interactions with the MB molecules.[393]

Further adsorption kinetics analyses are carried out, using the pseudo-first-order and pseudo-second-order kinetic model,[394] in an effort to understand the adsorption mechanism. The pseudo-first-order equation is given as follows:

$$\log(Q_e - Q_t) = logQ_e - \frac{k_1}{2.303}t \qquad (6.1)$$

where k_1 (min^{-1}) is the adsorption rate constant of pseudo-first-order model, Q_e (mg g^{-1}) and Q_t (mg g^{-1}) are the amount of solute on the adsorbent at equilibrium and time t, respectively.

The pseudo-second-order rate reaction is dependent on the amount of solute adsorbed on the surface of the adsorbent and the amount adsorbed at equilibrium. The pseudo-second-order equation is given as follows:

$$\frac{t}{Q_t} = \frac{1}{k_2 Q_e{}^2} + \frac{t}{Q_e} \qquad (6.2)$$

where k_2 (g mg^{-1} min^{-1}) is the adsorption rate constant for the pseudo-second-order adsorption; Q_e (mg g^{-1}) and Q_t (mg g^{-1}) are the amount of solute adsorbed at equilibrium and at time t.

The linear plots of $\log(Q_e - Q_t)$ *vs. t* and (t/Q_t) *vs. t* are drawn for the pseudo-first-order and pseudo-second-order models, respectively (See Figure 6.18). The adsorption rate constants k_1 and k_2 can be obtained from the plot of experimental data. The adsorption rate constants, the calculated Q_e, and the correlation coefficients R^2 for the two kinetic models of the as-synthesized materials are summarized in Table 6.2. As seen from Table 6.2, the correlation coefficients (R^2) of the pseudo-first-order model are 0.932, 0.949 and 0.956 for ZnO/C-S-*S*, ZnO/C-S-*L* and ZnO/C-A, respectively. For the pseudo-second-order model, the correlation coefficients (R^2) of the ZnO/C-S-*S*, ZnO/C-S-*L* and ZnO/C-A are all higher than 0.97. In addition, in the case of the pseudo-first-order model, the calculated Q_e values were 88.69 mg g^{-1} for ZnO/C-S-*S* and 82.14 mg g^{-1} ZnO/C-S-*L*. On the other hand, the calculated Q_e values from the pseudo-second-order model for the adsorption of MB by ZnO/C-S-*S* and ZnO/C-S-*L* were 105.72 and 97.56 mg g^{-1}, respectively. Obviously, the calculated Q_e values from the pseudo-second-order model are in agreement with the experimental measured data (shown in Figure 6.17a). It is therefore reasonable to assume that the adsorption of MB on these composites is dominated by the pseudo-second-order model, rather than the pseudo-first-order model. The MB dye molecules might be decomposed to form organic acids as the intermediate products in the pseudo-second-order rate reaction. This observation is consistent with the above discussion that the MB adsorption on the composites is mainly a process of MB interacting with the various functional sites.

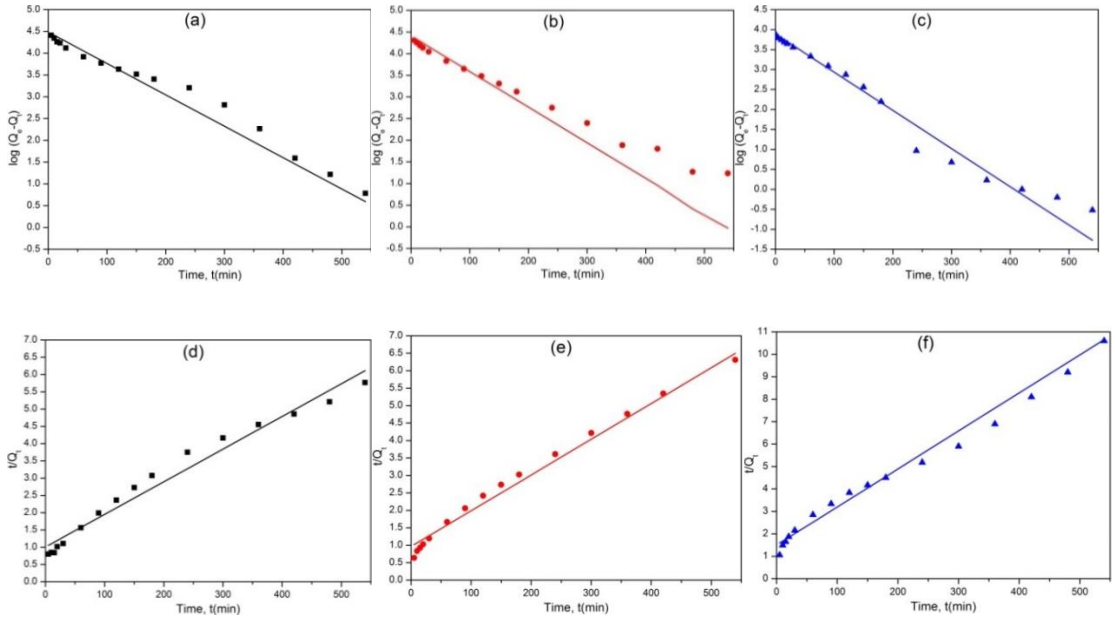

Figure 6.18 Fitting of adsorption kinetics of MB on (a and d) ZnO/C-S-*S*, (b and e) ZnO/C-S-*L*, and (c and f) ZnO/C-A, respectively. (a, b and c) pseudo-first-order model and (d, e and f) pseudo-second-order model.

Table 6.2 Kinetic parameters of the pseudo-first-order rate equation and the pseudo-second-order rate equation for MB adsorption on as-synthesized porous carbon-zinc oxide composites.

Samples	Pseudo-first-order kinetics			Pseudo-second-order kinetics		
	k_1 /min^{-1}	Q_e / mg g^{-1}	R^2	k_2 / g mg^{-1} min^{-1}	Q_e / mg g^{-1}	R^2
ZnO/C-S-*S*	0.0166	88.69	0.9322	0.00009	105.72	0.9739
ZnO/C-S-*L*	0.0189	82.14	0.9488	0.00011	97.56	0.9891
ZnO/C-A	0.0221	48.95	0.9557	0.00019	59.00	0.9873

ZnO, a direct wide band gap (3.37 eV) semiconductor with a large excitation binding energy (60 meV), has been investigated as a potential non-toxic photocatalyst to degrade organic pollutants.[395, 396] The adsorption and degradation of MB from water for different samples under visible light irradiation are presented in Figure 6.17b. After 4 h irradiation, up to 99, 83, 53 and 28 % MB has been removed from water by samples ZnO/C-S-*S*, ZnO/C-S-*L*, ZnO/C-A and pure ZnO respectively, which indicates that photo-degradation contributes to 32, 19, 7 and 28% of the MB removal, respectively. Considering that only 10, 13 and 15% ZnO exist in the obtained composite ZnO/C-S-*L*, ZnO/C-S-*S* and ZnO/C-A respectively, the photo-degradation efficiency of ZnO in all composites outperforms the pure ZnO in the photocatalytic removal of MB from water. This is due to the fact that carbon species in the composites can effectively modify the bandgaps of ZnO, generating localized states in the bandgap which results in the presence of an absorption tail extending into the visible range.[397] For comparison, both commercial ZnO (size ~200nm) and TiO_2 (P25) were used as reference materials for the photocatalytic activity (shown in Figure 6.19). The photo catalysis activity of commercial ZnO exhibited the similar performance with the pure ZnO which was obtained from annealing of ZIF-8 in air. However, for the other reference material P25, it seems that there is no photocatalytic activity under visible light radiation, which is in consistent with the reported result that P25 has photocatalytic activity under UV radiation, not visible light.[398]

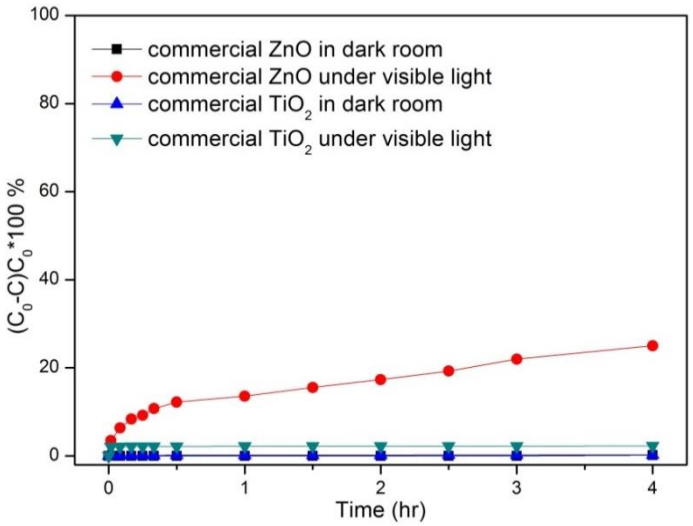

Figure 6.19 The adsorption/photodegradation performances of the reference materials for the removal of methylene blue from water in dark room and under visible light irradiation.

Consequently, the carbon species in ZnO/C composite promote the photodegradation performance. Moreover, compared to the sample ZnO/C-A obtained from the carbonization of ZIF-8 in Ar atmosphere, the composites ZnO/C-S-*L* and ZnO/C-S-*S* derived from steam carbonization possessing abundant hydrophilic oxygen-containing functional groups may facilitate the approach and accommodation of MB molecules, which may result in samples ZnO/C-S-*L* and ZnO/C-S-*S* exhibiting higher photo-degradation performances than ZnO/C-A. In addition, composite ZnO/C-S-*S* out-performs the composite ZnO/C-S-*L* in photo-degradation of MB in water due to the higher ZnO content in the former sample.

The reusability of sample ZnO/C-S-*S* is also assessed for the removal of MB from water under visible-light irradiation. In the consecutive tests, the composite catalysts were separated from the solution by filtration, washed several times with deionized water, followed by drying in an oven at 120 ^{o}C for 3 h and then used for the next run. As shown in Figure 6.20, the MB removal efficiency remained high and was still higher than 95% after six consecutive runs, suggesting a good stability and reusability for the ZnO/C-S-*S* materials. It is likely that the physical walls of the porous carbon provide a confined space for photocatalysis,[366] which can prevent the aggregation of ZnO nanoparticles, maintain the high dispersibility of ZnO particles in porous carbon matrix, therefore the composite materials can keep the high adsorption and degradation activity and enhance the stability for MB removal from water.

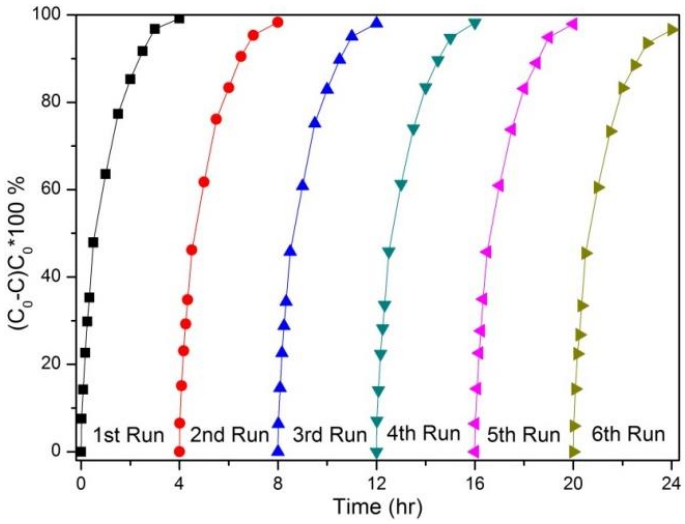

Figure 6.20 Reuse of the composite ZnO/C-S-*S* in the adsorption and photodegradation of MB in water under visible-light irradiation.

6.4 Summary

In summary, a simple one-step water steam carbonization route to synthesize homogeneously-dispersed ZnO nanocrystal particles embedded within N-doped porous carbon matrix using ZIF-8 as a precursor has been successfully developed. This new and green method holds several advantages: (1) the porosity of composites can be significantly improved; (2) the crystallinity of metal oxide can be remarkably improved and (3) abundant oxygen-containing hydrophilic functional groups have been introduced into the N-doped porous carbon in the composites. The resultant ZnO/C-S-*S* and ZnO/C-S-*L* exhibit promising CO_2 uptake capacities, high CO_2 selectivity, with a significant high CO_2 adsorption energy at low surface coverages due to the high porosity, high N content and a strong chemical interaction between CO_2 and the composites. Furthermore, with excellent adsorption and degradation abilities, these composites are also highly efficient for methylene blue (MB) removal from wastewater under visible-light irradiation, which can be attributed to the high porosity, additional functional groups, open network structure of the carbon matrix and the excellent photocatalytic performance of ZnO nanocrystals. Kinetics studies show that the adsorption process is dominated with a pseudo-second-order adsorption model. This present work offers a new approach for the design and syntheses of highly homogeneous dispersed porous carbon-metal oxide composite materials that display enhanced sorption and efficient catalytic behaviours.

7. Chapter 7: Cobalt/nanoporous carbon composites derived from ZIF-67 and its applications

7.1 Introduction

Developing highly efficient electrocatalysts for energy technologies has been increasingly popular due to the growing global energy crisis.[399] Electrocatalytic oxygen reduction reaction (ORR), and oxygen evolution reaction (OER) play key roles in energy conversion and storage applications such as fuel cells,[31-33, 400] metal-air batteries[401-403] and water splitting.[34, 35, 404, 405] To date, the most efficient catalyst for ORR and OER contains precious metal, which are usually high-cost and scarce.[406] Therefore, exploring and developing efficient and cost-effective electrocatalysts is an important task of urgency. Recent studies have shown that noble metal free catalysts such as non-precious transition metal and heteroatom-doped carbons are extensively investigated. For example, Dai et al reported a mesoporous carbon foam co-doped with nitrogen and phosphorus as an excellent bifunctional electrocatalyst for ORR and OER.[38] Wang et al prepared cobalt-embedded nitrogen doped carbon/nanodiamond electrocatalysts for high performance ORR and OER in alkaline media. [407]

Metal organic frameworks (MOFs, including Zeolitic Imidazolate Frameworks (ZIFs)) have attracted attention widely due to their tuneable structures, versatile functionalities and fascinating properties.[5-7] Recently, inspired by this molecular-like organic-inorganic crystal structure, MOFs have been used as self-sacrifical templates for the synthesis of metal nanoparticles embedded within the heteroatom-doped (typically N-doped) nanoporous carbon matrices through thermal decomposition. This strategy is advantageous due to the homogeneous dispersion of metal nanoparticles within the heteroatom-doped porous carbon matrix and the ease of synthesis directly from the MOFs without any additional source. Nowadays, various metal/heteroatom-doped carbon composites synthesized from the MOFs at relatively low temperatures below 1000 ^{o}C have been reported in literature[261, 271, 272, 408-413] , and their applications for ORR have also been well studied. [261, 271, 272, 411-413] For instance, cobalt/porous carbon composites derived from ZIF-67 exhibited excellent ORR performance.[261, 271, 272] However, the research on the MOF derivatives as bifunctional ORR/OER catalysts has been rarely reported. In addition, the synthesis of MOF derivatives at relatively high temperatures (above 1000 ^{o}C) also requires further study, considering the

interactions between metal and carbon during the carbonization.[410, 414] The structure change of carbon could affect the final electrocatalytic performance.[410, 414]

In this chapter, we present the structural evolution of MOF-derived materials ranging from cobalt-embedded porous N-doped carbon/carbon nanotubes to hollow carbon nano-onions. The structure of the as-synthesized materials was modulated by the carbonization temperature. In addition, both ORR and OER performances of these MOF-derived materials have been systematically discussed. In the resultant materials, the cobalt-embedded porous N-doped carbon/carbon nanotubes composite (Co@C-800) exhibits excellent ORR and OER catalytic performance due to its favourable porous nanostructure, N-doping effect and homogeneous cobalt dispersion. ZIF-67 was selected as the precursor and template due to its high porosity, high nitrogen content, and rich content of cobalt ions.

7.2 Characterizations of the cobalt/nanoporous carbon composites

As shown in transmission electron microscopy (TEM) images (Figure 7.1a), the precursor ZIF-67 has a particle size of approximately 400 nm with sodalite topology.[275] The structure and morphology of the as-synthesized Co@C composites are also investigated by TEM (Figure 7.2 and 7.3). After carbonization at 600 ^{o}C and 800 ^{o}C, the obtained sample Co@C-600 and Co@C-800 inherited the original morphology of ZIF-67 crystals with a uniform particle size of 300 nm, although the particle surface was rough (Figure 7.2a and 7.2c, and Figure 7.4). The particle framework began to be destroyed when the carbonization temperature reached 1000 ^{o}C (Figure 7.2e). For the sample Co@C-600, it can be seen that darker dots with the size of ~10nm are well dispersed into the carbon matrix. These dark dots were further proved to be cobalt nanoparticles by selected area electron diffraction (SAED) (Figure 7.3a, 7.3c, and 7.3e) and X-ray diffraction (XRD) (Figure 7.5a) analyses. The cobalt nanoparticles tend to agglomerate and form larger particles with the increase of carbonization temperature (800 ^{o}C and 1000 ^{o}C). In addition, their corresponding SAED patterns (Figure 7.2a, 7.2c, and 7.2e) are also enhanced due to the increased temperature, resulting in the improved crystallization of cobalt nanoparticles and carbon. Interestingly, the high resolution TEM images (Figure 7.2b, 7.2d, and 7.2f) show carbon nanotubes on the surface of the carbon matrix, which are formed due to the catalytic effect of cobalt during the carbonization process,[415] together with the cobalt nanoparticles can be observed. The carbon nanotubes could enhance the

electronic conductivity of the composites.[416] For sample Co@C-800, it still has a similar morphology compared to the ZIF-67 backbone, thus the dense catalytic active sites and high porosity can be still maintained. The *in-situ* formation of carbon nanotubes in Co@C-800 is also beneficial to the electrocatalytic activity. The TEM results of Co@C composites synthesized under low temperatures are consistent with previous studies.[271, 272, 409]

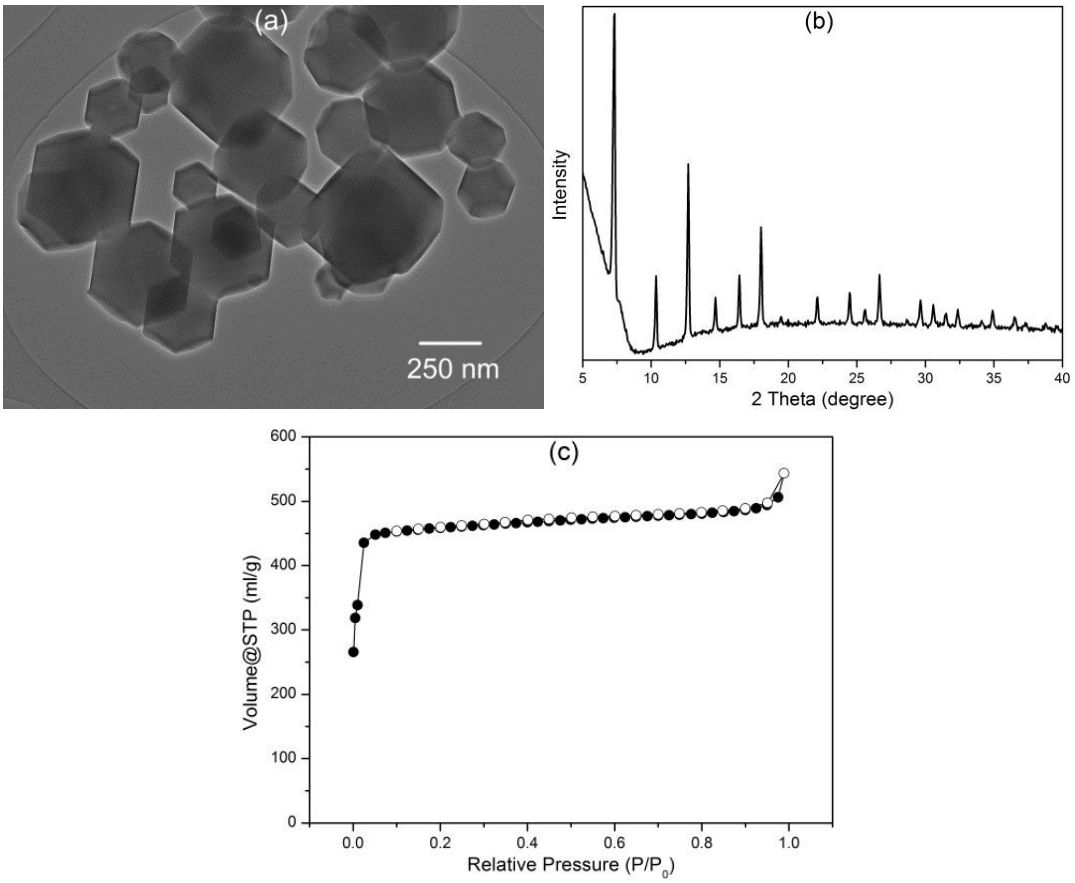

Figure 7.1 (a) TEM image, (b) powder XRD pattern and (c) nitrogen sorption isotherms of the parental ZIF-67 material.

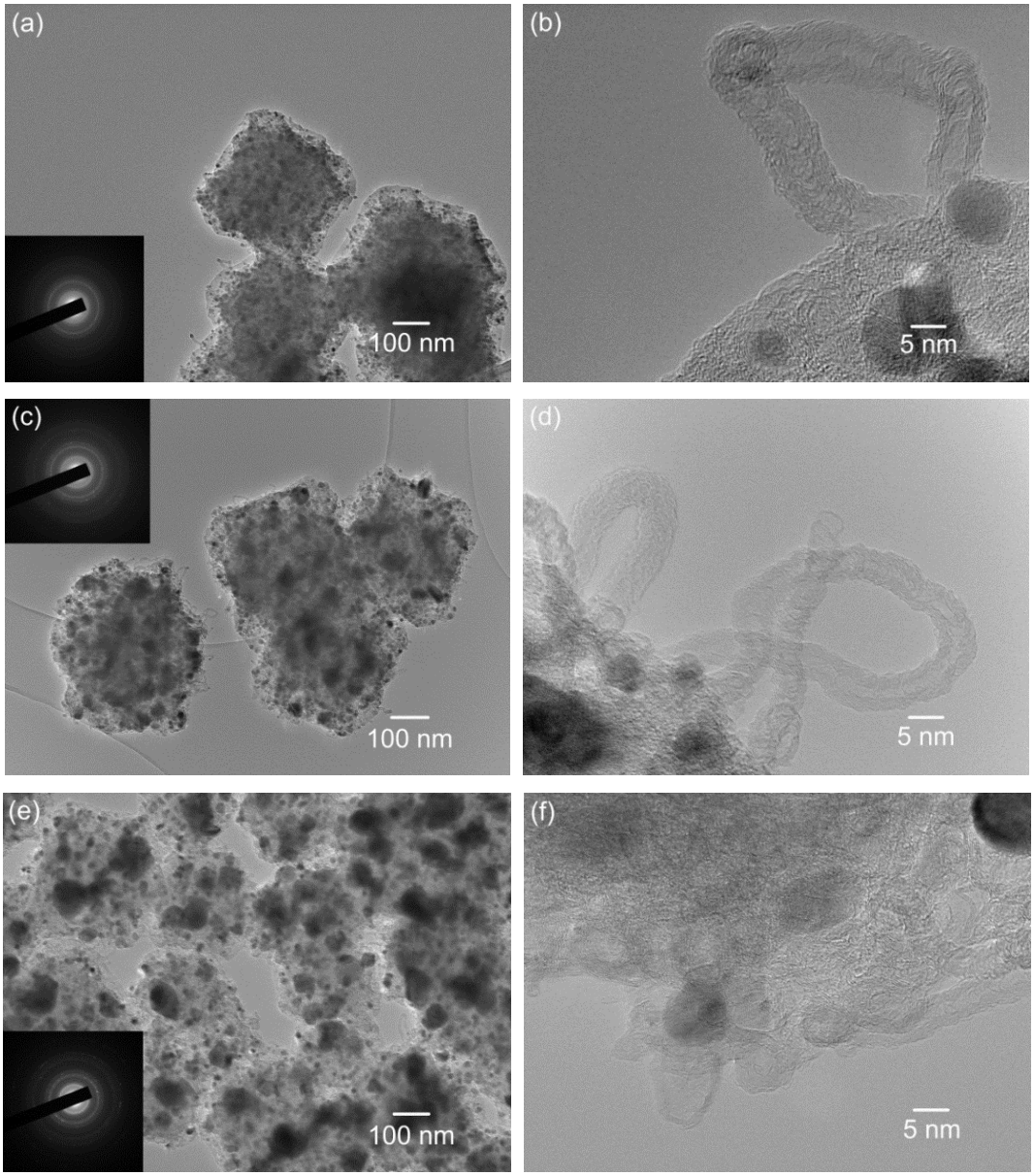

Figure 7.2 TEM images of the as-synthesized samples which were prepared at relatively low temperatures via pyrolysis: (a-b) Co@C-600; (c-d) Co@C-800 and (e-f) Co@C-1000. Inset are SAED patterns for the corresponding sample.

Unlike the sample Co@C-600, Co@C-800, and Co@C-1000, the morphology of the Co@C composites synthesized at higher pyrolysis temperatures (1200 ^{o}C, 1600 ^{o}C, and 2000 ^{o}C) is different. The ZIF-67 backbone was totally destroyed in sample Co@C-1200, Co@C-1600, and Co@C-2000. For sample Co@C-1200, cobalt nanoparticles with the size of ~50 nm are wrapped by a few layers of graphite sheets (Figure 7.3a), which is similar to Klose's work.[414] The d-spacing of 0.31 nm corresponds to the distance of individual basal planes in graphite.[414] For the sample Co@C-1600 and Co@C-2000, interestingly, they predominantly consist of hollow

carbon nano-onions with a uniform size of ~5-10 nm (Figure 7.3c and 7.3e). The hollow carbon nano-onions are generated *in situ* from the catalytic effect of metallic cobalt at high temperature. Especially for the sample Co@C-2000, the carbon nano-onions structure becomes clearer due to the high crystallization of graphite. To the best of our knowledge, such small hollow carbon nano-onion structures have not been synthesized by using a MOF as a precursor. In addition, based on the all TEM results, we found that the structure of MOF derived materials varies from cobalt-embedded porous N-doped carbon/carbon nanotubes to hollow carbon nano-onions under the different carbonization temperatures.

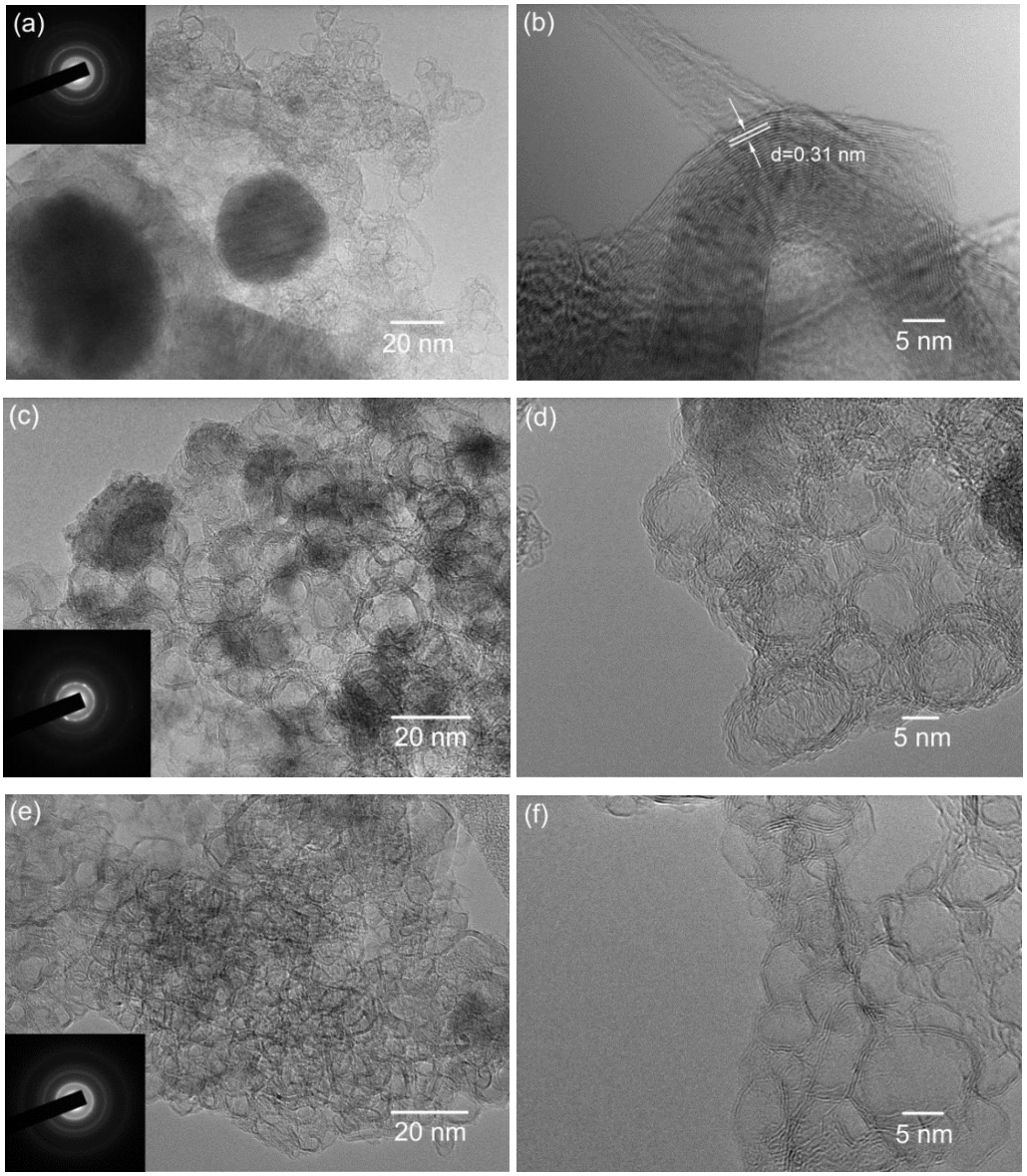

Figure 7.3 TEM images of the as-synthesized samples which were prepared under relatively high temperatures via pyrolysis: (a-b) Co@C-1200; (c-d) Co@C-1600 and (e-f) Co@C-2000. Inset is SAED patterns for the corresponding sample.

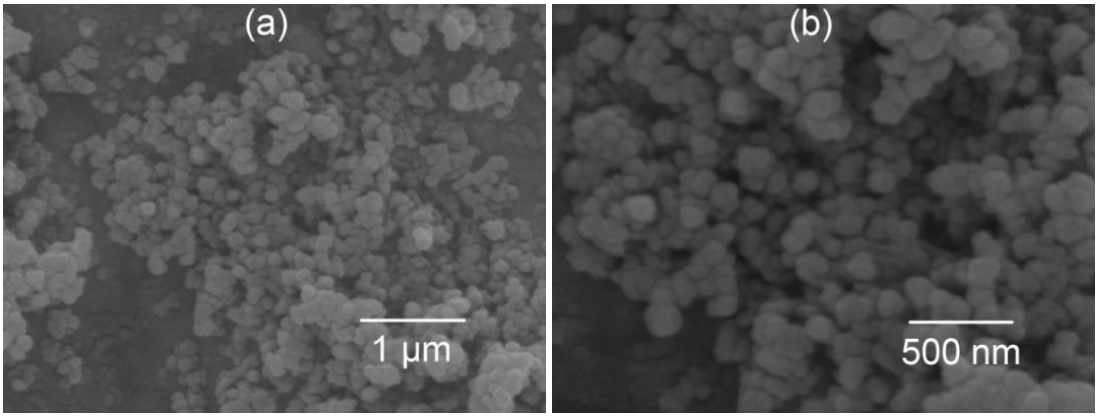

Figure 7.4 SEM images of the as-synthesized Co@C-800 nanocomposites

The XRD pattern of as-synthesized precursor ZIF-67 shows the pure standard crystallinity without any by-products (Figure 7.1b). After thermal decomposition, the characteristic peaks of ZIF-67 disappeared in the XRD pattern of the Co@C samples (shown in Figure 7.5a). For sample Co@C-600, Co@C-800, Co@C-1000, and Co@C-1200, two peaks appeared at $2\theta=44.2^{o}$ and 51.6^{o}, indicating the existence of cobalt nanoparticles (ICDD PDF #15-0806). These two peaks became more intense and sharper with the increase of carbonization temperature, suggesting an increase in cobalt crystallinity and cobalt particle size.[261] In addition, a broad peak appeared at around $2\theta=26^{o}$ indicating the formation of graphic carbon. For sample Co@C-1600, apart from the characteristic peaks of cobalt, another three peaks, including the sharp peak at $2\theta=26^{o}$, shows the existence of highly crystallized graphite carbon. For the sample Co@C-2000, only characteristic peaks of graphic carbon can be observed without the appearance of cobalt. This may be due to the migration of liquid metallic cobalt (melting point is 1495 ℃) under high temperature. The high crystallization of graphite carbon is beneficial to the electrical conductivity.

The Raman spectra of the as-synthesized Co@C composites (shown in Figure 7.5b) present the characteristic D and G bands at 1335 and 1590 cm^{-1}, where D band indicates the disordered carbon atoms and G band indicates the sp2 hybridized graphitic carbon atoms, respectively.[417] The intensity ratio (I_D/I_G) of the sample decreases with the increase in carbonization temperatures, where the value of Co@C-600, Co@C-800, Co@C-1000, Co@C-1200, Co@C-1600, and Co@C-2000 is 0.69, 0.60, 0.55, 0.46, 0.42, and 0.40, respectively. Generally, the applied carbonization

temperature is critical for determination of the graphitization degree in the as-synthesized Co@C composites.[418] That is, the graphitization degree increases with the increase of carbonization temperature. Furthermore, the appearance of distinct peaks at 2680 cm^{-1} (2D band) and 2900 cm^{-1} (D+G band) in the Raman spectrum of sample Co@C-2000 further confirms the presence of a highly graphitized nanostructure with carbon nano-onions.

To probe the chemical composition and effect of N-doping in the as-synthesized Co@C composites, X-ray photoelectron spectroscopy (XPS) was carried out and demonstrated the presence of C, N, O, and Co (Figure 7.6a). Specifically, as an n-type carbon dopant, nitrogen can facilitate the ORR and OER performance.[419] The high-resolution N 1s spectrum (shown in Figure 7.5c) can be deconvoluted into four characteristic peaks at binding energy of 398.9, 400.4, 401.3, and 403.8 eV, which represented pyridinic, pyrrolic, graphitic, and oxidized nitrogen, respectively.[420] For sample Co@C-800, pyridinic N was found to be the main specious together with a few pyrrolic N and less graphitic, and oxidized N. The predominance of pyridinic and pyrrolic N could prove the presence of Co-N_x.[261, 271] For the sample prepared at 1000 ^oC, the pyrrolic/pyridinic N ratio increases, which is consistent with previous study.[271] When the carbonization temperature increases, it can be seen that N content decreases. This may be due to the high volatility of N species at high temperatures. For sample Co@C-1200, the overall N content is quite low, thus the samples synthesized at relatively high temperatures (above 1200 ^oC) have a weak N-doping effect.

Nitrogen sorption experiments were carried out to measure the textural properties of the as-synthesized Co@C composites (shown in Figure 7.5d). Before the thermal treatment, the precursor ZIF-67 exhibits a typical type-I isotherms (Figure 7.1c) indicating the dominance of the microporous structure. The specific surface area of ZIF-67 is 1630 m^2g^{-1}. After heat treatment, the sample Co@C-600, Co@C-800, Co@C-1000, Co@C-1200, Co@C-1600, and Co@C-2000 exhibit specific surface areas of 372, 369, 275, 102, 50, and 30 m^2g^{-1}, respectively. For these samples, a slight hysteresis loop appeared between the adsorption and desorption branches, implying the existence of mesoporous features because of the voids between particles. Generally, the specific surface area and porosity decreases with the increase in the carbonization temperature, because the higher temperatures lead to the improvement of crystallinity. For sample Co@C-600, Co@C-800, Co@C-1000, they displayed a

similar isotherm to that of the precursor ZIF-67, and their high uptake at low relative pressure suggests the dominance of micropores. The larger surface area of the composites can provide better exposure and enhanced utilization of electroactive sites, leading to a higher elctrocatalytic activity. However, after heat treatment at higher temperature (1200 ^{o}C-2000 ^{o}C), the porous structure of the template collapsed and the BET surface area decreases dramatically.

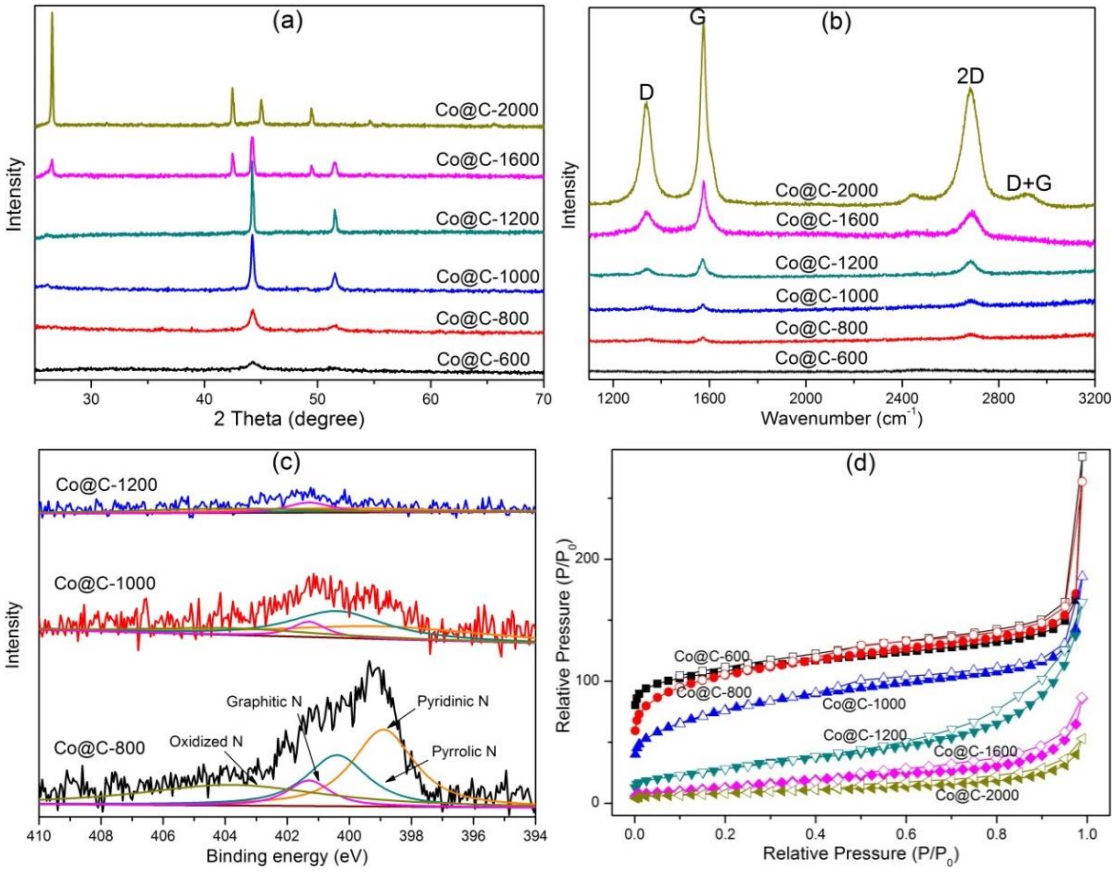

Figure 7.5 (a) XRD patterns, (b) Raman spectra, (c) high-resolution N 1s XPS spectra, and Nitrogen adsorption-desorption isotherm curves of the as-synthesized Co@C composites

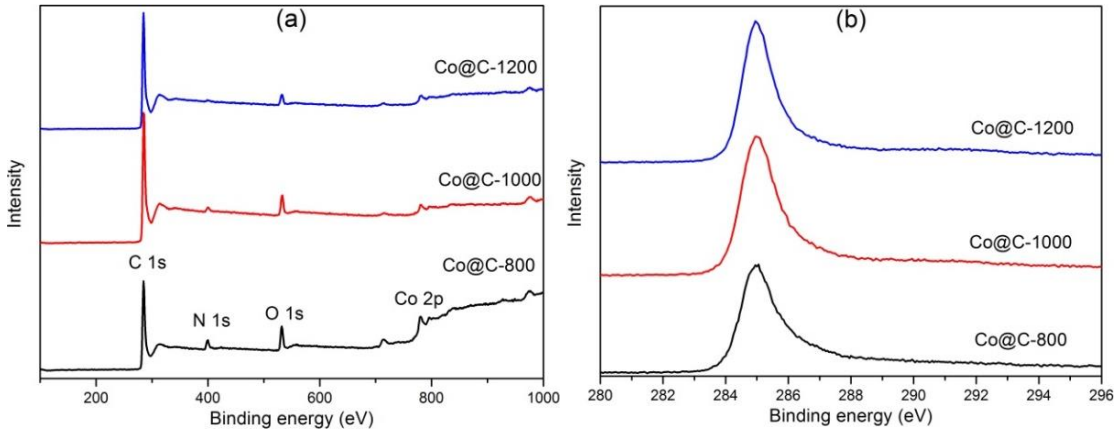

Figure 7.6 (a) Element survey by XPS and high-resolution XPS spectrum of (b) C 1s for the as-synthesized nanocomposites.

7.3 Applications

7.3.1 Oxygen reduction reaction

The oxygen reduction properties of the as-synthesized Co@C composites were measured by linear sweep voltammetry (LSV) curves on a rotating disk electrode (RDE) in O_2 saturated 0.1 M KOH solution. The results of the commercial Pt/C catalysts with 10% Pt loading are also presented for comparison. Obviously, among the as-synthesized products (shown in Figure 7.7a), Co@C-800 exhibits the highest onset potential (0.92 V) and halfwave potential (0.82 V), which is close to that of the benchmark Pt/C catalyst (0.95 V for onset and 0. 83 V for halfwave potential). Moreover, the saturated current density of Co@C-800 is about 5 mA cm^{-2}, which is comparable to that of Pt/C. The ORR activity of Co@C-600 is lower than that of Co@C-800. This is probably due to uncompleted decomposition and insufficient carbonization of the precursor ZIF-67 according to the relevant XRD and Raman results. It is worth noting that the ORR activity of Co@C catalysts was negatively related to the carbonization temperature ranging from 800 to 2000 ^{o}C. This weakened ORR activity may be the consequences of highly graphitized carbon species, aggregation of cobalt nanoparticles, and less content of nitrogen species. Undoubtedly, proper graphitization of carbon species can increase the electroconductivity and thus improve the ORR activity. However, excessive graphitization of carbon species may destroy the porous structure and decrease the surface area. The higher carbonization temperature may also lead to particle aggregation of cobalt and volatilization of nitrogen species, which is to the disadvantage of ORR activity. Therefore, the cobalt-

embedded porous N-doped carbon/carbon nanotubes composite Co@C-800 with large surface area and high content of nitrogen dopants should be favourable for ORR.

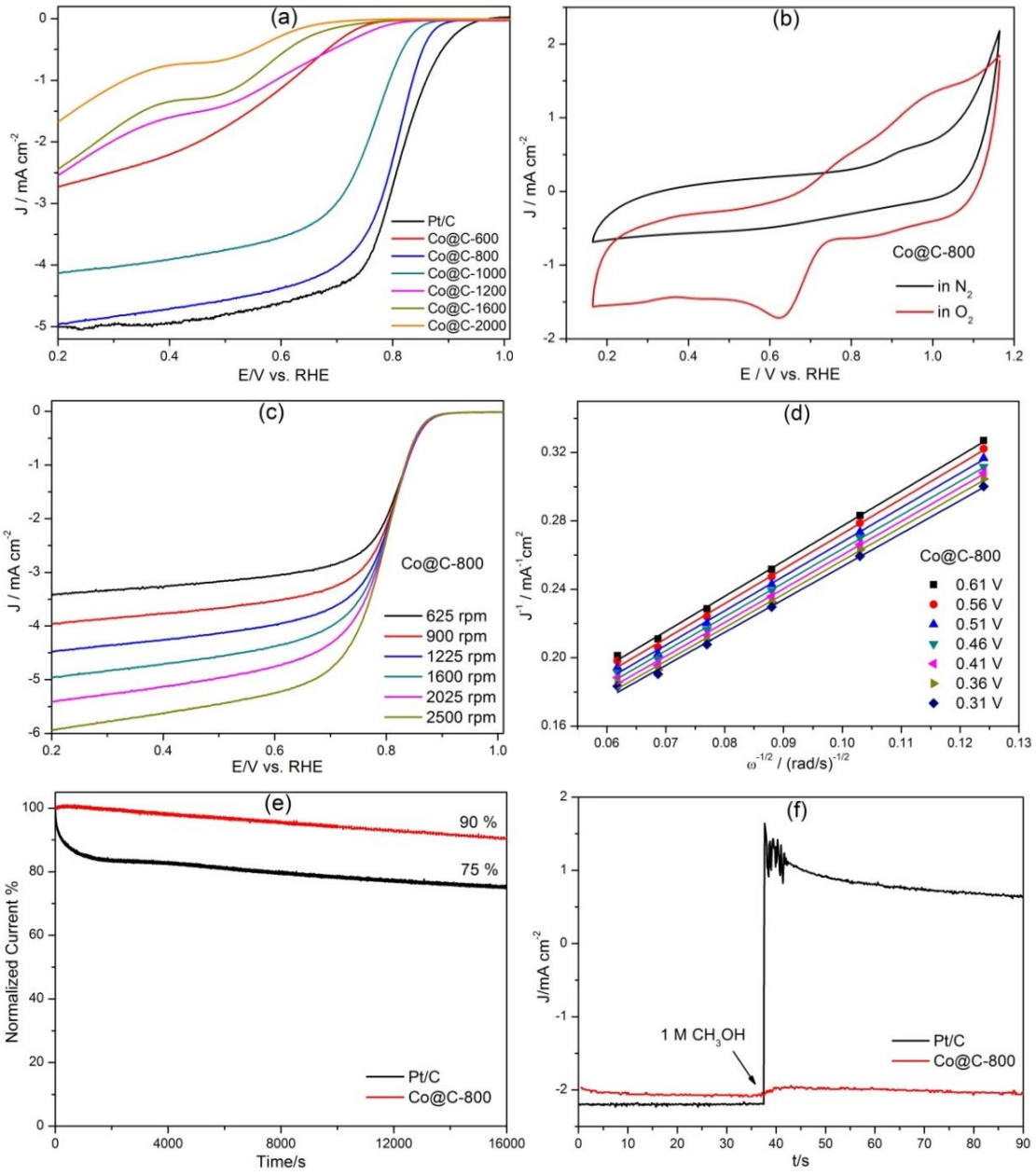

Figure 7.7 (a) Linear sweep voltammetry (LSV) curves of the as-synthesized Co@C composites and Pt/C at 1600 rpm in O_2-saturated 0.1 M KOH solution. (b) CV curves of Co@C-800 composite in N_2- or O_2-saturated 0.1 M KOH. (c) ORR polarization curves of Co@C-800 at different rotating speeds. (d) K-L plots of Co@C-800 at different potentials. (e) Current–time chronoamperometric responses of Co@C-800 and Pt/C at 0.8 V in O_2-saturated 0.1 M KOH solution at 1600 rpm. (f) Chronoamperometric responses of Co@C-800, and Pt/C at 0.8 V in O_2-saturated 0.1 M KOH solution (1600 rpm) followed by the addition of 1 M methanol.

The electrocatalytic activities of Co@C-800 were then evaluated by cyclic voltammetry (CV) measurements in 0.1 M KOH at 25 ℃ in O_2- and N_2-saturated electrolyte solution. As shown in Figure 7.7b, no obvious redox peak is observed for Co@C-800 in the N_2-saturated solution; while a well-defined cathodic peak appears at 0.64 V in the O_2-saturated solution, confirming the electrocatalytic activity for ORR. Sample Co@C-800 was also measured by using RDE under different rotating speeds ranging from 625 to 2500 rpm. As shown in Figure 7.7c, an increase in the rotation speed results in large current densities, due to the improved diffusion of oxygen at the surface of the electrode. Based on RDE results under different rotating speed, K-L plots were shown in Figure 7.7c. Co@C-800 exhibits a good linearity and near parallelism properties of K–L plots (shown in Figure 7.7d). According to Koutecky-Levich (K-L) equation, the ORR electron transfer number of Co@C-800 was close to 4.0, suggesting that the ORR proceeded through a four-electron pathway. The stability of the Co@C-800 composites and Pt/C in ORR was tested and compared at 0.8 V in 0.1 M KOH over 16000 s. After 16000 s, the normalized current for Co@C-800 can still remain 90 % compared with 75 % for Pt/C (shown in Figure 7.7e). Clearly, sample Co@C-800 is more durable than commercial Pt/C. To investigate the methanol tolerance of sample Co@C-800, 1 M methanol was added into a 0.1 M KOH electrolyte solution under the same conditions as for Pt/C. The results show that the introduction of methanol caused a sharp decrease in the current density for Pt/C catalyst, however, the introduction of methanol has a negligible effect on the performance of Co@C-800 in ORR. Therefore, sample Co@C-800 exhibits remarkable methanol tolerance (shown in Figure 7.7f). This high durability and excellent methanol tolerance of Co@C-800 may be attributed to the protection of the carbon matrix.

7.3.2 Oxygen evolution reaction

Additionally, the catalytic ability of Co@C composites in the oxygen evolution reaction was also evaluated in 0.1 M KOH solution. The OER performance of Co@C composites and reference IrO_2/C were firstly examined by linear scan voltammograms (Figure 7.8a). The catalytic current is observed to increase as the potential becomes more positive. The sample Co@C-800 exhibits a higher OER current density and an earlier onset of catalytic current compared with other Co@C materials. Co@C-800 demonstrates a small onset potential of 1.43 V, which is only marginally higher than

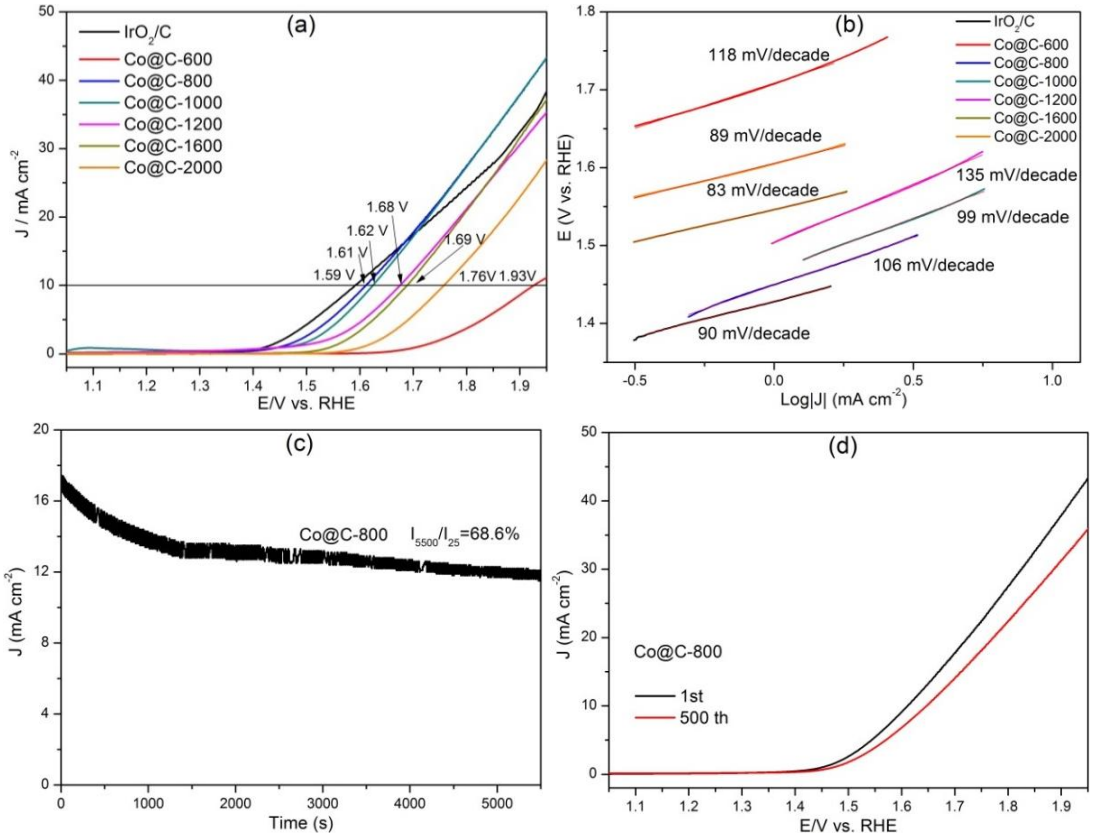

Figure 7.8 (a) LSV curves and (b) the corresponding Tafel plots of the as-synthesized Co@C composites and IrO_2/C at 5 mV s^{-1} in O_2-saturated 0.1 M KOH solution. (c) Chronoamperometric response for Co@C-800 at 1.7 V vs RHE. (d) Polarization curves of Co@C-800 before and after 500 scan cycles.

that of IrO_2/C catalyst (1.42 V). Notably, the current density of IrO_2/C even drops below that of Co@C-800 at the potential higher than 1.68 V, indicating Co@C-800 is a highly active OER catalyst. As shown in Figure 7.8a, the sample Co@C-600, Co@C-800, Co@C-1000, Co@C-1200, Co@C-1600, and Co@C-2000 exhibits a current density of 10.0 mA cm^{-2} at 1.93, 1.61, 1.62, 1.68, 1.69, and 1.76 V, respectively. The value of Co@C-800 (1.61 V) is comparable to that of IrO_2/C (1.59 V), or even better than other reported catalysts, including N-doped graphene/cobalt/carbon hybrid (1.66 V),[408] N-doped graphene/carbon nanotube composite (>1.65 V),[421] and $Mn_3O_4/CoSe_2$ hybrid (1.68 V).[422] In addition, to analyse the kinetics for catalytic OER, the linear fittings of the Co@C composites and IrO_2/C were calculated (shown in Figure 7.8b). Generally, Co@C composites exhibit the relatively low Tafel slopes ranging from 83 to 135 mV dec^{-1}, suggesting good OER kinetics. Similarly to the ORR, the OER activity of Co@C catalysts was also

negatively related to the carbonization temperature ranging from 800 to 2000 ^{o}C. The comparison of the OER catalytic performances of the as-synthesized Co@C composites and IrO_2/C is listed in Table 7.1. For Co@C-800, the introduction of cobalt and N-dopants in Co@C-800 could render the adjacent carbon atoms positively charged, facilitating adsorption of OH^- and promoting the electron transfer.[423, 424] The high surface area of Co@C-800 could also enhanced utilization of electroactive sites. The stability of Co@C-800 was then measured by the chronoamperometric test. Co@C-800 exhibits 68.6% current densities remain after 5500 s at 1.7 V (Figure 7.8c). In addition, in the further stability test, Co@C-800 shows that only a sustainable drop of the current density happened after 500 potential cycles (Figure 7.8d), indicating a good durability for OER. It has been reported that during the oxygen evolution reaction, metallic cobalt would be partially oxidized into cobalt oxide to form the cobalt oxide/complex species, which could decay the OER activity.[425, 426] For Co@C-800, as the cobalt nanoparticles were homogeneously dispersed into the carbon matrix, the carbon surrounding the cobalt could protect and retard the oxidation.

Table 7.1 Comparison of the OER catalytic performances of the as-synthesized Co@C composites and IrO_2/C

Materials	Potential (V vs. RHE) acquired for the current density of 10 mA cm^{-2}	Tafel slope (mV dec^{-1})	Onset potential (V vs. RHE)
Co@C-600	1.93	118	1.63
Co@C-800	1.61	106	1.43
Co@C-1000	1.62	99	1.47
Co@C-1200	1.68	135	1.50
Co@C-1600	1.69	83	1.49
Co@C-2000	1.76	89	1.55
IrO_2/C	1.59	90	1.42

7.4 Summary

In summary, we have successfully prepared ZIF-67 derivatives ranging from cobalt-embedded porous N-doped carbon/carbon nanotubes to hollow carbon nano-onions under different carbonization temperatures. The carbonization temperature effects on the morphology and catalytic properties of final products are systematically studied in this work. At the relatively low carbonization temperatures (600-1000 ^{o}C), cobalt-embedded porous N-doped carbon/carbon nanotubes composites were formed; at the relatively high carbonization temperature (1200-2000 ^{o}C), the precursor ZIF-67 was converted into hollow carbon nano-onions. There is an optimum carbonization temperature for electrocatalytic performance during the range 600-2000 ^{o}C. As the carbonization temperature increases from 600 to 800 ^{o}C, an ordered graphic structure was formed, hence improving its electrical conductivity. In the meantime, the surface area and the porosity of the frameworks can still be maintained, and so are cobalt particle sizes. Therefore, an enhanced electrocatalytic performance was achieved at 800 ^{o}C. As the carbonization temperature increases from 800 to 2000 ^{o}C, the graphic structure becomes more ordered. However, the surface area, porosity and nitrogen content decreased dramatically due to the collapse of framework structure and the volatilization of nitrogen. The aggregation of cobalt nanoparticles became severe, resulting in the weakened electrocatalytic performance. Thanks to the hierarchical porous carbon structure, N-doping effect and the homogeneous cobalt dispersion, the Co@C-800 nanocomposite exhibits excellent catalytic activities for both ORR and OER with good stability.

Due to the possibility of tailorability of building units (organic ligands and metallic species) depending on reaction conditions and requirements, ZIFs are treated as ideal sacrificial materials to derive metal-free carbon, and carbon based nanocomposites, even though the cost of ZIFs is relative high. Therefore, these ZIFs derivatives will be excellent alternatives in the fields of energy storage and conversion technologies.

8. Chapter 8: Cobalt sulfides/N, S co-doped porous carbon composites and relevant cobalt-nickel sulfides/N, S co-doped porous carbon composites derived from ZIF-67 with their applications

8.1 Introduction

With the depletion of hydrocarbon-based energy resources and the increasing global energy demands, it is imperative to develop green and sustainable energy storage and conversion technologies as alternatives to currently widely used fossil fuels.[399, 427, 428] Electrocatalytic oxygen reduction reaction (ORR) and oxygen evolution reaction (OER) play key roles in several important next-generation energy storage and conversion technologies, such as fuel cells, metal-air batteries and water splitting.[29-38] Hitherto, most efficient electrocatalysts for ORR/OER contain precious metals including Pt or Ir; however, due to the prohibitive cost, poor stability of precious metals, the sluggish kinetics for ORR and the large polarisation, it is highly desirable to discover highly efficient and low-cost earth-abundant non-precious electroactive materials that can rival the performances of precious metal-based catalysts.[39-42]

Much effort has, therefore, been devoted to transition metal oxide/sulfide based materials, as many transition metals like cobalt, and manganese have been widely considered to be electrochemically active for ORR and OER. Particularly, cobalt sulfides (Co_xS_y) with different phases have been previously investigated as ORR and OER electrode catalysts and exhibited attractive electrocatalytic performance among different non-precious and late transition metal chalcogenides.[161, 429-433] For instance, CoS_2 is a good electrocatalyst for ORR and OER;[434] Co_3S_4 has excellent performance for ORR[435, 436] and OER;[436] while $Co_{1-x}S$ is a promising electrocatalyst for ORR[429, 436] and OER,[436] Co_9S_8 is a good catalyst for ORR.[432] However, the complicated preparation procedures coupled with the low electrical conductivities of cobalt sulfides usually result in unsatisfactory catalytic durability. As alternatives, transition metal oxide/sulfide-carbon composites have been considered as promising electrocatalysts for ORR/OER since they hold a reasonable balance between catalytic activity, cost, and durability.[437] In particular, heteroatom (e.g., N, S, B, or P) doped carbon based materials have emerged and attracted great attention because heteroatoms can tune the electronic and geometric properties of carbon, offering more

active sites and enhancing the interaction between carbon structure and active sites.[437-440] Remarkably, the combination of transition-metal metal oxide/sulfide with heteroatom-doped carbon can achieve high catalytic activity and improve durability because of the synergistic effects.[437]

Metal organic frameworks (MOFs, including Zeolitic Imidazolate Frameworks (ZIFs)), a class of nanoporous materials assembled from metal ions and organic ligands,[5-7] exhibit tuneable structures, versatile functionalities and fascinating properties. Owing to the molecular-like organic-inorganic crystal structure of MOFs, thermal treatment the parental MOFs can result in the formation of metal or metal oxide nanoparticles homogeneously dispersed within the nanoporous carbon matrices which frequently exhibit excellent electrochemical properties.[271, 272, 408, 409, 415, 441] Therefore, MOFs have emerged as excellent precursors or sacrificial templates for the preparation of porous carbon based nanocomposites, which offer a new approach to improve the catalytic activity and overcome the intrinsic limitations of the existing transition metal/metal oxide electrocatalysts.[271, 272, 408, 409, 441] Metal sulfides derived from MOFs were recently reported;[442, 443] however, to the best our knowledge, carbon-based metal sulfide composites derived from MOFs as highly efficient electrocatalysts for ORR/OER are rarely reported previously.

In this chapter, for the first time, we present the successful synthesis of atomically homogeneous dispersed cobalt sulfide/N,S Co-doped porous carbon nanocomposites by a facile one-step sulfurization and carbonization of ZIF-67 simultaneously. ZIF-67 was chosen as a model precursor owing to its abundant Co–N moieties, rich organic resources and unique dodecahedral morphology.[7] Possessing a unique core-shell structure, high porosity, and homogeneous dispersion of active components together with N and S-doping effects, the resulting composites exhibit excellent ORR and OER activities, superior durability, a four-electron pathway and high methanol tolerance in alkaline media, which outperformed the traditional Pt/C electrocatalyst. This may pave the way to further develop novel highly-efficient and low-cost composite electrocatalysts for the next generation of energy storage and conversion applications.

In addition, the research on the synthesis of bimetallic oxide/sulfide nanoparticles embedded within heteroatom-codoped carbon networks derived from MOFs is rare.[444]

Actually, to the best of our knowledge, there are no reports on the using of MOFs to prepare bimetallic oxide/sulfide nanoparticles and heteroatom-codoped carbon composites. For bimetallic oxides/sulfides, there could be synergistic effects between the various transition metal atoms e.g. Fe, Ni or Co.[445] Moreover, synergistic effects the from various doping heteroatoms e.g. N, S, B, or P may also exist.[446] In addition, the combination of transition-metal oxides/sulfides with heteroatom-codoped carbon could also generate a synergistic effect.[447-449] These synergistic effects in a composite catalyst system can frequently result in the increase of in electrocatalytic activities of composite system compared to the monometallic oxide/sulfide or single heteroatom doped carbons, thus enhancing the intrinsic electrocatalytic behaviours of each component. Consequently, non-noble metal based transition-metal oxides/sulfides within heteroatom-codoped porous carbon composites with superior electrocatalytic performances may emerge.

In this chapter, we also utilised a facile strategy for the preparation of Ni-Co based sulfide nanoparticles homogeneously embedded in N, S co-doped porous carbon by a one-step sulfurization and carbonization of Ni-substituted ZIF-67 simultaneously. The Ni-substituted ZIF-67 was chosen as the precursor since it contains high level of Co-N and Ni-N moieties. Remarkably, the resulting composite Ni_1Co_4S@C-1000 not only exhibits excellent OER catalytic activity with low over-potential which is comparable with that of a commercial IrO_2/C catalyst, but is also a highly efficient electrocatalyst in ORR with a four-electron pathway. Moreover, Ni_1Co_4S@C-800 composites show enhanced electrocatalytic activity for HER in water splitting.

8.2 Characterizations of cobalt sulfides/N, S co-doped porous carbon composites

The structure and morphology of cobalt sulfide/N,S Co-doped porous carbon composite samples are firstly investigated by transmission electron microscopy (TEM). The parental ZIF-67 precursor exhibits a typical rhombic dodecahedron with an average particle size of 350 nm.[82] After the sulfurization and carbonization process in a hydrogen sulfide atmosphere at high temperatures, as presented in Figure 8.1, the resulting cobalt sulfide/N,S Co-doped porous carbon composites maintain the rhombic dodecahedron particles with a smaller size of 250 nm due to the shrinkage during the annealing process, and the particles tend to agglomerate and form larger particles at higher temperatures. Generally, all the composites are composed of

numerous cobalt sulfides nanoparticles and continuous carbon networks, in which the cobalt sulfides nanoparticles are homogeneously embedded into the carbon matrix, with lattice fringes of ~0.29 nm. The selected area electron diffraction (SAED) patterns shown in the Insets of Figure 8.1b, d and f, clearly suggest that the bright scattered spots are a contribution from the crystalline cobalt sulfide nanoparticles while the dimmed diffraction rings are from the amorphous porous carbon matrix.[429] In addition, the particle sizes for cobalt sulfide grow from 5 to 50 nm with the increase of annealing temperature from 600 ^{o}C to 1000 ^{o}C, and the corresponding intensity of SAED patterns are also enhanced due to the increased annealing temperature resulting in the improved crystallization of cobalt sulfide particles. In particular, sample Co_xS_y@C-600 still maintains the original rhombic dodecahedron of the ZIF-67 precursor. Small cobalt sulfide nanoparticles (5 nm) are homogeneously dispersed into the carbon matrix. The surface of the sample Co_xS_y@C-600 is smooth (see the SEM in Figure 8.2a). While the sample Co_xS_y@C-800 shows slightly changed morphology because the cobalt sulfide crystals grow bigger and the crystal surfaces become rough (see Figure 8.2b), which is consistent with TEM results (Figure 8.1c). Furthermore, high resolution TEM (Figure 8.1d) indicates that onion-like carbon, which is formed due to the catalytic effect of metallic cobalt during the graphitization stage,[409, 415] together with bigger cobalt sulfide particles (20 nm) can be observed. However, the sample Co_xS_y@C-1000 exhibits a damaged or distorted rhombic dodecahedron morphology due to the higher annealing temperature, and the cobalt sulfide crystals grow up to 50 nm (shown in Figure 8.1e and Figure 8.2c). Interestingly, a crystalline cobalt sulfide core and carbon shell structure is formed in the sample Co_xS_y@C-1000 (shown in Figure 8.1e and f). This core-shell structure is also confirmed by using linear EDX analysis in STEM measurements (shown in Figure 8.3). The thickness of carbon shell is about 5 nm, which has tightly wrapped around the cobalt sulfide crystals. Actually, a core-shell structure has been proven to be beneficial to the improvement of electrocatalytic activities towards ORR and OER, where the core offers the catalytically active sites while the shell will provide facile electron transfer pathways and mass transport channels for the active cores due to the porous structures of carbon shell.[437, 450]

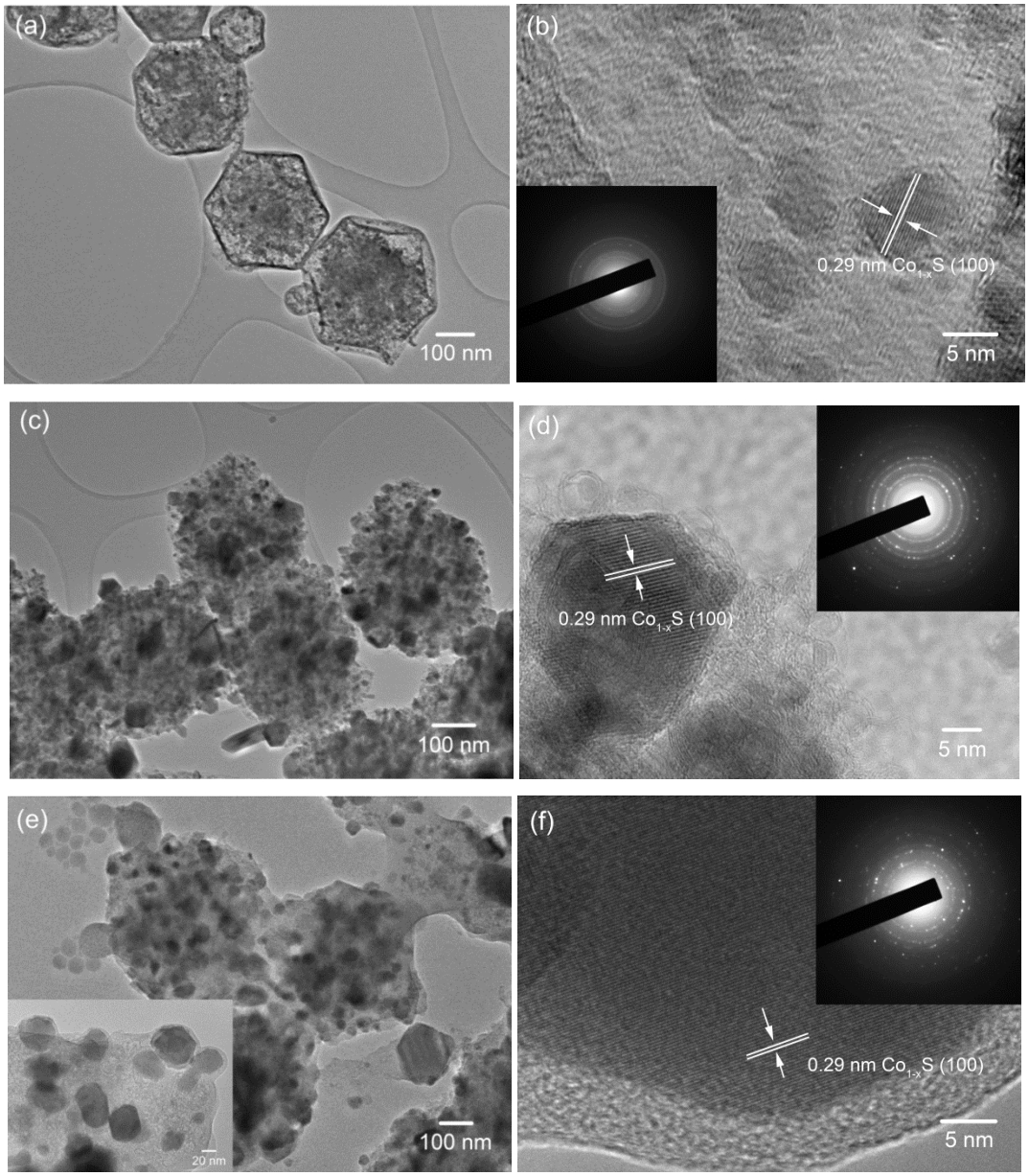

Figure 8.1 TEM images of (a-b) Co_xS_y@C-600; (c-d) Co_xS_y@C-800 and (e-f) Co_xS_y@C-1000. Inset in (b), (d) and (f) is SAED patterns for corresponding sample.

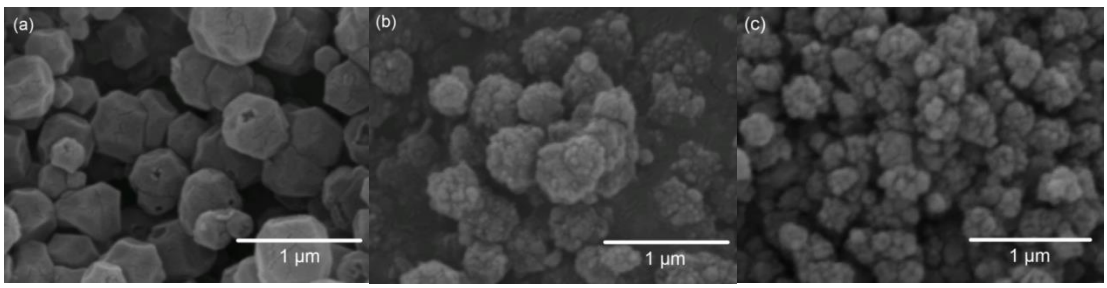

Figure 8.2 SEM images of the as-synthesized nanocomposites where (a) Co_xS_y@C-600; (b) Co_xS_y@C-800 and (c) Co_xS_y@C-1000.

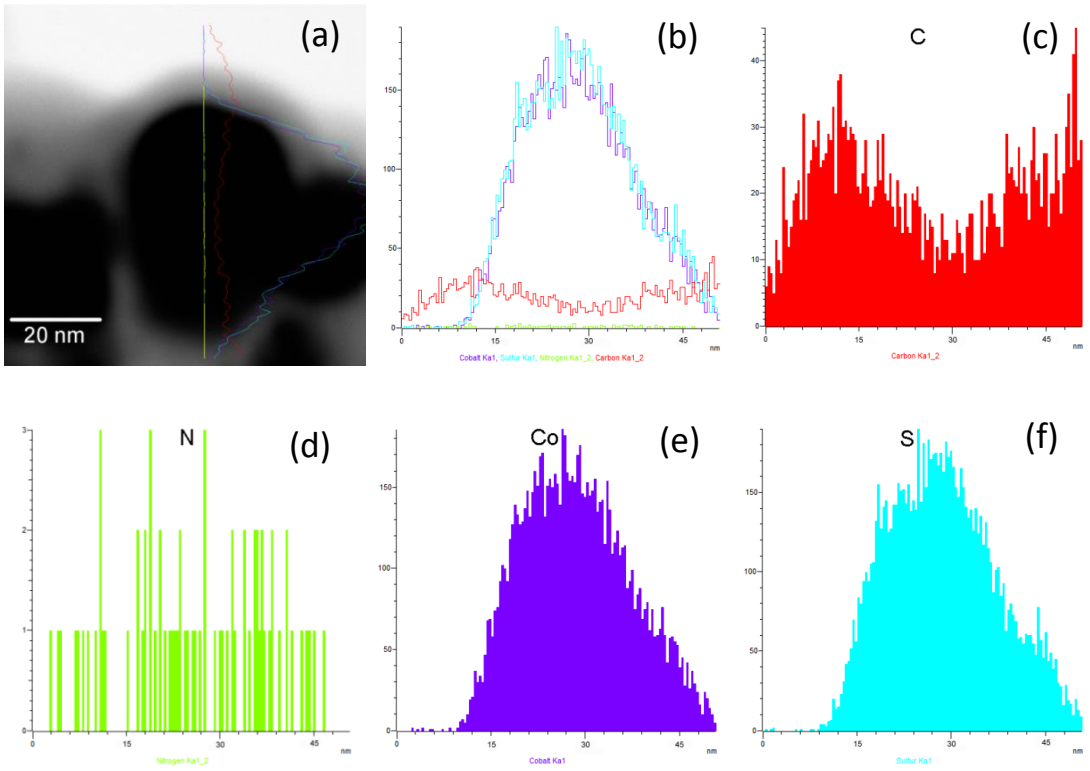

Figure 8.3 STEM image and linear EDX for sample Co_xS_y@C-1000. C, N, S and Co signals are clearly detected from the sample. The compositional line profile shows that while C signal is observed on the outer surface of cobalt sulfide particles, S and Co signals are detected only in the inner core of the nanoparticles. The results indicate that the nanoparticle consists of a cobalt sulfide core, surrounded by a 5 nm thickness of carbon shell.

Moreover, SEM combined with elemental mapping technique was used to ascertain the distribution of cobalt sulfide nanoparticles in the composite samples. As shown in Figure 8.4, element Co, S and C exhibit similar elemental mapping patterns to their selected area of SEM image, indicating the uniform dispersion of cobalt sulfide nanoparticles in the carbon matrix of sample Co_xS_y@C-1000. In addition, N is also observed in the elemental mapping, although N content is much less than that of C, possibly due to the high volatility of N species at high annealing temperature.

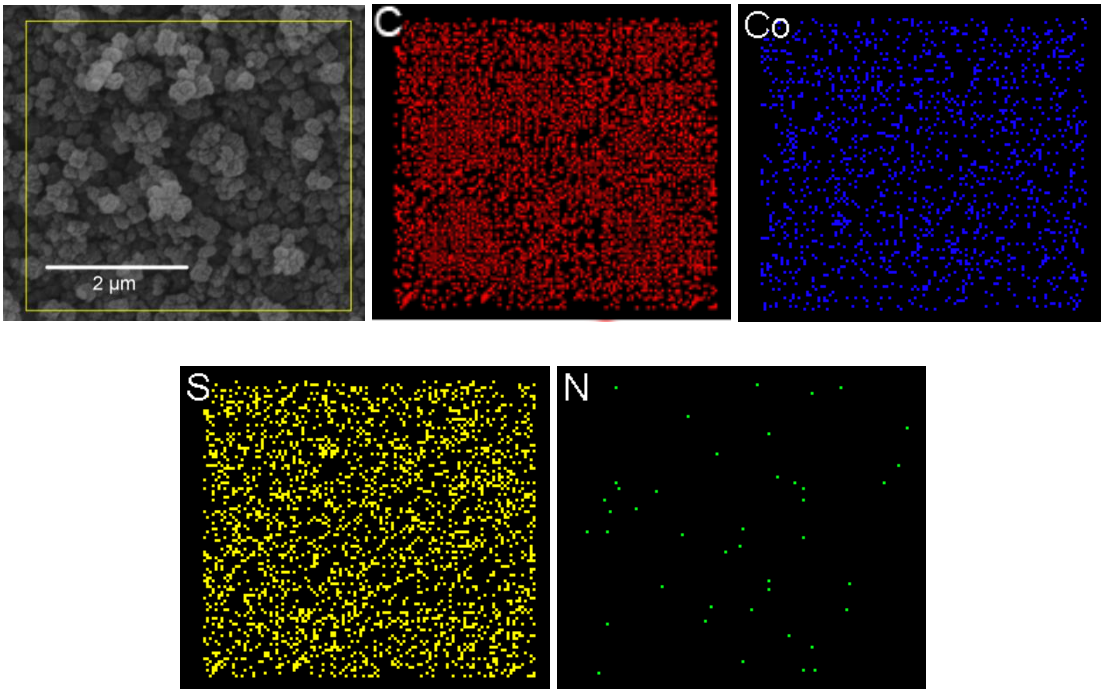

Figure 8.4 SEM image and elemental mappings for sample Co_xS_y@C-1000.

The crystal structures of the as-synthesized Co_xS_y@C composites were further characterized by XRD (shown in Figure 8.5a). Different from the sodalite structure of the ZIF-67 precursor, the as-prepared composites show a broad XRD peak centred at 2θ of around 25°, representing the (002) diffraction of carbon.[246] Moreover, the XRD patterns of the composites indicate that they contain mainly $Co_{1-x}S$ (ICDD PDF #42-0826) with the hexagonal structure in the P63/mmc space group (no. 194).[429] In addition, in sample Co_xS_y@C-1000, XRD peaks originating from Co_3S_4 (ICDD PDF #02-0825) can also be observed, indicating the phase transition of cobalt sulfide crystals occurs at higher annealing temperature (1000 °C). Clearly, the high sulfurization and carbonization temperature results in highly crystalized cobalt sulfide dispersed in carbon matrix. The XRD results are consistent with the lattice fringes of the $Co_{1-x}S$ nanocrystals (Figure 8.1b, d and f) and their electron diffraction patterns (the inset in Figure 8.1d and Figure 8.1f). Although it is ideal to achieve phase pure cobalt sulfide materials via control over the sulfurization temperature, it is actually difficult to achieve this using the proposed experimental procedure, which is consistent with the recent reports,[416, 449] where the authors used sulfur for the sulfurization of ZIF-67 under different temperatures and the formation of the as-synthesized composites is complicated during the sulfurization and carbonization procedure. The XRD results clearly showed that with the increase of sulfurization

temperatures, the XRD peaks for cobalt sulfide (mainly the $Co_{1-x}S$ phase) became more intense and sharper, accompanied with the appearance of Co_3S_4, indicating the growth of crystallites and crystallinity improvement of cobalt sulfide. And both $Co_{1-x}S$ and Co_3S_4 are regarded as good electrocatalysts for ORR and OER.[429, 436] It is, however, worthy to understand the formation mechanism of cobalt sulfide in this relatively complicated system.

Raman spectroscopy is a powerful technique to investigate carbonaceous materials. As shown in Figure 8.5b, all the composites clearly exhibit G band and D band in the Raman spectra, due to the bond stretching of all pairs of sp^2 atoms in both rings and chains and the breathing modes of sp^2 atoms in rings, respectively.[290, 291] The G band at around 1590 cm^{-1} supports the presence of some nanocrystalline carbon and a high content of sp^2-hybridized carbon atoms caused by the carbonization of the samples. The D band at around 1340 cm^{-1} is an indication of less disordered carbon. The appearance of both G band and D band in sample Co_xS_y@C-600, Co_xS_y@C-800, Co_xS_y@C-1000, suggests the formation of abundant defects and amorphous carbon in the composites during the sulfurization and carbonization process.

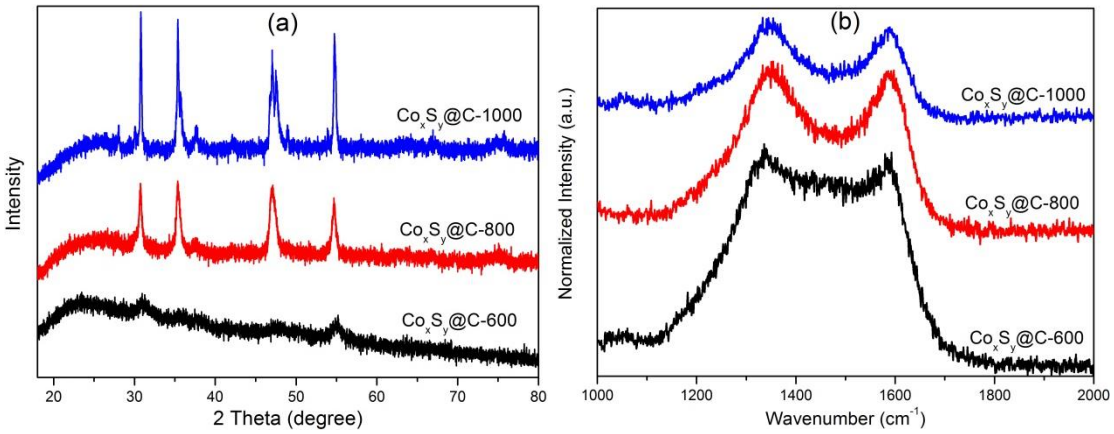

Figure 8.5 (a) XRD patterns and (b) Raman spectra of the as-synthesized Co_xS_y@C composites.

X-ray photoelectron spectroscopy (XPS) analysis was utilised to ascertain the structures of as-synthesized composites owing to the fairly complex phase diagram of cobalt sulphide.[451] Element survey by XPS (Figure 8.6a) clearly suggests the presence of Co, S, C, N, and O in all the composites.[437, 452] The spectrum of Co 2p (shown in

Figure 8.6b) for sample obtained at sulfurization temperature of 600 ^{o}C (Co_xS_y@C-600) exhibits two spin-orbit doublets at 781.2 and 796.9 eV, implying the existence of the Co^{2+} oxidation state. However, except the spin-orbit doublets for Co^{2+} oxidation state, other doublets in the sample Co_xS_y@C-800 and Co_xS_y@C-1000 are found at 778.4 and 793.5 eV, which indicate the existence of the Co^{3+} oxidation state,[453, 454] suggesting that a mixed Co^{2+} and Co^{3+} oxidation states are formed in these two samples.[453-455] In the S 2p spectrum (shown in Figure 8.6c), the first two peaks located at 161.4 and 162.5 eV were due to the spin−orbit coupling in metal sulfide,[455, 456] while the S 2p peak at 163.5 eV suggested the existence of covalent S-C bonds in the as-synthesized composites[457, 458] indicating that S has been covalently inserted in N-doped porous carbon.[450] No peaks at around 164.5 eV corresponding to polysulfides (S_n^{2-}) can be found in any sample,[459-461] and the peaks at 168.5 and 169.5 eV in the S 2p spectrum indicate that an inconsequential amount of Co_xS_y compounds were also formed during the thermal treatment process.[462, 463] Moreover, the main peaks for the N 1s spectra (shown in Figure 8.6d) can be deconvoluted into four different types of nitrogen species: pyridinic-N (397.8 eV), Co-N (399.1 eV), pyrrolic-N (400.1 eV), and graphitic-N (401.8 eV), respectively.[408] The N species is widely considered to play an important role in the ORR and OER processes,[464, 465] where pyridinic N could improve the onset potential and graphitic N determined the limiting current for ORR.[437, 452] It is clear that high temperature results in low N content remaining in the samples, maybe due to the high volatility of N species under the high temperature sulfurization process. From XPS results, the nitrogen doping level in sample Co_xS_y@C-1000 and Co_xS_y@C-800 is relatively low (2.51% and 3.64% respectively), sample Co_xS_y@C-600 possesses relatively high nitrogen content, and all the samples contain different levels of sulfur content. However, it is not easy to evaluate the contribution of S doping to the catalytic activity separately in these complicated system. The C 1s spectrum of the composites (Figure 8.6e) exhibits a main peak at 284.6 eV suggesting the formation of a sp^2 hybridized graphitic structure that can improve the electroconductivity of the samples, and which is beneficial to fast electron transfer throughout the structural frameworks.[437] In addition, the C 1s can be further deconvoluted into peaks positioned at 284.8, 285.8, and 288.8 eV, which may be attributed to C=C, C=N/C-O/C-S, and C-N, respectively.[355, 457, 466, 467] Combining XPS analysis with XRD results, it is believed that the products derived from the

sulfurization of ZIF-67 at high temperatures are basically Co_xS_y supported on N,S Co-doped carbon composites.

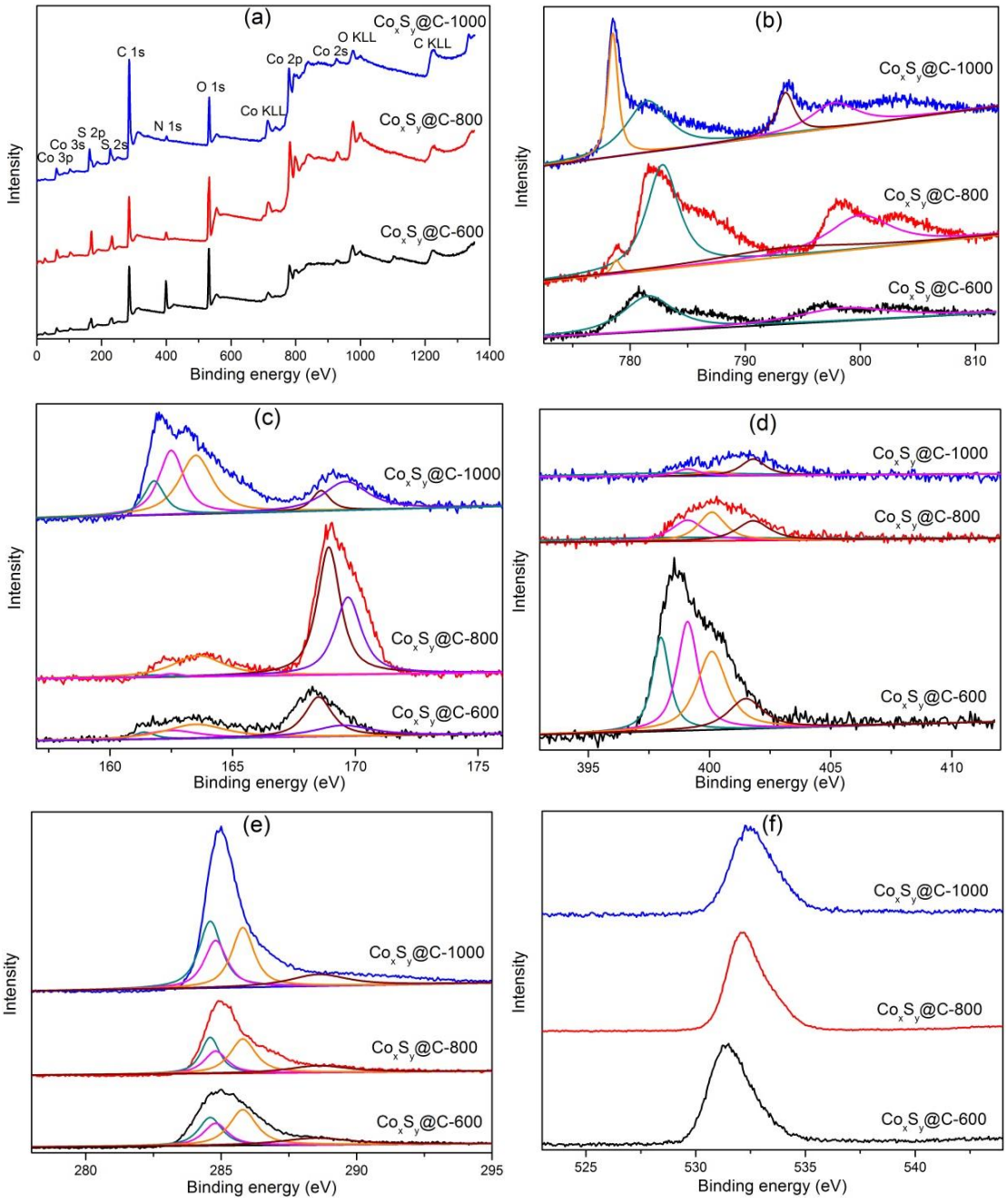

Figure 8.6 (a) Element survey by XPS and high-resolution XPS spectrum of (b) Co 2p, (c) S 2p, (d) N 1s, (e) C 1s, and (f) O 1s for the as-synthesized Co_xS_y@C composites.

The textural characteristics of the as-synthesized composites were analysed by N_2 sorption at -196 ^oC. While sample Co_xS_y@C-600 exhibits a large hysteresis loop between its adsorption and desorption branches, implying the existence of

mesoporous features due to the voids between particles, the other two samples Co_xS_y@C-800, and Co_xS_y@C-1000 show largely reversible adsorption–desorption isotherms. These 3 samples exhibited specific surface areas of 178, 238, and 248 $m^2 g^{-1}$ and pore volume of 0.80, 0.35, and 0.31 $cm^3 g^{-1}$, respectively (shown in Table 8.1), much lower than that of the ZIF-67 precursor (shown in Figure 8.7), probably due to the dominance of cobalt sulfide weight percentage in the as-synthesized composites. The relative large surface area of the composites is beneficial to provide more accessible active sites, which is likely to result in a higher electrocatalytic activity.[408]

Table 8.1 Textural properties of the as-synthesized Co_xS_y@C composites.

	Specific surface area ($m^2 g^{-1}$)	Microporous surface area ($m^2 g^{-1}$)	External surface area ($m^2 g^{-1}$)	Pore volume ($cm^3 g^{-1}$)	Micropore volume ($cm^3 g^{-1}$)
Co_xS_y@C-600	178	19	159	0.80	0.008
Co_xS_y@C-800	238	92	146	0.35	0.038
Co_xS_y@C-1000	248	39	209	0.31	0.019

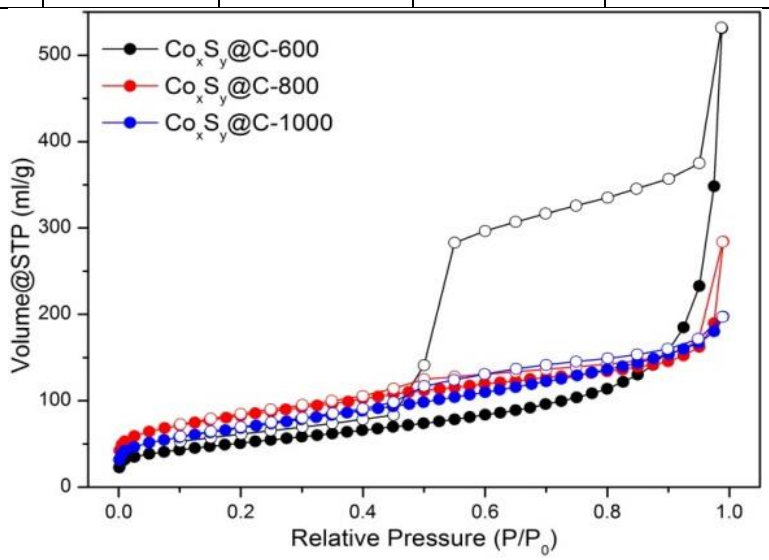

Figure 8.7 Nitrogen adsorption-desorption isotherm curves of the as-synthesized Co_xS_y@C composites.

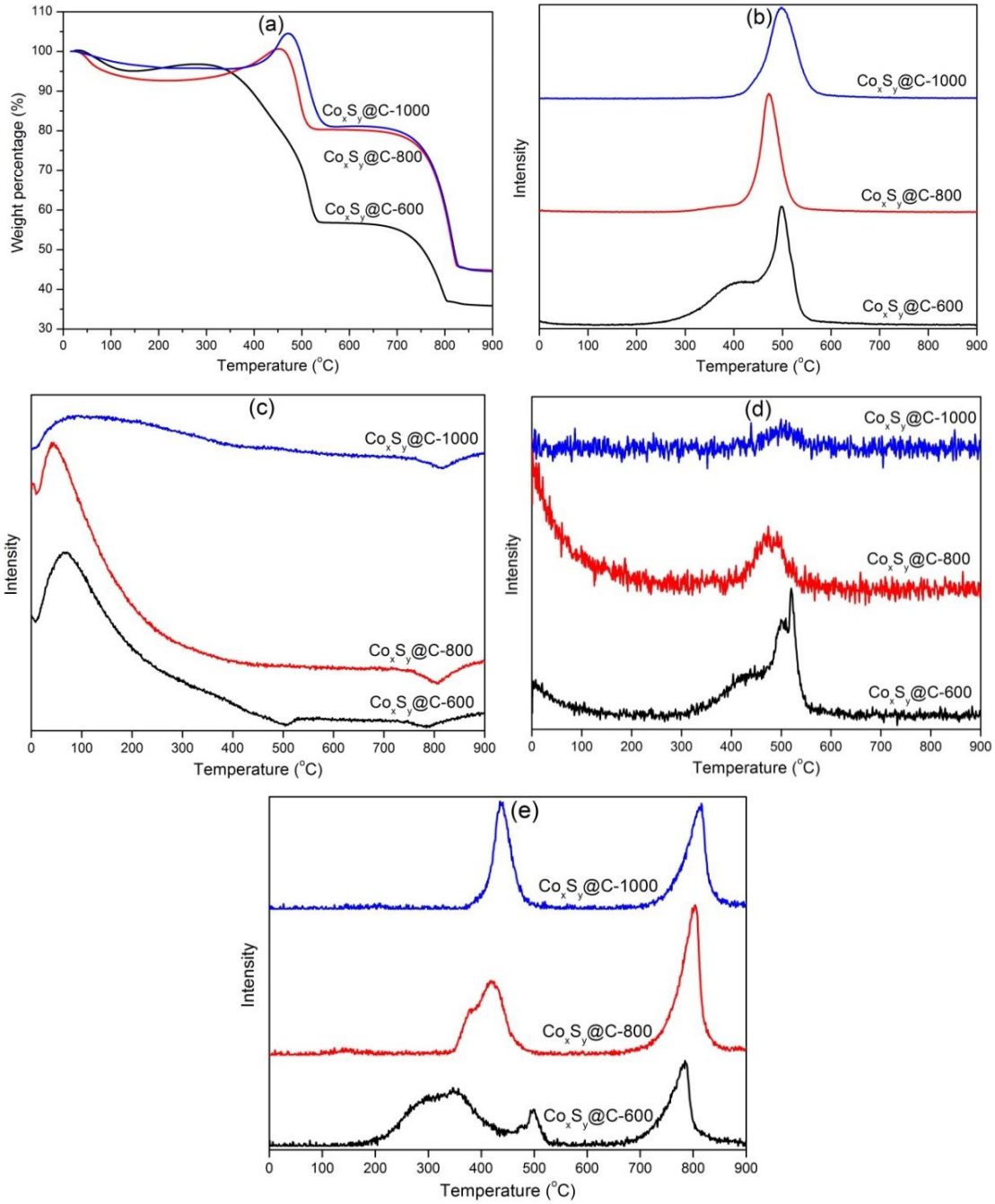

Figure 8.8 TGA (a) and their corresponding MS curves of CO_2 (b), H_2O (c), NO_2 (d), and SO_2 (e) for different nanocomposites.

The thermal stabilities of the composites in air were evaluated by TGA-MS. As shown in the TGA profiles (Figure 8.8a), all the as-synthesized composites exhibit a minor weight loss event below 100 ^oC due to the removal of adsorbed water from the composites (Figure 8.8c), followed by a small weight increase in the temperature range of 300-500 ^oC, due to the oxidation of cobalt sulfide to high valence state. There are then two major weight loss events at 450-500 and 790 ^oC for all the samples,

corresponding to the burn off the N,S Co-doped carbon species in air, as confirmed by the emission of CO_2, NO_2 and SO_2 in their MS signals (see Figure 8.8b, d and e), and the decomposition and oxidation of cobalt sulfides (Figure 8.8e). It is worth noting that the sample Co_xS_y@C-600 shows a different weight loss event in the temperature range of 300 - 500 ^oC, accompanying the evolving CO_2, NO_2 and SO_2 (see Figure 8.8b, d and e), maybe due to the oxidation of incompletely decomposed organic ligands from the precursor.

8.3 Applications of cobalt sulfides/N, S co-doped porous carbon composites

8.3.1 Oxygen reduction reaction

The electrocatalytic activities of the as-prepared composites towards ORR were then evaluated by cyclic voltammetry (CV) measurements in 0.1 M KOH at 25 ^oC. Comparing the CV curves in O_2-versus N_2-saturated electrolyte solution, it clearly reveals that the composites are electrocatalytic active in ORR (Figure 8.9). As shown in Figure 8.9c, no obvious redox peak is observed for Co_xS_y@C-1000 in N_2-saturated solution. In contrast, when the electrolyte is saturated with O_2, a well-defined cathodic peak clearly appears at 0.803 V, confirming the electrocatalytic activity for ORR.[468, 469] Other samples Co_xS_y@C-600 and Co_xS_y@C-800 (Figure 8.9a and Figure 8.9b) show a cathodic peak at 0.540 and 0.809 V, respectively. Noticeably, the sample Co_xS_y@C-1000 shows a much higher peak current (2.94 mA cm^{-2}) than those of Co_xS_y@C-600 (0.735 mA cm^{-2}) and Co_xS_y@C-800 (1.48 mA cm^{-2}), implying that pronounced ORR catalytic activity is observed for Co_xS_y@C-1000.

Rotating disk electrode (RDE) measurements were performed to gain further insight into the ORR kinetics of the Co_xS_y@C composites. As shown in the polarization curves at 1600 rpm in 0.1 M KOH (Figure 8.10), Co_xS_y@C-1000 obviously holds the highest onset potential (around 0.924 V) and largest cathodic current density (-4.6 mA cm^{-2}), indicating its superior activity. The onset potential for Co_xS_y@C-1000 is close to that of the benchmark Pt/C catalyst (0.944 V) while the half-wave potentials of them are very close, suggesting that Co_xS_y@C-1000 is a promising alternative catalyst for the cathodic ORR. In addition, the polarization curve of Co_xS_y@C-1000 is significantly different from that of Co_xS_y@C-600 and Co_xS_y@C-800 but resembles that of Pt/C, indicating that the ORR mechanism of Co_xS_y@C-1000 is different from those of the other Co_xS_y@C composites but is more like that of Pt/C, which exhibited

an efficient four-electron ORR pathway.[470, 471] The mechanism of four-electron ORR pathway proceeds through two-oxygen atom side and/or bridge adsorption for oxygen dissociation simultaneously.[471]

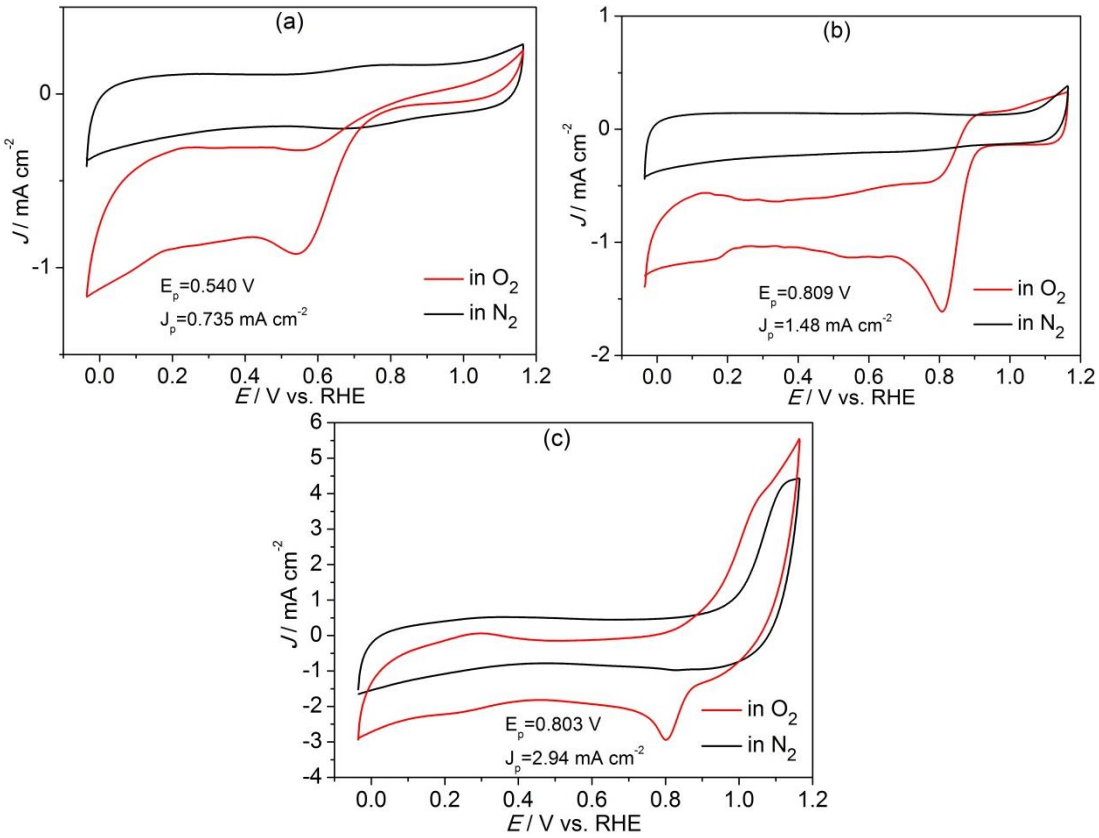

Figure 8.9 CV curves of (a) Co_xS_y@C-600, (b) Co_xS_y@C-800, and (c) Co_xS_y@C-1000 nanocomposites in N_2-saturated and O_2-saturated 0.1M KOH solution.

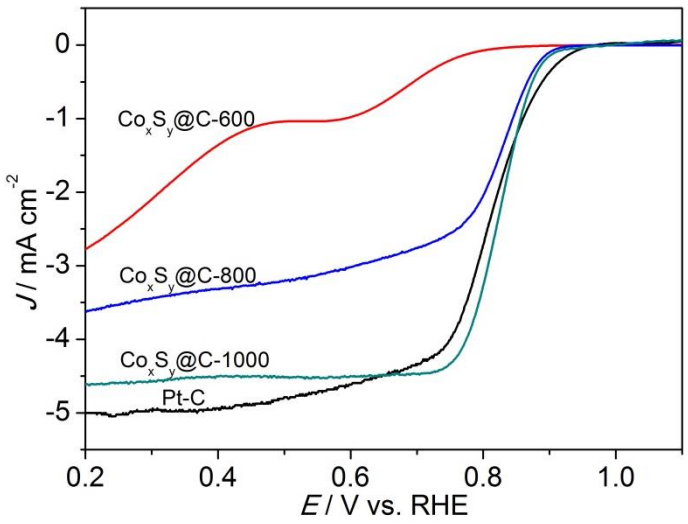

Figure 8.10 ORR polarization curves of Co_xS_y@C-600, Co_xS_y@C-800, Co_xS_y@C-1000, and Pt/C at 1600 rpm.

RDE measurements at different rotating speeds were carried out and the kinetic parameters were analysed with the Koutecky-Levich (K-L) equation. An increase in the rotation speed leads to an increase in the diffusion of oxygen at the surface of the electrode, which results in large current densities as shown in Figure 8.11a, c and e. The good linearity and near parallelism properties of K-L plots for Co_xS_y@C-1000 indicates first-order reaction kinetics with regard to the concentration of dissolved oxygen and similar electron transfer numbers (n) for ORR at various potentials (Figure 8.11f).[472]

The value of *n* and kinetic current density (J_k) can be respectively derived from the slope and intercept of the K-L plots (Figure 8.11b, d and f) at various potentials,[473] and the results are depicted in Figure 8.12. Obviously, the values of *n* for Co_xS_y@C-1000 varied from 3.69 to 3.78 in the potential range of 0.30 – 60 V, suggesting that the ORR proceeded mainly through a four-electron pathway. This was further confirmed by the low HO_2^- yield (~12%) and high *n* value (> 3.7) measured by the RRDE tests as shown in Figure 8.13. The mechanism of the four-electron transfer for ORR has been suggested to proceed through simultaneous two-oxygen atom side and/or bridge adsorption for oxygen dissociation.[471] In contrast, the *n* values for the other two composites decreased with the sulfurization temperature, and they are only 2.13-3.28 for the Co_xS_y@C-600, indicating that a two-electron pathway might dominate the Co_xS_y@C-600 catalysed ORR process. Moreover, the J_k values for Co_xS_y@C-1000 were always much higher than those for the other two composites, reflecting the enhanced electron transfer kinetics of oxygen reduction. Compared with other different previously reported catalysts,[274, 474-478] the ORR catalytic performance of Co_xS_y@C-1000 is competitive.

The superior ORR activity of the Co_xS_y@C-based composites is attributed to their novel structures. The pristine cobalt sulfides have major drawbacks in capacity fading and low conductivity. To overcome these obstacles, the cobalt sulfide nanoparticles can be uniformly dispersed into the heteroatom-doped carbon matrix, which formed a conducting network to the electrode and facilitated ORR through effective charge transport between oxygen molecules adsorbed on cobalt sulfide active sites and the electrode. The utilisation of molecular-like porous ZIF-67 as a precursor enables the generated cobalt sulfide nanoparticles to be homogeneously dispersed on porous carbon matrix. In addition, the porous carbons can serve as a substrate and good

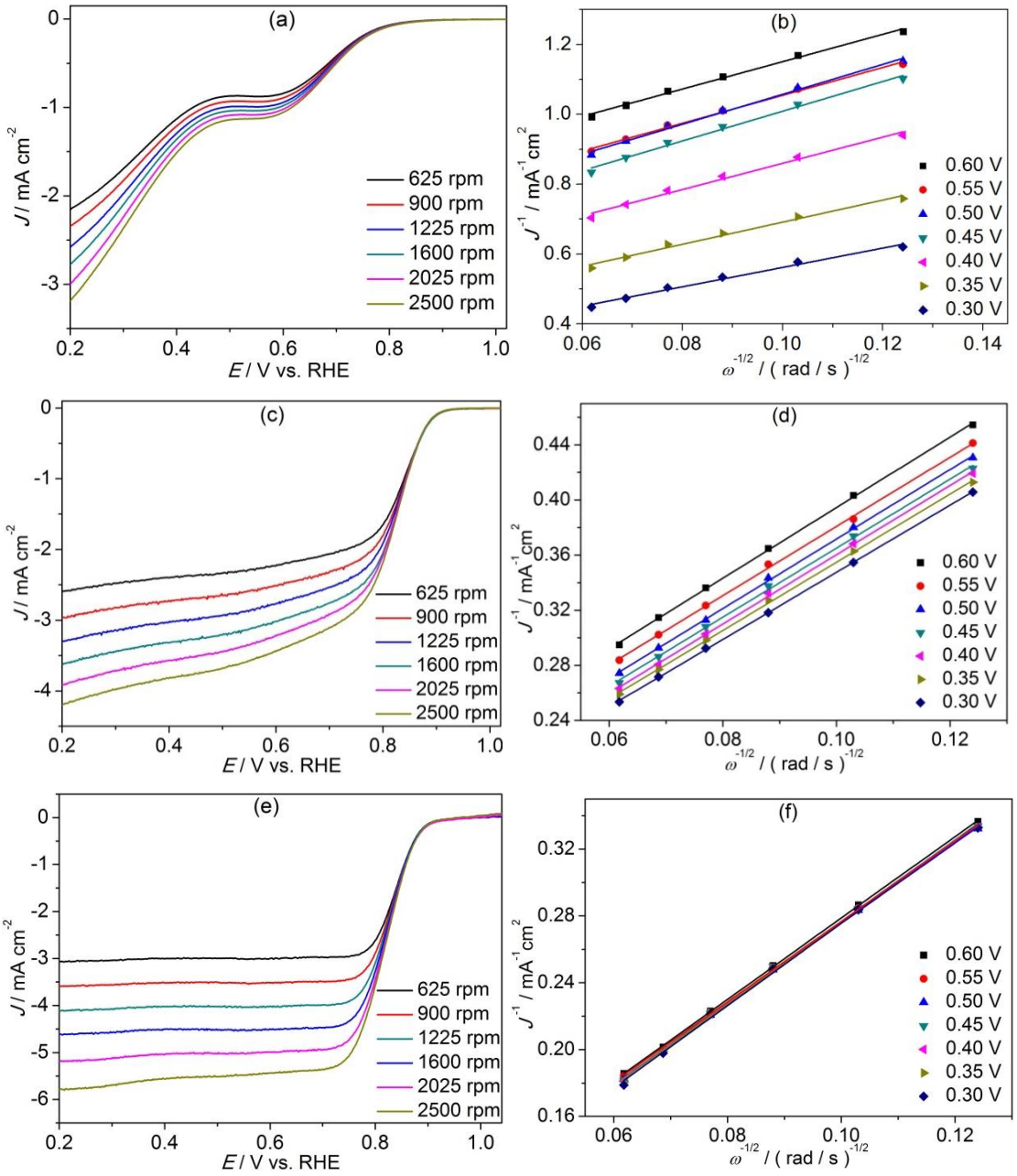

Figure 8.11 ORR polarization curves (a), (c), and (e) of Co_xS_y@C-600, Co_xS_y@C-800, and Co_xS_y@C-1000 at different rotating speeds, respectively. K-L plots (b), (d) and (f) of Co_xS_y@C-600, Co_xS_y@C-800 and Co_xS_y@C-1000 at different potentials, respectively.

conductor that provide more accessible cobalt sulfide active sites, consequently further enhancement of the ORR activity can be realised. Specifically, for sample Co_xS_y@C-1000, the core-shell structure between the active cobalt sulfide nanoparticles and the porous carbon shells provides superior facile pathways for electron and mass transport.[450] In addition, heteroatom doped (N and S-doped)

carbon also plays an important role in the ORR activity enhancement. By modifying the electronic and geometric properties of carbon matrix, N and S doping can not only provide more active sites, but also enhance the interaction between carbon structure and active catalytic sites.[437] The defects in carbon caused by N and S doping can result in much stronger adsorption of oxygen molecules and the higher activity for heterogeneous peroxide decomposition.[437]

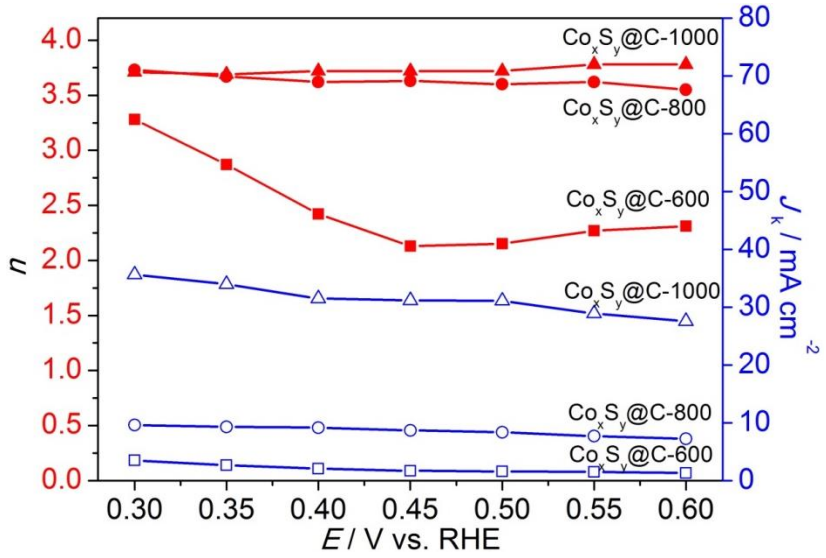

Figure 8.12 Electron transfer numbers (n) and the corresponding kinetic current density (J_k) of Co_xS_y@C-600, Co_xS_y@C-800, and Co_xS_y@C-1000 as a function of the electrode potentials.

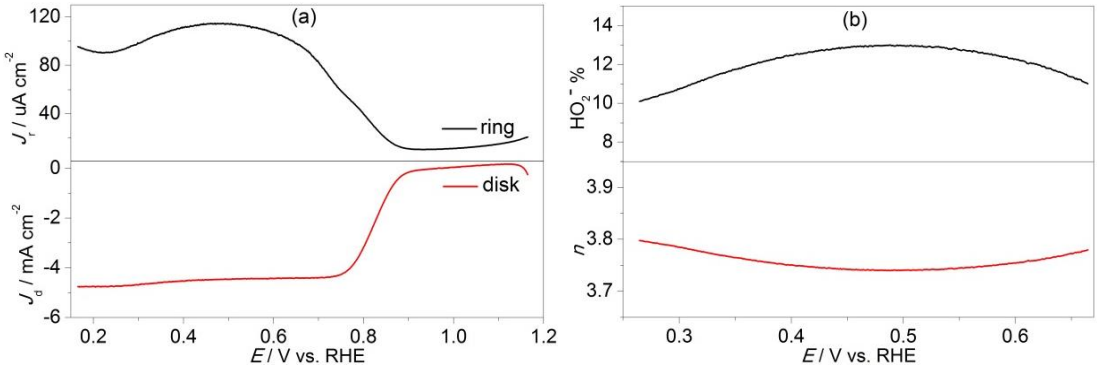

Figure 8.13 (a) Disk current and ring current from RRDE measurements of Co_xS_y@C-1000 with various loadings in O_2-saturated 0.1M KOH at a rotating speed of 1600rpm. (b) Percentage of 2e reduction and electron transfer number n in ORR at different potentials calculated from RRDE curves in (a).

Besides the catalytic activities, the durability of the Co_xS_y@C-1000 composites and commercial Pt/C was tested at 0.80 V in 0.1 M KOH over 18000 s. It is observed that the sample Co_xS_y@C-1000 is more durable than commercial Pt/C (see Figure 8.14a). The relative current of the sample Co_xS_y@C-1000, which was measured by chronoamperometry at a constant potential of 0.80 V after 18000 s, is 92%, but for Pt/C the value is only 74%. Such a high durability of the Co_xS_y@C-1000 composite is due to the presence of the porous carbon matrix, which provides a conducting substrate and good electrochemical coupling between the substrate and oxygen molecules, and thus facilitates the ORR through the effective transportation of electrons between the oxygen molecules and the active sites of electrode. Moreover, the N and S co-doping on the porous carbon shell may also play a role to allow much stronger adsorption of oxygen molecules and higher activity for heterogeneous peroxide decomposition. In addition, the unique core-shell structure of Co_xS_y@C-1000 composites also offers a better conducting substrate and excellent electrochemical coupling between the substrate and oxygen molecules.

Methanol crossover is one of the major disadvantages for Pt/C catalyst in ORR.[161, 479] Thus, 1 M methanol was added into the 0.1 M KOH electrolyte solution to investigate the methanol tolerance for the as-synthesized composites under the same conditions as Pt/C. The results (see Figure 8.14b) show that the introduction of methanol causes a sharp decrease in the current density for the Pt/C catalyst. In contrast, methanol has negligible effect on the performance of Co_xS_y@C-1000 composite at the cathode. The high durability and remarkable methanol tolerance give Co_xS_y@C-1000 superiority over the commercial Pt/C and thus it is a promising electrocatalyst for the cathodic ORR.

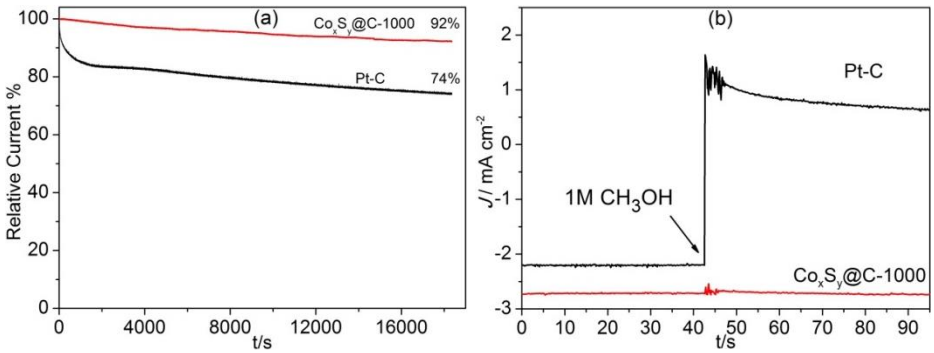

Figure 8.14 (a) Current–time chronoamperometric responses of Co_xS_y@C-1000 and Pt/C at 0.80 V. (b) Chronoamperometric responses of Co_xS_y@C-1000, and Pt/C at 0.80 V in 0.1 M KOH solution with the addition of 1 M methanol.

8.3.2 Oxygen evolution reaction

Excitingly, besides the high ORR activities, the Co_xS_y@C composites also exhibit excellent electrocatalytic performances in OER (Figure 8.15). Obviously, Pt/C is not a good catalyst for OER and much higher overpotential is required to achieve the required current density of 10 mA cm^{-2}. Compared with sample Co_xS_y@C-600, Co_xS_y@C-800 and Pt/C, the higher OER current density and an earlier onset of catalytic current are observed for sample Co_xS_y@C-1000, indicating that Co_xS_y@C-1000 is a highly active OER catalyst. As shown in Figure 8.15a, an anodic peak of Co_xS_y@C-1000 is seen at around 0.3 V preceding the oxygen evolution, which can be attributed to the fact that cobalt sulfide nanoparticles in Co_xS_y@C-1000 are partly oxidized into cobalt oxide, forming the cobalt oxide/cobalt sulfide complex species.[425] The current density of 10 mA cm^{-2} can be achieved at a small overpotential of 0.47 V vs RHE for Co_xS_y@C-1000, much lower than that of Co_xS_y@C-800 (0.63 V vs RHE), but slightly higher than that of IrO_2 (0.45V vs RHE). It is believed that the introduction of cobalt sulfide and N, S dopants results in the adjacent carbon atoms being positively charged, which can not only facilitate the adsorption of OH ions, but also promote the electron transfer between the catalyst surfaces and reaction intermediates.[423, 424, 480] Significantly, the potential acquired for the current density of 10 mA cm^{-2} of Co_xS_y@C-1000 is comparable to those of other reported OER catalysts.[274, 476, 477, 481-483] Furthermore, in the chronoamperometric test, the sample Co_xS_y@C-1000 can retain 80% its relative current after 10000 s (Figure 8.15b), implying high durability of the sample Co_xS_y@C-1000 in OER. Although oxidation may occur in Co-based OER catalysts [484, 485], it is believed that the surface property of the cobalt sulfide can be still maintained during the OER stability test, even though the cobalt sulfide was partly oxidized.[434] In the case of the sample Co_xS_y@C-1000, we believe the composite was largely maintained during the OER stability test since the unique core-shell structures of the composites can protect the catalytic active cobalt sulfide from oxidation. It is likely that the a small amount of cobalt sulfide nanoparticles without carbon shell protection may be partly oxidized in the process of OER at 1.75 V for 2000 s which causes the slight decay of catalytic performance.

In our work, the whole system of the cobalt sulfide/porous carbon materials is complicated as the as-synthesized composites containing different phases of cobalt sulfides, and nitrogen, sulfur (with different contents) co-doped porous carbons, and

even the structure of the composites can affect the ORR and OER performance. Therefore, it is difficult to analyse each contribution of the materials separately. But it is believed that the higher electrocatalytic activity is led by the whole system.[416, 449] Clearly, the sample Co_xS_y-1000 shows the best performance in ORR and OER. We believe that the main parameters that contribute to the higher electrocatalytic activity may be due to the highly crystalized cobalt sulfides combined with the synergistic effect between Co_xS_y and the porous carbons, the N and S doping may play auxiliary roles. Moreover, the protective porous carbon substrate (for catalytically active CoxSy) and the unique core-shell structure of CoxSy@C-1000 may contribute to the excellent electrochemical stability.

Considering the ease of preparation of Co_xS_y@C-1000 via a simple one-step sulfurization and carbonization of zeolitic imidazolate frameworks simultaneously, it is cost-effective and much cheaper than the benchmarked Pt/C catalyst,[408] the remarkable features of excellent activities, favourable kinetics and high electrochemical stabilities, the current Co_xS_y@C-1000 sample may be one of the most promising alternative bifunctional electrocatalysts in both ORR and OER.

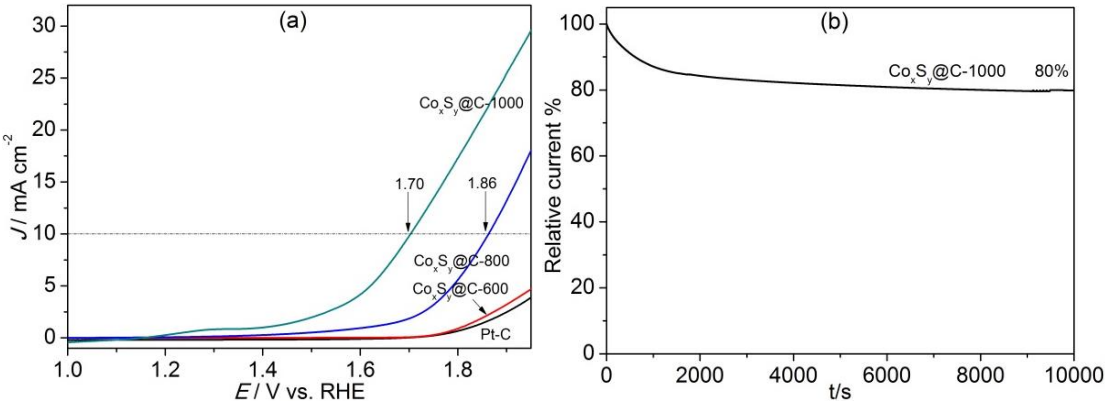

Figure 8.15 (a) Linear sweep voltammetry (LSV) polarization curves of Co_xS_y@C-600, Co_xS_y@C-800, Co_xS_y@C-1000, and Pt/C at 5 mV s^{-1} in N_2-saturated 0.1 M KOH solution. (b) Chronoamperometric response for Co_xS_y@C-1000 at 1.75 V.

8.3.3 Conclusions

In this part, we present a simple but efficient method that utilizes ZIF-67 as the precursor and template for the one-step generation of homogeneous dispersed cobalt sulfide/N,S Co-doped porous carbon nanocomposites as high-performance electrocatalysts. Due to the favourable molecular-like structural features and uniform dispersed active sites in the precursor, the resulting nanocomposites, possessing a

unique core–shell structure, high porosity, homogeneous dispersion of active components together with N and S-doping effects, not only show excellent electrocatalytic activity towards ORR with the high onset potential (around 0.924 V vs. 0.944 V for the benchmark Pt/C catalyst) and four-electron pathway and OER with a small overpotential of 0.47 V for 10 mA cm^{-2} current density, but also exhibit superior stability (92%) to the commercial Pt/C catalyst (74%) in ORR and promising OER stability (80%) with good methanol tolerance. Our findings suggest that the transition metal sulfide– porous carbon nanocomposites derived from the one-step simultaneous sulfurization and carbonization of zeolitic imidazolate frameworks are excellent alternative bifunctional electrocatalysts towards ORR and OER in the next generation of energy storage and conversion technologies.

8.4 Characterizations of cobalt-nickel sulfides/N, S co-doped porous carbon composite

The parental ZIF-67 precursor exhibits a typical rhombic dodecahedron with an average particle size of 350 nm (Figure 8.16a), which is consistent with previous report.[448, 486] Interestingly, with the introduce of increased Ni species, the particles for the Ni-substituted ZIF-67 precursors turn to be sphere-like shapes with an average particle size of 150 nm to 0.5 μm (Figure 8.16b and c). Clearly, the addition of Ni can remarkably affect and modulate the morphology of ZIF-67, which also suggests that Ni atoms may partially substitute Co atoms in ZIF-67 frameworks.[487] After the sulfurization and carbonization process in a hydrogen sulfide atmosphere, the structure and morphology of the Ni-Co based sulfides/N, S co-doped carbon nanocomposites samples, Ni_1Co_4S@C-600, Ni_1Co_4S@C-800 and Ni_1Co_4S@C-1000, are first investigated by transmission electron microscopy (TEM). As presented in Figure 8.17, the resulting composite Ni_1Co_4S@C-600 maintained sphere-like particles with a smaller size due to the shrinkage during the annealing process. For Ni_1Co_4S@C-800, the particles hold the original shapes of precursor with some deformation. However, for Ni_1Co_4S@C-1000 sample, the original morphology of precursor was completely damaged. The particle size of sulfides grew from 5 to 50 nm with the increase of sulfurization temperature from 600 to 1000 ^oC (shown in Figure 8.17a, c and e). The corresponding diffraction intensity of selected area electron diffraction (SAED) patterns is also enhanced due to the increased sulfurization and carbonization temperature resulting in the improved crystallization

of cobalt sulfides. It is interesting to note that multiwall carbon nanotubes (CNT) or carbon onions were also observed via high resolution TEM in sample Ni_1Co_4S@C-1000 (Figure 8.17f), which may be due to the catalytic effect of metallic cobalt and nickel during the graphitization stage. [250, 409] A carbon shell with thickness of 2 nm was also formed around the sulfide crystals. In addition, the interlayer spacing was measured as 0.178 nm, which is lower than the theoretical value of 0.194 nm for $Co_{1-x}S$. The observed decreased interlayer spacing for Ni-containing $Co_{1-x}S$ is due to the fact that Ni atoms are partially substituted into the cobalt sulfides and the atomic and ionic radius of Ni is smaller than that of Co.

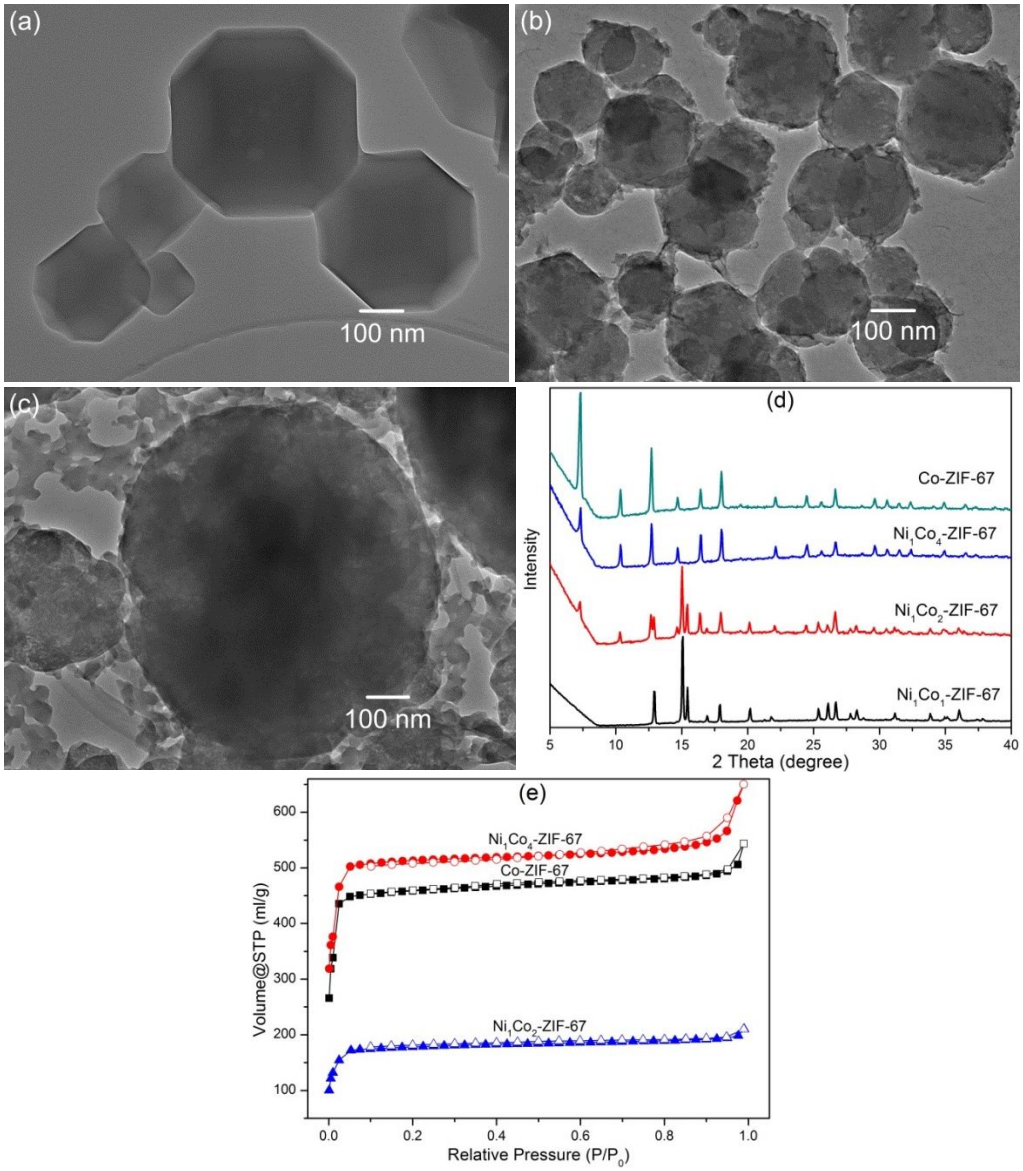

Figure 8.16 (a, b, c) TEM images, (d) powder XRD pattern, (e) nitrogen sorption isotherms for the parental ZIF-67 materials: Co-ZIF-67 (ZIF-67), Ni_1Co_4-ZIF-67, and Ni_1Co_2-ZIF-67.

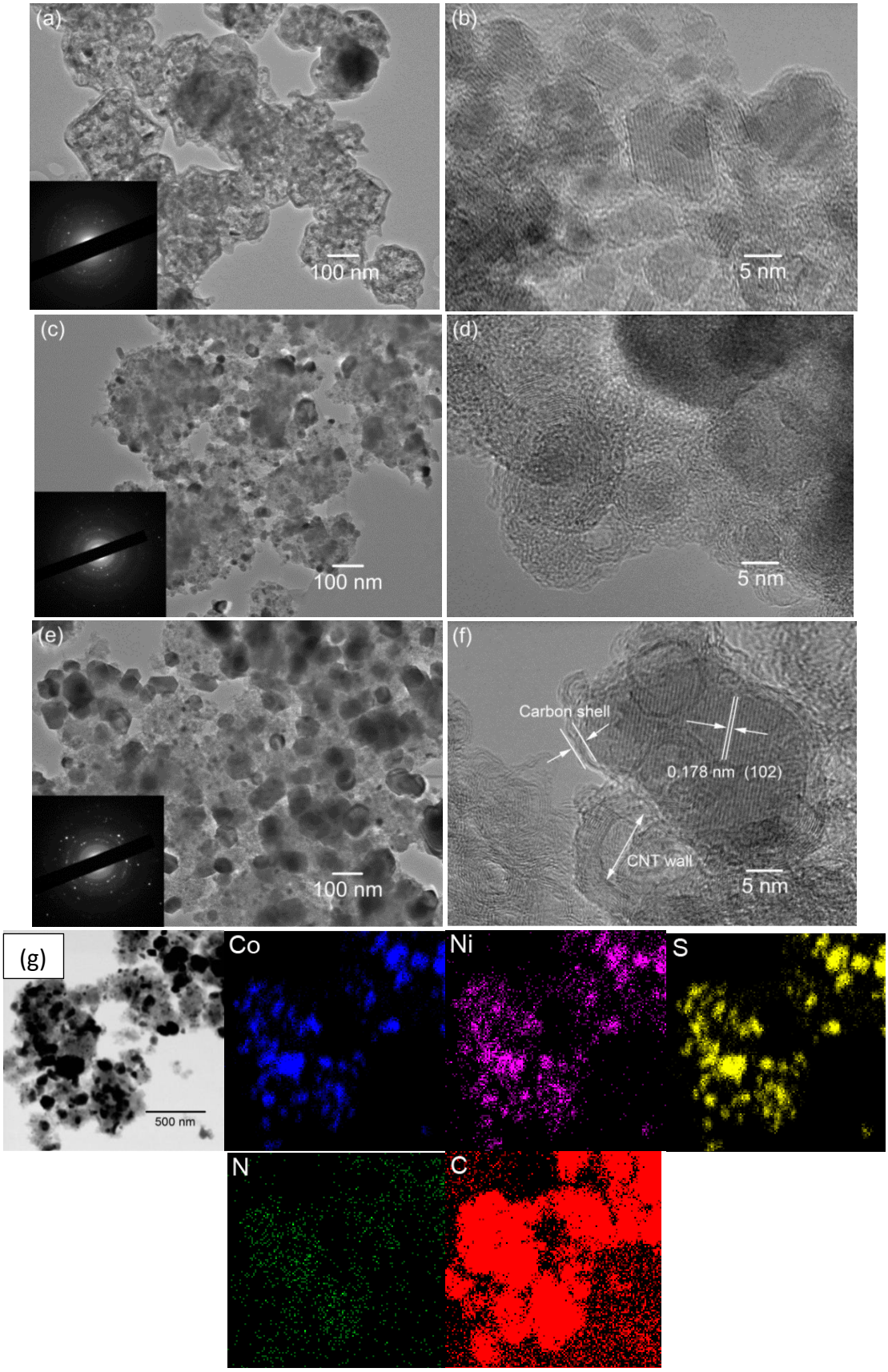

Figure 8.17 TEM images of (a-b) Ni_1Co_4S@C-600; (c-d) Ni_1Co_4S@C-800 and (e-f) Ni_1Co_4S@C-1000. STEM image and elemental mapping for sample Ni_1Co_4S@C-1000.(g) Inset in (b), (d) and (f) is SAED patterns for corresponding sample.

Scanning transmission electron microscope (STEM) combined with an elemental mapping technique was used to ascertain the distribution of the Ni-Co based sulfide nanoparticles in the composite samples. Take sample Ni_1Co_4S@C-1000 as an example, element Co, Ni, and S (shown in Figure 8.17g) exhibit similar elemental mapping patterns to their selected area of STEM image, indicating that the Ni-Co based sulfide nanoparticles were uniformly dispersed in the carbon matrix. N is also observed in the elemental mapping, where N content is much less than that of C, possibly due to the high volatility of N species at high annealing temperature. These elements are also confirmed by using linear EDX analysis in STEM measurements (shown in Figure 8.18 and Figure 8.19). The elemental analysis (shown in Figure 8.19) illustrates that Ni_1Co_4S@C-1000 possesses only 2.25 wt% Ni species.

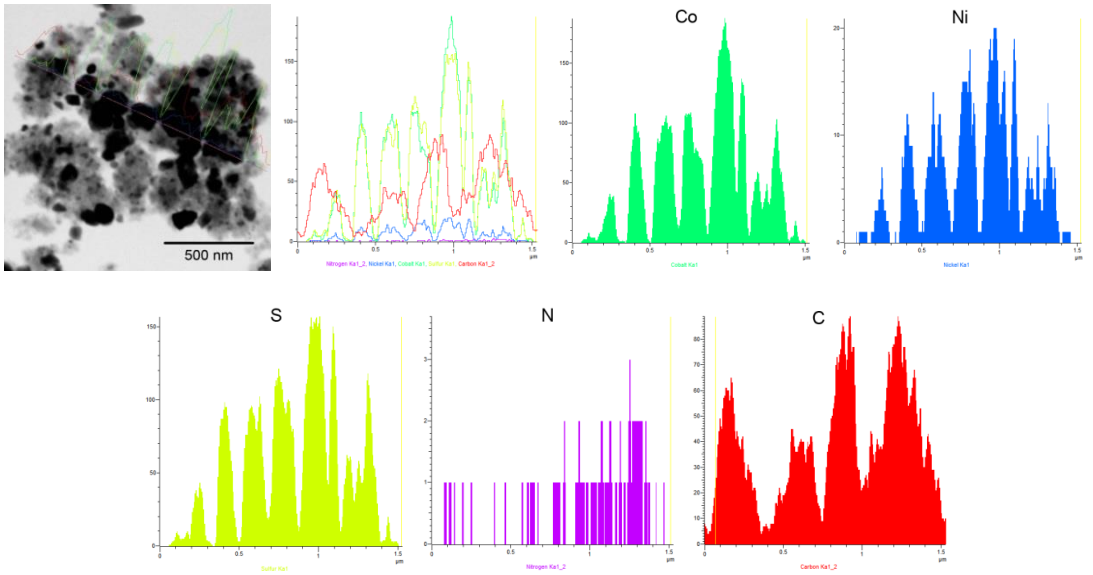

Figure 8.18 STEM image and linear EDX for sample Ni_1Co_4S@C-1000. Signals Co, Ni, S, N and C are clearly detected from the sample.

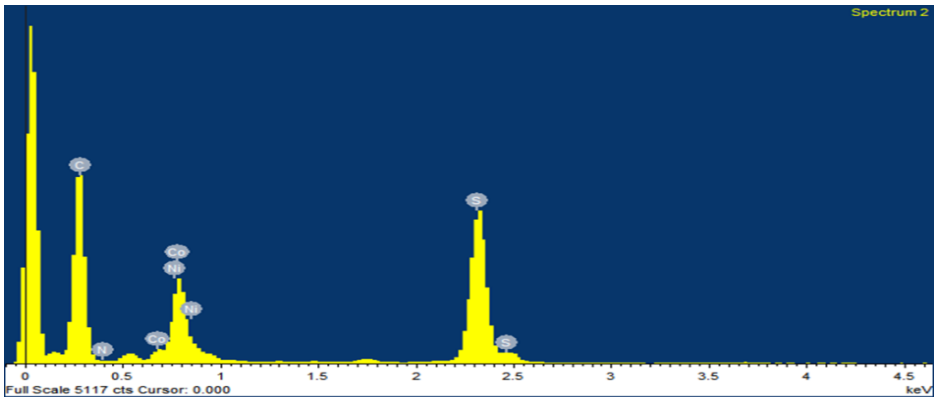

Element	Peak Area	Area Sigma	k factor	Abs Corrn.	Weight%	Weight% Sigma	Atomic%
C K	9606	166	2.504	1.000	45.91	0.53	75.39
N K	21	52	3.139	1.000	0.13	0.31	0.18
S K	12931	210	0.959	1.000	23.67	0.37	14.56
Co K	11755	172	1.261	1.000	28.30	0.40	9.47
Ni K	930	75	1.268	1.000	2.25	0.18	0.76
Totals					100.00		

Figure 8.19 EDX spectrum and element table for sample Ni_1Co_4S@C-1000. Signals Co, Ni, S, N and C are clearly detected from the sample.

The elemental composition and chemical state of the Ni_1Co_4S@C composites have been further investigated by X-ray photoelectron spectroscopy (XPS) analysis, and the corresponding results are presented in Figure 8.20. As shown in Figure 8.20a, the element survey illustrates the presence of Co, Ni, S, C, and N in all the Ni_1Co_4S@C composites. For the spectrum of Co 2p (shown in Figure 8.20c), the sample Ni_1Co_4S@C-600 shows two spin-orbit doublets at 781.2 and 796.9 eV, which means the existence of Co^{2+} oxidation state. The sample Ni_1Co_4S@C-800 and Ni_1Co_4S@C-1000 not only exhibit the two spin-orbit doublets at 781.2 and 796.9 eV, but also show doublets at 778.4 and 793.5 eV. This indicates the co-existence of Co^{2+} and Co^{3+} oxidation states in sample Ni_1Co_4S@C-800 and Ni_1Co_4S@C-1000.[448, 453, 477, 488] In Ni 2p spectrum (shown in Figure 8.20d), the sample Ni_1Co_4S@C-600 shows two peaks at around 855.6 and 873.3 eV in Ni $2p_{3/2}$ and Ni $2p_{1/2}$, respectively, corresponding to the characteristic of Ni^{2+}.[489-491] Apart from the Ni^{2+} state, Ni 2p spectrum of the sample Ni_1Co_4S@C-800 and Ni_1Co_4S@C-1000 also show the binding energy at 856.2 eV in Ni $2p_{3/2}$ and 870.6 eV in Ni $2p_{1/2}$, which are characteristic of Ni^{3+},[477] indicating the co-existence of Ni^{2+} and Ni^{3+} states in sample Ni_1Co_4S@C-800 and Ni_1Co_4S@C-1000. In S 2p region (shown in Figure 8.20e), two peaks located at 161.4 and 162.5 eV can be found due to the spin−orbit coupling in metal sulfide,[456, 477] and the peak at 163.5 eV suggested the existence of covalent S-C bonding.[458, 476, 492] In addition, another two peaks at around 168.5 and 169.5 eV indicate the formation of inconsequential amount of sulfide compounds during the carbonization and sulfurization process.[462, 493] As shown in Figure 8.20f, the N 1s spectrum can be deconvoluted into four peaks, which correspond to the pyridinic-N

(397.8 eV), Co-N (399.1 eV), pyrrolic-N (400.1 eV), and graphitic-N (401.8 eV), respectively.[274, 420] It can be seen that low S and N content remaining in the Ni_1Co_4S@C-1000 sample, which may be due to the high volatility of S, N species under high temperature. Based on XPS analysis, the near-surface of the sample Ni_1Co_4S@C-1000 is composed of Co^{2+}, Co^{3+}, Ni^{2+}, Ni^{3+} and S^{2-}. Furthermore, combined the XPS analysis with the elemental mapping results of Ni_1Co_4S@C-1000, it is clear that Ni-Co based sulfides have been successfully prepared in the simple one-step sulfurization and carbonization process.[494]

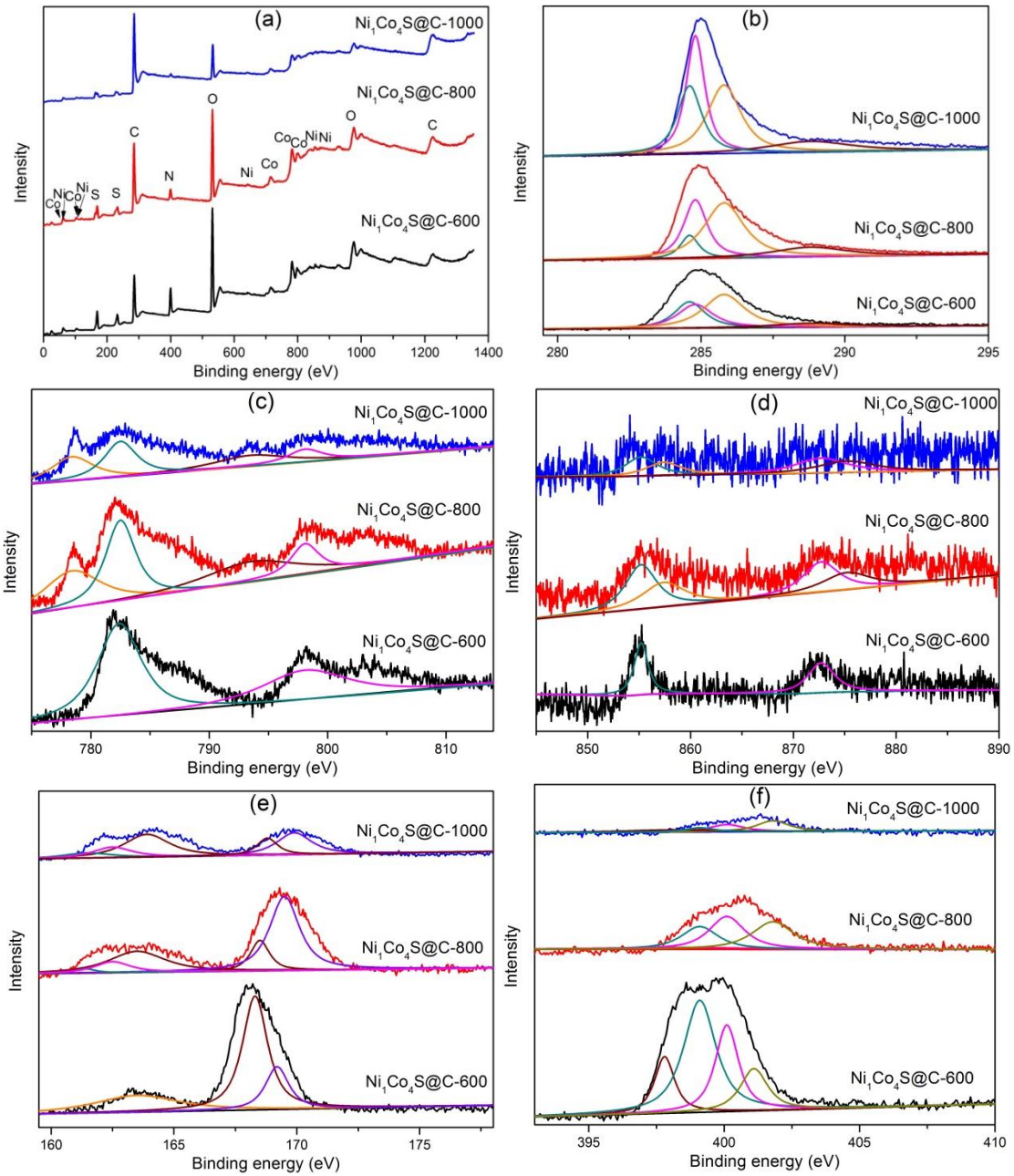

Figure 8.20 (a) Element survey by XPS and high-resolution XPS spectrum of (b) C 1s, (c) Co 2p, (d) Ni 2p, (e) S 2p and (f) N 1s for the as-synthesized composites.

The crystal structures of the as-synthesized Ni_1Co_4S@C composites were further characterized by XRD. Different from the sodalite structure of Ni-substituted ZIF-67 precursor with molar ratio of n(Ni)/n(Co)=1/4 (Figure 8.16d), the XRD patterns of the Ni_1Co_4S@C composites (shown in Figure 8.21a) indicate that they mainly contain $Co_{1-x}S$ (ICDD PDF #42-0826) with hexagonal structure in the P63/mmc (no. 194) space group.[474, 495] The XRD peaks for the $Co_{1-x}S$ phase became more intense and sharper with the increase of sulfurization temperature. No obvious diffraction peaks from Ni were detected in the XRD results, probably due to the fact that only very small amount of Ni atoms were substituted into cobalt sulfides. The carbon matrix of as-synthesized Ni_1Co_4S@C samples is supported by Raman spectra (shown in Figure 8.21b), where the two broad bands at 1340 and 1590 cm^{-1} are assigned to the typical D and G band of amorphous carbon, respectively. The I_D/I_G value of 1.09 for sample Ni_1Co_4S@C-1000 is relative higher than that of 1.05 and 1.01 for sample Ni_1Co_4S@C-800 and Ni_1Co_4S@C-600, respectively. The higher I_D/I_G value indicates that the sample Ni_1Co_4S@C-1000 formed more abundant defects under higher carbonization temperature (1000 ^oC).[496]

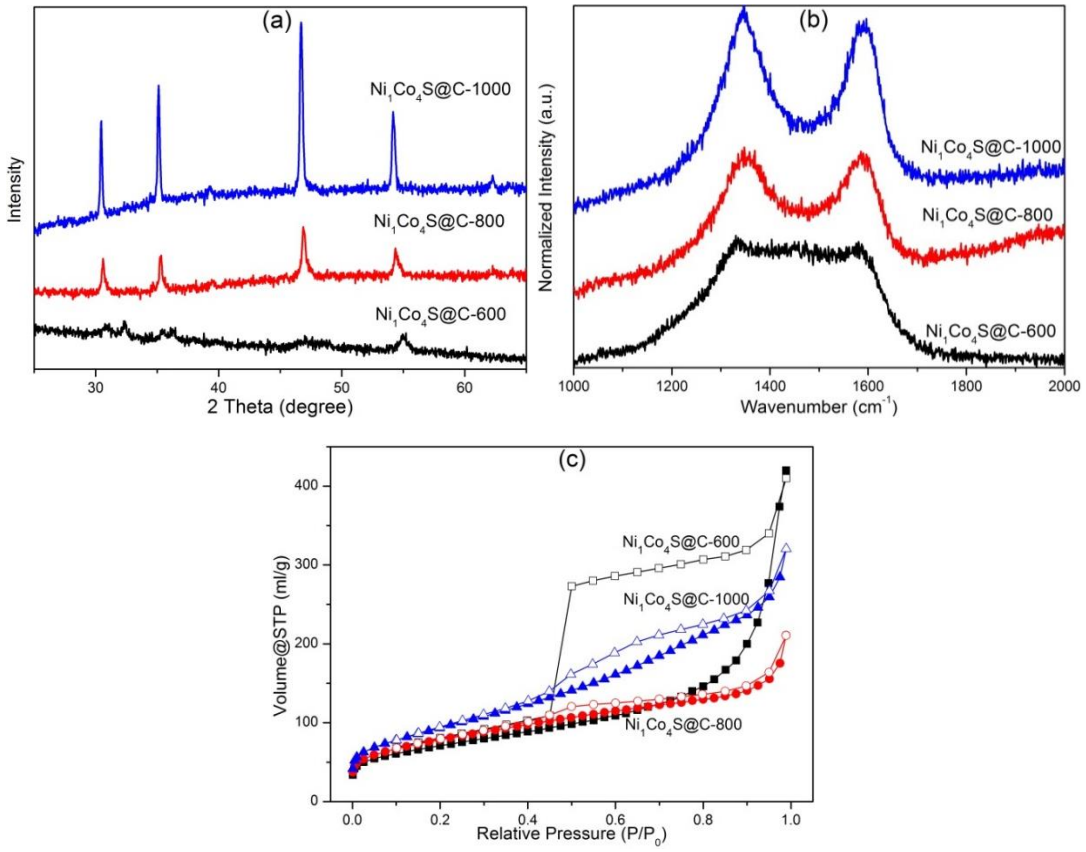

Figure 8.21 (a) XRD patterns, (b) Raman spectra, and (c) N_2 sorption isotherms of the as-synthesized Ni_1Co_4S@C composites.

The textural properties of the as-synthesized Ni_1Co_4S@C composites were analysed by N_2 sorption at -196 ^oC. As shown in Figure 8.21c, the sample Ni_1Co_4S@C-600 exhibits a large hysteresis loop between its adsorption and desorption branches. The other two samples Ni_1Co_4S@C-800, and Ni_1Co_4S@C-1000, both present a small hysteresis loop between its adsorption and desorption branches, indicating the existence of mesoporous structure due to the voids between particles. Sample Ni_1Co_4S@C-600, Ni_1Co_4S@C-800 and Ni_1Co_4S@C-1000 possesses a specific surface area of 253, 283, and 340 $m^2\ g^{-1}$ and pore volume of 0.68, 0.33, and 0.50 $cm^3\ g^{-1}$, respectively (Table 8.2). These value are much lower than those of the Ni-substituted ZIF-67 precursors (Figure 8.16e), which is probably due to the dominance of the sulfides weight percentage in the Ni_1Co_4S@C composites and the damage of the porous structures of ZIF-67 during the sulfurization/carbonization process.

TGA-MS was utilised to evaluate the thermal stabilities of the as-synthesized Ni_1Co_4S@C composites in air. As shown in Figure 8.22a, the TGA profiles of all the Ni_1Co_4S@C composites exhibit a minor weight loss event below 100 ^oC due to the removal of the water (shown in Figure 8.22c), followed by a small weight increase in the temperature range of 300-500 ^oC, due to the oxidation of sulfides to high valence states. Two major weight loss events at around 450-500 and 700 ^oC can be observed for all the samples, corresponding to the burn off of the N,S Co-doped carbon species and the decomposition of the sulfides, respectively, which are confirmed by the emission of CO_2, NO_2 and SO_2 in their corresponding MS signals (Figure 8.22b, d and e). The sample Ni_1Co_4S@C-600 shows a different weight loss event in the temperature range of 300-500 ^oC, which is possibly due to the burn off incomplete carbonized organic ligands from precursors.

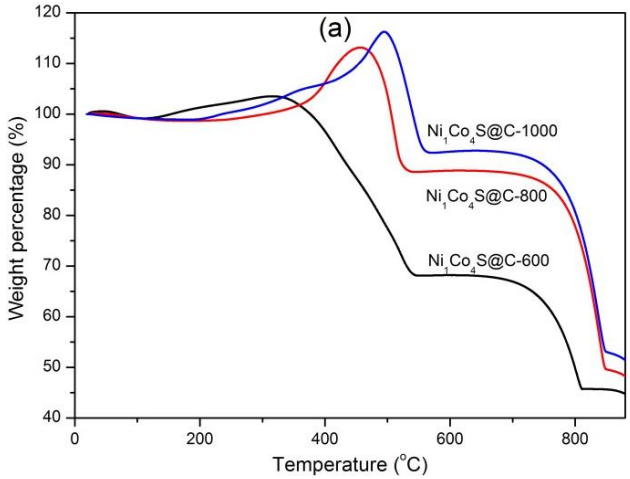

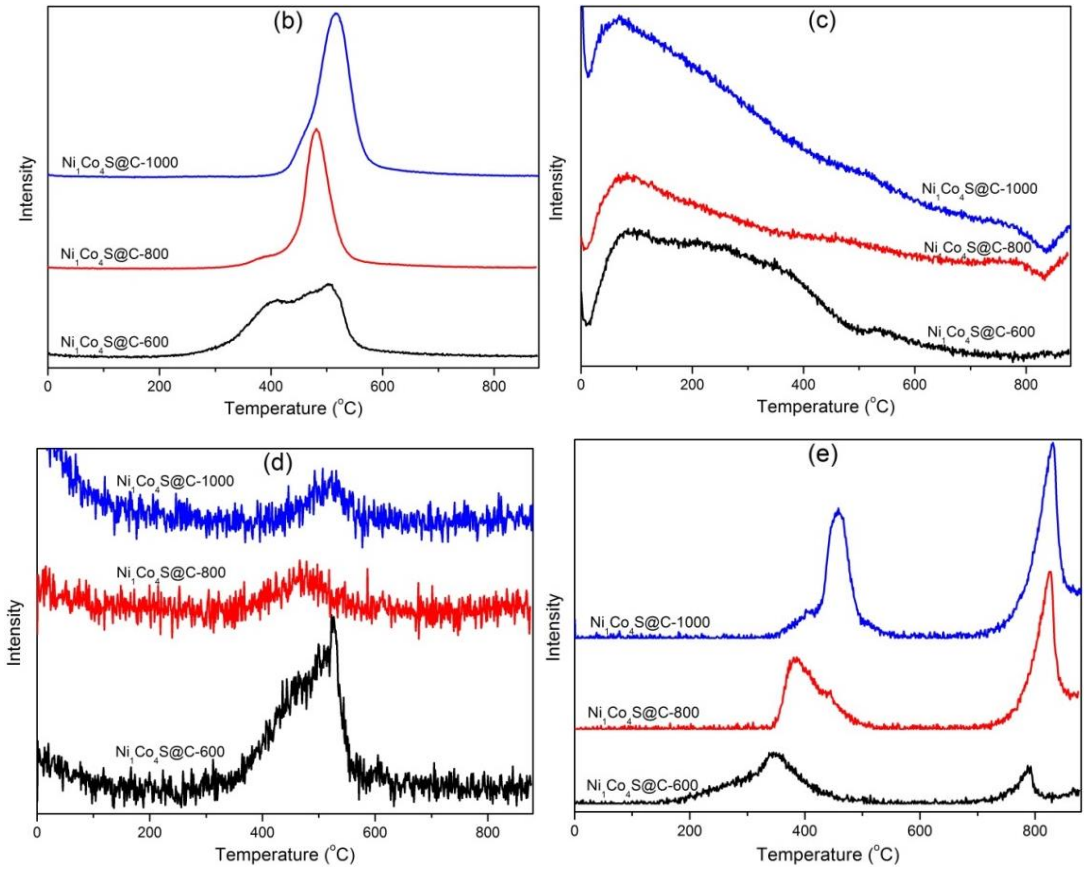

Figure 8.22 (a) TGA and their corresponding MS curves of (b) CO_2, (c) H_2O, (d) NO_2, and (e) SO_2 for the as-synthesized Ni_1Co_4S@C composites.

Table 8.2 Comparison of the textural properties and the OER catalytic performances of the as-synthesized Ni_1Co_4S@C composites and IrO_2/C

Materials	Surface area ($m^2 g^{-1}$)	Pore volume ($cm^3 g^{-1}$)	Potential (V vs. RHE) acquired for the current density of 10 mA cm^{-2}	Tafel slope (mV dec^{-1})	Onset potential (V vs. RHE)
Ni_1Co_4S@C - 600	253	0.68	1.85	108	1.62
Ni_1Co_4S@C - 800	283	0.33	1.66	99	1.48
Ni_1Co_4S@C - 1000	340	0.50	1.52	68	1.44
IrO_2/C	N/A	N/A	1.59	90	1.42

8.5 Applications of cobalt-nickel sulfides/N, S co-doped porous carbon composites

8.5.1 Oxygen evolution reaction

The electrocatalytic activities of the as-synthesized Ni_1Co_4S@C composites for OER were evaluated in 0.1 M KOH solution (Figure 8.23). In our previous study, the samples without adding nickel were also evaluated the OER performance under the same condition. In details, the samples which were sulfurized at 600, 800, and 1000 ^oC, exhibited an onset potential of 1.74, 1.67, and 1.47 V, respectively, and they required >1.96, 1.86, and 1.70 V at the current density of 10 mA cm^{-2}, respectively.[448] The linear sweeps of all the Ni_1Co_4S@C composites and IrO_2/C in an anodic direction are shown in Figure 8.23a. The sample Ni_1Co_4S@C-1000 demonstrates a smaller onset potential of 1.44 V than that of Ni_1Co_4S@C-800 (1.48 V) and Ni_1Co_4S@C-600 (1.62 V), respectively. It is worth noting that the onset potential of Ni_1Co_4S@C-1000 is only marginally higher than that of IrO_2/C catalyst (1.42 V). Moreover, the OER current density of Ni_1Co_4S@C-1000 is higher than that of Ni_1Co_4S@C-600, Ni_1Co_4S@C-800 and even IrO_2/C over the whole potential range, indicating that the sample Ni_1Co_4S@C-1000 is a highly active OER electrocatalyst. In addition, sample Ni_1Co_4S@C-1000 also exhibits much higher OER performances than IrO_2/C even in neutral and acidic solutions (shown in Figure 8.24), suggesting that the composite Ni_1Co_4S@C-1000 is superior to other relevant composites and IrO_2/C in all pH value ranges.

The operating potentials to deliver a 10.0 mA cm^{-2} current density, which is a metric relevant to solar fuel chemistry,[497] was further compared. Ni_1Co_4S@C-1000 holds a current density of 10.0 mA cm^{-2} at 1.52 V (Figure 8.23a), which is comparable to, or even better than the value of many other reported catalysts.[483, 498, 499] In addition, the excellent OER activity of Ni_1Co_4S@C-1000 is not only better than monometallic cobalt sulfides/N, S co-doped carbon (Co_xS_y@C-1000, 1.70 V, 0.1 M KOH)[448] and other non-metal/carbon catalysts,[262, 500] but also superior to that of many bimetallic oxides/sulfides reported to date, such as $Zn_xCo_{3-x}O_4$ nanowire (1.55 V, 1.0 M KOH),[501] $NiFeO_x$ film (> 1.58 V, 1.0 M NaOH),[497] and $Ni_xCo_{3-x}O_4$ nanowire (~1.60 V, 1.0 M NaOH).[502] Clearly, Ni_1Co_4S@C-1000 is one of best active electrocatalysts for OER.[262, 448, 497, 499, 501-506]

To examine the kinetics for catalytic OER, the linear fitting of the Ni_1Co_4S@C-1000 Tafel plot shows a low Tafel slope of 68 mV dec^{-1}, even smaller than that of IrO_2/C (90 mV dec^{-1}) (Figure 8.23b), suggesting the outstanding intrinsic OER kinetics. The reason why Ni_1Co_4S@C-1000 exhibits a lower Tafel slope is probably due to a strong affinity for OH^- intermediates on the active sites of Ni_1Co_4S@C-1000.[507] The introduction of nickel promoted cobalt sulfide and N, S dopants results in the adjacent carbon atoms positively charged, which can facilitate the adsorption of OH^-, and also promote the electron transfer between the surfaces of Ni_1Co_4S@C-1000 and reaction intermediates. The decreased Tafel slope for Ni_1Co_4S@C-1000 compared with IrO_2/C suggests an efficient OER process, which is in consistent with the higher current density for Ni_1Co_4S@C-1000 relative to IrO_2/C. In OER, the oxidation of hydroxide ions produces O_2 and H_2O in alkaline solution, where the half reaction is $4OH^- \rightarrow 2H_2O + O_2 + 4e^-$. The comparison of the OER catalytic performances of the as-synthesized Ni_1Co_4S@C composites and IrO_2/C is listed in Table 8.2.

Catalyst durability towards OER is another major challenge for energy conversion and storage. As shown in Figure 8.23c, the sample Ni_1Co_4S@C-1000 exhibits superior durability to the IrO_2/C catalyst, with a small decay (10%) in OER activity after continuous operation at 1.6 V for 6000 s, whereas the current density for IrO_2/C catalyst decreased up to 50% under the same conditions. Moreover, sample Ni_1Co_4S@C-1000 can still hold up to 77 % OER activity after continuous operation for 6000 s at potential as high as 1.8 V, but the IrO_2/C catalyst has a 54% decay of activity under the similar operation conditions. The excellent durability of Ni_1Co_4S@C-1000 for OER is probably due to the protection of the doped carbon matrix surrounding the sulfides nanoparticles.[262, 508] In addition, a further stability test (Figure 8.23d) shows that Ni_1Co_4S@C-1000 exhibits a similar I-V curve to the initial one with only a small drop of the current density after 1000 scanning cycles. This is probably due to the fact that the carbon matrix could be partially oxidized at higher potential (e. g. 1.8 V), which can further result in the sulfide nanoparticles in Ni_1Co_4S@C-1000 becoming partly oxidized.[448]

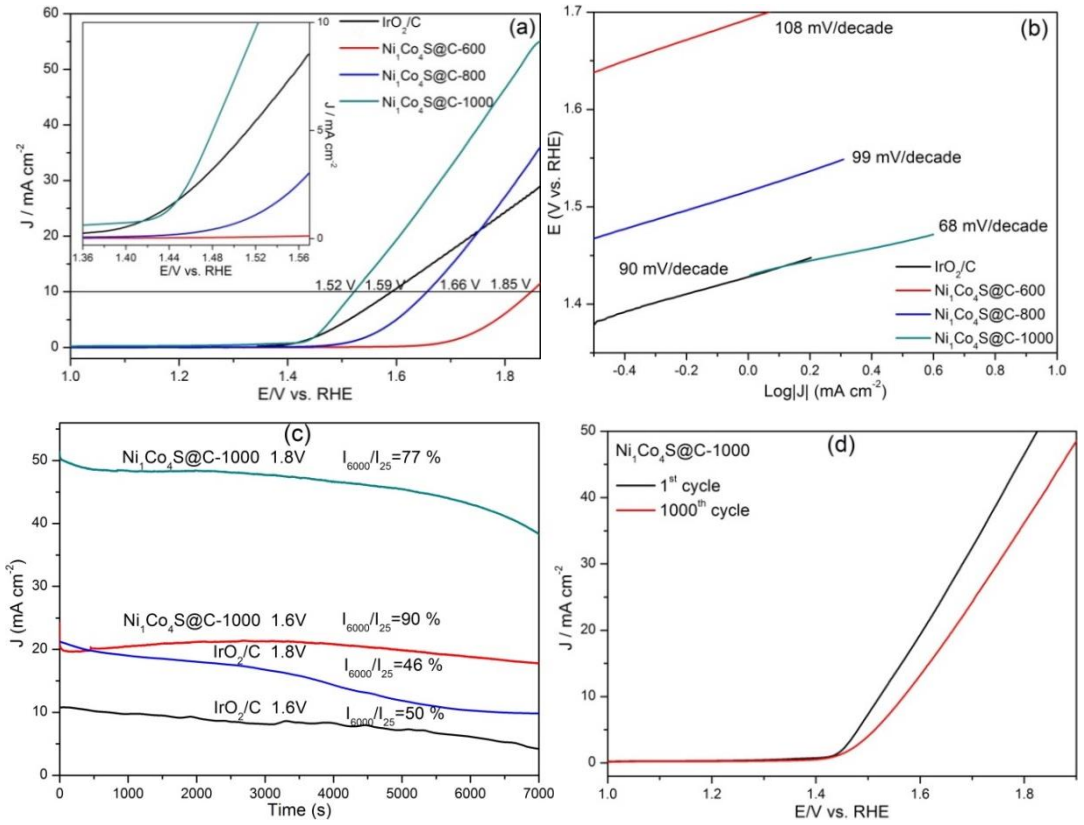

Figure 8.23 (a) Polarization curves of OER on IrO_2/C and the as-synthesized Ni_1Co_4S@C composites in 0.1 M KOH solution, respectively. (b) Corresponding Tafel plot (potential versus log current) derived from (a). (c) Current–time plot of the IrO_2/C and Ni_1Co_4S@C-1000 electrode with the applied potential at 1.6 V and 1.8 V (vs. RHE) under the same conditions. (d) Polarization curves of Ni_1Co_4S@C-1000 before and after 1000 scan cycles at 5 mV s^{-1}.

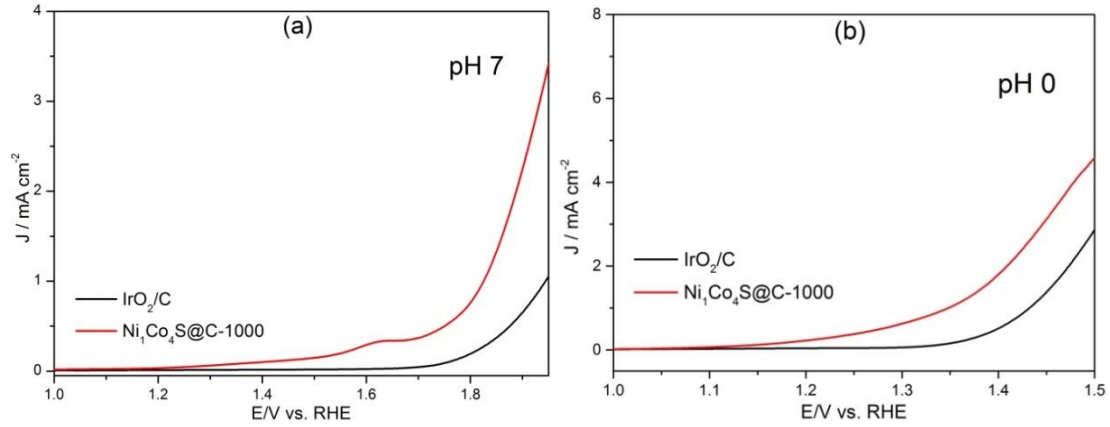

Figure 8.24 Linear sweep voltammetry curves of Ni_1Co_4S@C-1000 and IrO_2/C for OER in (a) neutral PBS (phosphate buffered saline) solution and (b) acidic 0.5 M H_2SO_4 solution.

The excellent electrocatalytic OER performance of composite Ni_1Co_4S@C-1000 can be attributed to several factors. First, the use of a molecular-like MOF as the precursor can afford nickel promoted cobalt sulfide nanoparticles homogeneously embedded into porous carbon, leading to a structure with strong interaction between metal sulfides and carbon matrix, with remarkably improved conductivity. Second, the high surface area of the composite can provide better accessible and enhanced utilization of electrocatalytic active sites. Third, the core-shell carbon structure can protect the sulfide nanoparticles from degradation and improve the stability of the electrocatalyst. Fourth, in composite Ni_1Co_4S@C-1000, both Ni and Co are generally considered as the active centres for OER because of their suitable binding energy to oxygen intermediates,[509-511] where transition metal chalcogenides indeed showed high OER activities.[490, 506] Fifth, the N,S Co-doped carbon not only acts as a conduction path for shuttling electrons but also serves as an active site for OER.[262] Last but not least, the synergetic effect at the interfaces of nanostructured sulfides and the N, S co-doped carbon matrix can also inevitably play an important role.

The reaction reversibility initiated on an oxygen evolution electrode is an important parameter for the regenerated fuel cells and rechargeable metal−air batteries.[504] Figure 8.25 presents the polarization curve of Ni_1Co_4S@C-1000 which was measured in the whole region of OER and ORR (Oxygen Reduction Reaction). The overall oxygen electrode activity can be evaluated by the difference between OER and ORR metrics, with the equation $\Delta E = E_{j=10} - E_{1/2}$. The smaller value of ΔE, the better reversible oxygen electrode performance.[512, 513] Sample Ni_1Co_4S@C-1000 exhibits a half-wave potential ($E_{1/2}$) of 0.60 V in the ORR region (shown in inset Figure 8.25) and a potential of 1.52 V at current density of 10.0 mA cm^{-2} ($E_{j=10}$) in the OER region. As a result, Ni_1Co_4S@C-1000 possesses a ΔE value of 0.92 V, which is comparable to, or even lower than other reported active reversible oxygen electrodes, including $Pt/CaMnO_3$ (ΔE = 1.01 V)[512] and Co_3O_4/N-doped carbon (ΔE = 0.86 V).[513] It is, therefore, that Ni_1Co_4S@C-1000 is a promising reversible oxygen electrode material. In addition, the value of electron transfer numbers (n) for ORR derived from the slope of the K-L plot (Figure 8.26) at various potentials is about 4,[473] suggesting that the ORR proceeded mainly through a desirable four-electron pathway.

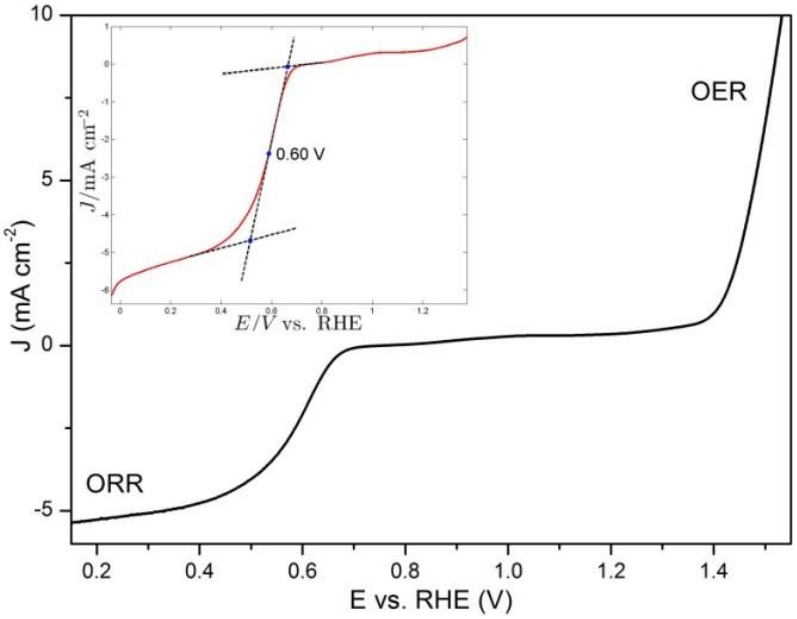

Figure 8.25 Polarization curve measured in O_2-saturated 0.1 M KOH solution for Ni_1Co_4S@C-1000 in the whole region of OER and ORR.

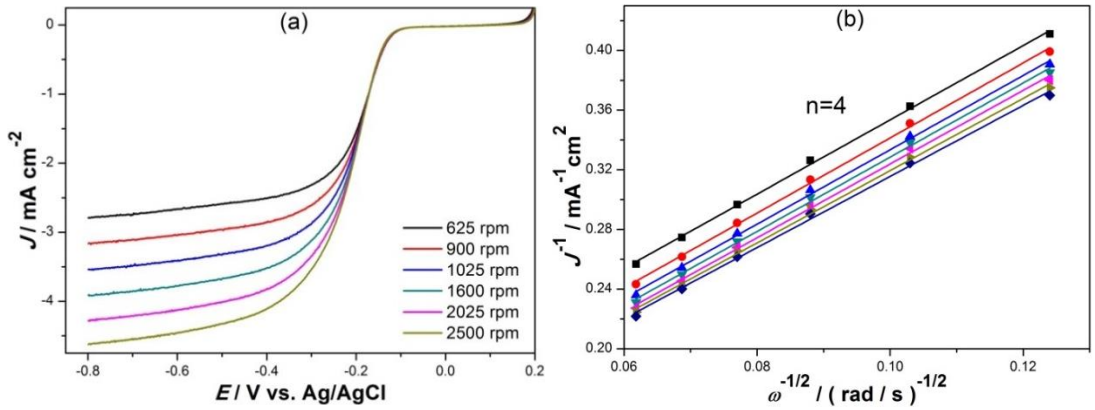

Figure 8.26 (a) ORR polarization curves of Ni_1Co_4S@C-1000 at different rotating speeds and (b) corresponding K-L plots of Co_xS_y@C-1000 at different potentials.

To illustrate the effect of Ni content on the electrocatalytic performance, Ni-substituted ZIF-67 with variable Ni:Co molar ratio was produced first. XRD results demonstrated that with increase of the Ni content gradually, the resulting materials changed from pure ZIF-67 phase for Ni:Co molar ratio of 1:4 to ZIF-67 together with a new phase when the Ni:Co molar ratio is 1:2 (Figure 8.16a), and eventually the ZIF-67 phase disappeared when the Ni:Co molar ratio is 1:1 (Figure 8.16a). In addition, the specific surface area of the material with the Ni:Co molar ratio of 1:2 is only 602

m^2 g^{-1} (Figure 8.16b), which is only *ca.* 35% of the pure ZIF-67 and Ni_1Co_4-ZIF-67, implying the remarkably low porosity of the new formed phase. The metal sulfides/carbon composites derived from Ni_1Co_2-ZIF-67 in H_2S atmosphere at different temperatures exhibited similar XRD, Raman and porosity results to the composites originated from Ni_1Co_4-ZIF-67 (Figure 8.27 and 8.28), whereas the sizes of spherical particles for the Ni_1Co_2S@C products is bigger than those of Ni_1Co_4S@C particles (Figure 8.29). Electrochemical OER performance of the Ni_1Co_2S@C composites in Figure 8.30a indicated that sample Ni_1Co_2S@C-600 shows low OER activity, while sample Ni_1Co_2S@C-800 and Ni_1Co_2S@C-1000 exhibit relative high OER activities, which is in consistent with their Tafel slopes (Figure 8.30b). However, it is worth noting that the OER performances of all Ni_1Co_2S@C samples are generally inferior to that of IrO_2/C and the sample Ni_1Co_4S@C-1000. Clearly, the introduce of increased amount of Ni into the precursors result in the formation of a non-pure ZIF-67 phase with relative low porosity; consequently, metal sulfides/carbon composites with inhomogeneous dispersion of the sulfides particles were generated, which leads to the poor OER performances of Ni_1Co_2S@C compared to that of Ni_1Co_4S@C-1000.

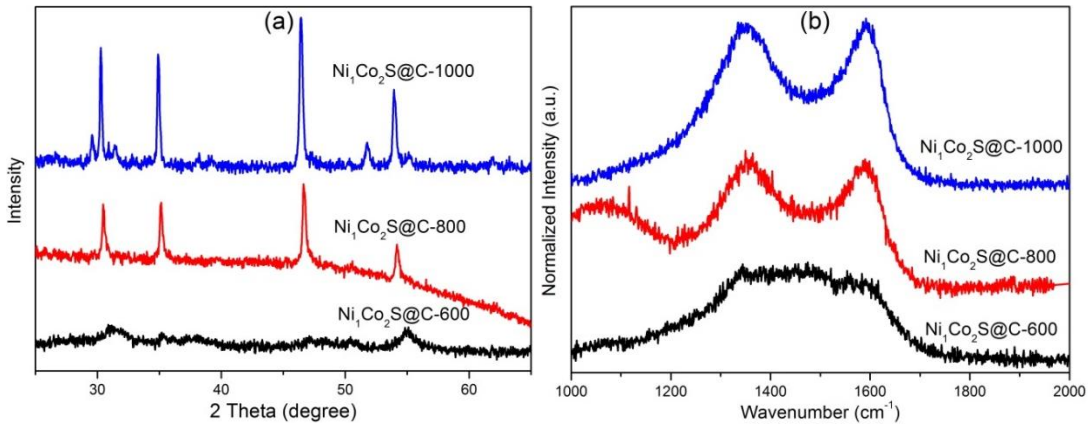

Figure 8.27 (a) XRD patterns and (b) Raman spectra of the as-synthesized Ni_1Co_2S@C composites.

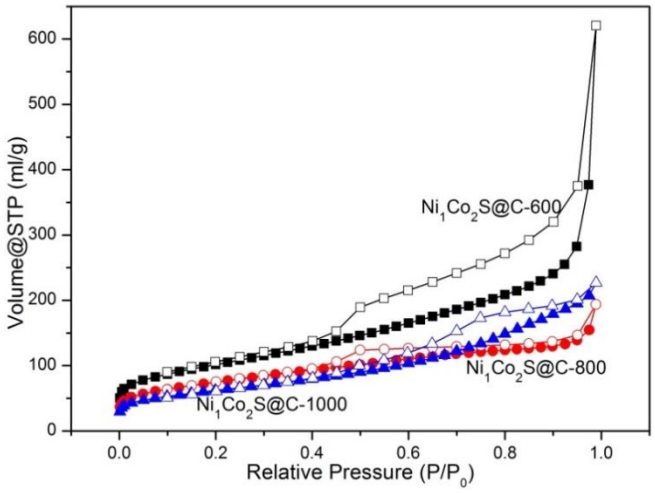

Figure 8.28 N_2 sorption isotherms of the as-synthesized Ni_1Co_2S@C composites.

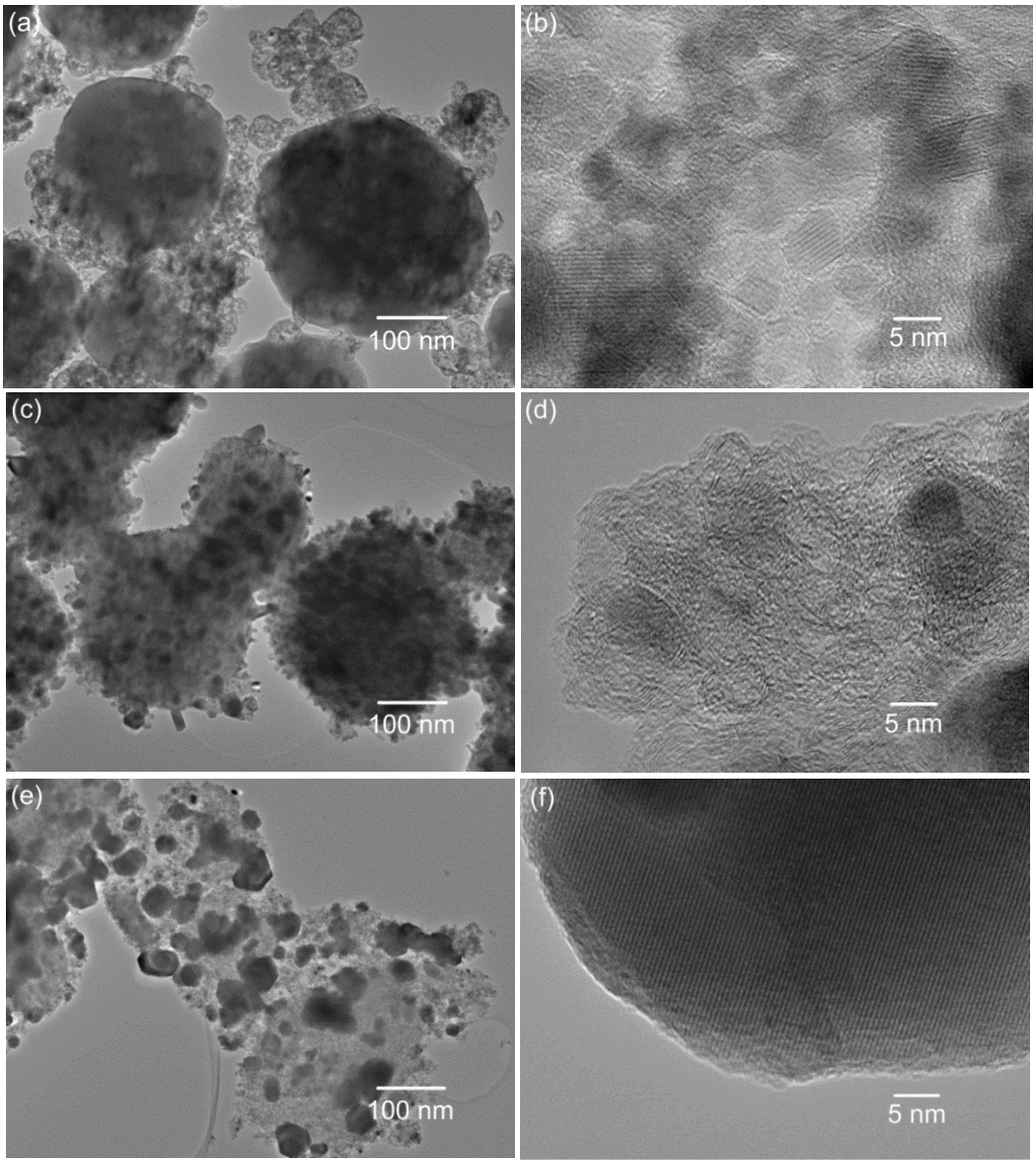

Figure 8.29 TEM images of (a-b) Ni_1Co_2S@C-600; (c-d) Ni_1Co_2S@C-800 and (e-f) Ni_1Co_2S@C-1000.

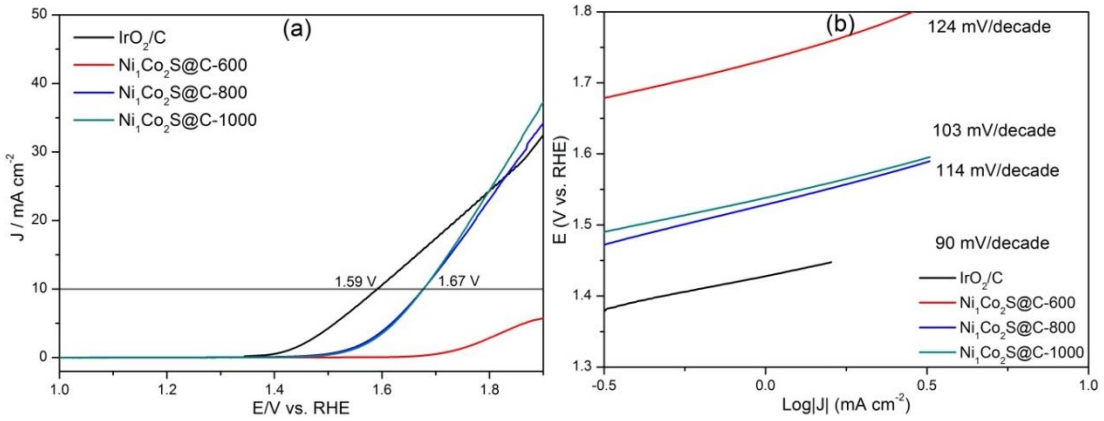

Figure 8.30 (a) Polarization curves for OER on IrO_2/C and the as-synthesized Ni_1Co_2S@C composites, respectively. (b) The corresponding Tafel plot (over-potential versus log current) derived from the OER polarization curves.

8.3.2 Hydrogen evolution reaction

The hydrogen evolution reaction (HER) catalytic activities of the CoS@C (without Ni addition), Ni_1Co_2S@C, and Ni_1Co_4S@C were all evaluated in an Ar-saturated 0.5 M H_2SO_4 solution (shown in Figure 8.31, 32, 33 and Table 8.3). The polarization curve recorded with Ni_1Co_4S@C-800 shows an onset overpotential of 98 mV for the HER (Figure 8.31). In contrast, CoS@C and Ni_1Co_2S@C samples (shown in Table 8.3) exhibit lower HER activity (onset overpotential ranging from 120 to 306 mV). Notably, to achievie a current density of 10 mA cm^{-2}, the sample Ni_1Co_4S@C-800 only requires an overpotential of 247 mV, which is comparable to that of the most active non-precious metal HER electrocatalysts: Co/N-doped carbon(229 mV in 0.5 M H_2SO_4),[274] double-grid MoS_2 (270 mV in 0.5 M H_2SO_4)[514] and C_3N_4/N-doped graphene (270 mV in 0.5 M H_2SO_4).[515] The dramatic enhancement in HER activity is even more apparent by the comparison of the slopes of Tafel plots (Figure 8.31b, 32b, 33b and Table 8.3), where slope value is 58 mV/decade for the Ni_1Co_4S@C-800 and in range of 119 to 488 mV/decade for other Ni_0Co_1S@C and Ni_1Co_2S@C samples, respectively. Obviously, Ni_1Co_4S@C samples show enhanced HER catalytic activities compared with other Ni_0Co_1S@C and Ni_1Co_2S@C samples under the same conditions. It is believed that the introduce of nickel promoted cobalt sulfides and N,S dopants can synergistically optimize the electronic structure of the carbon and the adsorption energy of H atoms on carbon, thus promoting the electron transformation.[274]

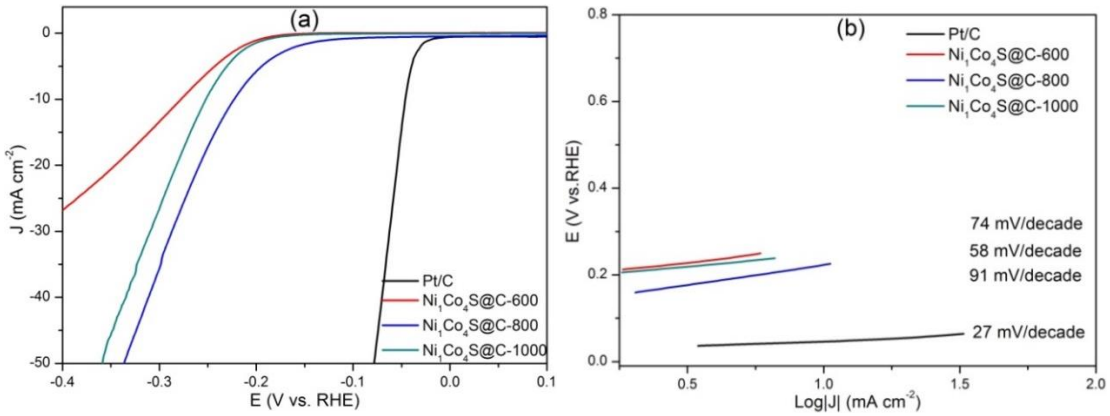

Figure 8.31 (a) HER polarization curves and (b) corresponding Tafel plots of Pt/C and the as-synthesized Ni_1Co_4S@C composites. Measured in 0.5 M H_2SO_4 electrolyte.

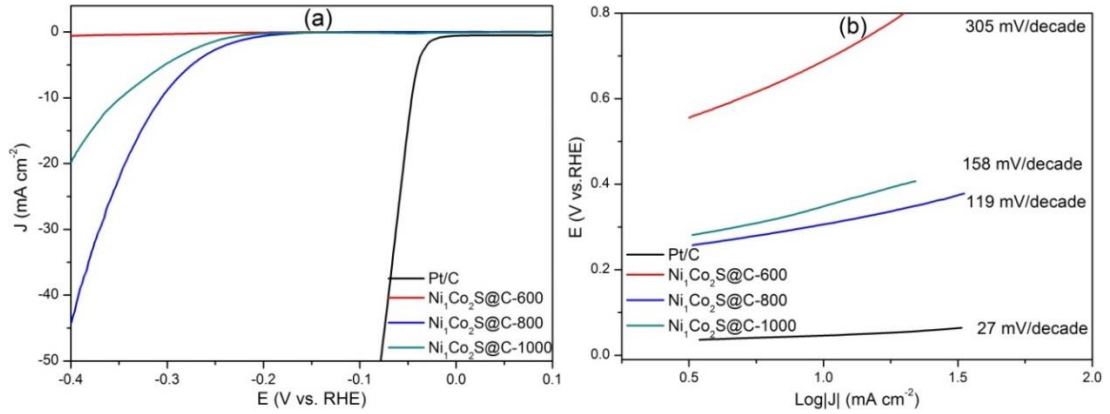

Figure 8.32 (a) HER polarization curves and (b) corresponding Tafel plots of Pt/C and the as-synthesized Ni_1Co_2S@C composites. Measured in 0.5 M H_2SO_4 electrolyte.

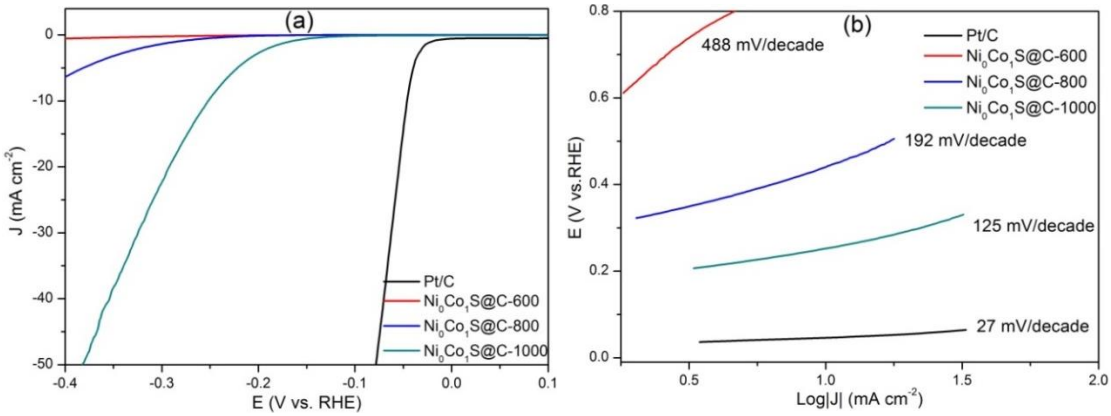

Figure 8.33 (a) HER polarization curves and (b) corresponding Tafel plots of Pt/C and the as-synthesized Ni_0Co_1S@C composites. Measured in 0.5 M H_2SO_4 electrolyte.

The HER generally consists of three main reaction steps in acidic media, while the HER mechanism in alkaline media is still unclear. The first step in acidic media is the Volmer step: $H^+ + e^- \rightarrow H_{ads}$. The reaction of a proton with an electron forms an adsorbed hydrogen atom (H_{ads}). After the formation of H_{ads}, HER then proceeds to the Tafel step ($2H_{ads} \rightarrow H_2$) or the Heyrovsky step ($H_{ads} + H^+ + e^- \rightarrow H_2$) or both. Thus, the half reaction is $2H^+ + 2e^- \rightarrow H_2$.

Table 8.3 Comparison of the HER catalytic performances between our materials.

Catalyst	Onset (mV)	Tafel slope (mV/decade)	Over-potential at the Current density of 10 mA cm^{-2} (mV)
Ni_1Co_4S@C-600	165	74	264
Ni_1Co_4S@C-800	98	58	247
Ni_1Co_4S@C-1000	155	91	222
Ni_1Co_2S@C-600	306	305	693
Ni_1Co_2S@C-800	168	119	308
Ni_1Co_2S@C-1000	198	158	349
Ni_0Co_1S@C-600	287	488	979
Ni_0Co_1S@C-800	205	192	443
Ni_0Co_1S@C-1000	110	125	256
Pt-C	0	27	46

8.5.3 Conclusions

In this part, a metal sulfide/carbon nanocomposite system, consisting of nickel promoted cobalt sulfides and N, S co-doped porous carbon, was developed as highly efficient non-noble metal electrocatalyst for oxygen evolution reaction (OER). The Ni-Co based sulfides/N, S co-doped carbon nanocomposites were facilely synthesized from a simple one-step process via the simultaneous carbonization and sulfurization of Ni-substituted ZIF-67 in hydrogen sulfide atmosphere. Due to the effect of Ni substitution, the featured morphology, the high porosity (340 m^2 g^{-1}), the homogeneous dispersed active components combined with N,S Co-doping effect, the sample Ni_1Co_4S@C-1000 functions as an efficient and stable non-noble metal electrocatalyst for OER. This novel material exhibited a low onset potential of 1.44 V (vs reversible hydrogen electrode) and a stable current density of 10 mA cm^{-2} at 1.52 V in 0.1 M KOH alkaline solution over a long-term operation, better than the benchmark IrO_2/C and other composites synthesized under the same conditions. The Ni_1Co_4S@C-1000 can also efficiently catalyse oxygen reduction reaction (ORR), with a four-electron pathway for reversible oxygen evolution and reduction. Furthermore, Ni_1Co_4S@C-800 showed enhanced electrocatalytic activity for hydrogen evolution reaction (HER) in water splitting. These findings indicate that ZIFs-derived nickel promoted cobalt sulfides on N, S co-doped porous carbon nanocomposites are cost-effective and promising alternative electrocatalysts towards OER, ORR and HER in the next generation of energy storage and conversion technologies.

8.6 Summary

In this chapter, using ZIF-67 as a precursor, a facile one-step sulfurization and carbonization route has been successfully developed to synthesize atomically uniformly dispersed cobalt sulfide nanocrystal particles embedded in N, S co-doped porous carbon matrices, which are promising advanced bifunctional electrocatalyst for ORR and OER. Due to the high porosity, unique core-shell structure, homogeneous dispersion and N and S-doping effect, the as-synthesized nanocomposite Co_xS_y@C-1000 not only exhibits exceptionally prominent electrocatalytic activity, good methanol tolerance and superior durability for ORR, but also offers promising catalytic performance for OER in alkaline medium. This work may open up a new avenue for the design and syntheses of highly homogeneous dispersed porous carbon-metal sulfides nanocomposite materials that display low-cost and efficient

bifunctional electrocatalytic behaviours for the next generation of energy conversion and storage applications.

In addition, a facile method for the synthesis of porous Ni-Co based sulfides/S,N-codoped carbon nanocomposites has been presented and their excellent electrochemical performances for water splitting have been demonstrated. The as-synthesized nanocomposite Ni_1Co_4S@C-1000 exhibits superior OER activity, more favourable kinetics, and longer durability compared with those of IrO_2/C and other composites synthesized under the similar conditions (Ni_1Co_4S@C-600, Ni_1Co_4S@C-800 and Ni_1Co_2S@C). Ni_1Co_4S@C-1000 also shows the excellent reversible oxygen electrode nature. The generated metal sulfides/carbons composites display enhanced HER activities as well. Generally, these excellent catalytic abilities could be attributed to: 1) The uniformly distributed nickel promoted cobalt sulfides nanoparticles supported on high surface area carbon enables the full use of catalytic active sites, with the high conductivity of carbon that is favourable to the electron transfer; 2) The core-shell carbon structure protected the encapsulated sulfides nanoparticles to maintain the stability; 3) The synergistic effect of nickel promoted cobalt sulfide nanoparticles; 4) The doping of N, S into carbon architecture can improve the catalytic activity; 5) The synergistic effect between metal sulfides and S,N codoped carbon can also enhance the catalytic activity. Using this novel synthesis strategy, other homogeneously distributed novel bimetal sulfides/heteroatom codoped porous carbon composites could be facilely prepared. These materials will be promising in metal-air batteries, fuel cells, and water splitting and other energy systems, which pave a new way to develop alternative cost-effective non-noble metal based advanced functional catalysts for energy applications.

9. Chapter 9: Conclusions and future work

9.1 Conclusions

In this thesis, novel nanostructured materials with appropriate functionalities have been designed and developed, and their applications in energy-related fields have also been evaluated. This thesis presents the synthesis of a series of ZIFs and ZIF derivatives, including ZIF-8, ZIF-8/graphene oxide composites, zinc oxide/nanoporous carbon composites derived from ZIF-8, cobalt/nanoporous carbon composites derived from ZIF-67, cobalt sulfides/N, S co-doped porous carbon composites and relevant cobalt-nickel sulfides/N, S co-doped porous carbon composites derived from ZIF-67. The morphologies, crystal structures, thermal properties, and textural properties of these as-synthesized products were characterised in detail using combined techniques. In addition, this thesis also reports the excellent performances in the applications of these as-synthesized products, including CO_2 uptake, adsorption and photodegradation of organic dye, electrocatalytic oxygen reduction reaction, oxygen evolution reaction and hydrogen evolution reaction. Therefore, my initial PhD objectives have been achieved. In details:

In Chapter 4, a cost-effective and facile method for the synthesis of ZIF-8 from stoichiometric molar ratio of precursors in aqueous ammonia was presented. Ammonia not only can promote the deprotonation of the ligand, but also accelerate the formation of ZIF-8. The concentration of ammonia can control the structures, particle crystal sizes and textural properties of the resulting products. In addition, a series of anions that affects the formation of ZIF-8 has also been demonstrated. The anion types and concentrations have significant effect on the formation of pure ZIF-8 and the anion effect capacity follows the classic Hofmeister anion sequence.

In Chapter 5, ZIF-8/graphene oxide composites have been synthesized by an *in-situ* approach. The formation of strong interactions between ZIF-8 and GO in the synthesized composites has been confirmed. These *in-situ* synthesized composites exhibit enhanced CO_2 adsorption energy and significant CO_2 storage capacity, which is probably due to the strong interactions and the synergistic effect between GO and ZIF-8.

In Chapter 6, advanced functional composites of ZnO nanoparticles embedded in N-doped nanoporous carbons have been synthesized by a simple one-step carbonization of ZIF-8 under a water stream atmosphere. A variety of characterization techniques show that the introduction of water steam during the carbonization process holds the key to obtain the fine and homogeneously dispersed ZnO nanoparticles within the functionalised nanoporous carbon matrix. Possessing a higher specific surface area, a larger pore volume and abundant oxygen-containing hydrophilic functional groups, the resulting composite exhibits a stronger interaction with CO_2 and is more efficient to promote the photocatalytic degradation-adsorption of methylene blue under visible light than the composite obtained without steam treatment.

Chapter 7, demonstrates a series of ZIF derivatives of cobalt/nanoporous N-doped carbon nanocomposites and hollow carbon nano-onions synthesized by one-step carbonization of ZIF-67. The effect of the carbonization temperature on the structural evolution of the ZIF derivatives was discussed. Among the as-synthesized products, the cobalt/nanoporous N-doped carbon composites have demonstrated excellent catalytic activities toward ORR in alkaline medium. Compared to the commercial Pt/C catalyst, the optimized nanocomposite (annealed at 800 ^{o}C) exhibits superior catalytic activity, a four-electron pathway, high durability and excellent methanol tolerance. Moreover, the optimized nanocomposite also showed enhanced electrocatalytic activity for OER from water splitting.

In Chapter 8, homogeneous dispersed cobalt sulfide/N,S co-doped porous carbon nanocomposites as high-performance bifunctional electrocatalysts towards ORR and OER have been synthesized by suing a simple and efficient method that utilizes ZIF-67 as the precursor and template. The resulting nanocomposites possess a unique core–shell structure, high porosity, homogeneous dispersion of active components together with N and S-doping effects. The as-synthesized bifunctional electrocatalysts show excellent electrocatalytic activity towards ORR with the high onset potential and a four-electron pathway and OER with a small overpotential, they also exhibit superior stability to the commercial Pt/C catalyst in ORR and good OER stability. Furthermore, a Ni-Co based bi-metallic sulfide/N, S co-doped carbon nanocomposite system was developed as highly efficient non-noble metal electrocatalyst for OER. The nanocomposites were facilely synthesized via a simple one-step process from the

simultaneous carbonization and sulfurization of Ni-substituted ZIF-67 in hydrogen sulfide atmosphere. Due to the effect of Ni substitution, the featured morphology, the high porosity, the homogeneous dispersed active components combined with N,S-codoping effect, the resulting nanocomposite functions as a superior active and stable non-noble metal electrocatalyst for OER.

9.2 Suggestions for future work

Based on the obtained results, some suggestions for the future work are proposed as follows:

- We have successfully prepared zinc oxide/nanoporous carbon composites derived from ZIF-8 with excellent CO_2 uptake. However, the pure N-doped porous carbon derived from ZIF-8 by using the similar preparation method is still needed to investigate. These N-doped porous carbon materials are potential promising in CO_2 storage application and some electrochemical applications.
- We have obtained cobalt sulfides/N, S Co-doped porous carbon nanocomposites from ZIF-67. The investigation of the pure S, N-codoped porous carbon derived from ZIF-67 by using similar synthesis method will be an interesting subject, including its CO_2 storage application and ORR, OER applications.
- Polymer composite membranes containing nanostructured fillers have many potential applications in industrial sectors, ranging from carbon dioxide capture and sequestration to hydrogen purification, and use in water desalination and vapour recovery systems. Next generation mixed-matrix membranes (MMMs) which incorporate porous ZIFs, offer the unique opportunity for combining high selectivity and chemical tuneability of ZIFs with the ease of processing and robustness intrinsic to conventional polymers.
- ZIF materials normally can provide high surface area with micropores. The investigation of the synthesis of hierarchical structural porous materials including micropore, mesopore, and macropore will be an interesting topic.
- Doping effects can offer an excellent electrocatalytic performance. In this thesis, nitrogen and sulfur doping have been studied. It will be very interesting to investigate other heteroatom doping effect such as P, and B on the

electrocatalytic performance. It is also very necessary to study the mechanism of doping effect.

References

1. M. E. Davis, *Nature*, 2002, **417**, 813-821.
2. M. Eddaoudi, J. Kim, N. Rosi, D. Vodak, J. Wachter, M. O'Keeffe and O. M. Yaghi, *Science*, 2002, **295**, 469-472.
3. J. Y. Ying, C. P. Mehnert and M. S. Wong, *Angew. Chem. Int. Ed.*, 1999, **38**, 56-77.
4. K. S. Sing, *Pure and applied chemistry*, 1985, **57**, 603-619.
5. B. Chen, Z. Yang, Y. Zhu and Y. Xia, *J. Mater. Chem. A*, 2014, **2**, 16811-16831.
6. B. Wang, A. P. Cote, H. Furukawa, M. O/'Keeffe and O. M. Yaghi, *Nature*, 2008, **453**, 207-211.
7. A. Phan, C. J. Doonan, F. J. Uribe-Romo, C. B. Knobler, M. O'Keeffe and O. M. Yaghi, *Acc. Chem. Res.*, 2010, **43**, 58-67.
8. K. S. Park, Z. Ni, A. P. Côté, J. Y. Choi, R. Huang, F. J. Uribe-Romo, H. K. Chae, M. O'Keeffe and O. M. Yaghi, *Proc. Natl. Acad. Sci.*, 2006, **103**, 10186-10191.
9. X. Huang, Y. Lin, J. Zhang and X. Chen, *Ange. Chem. Int. Ed.*, 2006, **45**, 1557-1559.
10. J. Cravillon, S. Münzer, S. Lohmeier, A. Feldhoff, K. Huber and M. Wiebcke, *Chem. Mater.*, 2009, **21**, 1410-1412.
11. S. K. Nune, P. K. Thallapally, A. Dohnalkova, C. Wang, J. Liu and G. J. Exarhos, *Chem. Commun.*, 2010, **46**, 4878-4880.
12. S. R. Venna, J. B. Jasinski and M. A. Carreon, *J. Am. Chem. Soc.*, 2010, **132**, 18030-18033.
13. R. Ameloot, E. Gobechiya, H. Uji, J. A. Martens, J. Hofkens, L. Alaerts, B. F. Sels and D. E. De Vos, *Adv. Mater.*, 2010, **22**, 2685-2688.
14. J. Cravillon, R. Nayuk, S. Springer, A. Feldhoff, K. Huber and M. Wiebcke, *Chem. Mater.*, 2011, **23**, 2130-2141.
15. Y. Tian, Y. Zhao, Z. Chen, G. Zhang, L. Weng and D. Zhao, *Chem. Eur. J.*, 2007, **13**, 4146-4154.
16. W. Morris, C. J. Doonan, H. Furukawa, R. Banerjee and O. M. Yaghi, *J. Am. Chem. Soc.*, 2008, **130**, 12626-12627.
17. D. J. Tranchemontagne, J. R. Hunt and O. M. Yaghi, *Tetrahedron*, 2008, **64**, 8553-8557.
18. A. F. Gross, E. Sherman and J. J. Vajo, *Dalton Trans.*, 2012, **41**, 5458-5460.
19. T. Yang and T.-S. Chung, *J. Mater. Chem. A*, 2013, **1**, 6081-6090.
20. Y. Pan, Y. Liu, G. Zeng, L. Zhao and Z. Lai, *Chem. Commun.*, 2011, **47**, 2071-2073.
21. J. Cravillon, R. Nayuk, S. Springer, A. Feldhoff, K. Huber and M. Wiebcke, *Chem. Mater.*, 2011, **23**, 2130-2141.
22. B. Chen, F. Bai, Y. Zhu and Y. Xia, *Microporous Mesoporous Mater.*, 2014, **193**, 7-14.
23. Q. Shi, Z. Chen, Z. Song, J. Li and J. Dong, *Angew. Chem. Int. Ed.*, 2011, **50**, 672-675.
24. Y. Tian, Y. Zhao, Z. Chen, G. Zhang, L. Weng and D. Zhao, *Chem. Eur. J.*, 2007, **13**, 4146-4154.
25. W. Morris, C. J. Doonan, H. Furukawa, R. Banerjee and O. M. Yaghi, *J. Am. Chem. Soc.*, 2008, **130**, 12626-12627.
26. A. F. Gross, E. Sherman and J. J. Vajo, *Dalton Trans.*, 2012, **41**, 5458-5460.
27. D. R. Dreyer, S. Park, C. W. Bielawski and R. S. Ruoff, *Chem. Soc. Rev.*, 2010, **39**, 228-240.
28. J. K. Sun and Q. Xu, *Energy Environ. Sci.*, 2014, **7**, 2071-2100.
29. B. C. H. Steele and A. Heinzel, *Nature*, 2001, **414**, 345-352.
30. H. A. Gasteiger and N. M. Marković, *Science*, 2009, **324**, 48-49.
31. G. Wu and P. Zelenay, *Acc. Chem. Res.*, 2013, **46**, 1878-1889.
32. S. Xie, S.-I. Choi, N. Lu, L. T. Roling, J. A. Herron, L. Zhang, J. Park, J. Wang, M. J. Kim, Z. Xie, M. Mavrikakis and Y. Xia, *Nano Lett.*, 2014, **14**, 3570-3576.
33. K. A. Kuttiyiel, K. Sasaki, Y. Choi, D. Su, P. Liu and R. R. Adzic, *Nano Lett.*, 2012, **12**, 6266-6271.

34. D. J. Li, U. N. Maiti, J. Lim, D. S. Choi, W. J. Lee, Y. Oh, G. Y. Lee and S. O. Kim, *Nano Lett.*, 2014, **14**, 1228-1233.
35. H. Wang and H. Dai, *Chem. Soc. Rev.*, 2013, **42**, 3088-3113.
36. L. Dai, Y. Xue, L. Qu, H.. Choi and J. Baek, *Chemical Reviews*, 2015, **115**, 4823-4892.
37. S.-L. Li and Q. Xu, *Energy Environ. Sci.*, 2013, **6**, 1656-1683.
38. J. Zhang, Z. Zhao, Z. Xia and L. Dai, *Nat Nano*, 2015, **10**, 444-452.
39. Y. Liang, Y. Li, H. Wang, J. Zhou, J. Wang, T. Regier and H. Dai, *Nat Mater*, 2011, **10**, 780-786.
40. H. A. Gasteiger, S. S. Kocha, B. Sompalli and F. T. Wagner, *Appl. Catal., B*, 2005, **56**, 9-35.
41. M. Lefèvre, E. Proietti, F. Jaouen and J. Dodelet, *Science*, 2009, **324**, 71-74.
42. J. Duan, S. Chen, S. Dai and S. Z. Qiao, *Adv. Funct. Mater.*, 2014, **24**, 2072-2078.
43. R. F. Cracknell, P. Gordon and K. E. Gubbins, *J. Phys. Chem.*, 1993, **97**, 494-499.
44. T. J. Barton, L. M. Bull, W. G. Klemperer, D. A. Loy, B. McEnaney, M. Misono, P. A. Monson, G. Pez, G. W. Scherer, J. C. Vartuli and O. M. Yaghi, *Chem. Mater.*, 1999, **11**, 2633-2656.
45. A. K. Cheetham, G. Férey and T. Loiseau, *Angew. Chem. Int. Ed.*, 1999, **38**, 3268-3292.
46. A. Phan, C. J. Doonan, F. J. Uribe-Romo, C. B. Knobler, M. O'Keeffe and O. M. Yaghi, *Acc. Chem. Res.*, 2010, **43**, 58-67.
47. O. M. Yaghi, G. Li and H. Li, *Nature*, 1995, **378**, 703-706.
48. E. A. Tomic, *J. Appl. Polym. Sci.*, 1965, **9**, 3745-3752.
49. J. Li, R. J. Kuppler and H. Zhou, *Chem. Soc. Rev.*, 2009, **38**, 1477-1504.
50. A. K. Cheetham, C. N. R. Rao and R. K. Feller, *Chem. Commun.*, 2006, 4780-4795.
51. G. Férey, C. Mellot-Draznieks, C. Serre and F. Millange, *Acc. Chem. Res.*, 2005, **38**, 217-225.
52. M. O'Keeffe, M. A. Peskov, S. J. Ramsden and O. M. Yaghi, *Acc. Chem. Res.*, 2008, **41**, 1782-1789.
53. S. A. Moggach, T. D. Bennett and A. K. Cheetham, *Angew. Chem.*, 2009, **121**, 7221-7223.
54. D. Fairen-Jimenez, S. A. Moggach, M. T. Wharmby, P. A. Wright, S. Parsons and T. Düren, *J. Am. Chem. Soc.*, 2011, **133**, 8900-8902.
55. K. S. Park, Z. Ni, A. P. Côté, J. Y. Choi, R. Huang, F. J. Uribe-Romo, H. K. Chae, M. O'Keeffe and O. M. Yaghi, *Proc. Natl. Acad. Sci. U.S.A.*, 2006, **103**, 10186-10191.
56. R. Banerjee, A. Phan, B. Wang, C. Knobler, H. Furukawa, M. O'Keeffe and O. M. Yaghi, *Science*, 2008, **319**, 939-943.
57. F. Wang, Y. X. Tan, H. Yang, H. X. Zhang, Y. Kang and J. Zhang, *Chem. Commun.*, 2011, **47**, 5828-5830.
58. S. T. Meek, J. A. Greathouse and M. D. Allendorf, *Adv. Mater.*, 2011, **23**, 249-267.
59. N. Stock and S. Biswas, *Chem. Rev.*, 2011, **112**, 933-969.
60. Q. Zhu and Q. Xu, *Chem. Soc. Rev.*, 2014, **43**, 5468-5512.
61. H. Furukawa, K. E. Cordova, M. O'Keeffe and O. M. Yaghi, *Science*, 2013, **341**.
62. J. Yao and H. Wang, *Chem. Soc. Rev.*, 2014, **43**, 4470-4493.
63. D. Bradshaw, A. Garai and J. Huo, *Chem. Soc. Rev.*, 2012, **41**, 2344-2381.
64. Y. Lee, J. Kim and W. Ahn, *Korean J. Chem. Eng.*, 2013, **30**, 1667-1680.
65. B. Liu, H. Shioyama, T. Akita and Q. Xu, *J. Am. Chem. Soc.*, 2008, **130**, 5390-5391.
66. R. Banerjee, H. Furukawa, D. Britt, C. Knobler, M. O'Keeffe and O. M. Yaghi, *J. Am. Chem. Soc.*, 2009, **131**, 3875-3877.
67. H. Hayashi, A. P. Cote, H. Furukawa, M. O/'Keeffe and O. M. Yaghi, *Nat Mater*, 2007, **6**, 501-506.
68. B. Seoane, J. M. Zamaro, C. Tellez and J. Coronas, *RSC Adv.*, 2011, **1**, 917-922.
69. Y. Ban, Y. Li, X. Liu, Y. Peng and W. Yang, *Microporous Mesoporous Mater.*, 2013, **173**, 29-36.
70. T. Yang and T. Chung, *J. Mater. Chem. A*, 2013, **1**, 6081-6090.

71. D. Peralta, G. Chaplais, A. Simon-Masseron, K. Barthelet and G. D. Pirngruber, *Microporous Mesoporous Mater.*, 2012, **153**, 1-7.
72. X. Huang, Y. Lin, J.-P. Zhang and X.-M. Chen, *Angew. Chem. Int. Ed.*, 2006, **45**, 1557-1559.
73. J. Zhang, A. Zhu, R. Lin, X. Qi and X. Chen, *Adv. Mater.*, 2011, **23**, 1268-1271.
74. A. Zhu, R. Lin, X. Qi, Y. Liu, Y. Lin, J. Zhang and X. Chen, *Microporous Mesoporous Mater.*, 2012, **157**, 42-49.
75. J. Cravillon, S. Münzer, S. Lohmeier, A. Feldhoff, K. Huber and M. Wiebcke, *Chem. Mater.*, 2009, **21**, 1410-1412.
76. S. K. Nune, P. K. Thallapally, A. Dohnalkova, C. Wang, J. Liu and G. J. Exarhos, *Chem. Commun.*, 2010, **46**, 4878-4880.
77. J. Cravillon, C. A. Schroder, H. Bux, A. Rothkirch, J. Caro and M. Wiebcke, *CrystEngComm*, 2012, **14**, 492-498.
78. M. He, J. F. Yao, L. X. Li, K. Wang, F. Y. Chen and H. T. Wang, *ChemPhysChem*, 2013, **78**, 1222-1225.
79. T. D. Bennett, P. J. Saines, D. A. Keen, J. Tan and A. K. Cheetham, *Chem. Eur. J.*, 2013, **19**, 7049-7055.
80. S. Tanaka, K. Kida, M. Okita, Y. Ito and Y. Miyake, *Chem. Lett.*, 2012, **41**, 1337-1339.
81. K. Kida, M. Okita, K. Fujita, S. Tanaka and Y. Miyake, *CrystEngComm*, 2013, **15**, 1794-1801.
82. J. Qian, F. Sun and L. Qin, *Mater. Lett.*, 2012, **82**, 220-223.
83. J. Yao, M. He, K. Wang, R. Chen, Z. Zhong and H. Wang, *CrystEngComm*, 2013, **15**, 3601-3606.
84. F. Shieh, S. Wang, S. Leo and K. C. W. Wu, *Chem. Eur. J.*, 2013, **19**, 11139-11142.
85. M. He, J. Yao, Q. Liu, K. Wang, F. Chen and H. Wang, *Microporous Mesoporous Mater.*, 2014, **184**, 55-60.
86. E. R. Parnham and R. E. Morris, *Acc. Chem. Res.*, 2007, **40**, 1005-1013.
87. R. E. Morris, *Angew. Chem. Int. Ed.*, 2008, **47**, 442-444.
88. E. R. Cooper, C. D. Andrews, P. S. Wheatley, P. B. Webb, P. Wormald and R. E. Morris, *Nature*, 2004, **430**, 1012-1016.
89. G. A. V. Martins, P. J. Byrne, P. Allan, S. J. Teat, A. M. Z. Slawin, Y. Li and R. E. Morris, *Dalton Trans.*, 2010, **39**, 1758-1762.
90. L. Yang and H. Lu, *Chin. J. Chem.*, 2012, **30**, 1040-1044.
91. C. Liu, F. Sun, S. Zhou, Y. Tian and G. Zhu, *CrystEngComm*, 2012, **14**, 8365-8367.
92. K. Bernardo-Gusmão, L. F. Trevisan Queiroz, R. F. de Souza, F. Leca, C. Loup and R. Réau, *J. Catal.*, 2003, **219**, 59-62.
93. B. Wang, Y. Kang, L. Yang and J. Suo, *J. Mol. Catal. A: Chem.*, 2003, **203**, 29-36.
94. T. M. Letcher and N. Deenadayalu, *J. Chem. Thermodyn.*, 2003, **35**, 67-76.
95. W. J. Son, J. Kim, J. Kim and W. S. Ahn, *Chem. Commun.*, 2008, 6336-6338.
96. K. S. Suslick, D. A. Hammerton and R. E. Cline, *J. Am. Chem. Soc.*, 1986, **108**, 5641-5642.
97. K. S. Suslick, *Science*, 1990, **247**, 1439-1445.
98. S. J. Doktycz and K. S. Suslick, *Science*, 1990, **247**, 1067-1069.
99. B. Seoane, J. M. Zamaro, C. Tellez and J. Coronas, *CrystEngComm*, 2012, **14**, 3103-3107.
100. H.-Y. Cho, J. Kim, S.-N. Kim and W.-S. Ahn, *Microporous Mesoporous Mater.*, 2013, **169**, 180-184.
101. A. L. Garay, A. Pichon and S. L. James, *Chem. Soc. Rev.*, 2007, **36**, 846-855.
102. C. S. Cundy and P. A. Cox, *Microporous Mesoporous Mater.*, 2005, **82**, 1-78.
103. H. Zhang, Q. Shi, X. Kang and J. Dong, *J. Coord. Chem.*, 2013, **66**, 2079-2090.
104. K. Müller-Buschbaum and F. Schönfeld, *Z. Anorg. Allg. Chem.*, 2011, **637**, 955-960.
105. J. Lin, R. Lin, X. Cheng, J. Zhang and X. Chen, *Chem. Commun.*, 2011, **47**, 9185-9187.

106. M. Lanchas, D. Vallejo-Sanchez, G. Beobide, O. Castillo, A. T. Aguayo, A. Luque and P. Roman, *Chem. Commun.*, 2012, **48**, 9930-9932.
107. M. J. Cliffe, C. Mottillo, R. S. Stein, D. Bucar and T. Friščić, *Chem. Sci.*, 2012, **3**, 2495-2500.
108. C. Mottillo, Y. Lu, M. Pham, M. J. Cliffe, T. Do and T. Friščić, *Green Chem.*, 2013, **15**, 2121-2131.
109. J. C. Tan and A. K. Cheetham, *Chem. Soc. Rev.*, 2011, **40**, 1059-1080.
110. J. C. Tan, T. D. Bennett and A. K. Cheetham, *Proc. Natl. Acad. Sci. U.S.A.*, 2010, **107**, 9938-9943.
111. D. W. Lewis, A. R. Ruiz-Salvador, A. Gomez, L. M. Rodriguez-Albelo, F.-X. Coudert, B. Slater, A. K. Cheetham and C. Mellot-Draznieks, *CrystEngComm*, 2009, **11**, 2272-2276.
112. M. Schlesinger, S. Schulze, M. Hietschold and M. Mehring, *Microporous Mesoporous Mater.*, 2010, **132**, 121-127.
113. J. F. Fernández-Bertrán, M. P. Hernández, E. Reguera, H. Yee-Madeira, J. Rodriguez, A. Paneque and J. C. Llopiz, *J. Phys. Chem. Solids*, 2006, **67**, 1612-1617.
114. C. J. Adams, M. A. Kurawa and A. G. Orpen, *Dalton Trans.*, 2010, **39**, 6974-6984.
115. C. J. Adams, M. F. Haddow, R. J. I. Hughes, M. A. Kurawa and A. G. Orpen, *Dalton Trans.*, 2010, **39**, 3714-3724.
116. C. J. Adams, H. M. Colquhoun, P. C. Crawford, M. Lusi and A. G. Orpen, *Angew. Chem.*, 2007, **119**, 1142-1146.
117. P. J. Beldon, L. Fábián, R. S. Stein, A. Thirumurugan, A. K. Cheetham and T. Friščić, *Angew. Chem. Int. Ed.*, 2010, **49**, 9640-9643.
118. T. Friscic, S. L. Childs, S. A. A. Rizvi and W. Jones, *CrystEngComm*, 2009, **11**, 418-426.
119. D. Braga, M. Curzi, A. Johansson, M. Polito, K. Rubini and F. Grepioni, *Angew. Chem. Int. Ed.*, 2006, **45**, 142-146.
120. T. Friščić, D. G. Reid, I. Halasz, R. S. Stein, R. E. Dinnebier and M. J. Duer, *Angew. Chem. Int. Ed.*, 2010, **49**, 712-715.
121. T. Friščić, I. Halasz, P. J. Beldon, A. M. Belenguer, F. Adams, S. A. J. Kimber, V. Honkimäki and R. E. Dinnebier, *Nat Chem*, 2013, **5**, 66-73.
122. S. Tanaka, K. Kida, T. Nagaoka, T. Ota and Y. Miyake, *Chem. Commun.*, 2013, **49**, 7884-7886.
123. T. D. Bennett, S. Cao, J. C. Tan, D. A. Keen, E. G. Bithell, P. J. Beldon, T. Friščić and A. K. Cheetham, *J. Am. Chem. Soc.*, 2011, **133**, 14546-14549.
124. S. Cao, T. D. Bennett, D. A. Keen, A. L. Goodwin and A. K. Cheetham, *Chem. Commun.*, 2012, **48**, 7805-7807.
125. Y. Liu, G. Zeng, Y. Pan and Z. Lai, *J. Membr. Sci.*, 2011, **379**, 46-51.
126. S. R. Venna and M. A. Carreon, *J. Am. Chem. Soc.*, 2009, **132**, 76-78.
127. H. Bux, C. Chmelik, R. Krishna and J. Caro, *J. Membr. Sci.*, 2011, **369**, 284-289.
128. A. Demessence, C. Boissiere, D. Grosso, P. Horcajada, C. Serre, G. Ferey, G. J. A. A. Soler-Illia and C. Sanchez, *J. Mater. Chem.*, 2010, **20**, 7676-7681.
129. Y. Pan and Z. Lai, *Chem. Commun.*, 2011, **47**, 10275-10277.
130. Y. Pan, T. Li, G. Lestari and Z. Lai, *J. Membr. Sci.*, 2012, **390–391**, 93-98.
131. Y. Pan, B. Wang and Z. Lai, *J. Membr. Sci.*, 2012, **421–422**, 292-298.
132. J. Yao, L. Li, W. H. Benjamin Wong, C. Tan, D. Dong and H. Wang, *Mater. Chem. Phys.*, 2013, **139**, 1003-1008.
133. X. Dong and Y. S. Lin, *Chem. Commun.*, 2013, **49**, 1196-1198.
134. X. Dong, K. Huang, S. Liu, R. Ren, W. Jin and Y. S. Lin, *J. Mater. Chem.*, 2012, **22**, 19222-19227.
135. K. Tao, C. Kong and L. Chen, *Chem. Eng. J.*, 2013, **220**, 1-5.
136. Y. Li, F. Liang, H. Bux, A. Feldhoff, W. Yang and J. Caro, *Angew. Chem. Int. Ed.*, 2010, **49**, 548-551.
137. Y. Li, F. Liang, H. Bux, W. Yang and J. Caro, *J. Membr. Sci.*, 2010, **354**, 48-54.

138. Y. Li, H. Bux, A. Feldhoff, G. Li, W. Yang and J. Caro, *Adv. Mater.*, 2010, **22**, 3322-3326.
139. H. Bux, A. Feldhoff, J. Cravillon, M. Wiebcke, Y. Li and J. Caro, *Chem. Mater.*, 2011, **23**, 2262-2269.
140. L. Diestel, H. Bux, D. Wachsmuth and J. Caro, *Microporous Mesoporous Mater.*, 2012, **164**, 288-293.
141. K. Kida, K. Fujita, T. Shimada, S. Tanaka and Y. Miyake, *Dalton Trans.*, 2013, **42**, 11128-11135.
142. L. Li, J. Yao, R. Chen, L. He, K. Wang and H. Wang, *Microporous Mesoporous Mater.*, 2013, **168**, 15-18.
143. H. T. Kwon and H. Jeong, *Chem. Commun.*, 2013, **49**, 3854-3856.
144. V. N. Kislenko and L. P. Oliynyk, *J. Polym. Sci., Part A: Polym. Chem.*, 2002, **40**, 914-922.
145. A. J. Brown, J. R. Johnson, M. E. Lydon, W. J. Koros, C. W. Jones and S. Nair, *Angew. Chem. Int. Ed.*, 2012, **51**, 10615-10618.
146. L. Ge, W. Zhou, A. Du and Z. Zhu, *J. Phys. Chem. C*, 2012, **116**, 13264-13270.
147. M. Shah, M. C. McCarthy, S. Sachdeva, A. K. Lee and H. Jeong, *Ind. Eng. Chem. Res.*, 2011, **51**, 2179-2199.
148. H. Bux, F. Liang, Y. Li, J. Cravillon, M. Wiebcke and J. r. Caro, *J. Am. Chem. Soc.*, 2009, **131**, 16000-16001.
149. H. Bux, C. Chmelik, J. M. van Baten, R. Krishna and J. Caro, *Adv. Mater.*, 2010, **22**, 4741-4743.
150. G. Xu, J. Yao, K. Wang, L. He, P. A. Webley, C. Chen and H. Wang, *J. Membr. Sci.*, 2011, **385–386**, 187-193.
151. M. Zhu, J. B. Jasinski and M. A. Carreon, *J. Mater. Chem.*, 2012, **22**, 7684-7686.
152. Y. Liu, E. Hu, E. A. Khan and Z. Lai, *J. Membr. Sci.*, 2010, **353**, 36-40.
153. M. C. McCarthy, V. Varela-Guerrero, G. V. Barnett and H.-K. Jeong, *Langmuir*, 2010, **26**, 14636-14641.
154. A. Huang, W. Dou and J. Caro, *J. Am. Chem. Soc.*, 2010, **132**, 15562-15564.
155. A. Huang, H. Bux, F. Steinbach and J. Caro, *Angew. Chem. Int. Ed.*, 2010, **49**, 4958-4961.
156. A. Huang and J. Caro, *Angew. Chem. Int. Ed.*, 2011, **50**, 4979-4982.
157. A. Huang, Y. Chen, N. Wang, Z. Hu, J. Jiang and J. Caro, *Chem. Commun.*, 2012, **48**, 10981-10983.
158. C. Zhang, Y. Xiao, D. Liu, Q. Yang and C. Zhong, *Chem. Commun.*, 2013, **49**, 600-602.
159. M. Shah, H. T. Kwon, V. Tran, S. Sachdeva and H. Jeong, *Microporous Mesoporous Mater.*, 2013, **165**, 63-69.
160. H. T. Kwon and H.-K. Jeong, *J. Am. Chem. Soc.*, 2013, **135**, 10763-10768.
161. M. Gao, Q. Gao, J. Jiang, C. Cui, W. Yao and S. Yu, *Angew. Chem. Int. Ed.*, 2011, **50**, 4905-4908.
162. M. He, J. Yao, L. Li, Z. Zhong, F. Chen and H. Wang, *Microporous Mesoporous Mater.*, 2013, **179**, 10-16.
163. Z. Xie, J. Yang, J. Wang, J. Bai, H. Yin, B. Yuan, J. Lu, Y. Zhang, L. Zhou and C. Duan, *Chem. Commun.*, 2012, **48**, 5977-5979.
164. M. N. Shah, M. A. Gonzalez, M. C. McCarthy and H.-K. Jeong, *Langmuir*, 2013, **29**, 7896-7902.
165. M. J. C. Ordoñez, K. J. Balkus Jr, J. P. Ferraris and I. H. Musselman, *J. Membr. Sci.*, 2010, **361**, 28-37.
166. R. Mahajan, R. Burns, M. Schaeffer and W. J. Koros, *J. Appl. Polym. Sci.*, 2002, **86**, 881-890.
167. T. T. Moore, R. Mahajan, D. Q. Vu and W. J. Koros, *AlChE J.*, 2004, **50**, 311-321.
168. Q. Song, S. K. Nataraj, M. V. Roussenova, J. C. Tan, D. J. Hughes, W. Li, P. Bourgoin, M. A. Alam, A. K. Cheetham, S. A. Al-Muhtaseb and E. Sivaniah, *Energy Environ. Sci.*, 2012, **5**, 8359-8369.

169. S. Basu, M. Maes, A. Cano-Odena, L. Alaerts, D. E. De Vos and I. F. J. Vankelecom, *J. Membr. Sci.*, 2009, **344**, 190-198.
170. X. Liu, Y. Li, G. Zhu, Y. Ban, L. Xu and W. Yang, *Angew. Chem. Int. Ed.*, 2011, **50**, 10636-10639.
171. S. Basu, A. Cano-Odena and I. F. J. Vankelecom, *Sep. Purif. Technol.*, 2011, **81**, 31-40.
172. J. A. Thompson, K. W. Chapman, W. J. Koros, C. W. Jones and S. Nair, *Microporous Mesoporous Mater.*, 2012, **158**, 292-299.
173. T. Bae, J. S. Lee, W. Qiu, W. J. Koros, C. W. Jones and S. Nair, *Angew. Chem. Int. Ed.*, 2010, **49**, 9863-9866.
174. C. Zhang, Y. Dai, J. R. Johnson, O. Karvan and W. J. Koros, *J. Membr. Sci.*, 2012, **389**, 34-42.
175. M. Askari and T. Chung, *J. Membr. Sci.*, 2013, **444**, 173-183.
176. K. Díaz, L. Garrido, M. López-González, L. F. del Castillo and E. Riande, *Macromolecules*, 2009, **43**, 316-325.
177. B. Zornoza, B. Seoane, J. M. Zamaro, C. Télez and J. Coronas, *ChemPhysChem*, 2011, **12**, 2781-2785.
178. K. Díaz, M. López-González, L. F. del Castillo and E. Riande, *J. Membr. Sci.*, 2011, **383**, 206-213.
179. H. Vogel and C. S. Marvel, *J. Polym. Sci.*, 1961, **50**, 511-539.
180. Y. Tsur, H. H. Levine and M. Levy, *J. Polymer. Sci. Polymer. Chem. Ed.*, 1974, **12**, 1515-1529.
181. T. Yang, Y. Xiao and T. Chung, *Energy Environ. Sci.*, 2011, **4**, 4171-4180.
182. G. M. Shi, T. Yang and T. S. Chung, *J. Membr. Sci.*, 2012, **415–416**, 577-586.
183. G. M. Shi, H. Chen, Y. C. Jean and T. S. Chung, *Polymer*, 2013, **54**, 774-783.
184. T. Yang and T.-S. Chung, *Int. J. Hydrogen Energy*, 2013, **38**, 229-239.
185. D. Hua, Y. K. Ong, Y. Wang, T. Yang and T. Chung, *J. Membr. Sci.*, 2014, **453**, 155-167.
186. A. F. Bushell, M. P. Attfield, C. R. Mason, P. M. Budd, Y. Yampolskii, L. Starannikova, A. Rebrov, F. Bazzarelli, P. Bernardo, J. Carolus Jansen, M. Lanč, K. Friess, V. Shantarovich, V. Gustov and V. Isaeva, *J. Membr. Sci.*, 2013, **427**, 48-62.
187. T. Li, Y. Pan, K.-V. Peinemann and Z. Lai, *J. Membr. Sci.*, 2013, **425–426**, 235-242.
188. C. Kang, Y. Lin, Y. Huang, K. Tung, K. Chang, J. Chen, W. Hung, K. Lee and J. Lai, *J. Membr. Sci.*, 2013, **438**, 105-111.
189. Y. Dai, J. R. Johnson, O. Karvan, D. S. Sholl and W. J. Koros, *J. Membr. Sci.*, 2012, **401–402**, 76-82.
190. S. N. Wijenayake, N. P. Panapitiya, S. H. Versteeg, C. N. Nguyen, S. Goel, K. J. Balkus, I. H. Musselman and J. P. Ferraris, *Ind. Eng. Chem. Res.*, 2013, **52**, 6991-7001.
191. X. Liu, H. Jin, Y. Li, H. Bux, Z. Hu, Y. Ban and W. Yang, *J. Membr. Sci.*, 2013, **428**, 498-506.
192. V. M. Aceituno Melgar, H. T. Kwon and J. Kim, *J. Membr. Sci.*, 2014, **459**, 190-196.
193. V. M. Aceituno Melgar, H. Ahn, J. Kim and M. R. Othman, *J. Ind. Eng. Chem.*, 2014, **21**, 575-579.
194. L. M. Robeson, *J. Membr. Sci.*, 2008, **320**, 390-400.
195. L. Ge, A. Du, M. Hou, V. Rudolph and Z. Zhu, *RSC Adv.*, 2012, **2**, 11793-11800.
196. X. Zhang, Y. Liu, L. Kong, H. Liu, J. Qiu, W. Han, L. Weng, K. L. Yeung and W. Zhu, *J. Mater. Chem. A*, 2013, **1**, 10635-10638.
197. X. Zhang, Y. Liu, S. Li, L. Kong, H. Liu, Y. Li, W. Han, K. L. Yeung, W. Zhu, W. Yang and J. Qiu, *Chem. Mater.*, 2014, **26**, 1975-1981.
198. X. Wu, M. Niknam Shahrak, B. Yuan and S. Deng, *Microporous Mesoporous Mater.*, 2014, **190**, 189-196.
199. N. Hara, M. Yoshimune, H. Negishi, K. Haraya, S. Hara and T. Yamaguchi, *J. Membr. Sci.*, 2014, **450**, 215-223.
200. D. Liu, X. Ma, H. Xi and Y. S. Lin, *J. Membr. Sci.*, 2014, **451**, 85-93.

201. T. Yang, G. M. Shi and T.-S. Chung, *Adv. Energy Mater.*, 2012, **2**, 1358-1367.
202. M. E. Davis, *Acc. Chem. Res.*, 1993, **26**, 111-115.
203. C. Chizallet, S. Lazare, D. Bazer-Bachi, F. Bonnier, V. Lecocq, E. Soyer, A. Quoineaud and N. Bats, *J. Am. Chem. Soc.*, 2010, **132**, 12365-12377.
204. U. P. N. Tran, K. K. A. Le and N. T. S. Phan, *ACS Catal.*, 2011, **1**, 120-127.
205. L. T. L. Nguyen, K. K. A. Le, H. X. Truong and N. T. S. Phan, *Catal. Sci. Technol.*, 2012, **2**, 521-528.
206. L. T. L. Nguyen, K. K. A. Le and N. T. S. Phan, *Chin. J. Catal.*, 2012, **33**, 688-696.
207. L. H. Wee, T. Lescouet, J. Ethiraj, F. Bonino, R. Vidruk, E. Garrier, D. Packet, S. Bordiga, D. Farrusseng, M. Herskowitz and J. A. Martens, *ChemCatChem*, 2013, **5**, 3562-3566.
208. X. Zhou, H. P. Zhang, G. Y. Wang, Z. G. Yao, Y. R. Tang and S. S. Zheng, *J. Mol. Catal. A: Chem.*, 2013, **366**, 43-47.
209. C. M. Miralda, E. E. Macias, M. Zhu, P. Ratnasamy and M. A. Carreon, *ACS Catal.*, 2011, **2**, 180-183.
210. M. Zhu, D. Srinivas, S. Bhogeswararao, P. Ratnasamy and M. A. Carreon, *Catal. Commun.*, 2013, **32**, 36-40.
211. F. X. Llabrés i Xamena, O. Casanova, R. Galiasso Tailleur, H. Garcia and A. Corma, *J. Catal.*, 2008, **255**, 220-227.
212. J. Zakzeski, A. Dębczak, P. C. A. Bruijnincx and B. M. Weckhuysen, *Appl. Catal., A*, 2011, **394**, 79-85.
213. A. Zhang, L. Li, J. Li, Y. Zhang and S. Gao, *Catal. Commun.*, 2011, **12**, 1183-1187.
214. S. B. Kalidindi, D. Esken and R. A. Fischer, *Chem. Eur. J.*, 2011, **17**, 6594-6597.
215. Q. Li and H. Kim, *Fuel Process. Technol.*, 2012, **100**, 43-48.
216. H.-L. Jiang, B. Liu, T. Akita, M. Haruta, H. Sakurai and Q. Xu, *J. Am. Chem. Soc.*, 2009, **131**, 11302-11303.
217. D. Esken, S. Turner, O. I. Lebedev, G. Van Tendeloo and R. A. Fischer, *Chem. Mater.*, 2010, **22**, 6393-6401.
218. G. Lu, S. Li, Z. Guo, O. K. Farha, B. G. Hauser, X. Qi, Y. Wang, X. Wang, S. Han, X. Liu, J. S. DuChene, H. Zhang, Q. Zhang, X. Chen, J. Ma, S. C. J. Loo, W. D. Wei, Y. Yang, J. T. Hupp and F. Huo, *Nat Chem*, 2012, **4**, 310-316.
219. M. Zahmakiran, *Dalton Trans.*, 2012, **41**, 12690-12696.
220. T. T. Dang, Y. Zhu, J. S. Y. Ngiam, S. C. Ghosh, A. Chen and A. M. Seayad, *ACS Catal.*, 2013, **3**, 1406-1410.
221. M. Liu, B. Fan, X. Shi and R. Li, *Catal. Commun.*, 2013, **42**, 20-24.
222. P. Wang, J. Zhao, X. Li, Y. Yang, Q. Yang and C. Li, *Chem. Commun.*, 2013, **49**, 3330-3332.
223. H.-L. Jiang, T. Akita, T. Ishida, M. Haruta and Q. Xu, *J. Am. Chem. Soc.*, 2011, **133**, 1304-1306.
224. T. T. Isimjan, H. Kazemian, S. Rohani and A. K. Ray, *J. Mater. Chem.*, 2010, **20**, 10241-10245.
225. T. Zhang, X. Zhang, X. Yan, L. Kong, G. Zhang, H. Liu, J. Qiu and K. L. Yeung, *Chem. Eng. J.*, 2013, **228**, 398-404.
226. Q. Liu, Z.-X. Low, L. Li, A. Razmjou, K. Wang, J. Yao and H. Wang, *J. Mater. Chem. A*, 2013, **1**, 11563-11569.
227. C. Dey and R. Banerjee, *Chem. Commun.*, 2013, **49**, 6617-6619.
228. C. Kuo, Y. Tang, L. Chou, B. T. Sneed, C. N. Brodsky, Z. Zhao and C. Tsung, *J. Am. Chem. Soc.*, 2012, **134**, 14345-14348.
229. G. Lu and J. T. Hupp, *J. Am. Chem. Soc.*, 2010, **132**, 7832-7833.
230. W. Ma, Q. Jiang, P. Yu, L. Yang and L. Mao, *Anal. Chem.*, 2013, **85**, 7550-7557.
231. S. Liu, Z. Xiang, Z. Hu, X. Zheng and D. Cao, *J. Mater. Chem.*, 2011, **21**, 6649-6653.
232. S. Liu, L. Wang, J. Tian, Y. Luo, G. Chang, A. M. Asiri, A. O. Al-Youbi and X. Sun, *ChemPhysChem*, 2012, **77**, 23-26.
233. C. Shen, W. Chen and R. Liu, *Dalton Trans.*, 2012, **41**, 11885-11888.
234. X. Lin, G. Gao, L. Zheng, Y. Chi and G. Chen, *Anal. Chem.*, 2013, **86**, 1223-1228.

235. S. Eslava, L. Zhang, S. Esconjauregui, J. Yang, K. Vanstreels, M. R. Baklanov and E. Saiz, *Chem. Mater.*, 2012, **25**, 27-33.
236. W. Zhan, Q. Kuang, J. Zhou, X. Kong, Z. Xie and L. Zheng, *J. Am. Chem. Soc.*, 2013, **135**, 1926-1933.
237. M. Law, L. E. Greene, J. C. Johnson, R. Saykally and P. D. Yang, *Nat. Mater.*, 2005, **4**, 455-459.
238. Q. F. Zhang, C. S. Dandeneau, X. Y. Zhou and G. Z. Cao, *Adv. Mater.*, 2009, **21**, 4087-4108.
239. C. Sun, C. Qin, X. Wang and Z. Su, *Expert Opin Drug Deliv.*, 2013, **10**, 89-101.
240. C. Sun, C. Qin, X. Wang, G. Yang, K. Shao, Y. Lan, Z. Su, P. Huang, C. Wang and E. Wang, *Dalton Trans.*, 2012, **41**, 6906-6909.
241. I. B. Vasconcelos, T. G. d. Silva, G. C. G. Militao, T. A. Soares, N. M. Rodrigues, M. O. Rodrigues, N. B. d. Costa, R. O. Freire and S. A. Junior, *RSC Adv.*, 2012, **2**, 9437-9442.
242. H. Ren, L. Zhang, J. An, T. Wang, L. Li, X. Si, L. He, X. Wu, C. Wang and Z. Su, *Chem. Commun.*, 2014, **50**, 1000-1002.
243. L. He, T. Wang, J. An, X. Li, L. Zhang, L. Li, G. Li, X. Wu, Z. Su and C. Wang, *CrystEngComm*, 2014, **16**, 3259-3263.
244. N. Li édana, A. Galve, C. Rubio, C. T élez and J. Coronas, *ACS Appl. Mater. Interfaces*, 2012, **4**, 5016-5021.
245. J. Sun and Q. Xu, *Energy Environ. Sci.*, 2014, **7**, 2071-2100.
246. F. Bai, Y. Xia, B. Chen, H. Su and Y. Zhu, *Carbon*, 2014, **79**, 213-226.
247. H.-L. Jiang, B. Liu, Y.-Q. Lan, K. Kuratani, T. Akita, H. Shioyama, F. Zong and Q. Xu, *J. Am. Chem. Soc.*, 2011, **133**, 11854-11857.
248. W. Chaikittisilp, M. Hu, H. Wang, H.-S. Huang, T. Fujita, K. C. W. Wu, L. Chen, Y. Yamauchi and K. Ariga, *Chem. Commun.*, 2012, **48**, 7259-7261.
249. N. L. Torad, M. Hu, Y. Kamachi, K. Takai, M. Imura, M. Naito and Y. Yamauchi, *Chem Commun*, 2013, **49**, 2521-2523.
250. N. L. Torad, R. R. Salunkhe, Y. Li, H. Hamoudi, M. Imura, Y. Sakka, C. Hu and Y. Yamauchi, *Chem. Eur. J.*, 2014, **20**, 7895-7900.
251. Q. Wang, W. Xia, W. Guo, L. An, D. Xia and R. Zou, *Chem. Asian. J.*, 2013, **8**, 1879-1885.
252. P. Zhang, F. Sun, Z. Xiang, Z. Shen, J. Yun and D. Cao, *Energy Environ. Sci.*, 2014, **7**, 442-450.
253. W. Xia, A. Mahmood, R. Zou and Q. Xu, *Energy Environ. Sci.*, 2015, **8**, 1837-1866.
254. B. Chen, G. Ma, D. Kong, Y. Zhu and Y. Xia, *Carbon*, 2015, **95**, 113-124.
255. R. R. Salunkhe, J. Tang, Y. Kamachi, T. Nakato, J. H. Kim and Y. Yamauchi, *ACS Nano*, 2015, **9**, 6288-6296.
256. K. S. Park, Z. Ni, A. P. Cote, J. Y. Choi, R. Huang, F. J. Uribe-Romo, H. K. Chae, M. O'Keeffe and O. M. Yaghi, *Proc Natl Acad Sci U S A*, 2006, **103**, 10186-10191.
257. F. H. Bai, Y. D. Xia, B. L. Chen, H. Q. Su and Y. Q. Zhu, *Carbon*, 2014, **79**, 213-226.
258. W. Chaikittisilp, N. L. Torad, C. Li, M. Imura, N. Suzuki, S. Ishihara, K. Ariga and Y. Yamauchi, *Chemistry*, 2014, **20**, 4217-4221.
259. W. Xia, J. Zhu, W. Guo, L. An, D. Xia and R. Zou, *J. Mater. Chem. A*, 2014, **2**, 11606-11613.
260. X. Wang, J. Zhou, H. Fu, W. Li, X. Fan, G. Xin, J. Zheng and X. Li, *J. Mater. Chem. A*, 2014, **2**, 14064-14070.
261. S. You, X. Gong, W. Wang, D. Qi, X. Wang, X. Chen and N. Ren, *Adv. Energy Mater.*, 2015, **6**, 1501497-1501506.
262. Y. Hou, J. Li, Z. Wen, S. Cui, C. Yuan and J. Chen, *Nano Energy*, 2015, **12**, 1-8.
263. E. Frackowiak and F. B éguin, *Carbon*, 2001, **39**, 937-950.
264. A. G. Pandolfo and A. F. Hollenkamp, *J. Power Sources*, 2006, **157**, 11-27.
265. Z. Jiang, Z. Li, Z. Qin, H. Sun, X. Jiao and D. Chen, *Nanoscale*, 2013, **5**, 11770-11775.
266. A. J. Amali, J.-K. Sun and Q. Xu, *Chem. Commun.*, 2014, **50**, 1519-1522.

267. P. Zhang, F. Sun, Z. Shen and D. Cao, *J. Mater. Chem. A*, 2014, **2**, 12873-12880.
268. A. Aijaz, N. Fujiwara and Q. Xu, *J. Am. Chem. Soc.*, 2014, **136**, 6790-6793.
269. L. Zhang, Z. Su, F. Jiang, L. Yang, J. Qian, Y. Zhou, W. Li and M. Hong, *Nanoscale*, 2014, **6**, 6590-6602.
270. E. Proietti, F. Jaouen, M. Lefèvre, N. Larouche, J. Tian, J. Herranz and J.-P. Dodelet, *Nat Commun.*, 2011, **2**, 416.
271. X. Wang, J. Zhou, H. Fu, W. Li, X. Fan, G. Xin, J. Zheng and X. Li, *J. Mater. Chem. A*, 2014, **2**, 14064-14070.
272. W. Xia, J. Zhu, W. Guo, L. An, D. Xia and R. Zou, *J. Mater. Chem. A*, 2014, **2**, 11606-11613.
273. W. Xia, R. Zou, L. An, D. Xia and S. Guo, *Energy Environ. Sci.*, 2015, **8**, 568-576.
274. Y. Hou, Z. Wen, S. Cui, S. Ci, S. Mao and J. Chen, *Adv. Funct. Mater.*, 2015, **25**, 872-882.
275. J. Qian, F. Sun and L. Qin, *Mater. Lett.*, 2012, **82**, 220-223.
276. W. S. Hummers and R. E. Offeman, *J. Am. Chem. Soc.*, 1958, **80**, 1339-1339.
277. B. Chen, F. Bai, Y. Zhu and Y. Xia, *Microporous Mesoporous Mater.*, 2014, **193**, 7-14.
278. B. Chen, F. Bai, Y. Zhu and Y. Xia, *RSC Adv.*, 2014, **4**, 47421-47428.
279. B. E. Warren, *X-ray Diffraction*, Courier Corporation, 1969.
280. R. A. Young, *X-ray Diffraction*, Engineering Experiment Station, Georgia Institute of Technology, 1961.
281. I. M. Watt, *The Principles and Practice of Electron Microscopy*, Cambridge University Press, 1997.
282. B. C. Smith, *Fundamentals of Fourier Transform Infrared Spectroscopy*, Taylor & Francis, 1995.
283. H.-H. Perkampus, H.-C. Grinter and T. Threlfall, *UV-VIS Spectroscopy and its Applications*, Springer, 1992.
284. A. R. West, *Basic solid state chemistry*, John Wiley & Sons, 1999.
285. S. J. Rothenberg, D. K. Flynn, A. F. Eidson, J. A. Mewhinney and G. J. Newton, *Journal of Colloid and Interface Science*, 1987, **116**, 541-554.
286. J. Cravillon, S. Munzer, S. J. Lohmeier, A. Feldhoff, K. Huber and M. Wiebcke, *Chem. Mater.*, 2009, **21**, 1410-1412.
287. J. F. Watts, *Vacuum*, 1994, **45**, 653-671.
288. C. C. Chusuei and D. W. Goodman, *Encyclopedia of physical science and technology*, 2002, **17**, 921-938.
289. J. R. Ferraro, K. Nakamoto and C. W. Brown, in *Introductory Raman Spectroscopy (Second Edition)*, Academic Press, San Diego, 2003, 1-94.
290. A. C. Ferrari, *Solid State Commun.*, 2007, **143**, 47-57.
291. C. Castiglioni, F. Negri, M. Rigolio and G. Zerbi, *J. Chem. Phys*, 2001, **115**, 3769-3778.
292. Q. Li, S. Zhang, L. Dai and L.-s. Li, *J. Am. Chem. Soc.*, 2012, **134**, 18932-18935.
293. U. A. Paulus, T. J. Schmidt, H. A. Gasteiger and R. J. Behm, *J. Electroanal. Chem.*, 2001, **495**, 134-145.
294. A. Phan, C. J. Doonan, F. J. Uribe-Romo, C. B. Knobler, M. O'Keeffe and O. M. Yaghi, *Acc. Chem. Res.*, 2009, **43**, 58-67.
295. W. Zhou, H. Wu and T. Yildirim, *J. Am. Chem. Soc.*, 2008, **130**, 15268-15269.
296. K. Li, D. H. Olson, J. Seidel, T. J. Emge, H. Gong, H. Zeng and J. Li, *J. Am. Chem. Soc.*, 2009, **131**, 10368-10369.
297. H. Bux, F. Liang, Y. Li, J. Cravillon, M. Wiebcke and J. r. Caro, *J. Am. Chem. Soc.*, 2009, **131**, 16000-16001.
298. Y. Liu, E. Hu, E. A. Khan and Z. Lai, *J. Membr. Sci.*, 2010, **353**, 36-40.
299. H.-L. Jiang, B. Liu, T. Akita, M. Haruta, H. Sakurai and Q. Xu, *J. Am. Chem. Soc.*, 2009, **131**, 11302-11303.
300. C. Chizallet, S. Lazare, D. Bazer-Bachi, F. Bonnier, V. Lecocq, E. Soyer, A.-A. Quoineaud and N. Bats, *J. Am. Chem. Soc.*, 2010, **132**, 12365-12377.

301. U. P. N. Tran, K. K. A. Le and N. T. S. Phan, *ACS Catal.*, 2011, **1**, 120-127.
302. G. Lu and J. T. Hupp, *J. Am. Chem. Soc.*, 2010, **132**, 7832-7833.
303. S. Liu, Z. Xiang, Z. Hu, X. Zheng and D. Cao, *J. Mater. Chem.*, 2011, **21**, 6649-6653.
304. Q. Shi, Z. Chen, Z. Song, J. Li and J. Dong, *Ange. Chem. Int. Ed.*, 2011, **50**, 672-675.
305. C. Sun, C. Qin, X.Wang, G. Yang, K. Shao, Y. Lan, Z. Su, P. Huang, C. Wang and E. Wang, *Dalton Trans.*, 2012, **41**, 6906-6909.
306. N. Liédana, A. Galve, C. Rubio, C. Télez and J. Coronas, *ACS Appl. Mater. Interfaces*, 2012, **4**, 5016-5021.
307. J. Zhang, A. Zhu, R. Lin, X. Qi and X. Chen, *Adv. Mater.*, 2011, **23**, 1268-1271.
308. A. Zhu, R. Lin, X. Qi, Y. Liu, Y. Lin, J. Zhang and X. Chen, *Microporous Mesoporous Mater.*, 2012, **157**, 42-49.
309. Y. Pan, Y. Liu, G. Zeng, L. Zhao and Z. Lai, *Chem. Commun.*, 2011, **47**, 2071-2073.
310. H. Bux, F. Liang, Y. Li, J. Cravillon, M. Wiebcke and J. Caro, *J. Am. Chem. Soc.*, 2009, **131**, 16000-16001.
311. J. Cravillon, S. Münzer, S.-J. Lohmeier, A. Feldhoff, K. Huber and M. Wiebcke, *Chem. Mater.*, 2009, **21**, 1410-1412.
312. S. R. Venna, J. B. Jasinski and M. A. Carreon, *J. Am. Chem. Soc.*, 2010, **132**, 18030-18033.
313. E. Leontidis, *Curr. Opin. Colloid Interface Sci.*, 2002, **7**, 81-91.
314. S. Che, S. Lim, M. Kaneda, H. Yoshitake, O. Terasaki and T. Tatsumi, *J. Am. Chem. Soc.*, 2002, **124**, 13962-13963.
315. J. Tang, C. Yu, X. Zhou, X. Yan and D. Zhao, *Chem Commun*, 2004, 2240-2241.
316. Y. Wang, S. Yan, G. Tang, C. Zhao, T. Li and Y. Cui, *Inorg. Chim. Acta.*, 2011, **376**, 492-499.
317. S. Hou, Q. K. Liu, J. P. Ma and Y. B. Dong, *Inorg Chem*, 2013, **52**, 3225-3235.
318. C. Yeh, W. Chang, M. Suen, H. Lee, H. Tsai and C. Tsou, *Polyhedron*, 2013, **61**, 151-160.
319. Y. Wen, T. Sheng, S. Hu, Y. Wang, C. Tan, X. Ma, Z. Xue, Y. Wang and X. Wu, *CrystEngComm*, 2013, **15**, 2714.
320. Q. Shi, Z. Song, X. Kang, J. Dong and Y. Zhang, *CrystEngComm*, 2012, **14**, 8280-8285.
321. P. Y. Moh, M. Brenda, M. W. Anderson and M. P. Attfield, *CrystEngComm*, 2013, **15**, 9672-9678.
322. A. Phan, C. J. Doonan, F. J. Uribe-Romo, C. B. Knobler, M. O'Keeffe and O. M. Yaghi, *Acc. Chem. Res.*, 2009, **43**, 58-67.
323. J. Yao and H. Wang, *Chem. Soc. Rev.*, 2014, **43**, 4470-4493.
324. B. Chen, Z. Yang, Y. Zhu and Y. Xia, *J. Mater. Chem. A*, 2014, **2**, 16811-16831.
325. D. Liu, J. Gu, Q. Liu, Y. Tan, Z. Li, W. Zhang, Y. Su, W. Li, A. Cui, C. Gu and D. Zhang, *Adv. Mater.*, 2014, **26**, 1229-1234.
326. S. Stankovich, D. A. Dikin, G. H. B. Dommett, K. M. Kohlhaas, E. J. Zimney, E. A. Stach, R. D. Piner, S. T. Nguyen and R. S. Ruoff, *Nature*, 2006, **442**, 282-286.
327. D. A. Dikin, S. Stankovich, E. J. Zimney, R. D. Piner, G. H. B. Dommett, G. Evmenenko, S. T. Nguyen and R. S. Ruoff, *Nature*, 2007, **448**, 457-460.
328. S. Stankovich, D. A. Dikin, R. D. Piner, K. A. Kohlhaas, A. Kleinhammes, Y. Jia, Y. Wu, S. T. Nguyen and R. S. Ruoff, *Carbon*, 2007, **45**, 1558-1565.
329. D. Chen, H. Feng and J. Li, *Chem. Rev.*, 2012, **112**, 6027-6053.
330. G. Eda and M. Chhowalla, *Adv. Mater.*, 2010, **22**, 2392-2415.
331. X. Li, G. Zhang, X. Bai, X. Sun, X. Wang, E. Wang and H. Dai, *Nature Nanotechn.*, 2008, **3**, 538-542.
332. F. Kim, L. J. Cote and J. Huang, *Adv. Mater.*, 2010, **22**, 1954-1958.
333. J. Li, L. Vaisman, G. Marom and J.-K. Kim, *Carbon*, 2007, **45**, 744-750.
334. R. Kumar, K. Jayaramulu, T. K. Maji and C. N. Rao, *Chem Commun*, 2013, **49**, 4947-4949.
335. C. Petit and T. J. Bandosz, *Adv. Funct. Mater.*, 2010, **20**, 111-118.
336. C. Petit and T. J. Bandosz, *Adv. Mater.*, 2009, **21**, 4753-4757.

337. C. Petit and T. J. Bandosz, *Dalton Trans.*, 2012, **41**, 4027-4035.
338. Y. X. Zhao, M. Seredych, Q. Zhong and T. J. Bandosz, *RSC Adv.*, 2013, **3**, 9932-9941.
339. M. Jahan, Q. Bao, J. Yang and K. P. Loh, *J. Am. Chem. Soc.*, 2010, **132**, 14487-14495.
340. M. Jahan, Z. Liu and K. P. Loh, *Adv. Funct. Mater.*, 2013, **23**, 5363-5372.
341. C. Hontoria-Lucas, A. J. López-Peinado, J. d. D. López-González, M. L. Rojas-Cervantes and R. M. Martín-Aranda, *Carbon*, 1995, **33**, 1585-1592.
342. Y. Hu, H. Kazemian, S. Rohani, Y. Huang and Y. Song, *Chem Commun*, 2011, **47**, 12694-12696.
343. Y. Xu, H. Bai, G. Lu, C. Li and G. Shi, *J. Am. Chem. Soc.*, 2008, **130**, 5856-5857.
344. M. He, J. Yao, Q. Liu, K. Wang, F. Chen and H. Wang, *Microporous Mesoporous Mater.*, 2014, **184**, 55-60.
345. M. Seredych, C. Petit, A. V. Tamashausky and T. J. Bandosz, *Carbon*, 2009, **47**, 445-456.
346. Q. Wang, J. Luo, Z. Zhong and A. Borgna, *Energy Environ. Sci.*, 2011, **4**, 42-55.
347. N. Gargiulo, F. Pepe and D. Caputo, *J. Nanosci. Nanotechnol.*, 2014, **14**, 1811-1822.
348. N. Gargiulo, A. Peluso, P. Aprea, F. Pepe and D. Caputo, *J. Chem. Eng. Data*, 2014, **59**, 896-902.
349. N. Gargiulo, F. Pepe and D. Caputo, *J. Colloid Interface. Sci.*, 2012, **367**, 348-354.
350. W. Dong, X. Wang, B. Li, L. Wang, B. Chen, C. Li, X. Li, T. Zhang and Z. Shi, *Dalton Trans.*, 2011, **40**, 243-248.
351. S. Gadipelli, W. Travis, W. Zhou and Z. X. Guo, *Energy Environ. Sci.*, 2014, **7**, 2232-2238.
352. D. Gu, H. Bongard, Y. Deng, D. Feng, Z. Wu, Y. Fang, J. Mao, B. Tu, F. Schuth and D. Zhao, *Adv. Mater.*, 2010, **22**, 833-837.
353. Z. Wu and D. Zhao, *Chem Commun*, 2011, **47**, 3332-3338.
354. J. Liu, S. Z. Qiao, H. Liu, J. Chen, A. Orpe, D. Zhao and G. Q. Lu, *Angew. Chem. Int. Ed.*, 2011, **50**, 5947-5951.
355. Y. Dong, H. Pang, H. B. Yang, C. Guo, J. Shao, Y. Chi, C. M. Li and T. Yu, *Angew. Chem. Int. Ed.*, 2013, **52**, 7800-7804.
356. Y. D. Xia, Z. X. Yang and Y. Q. Zhu, *J. Mater. Chem. A*, 2013, **1**, 9365-9381.
357. S. H. Joo, S. J. Choi, I. Oh, J. Kwak, Z. Liu, O. Terasaki and R. Ryoo, *Nature*, 2001, **412**, 169-172.
358. L. Liu, Q. F. Deng, B. Agula, X. Zhao, T. Z. Ren and Z. Y. Yuan, *Chem Commun*, 2011, **47**, 8334-8336.
359. Z. X. Yang, Y. D. Xia and R. Mokaya, *Adv. Mater.*, 2004, **16**, 727-732.
360. J. Biener, M. Stadermann, M. Suss, M. A. Worsley, M. M. Biener, K. A. Rose and T. F. Baumann, *Energy Environ. Sci.*, 2011, **4**, 656-667.
361. Y. Gogotsi, A. Nikitin, H. Ye, W. Zhou, J. E. Fischer, B. Yi, H. C. Foley and M. W. Barsoum, *Nat Mater*, 2003, **2**, 591-594.
362. Y. Xia, Z. Yang and R. Mokaya, *Nanoscale*, 2010, **2**, 639-659.
363. W. J. Liu, H. Jiang, K. Tian, Y. W. Ding and H. Q. Yu, *Environ Sci Technol*, 2013, **47**, 9397-9403.
364. M. Bhagiyalakshmi, P. Hemalatha, M. Ganesh, P. M. Mei and H. T. Jang, *Fuel*, 2011, **90**, 1662-1667.
365. S. T. Kochuveedu, Y. J. Jang, Y. H. Jang, W. J. Lee, M. A. Cha, H. Shin, S. Yoon, S. S. Lee, S. O. Kim, K. Shin, M. Steinhart and D. H. Kim, *Green Chem.*, 2011, **13**, 3397-3405.
366. W. Wei, C. Yu, Q. Zhao, G. Li and Y. Wan, *Chemistry*, 2013, **19**, 566-577.
367. G. Xue, H. Liu, Q. Chen, C. Hills, M. Tyrer and F. Innocent, *J Hazard Mater*, 2011, **186**, 765-772.
368. F. Wang, L. Liang, L. Shi, M. Liu and J. Sun, *Dalton Trans.*, 2014, **43**, 16441-16449.
369. S. T. Kochuveedu, Y. H. Jang, Y. J. Jang and D. H. Kim, *J. Mater. Chem. A*, 2013, **1**, 898-905.

370. B. L. Chen, Z. X. Yang, Y. Q. Zhu and Y. D. Xia, *J. Mater. Chem. A*, 2014, **2**, 16811-16831.
371. A. Phan, C. J. Doonan, F. J. Uribe-Romo, C. B. Knobler, M. O'Keeffe and O. M. Yaghi, *Acc Chem Res*, 2010, **43**, 58-67.
372. W. Chaikittisilp, K. Ariga and Y. Yamauchi, *J. Mater. Chem. A*, 2013, **1**, 14-19.
373. R. Das, P. Pachfule, R. Banerjee and P. Poddar, *Nanoscale*, 2012, **4**, 591-599.
374. G. J. Zhang, C. X. Li, J. Liu, L. Zhou, R. H. Liu, X. Han, H. Huang, H. L. Hu, Y. Liu and Z. H. Kang, *J. Mater. Chem. A*, 2014, **2**, 8184-8189.
375. H. X. Zhong, J. Wang, Y. W. Zhang, W. L. Xu, W. Xing, D. Xu, Y. F. Zhang and X. B. Zhang, *Angew. Chem. Int. Ed.*, 2014, **53**, 14235-14239.
376. A. C. Ferrari, *Solid State Commun.*, 2007, **143**, 47-57.
377. C. Castiglioni, F. Negri, M. Rigolio and G. Zerbi, *J. Chem. Phys*, 2001, **115**, 3769.
378. Z. Li, Z. W. Xu, X. H. Tan, H. L. Wang, C. M. B. Holt, T. Stephenson, B. C. Olsen and D. Mitlin, *Energy Environ. Sci.*, 2013, **6**, 871-878.
379. K. Kotsis and V. Staemmler, *Phys Chem Chem Phys*, 2006, **8**, 1490-1498.
380. S. B. Yang, L. J. Zhi, K. Tang, X. L. Feng, J. Maier and K. Mullen, *Adv. Funct. Mater.*, 2012, **22**, 3634-3640.
381. J. Wang, H. X. Zhong, Y. L. Qin and X. B. Zhang, *Angew. Chem. Int. Ed.*, 2013, **52**, 5248-5253.
382. S. J. Yang, T. Kim, K. Lee, Y. S. Kim, J. Yoon and C. R. Park, *Carbon*, 2014, **71**, 294-302.
383. Z. B. Xiao, Z. Yang, H. G. Nie, Y. Q. Lu, K. Q. Yang and S. M. Huang, *J. Mater. Chem. A*, 2014, **2**, 8683-8689.
384. S. J. Yang, S. Nam, T. Kim, J. H. Im, H. Jung, J. H. Kang, S. Wi, B. Park and C. R. Park, *J Am Chem Soc*, 2013, **135**, 7394-7397.
385. Y. D. Xia, R. Mokaya, G. S. Walker and Y. Q. Zhu, *Adv. Energy Mater.*, 2011, **1**, 678-683.
386. H. Furukawa and O. M. Yaghi, *J Am Chem Soc*, 2009, **131**, 8875-8883.
387. G. Dutta, A. A. Sokol, C. R. Catlow, T. W. Keal and P. Sherwood, *ChemPhysChem*, 2012, **13**, 3453-3456.
388. I. Yasumoto, *J. Phys. Chem.*, 1984, **88**, 4041-4044.
389. R. J. Kokes and R. Glemza, *J. Phys. Chem.*, 1965, **69**, 17-21.
390. H. J. Freund and M. W. Roberts, *Surf. Sci. Rep.*, 1996, **25**, 225-273.
391. M. Sevilla, P. Valle-Vigon and A. B. Fuertes, *Adv. Funct. Mater.*, 2011, **21**, 2781-2787.
392. N. L. Torad, M. Hu, S. Ishihara, H. Sukegawa, A. A. Belik, M. Imura, K. Ariga, Y. Sakka and Y. Yamauchi, *Small*, 2014, **10**, 2096-2107.
393. Z. Li, W. Li, H. Xue, W. Kang, X. Yang, M. Sun, Y. Tang and C. Lee, *RSC Adv.*, 2014, **4**, 37180-37186.
394. Y. S. Ho and G. McKay, *Process Biochem*, 1999, **34**, 451-465.
395. Y. P. Zhu, M. Li, Y. L. Liu, T. Z. Ren and Z. Y. Yuan, *J. Phys. Chem. C*, 2014, **118**, 10963-10971.
396. R. J. Zou, G. J. He, K. B. Xu, Q. Liu, Z. Y. Zhang and J. Q. Hu, *J. Mater. Chem. A*, 2013, **1**, 8445-8452.
397. G. Liu, L. Z. Wang, H. G. Yang, H. M. Cheng and G. Q. Lu, *J. Mater. Chem.*, 2010, **20**, 831-843.
398. S. J. Yang, J. H. Im, T. Kim, K. Lee and C. R. Park, *J Hazard Mater*, 2011, **186**, 376-382.
399. S. Chu and A. Majumdar, *Nature*, 2012, **488**, 294-303.
400. H. Yin, C. Zhang, F. Liu and Y. Hou, *Adv. Funct. Mater.*, 2014, **24**, 2930-2937.
401. T. Y. Ma, J. Ran, S. Dai, M. Jaroniec and S. Z. Qiao, *Angew. Chem. Int. Ed.*, 2015, **54**, 4646-4650.
402. Z. Peng, S. A. Freunberger, Y. Chen and P. G. Bruce, *Science*, 2012, **337**, 563-566.
403. M. S. Dresselhaus and I. L. Thomas, *Nature*, 2001, **414**, 332-337.

404. Z. Chen, D. Cummins, B. N. Reinecke, E. Clark, M. K. Sunkara and T. F. Jaramillo, *Nano Lett.*, 2011, **11**, 4168-4175.
405. D. Kong, H. Wang, Z. Lu and Y. Cui, *J. Am. Chem. Soc.*, 2014, **136**, 4897-4900.
406. L. Gan, M. Heggen, S. Rudi and P. Strasser, *Nano Lett.*, 2012, **12**, 5423-5430.
407. Y. Wu, J. Zang, L. Dong, Y. Zhang and Y. Wang, *J. Power Sources*, 2016, **305**, 64-71.
408. Y. Hou, Z. Wen, S. Cui, S. Ci, S. Mao and J. Chen, *Adv. Funct. Mater.*, 2015, **25**, 872-882.
409. N. L. Torad, M. Hu, S. Ishihara, H. Sukegawa, A. A. Belik, M. Imura, K. Ariga, Y. Sakka and Y. Yamauchi, *Small*, 2014, **10**, 2096-2107.
410. L. Zhang, X. Wang, R. Wang and M. Hong, *Chem. Mater.*, 2015, **27**, 7610-7618.
411. J. Wei, Y. Hu, Z. Wu, Y. Liang, S. Leong, B. Kong, X. Zhang, D. Zhao, G. P. Simon and H. Wang, *J. Mater. Chem. A*, 2015, **3**, 16867-16873.
412. A. Kong, C. Mao, Q. Lin, X. Wei, X. Bu and P. Feng, *Dalton Trans.*, 2015, **44**, 6748-6754.
413. S. Chao, Z. Bai, Q. Cui, H. Yan, K. Wang and L. Yang, *Carbon*, 2015, **82**, 77-86.
414. M. Klose, K. Pinkert, M. Zier, M. Uhlemann, F. Wolke, T. Jaumann, P. Jehnichen, D. Wadewitz, S. Oswald, J. Eckert and L. Giebeler, *Carbon*, 2014, **79**, 302-309.
415. N. L. Torad, R. R. Salunkhe, Y. Li, H. Hamoudi, M. Imura, Y. Sakka, C.-C. Hu and Y. Yamauchi, *Chem. Eur. J.*, 2014, **20**, 7895-7900.
416. R. Wu, D. P. Wang, X. Rui, B. Liu, K. Zhou, A. W. K. Law, Q. Yan, J. Wei and Z. Chen, *Adv. Mater.*, 2015, **27**, 3038-3044.
417. C. Zhang, N. Mahmood, H. Yin, F. Liu and Y. Hou, *Adv. Mater.*, 2013, **25**, 4932-4937.
418. N. Chiodarelli, C. Xu, O. Richard, H. Bender, A. Klekachev, M. Cooke, M. Heyns, S. De Gendt, G. Groeseneken and P. M. Vereecken, *J.Nanomater*, **2012**, 1-10.
419. G. Wu, K. L. More, C. M. Johnston and P. Zelenay, *Science*, 2011, **332**, 443-447.
420. J. R. Pels, F. Kapteijn, J. A. Moulijn, Q. Zhu and K. M. Thomas, *Carbon*, 1995, **33**, 1641-1653.
421. S. Chen, J. Duan, M. Jaroniec and S. Qiao, *Adv. Mater.*, 2014, **26**, 2925-2930.
422. M. Gao, Y. Xu, J. Jiang, Y. Zheng and S. Yu, *J. Am. Chem. Soc.*, 2012, **134**, 2930-2933.
423. S. Chen, J. Duan, J. Ran, M. Jaroniec and S. Z. Qiao, *Energy Environ. Sci.*, 2013, **6**, 3693-3699.
424. J. Masa, W. Xia, I. Sinev, A. Zhao, Z. Sun, S. Grützke, P. Weide, M. Muhler and W. Schuhmann, *Angew. Chem. Int. Ed.*, 2014, **53**, 8508-8512.
425. S. Mao, Z. Wen, T. Huang, Y. Hou and J. Chen, *Energy Environ. Sci.*, 2014, **7**, 609-616.
426. B. Chen, R. Li, G. Ma, X. Gou, Y. Zhu and Y. Xia, *Nanoscale*, 2015, **7**, 20674-20684.
427. I. Katsounaros, S. Cherevko, A. R. Zeradjanin and K. J. J. Mayrhofer, *Angew. Chem. Int. Ed.*, 2014, **53**, 102-121.
428. C. Yuan, H. B. Wu, Y. Xie and X. W. Lou, *Angew. Chem. Int. Ed.*, 2014, **53**, 1488-1504.
429. H. Wang, Y. Liang, Y. Li and H. Dai, *Angew. Chem. Int. Ed.*, 2011, **50**, 10969-10972.
430. N. A. Vante and H. Tributsch, *Nature*, 1986, **323**, 431-432.
431. R. A. Sidik and A. B. Anderson, *J. Phys. Chem. B*, 2006, **110**, 936-941.
432. Y. Zhou, H. Yao, Y. Wang, H. Liu, M. Gao, P. Shen and S. Yu, *Chem. Eur. J.*, 2010, **16**, 12000-12007.
433. Y. Feng, T. He and N. Alonso-Vante, *Chem. Mater.*, 2008, **20**, 26-28.
434. P. Ganesan, M. Prabu, J. Sanetuntikul and S. Shanmugam, *ACS Catalysis*, 2015, **5**, 3625-3637.
435. N. Mahmood, C. Zhang, J. Jiang, F. Liu and Y. Hou, *Chem. Eur. J.*, 2013, **19**, 5183-5190.
436. Q. Liu and J. Zhang, *CrystEngComm*, 2013, **15**, 5087-5092.
437. Q. Li, R. Cao, J. Cho and G. Wu, *Adv. Energy Mater.*, 2014, **4**, 1301415-1301424.

438. Y. Zhao, R. Nakamura, K. Kamiya, S. Nakanishi and K. Hashimoto, *Nat Commun*, 2013, **4**.
439. R. Silva, D. Voiry, M. Chhowalla and T. Asefa, *J. Am. Chem. Soc.*, 2013, **135**, 7823-7826.
440. K. Gong, F. Du, Z. Xia, M. Durstock and L. Dai, *Science*, 2009, **323**, 760-764.
441. W. Chaikittisilp, N. L. Torad, C. Li, M. Imura, N. Suzuki, S. Ishihara, K. Ariga and Y. Yamauchi, *Chem. Eur. J.*, 2014, **20**, 4217-4221.
442. Z. Jiang, H. Sun, Z. Qin, X. Jiao and D. Chen, *Chem Commun*, 2012, **48**, 3620-3622.
443. Z. Jiang, W. Lu, Z. Li, K. H. Ho, X. Li, X. Jiao and D. Chen, *J. Mater. Chem. A*, 2014, **2**, 8603-8606.
444. Y. Chen, C. Wang, Z. Wu, Y. Xiong, Q. Xu, S. Yu and H. Jiang, *Adv. Mater.*, 2015, **27**, 5010-5016.
445. J. Wang, Y. Wang, F. Cao, Y. Guo and L. Wan, *J. Am. Chem. Soc.*, 2010, **132**, 12218-12221.
446. Q. Li, R. Cao, J. Cho and G. Wu, *Adv. Energy Mater.*, 2014, **4**, 1301415-1301434.
447. R. Wu, D. P. Wang, X. Rui, B. Liu, K. Zhou, A. W. K. Law, Q. Yan, J. Wei and Z. Chen, *Adv. Mater.*, 2015, **27**, 3038-3044.
448. B. Chen, R. Li, G. Ma, X. Gou, Y. Zhu and Y. Xia, *Nanoscale*, 2015, **7**, 20674-20684.
449. Q. Wang, R. Zou, W. Xia, J. Ma, B. Qiu, A. Mahmood, R. Zhao, Y. Yang, D. Xia and Q. Xu, *Small*, 2015, **11**, 2511-2517.
450. M. Shen, C. Ruan, Y. Chen, C. Jiang, K. Ai and L. Lu, *ACS Appl. Mater. Interfaces*, 2014, **7**, 1207-1218.
451. C. N. R. Rao and K. P. R. Pisharody, *Prog. Solid State Chem.*, 1976, **10, Part 4**, 207-270.
452. L. Lai, J. R. Potts, D. Zhan, L. Wang, C. K. Poh, C. Tang, H. Gong, Z. Shen, J. Lin and R. S. Ruoff, *Energy Environ. Sci.*, 2012, **5**, 7936-7942.
453. S. Bao, Y. Li, C. M. Li, Q. Bao, Q. Lu and J. Guo, *Cryst. Growth Des.*, 2008, **8**, 3745-3749.
454. J. F. Marco, J. R. Gancedo, M. Gracia, J. L. Gautier, E. I. Rios, H. M. Palmer, C. Greaves and F. J. Berry, *J. Mater. Chem.*, 2001, **11**, 3087-3093.
455. Q. Liu, J. Jin and J. Zhang, *ACS Appl. Mater. Interfaces*, 2013, **5**, 5002-5008.
456. X. Wang, Q. Xiang, B. Liu, L. Wang, T. Luo, D. Chen and G. Shen, *Sci. Rep.*, 2013, **3**, 2007-2013.
457. S. Wohlgemuth, R. J. White, M. Willinger, M. Titirici and M. Antonietti, *Green Chem.*, 2012, **14**, 1515-1523.
458. Z. Yang, Z. Yao, G. Li, G. Fang, H. Nie, Z. Liu, X. Zhou, X. a. Chen and S. Huang, *ACS Nano*, 2012, **6**, 205-211.
459. K. Polychronopoulou, C. D. Malliakas, J. He and M. G. Kanatzidis, *Chem. Mater.*, 2012, **24**, 3380-3392.
460. V. N. Bui, D. Laurenti, P. Delichère and C. Geantet, *Appl. Catal., B*, 2011, **101**, 246-255.
461. H. S. Kim, T. S. Arthur, G. D. Allred, J. Zajicek, J. G. Newman, A. E. Rodnyansky, A. G. Oliver, W. C. Boggess and J. Muldoon, *Nat Commun*, 2011, **2**, 427-432.
462. S. Das, P. Sudhagar, S. Nagarajan, E. Ito, S. Y. Lee, Y. S. Kang and W. Choi, *Carbon*, 2012, **50**, 4815-4821.
463. G. Wang, J. Zhang, S. Kuang, S. Liu and S. Zhuo, *J. Power Sources*, 2014, **269**, 473-478.
464. Z.-S. Wu, L. Chen, J. Liu, K. Parvez, H. Liang, J. Shu, H. Sachdev, R. Graf, X. Feng and K. Müllen, *Adv. Mater.*, 2014, **26**, 1450-1455.
465. X. Zou, X. Huang, A. Goswami, R. Silva, B. R. Sathe, E. Mikmeková and T. Asefa, *Angew. Chem.*, 2014, **126**, 4461-4465.
466. S. Yang, L. Zhi, K. Tang, X. Feng, J. Maier and K. Müllen, *Adv. Funct. Mater.*, 2012, **22**, 3634-3640.
467. J. Wang, H. Zhong, Y. Qin and X. Zhang, *Angew. Chem. Int. Ed.*, 2013, **52**, 5248-5253.

468. S. Chen, Z. Wei, X. Qi, L. Dong, Y. Guo, L. Wan, Z. Shao and L. Li, *J. Am. Chem. Soc.*, 2012, **134**, 13252-13255.
469. D.-S. Yang, D. Bhattacharjya, S. Inamdar, J. Park and J.-S. Yu, *J. Am. Chem. Soc.*, 2012, **134**, 16127-16130.
470. Y. Zheng, Y. Jiao, L. Ge, M. Jaroniec and S. Z. Qiao, *Angew. Chem. Int. Ed.*, 2013, **52**, 3110-3116.
471. S. Kattel, P. Atanassov and B. Kiefer, *Phys. Chem. Chem. Phys.*, 2013, **15**, 148-153.
472. Y. Li, W. Zhou, H. Wang, L. Xie, Y. Liang, F. Wei, J. Idrobo, S. J. Pennycook and H. Dai, *Nat Nano*, 2012, **7**, 394-400.
473. K. J. J. Mayrhofer, D. Strmcnik, B. B. Blizanac, V. Stamenkovic, M. Arenz and N. M. Markovic, *Electrochim. Acta*, 2008, **53**, 3181-3188.
474. H. Wang, Y. Liang, Y. Li and H. Dai, *Angew. Chem. Int. Ed.*, 2011, **50**, 10969-10972.
475. N. Mahmood, C. Zhang, J. Jiang, F. Liu and Y. Hou, *Chem. Eur. J.*, 2013, **19**, 5183-5190.
476. M. Shen, C. Ruan, Y. Chen, C. Jiang, K. Ai and L. Lu, *ACS Appl. Mater. Interfaces*, 2014, **7**, 1207-1218.
477. Q. Liu, J. Jin and J. Zhang, *ACS Appl. Mater. Interfaces*, 2013, **5**, 5002-5008.
478. C. Zhao, D. Li and Y. Feng, *J. Mater. Chem. A*, 2013, **1**, 5741-5746.
479. C. Zhang, R. Hao, H. Yin, F. Liu and Y. Hou, *Nanoscale*, 2012, **4**, 7326-7329.
480. M. Li, L. Zhang, Q. Xu, J. Niu and Z. Xia, *J. Catal.*, 2014, **314**, 66-72.
481. G. Tian, M. Zhao, D. Yu, X. Kong, J. Huang, Q. Zhang and F. Wei, *Small*, 2014, **10**, 2251-2259.
482. Y. Gorlin and T. F. Jaramillo, *J. Am. Chem. Soc.*, 2010, **132**, 13612-13614.
483. Y. Lee, J. Suntivich, K. J. May, E. E. Perry and Y. Shao-Horn, *J. Phys. Chem. Lett.*, 2012, **3**, 399-404.
484. H. S. Ahn and T. D. Tilley, *Adv. Funct. Mater.*, 2013, **23**, 227-233.
485. L. Trotochaud, J. K. Ranney, K. N. Williams and S. W. Boettcher, *J. Am. Chem. Soc.*, 2012, **134**, 17253-17261.
486. J. Qian, F. Sun and L. Qin, *Mater. Lett.*, 2012, **82**, 220-223.
487. R. Li, X. Ren, H. Ma, X. Feng, Z. Lin, X. Li, C. Hu and B. Wang, *J. Mater. Chem. A*, 2014, **2**, 5724-5729.
488. J. F. Marco, J. R. Gancedo, M. Gracia, J. L. Gautier, E. I. Rios, H. M. Palmer, C. Greaves and F. J. Berry, *J. Mater. Chem.*, 2001, **11**, 3087-3093.
489. Z. Peng, D. Jia, A. M. Al-Enizi, A. A. Elzatahry and G. Zheng, *Adv. Energy Mater.*, 2015, **5**, 1402031-1402038.
490. W. Zhou, X. Wu, X. Cao, X. Huang, C. Tan, J. Tian, H. Liu, J. Wang and H. Zhang, *Energy Environ. Sci.*, 2013, **6**, 2921-2924.
491. X. Lv, G. She, S. Zhou and Y. Li, *RSC Adv.*, 2013, **3**, 21231-21236.
492. S. Wohlgemuth, R. J. White, M. Willinger, M. Titirici and M. Antonietti, *Green Chem.*, 2012, **14**, 1515-1523.
493. G. Wang, J. Zhang, S. Kuang, S. Liu and S. Zhuo, *J. Power Sources*, 2014, **269**, 473-478.
494. H. Chen, J. Jiang, Y. Zhao, L. Zhang, D. Guo and D. Xia, *J. Mater. Chem. A*, 2015, **3**, 428-437.
495. R. Matsuzaki, A. Yajima, M. Eguchi and Y. Saeki, *Bull. Chem. Soc. Japan*, 1982, **55**, 1480-1483.
496. Z. Li, Z. Xu, X. Tan, H. Wang, C. M. B. Holt, T. Stephenson, B. C. Olsen and D. Mitlin, *Energy Environ. Sci.*, 2013, **6**, 871-878.
497. C. C. L. McCrory, S. Jung, J. C. Peters and T. F. Jaramillo, *J. Am. Chem. Soc.*, 2013, **135**, 16977-16987.
498. N. Mamaca, E. Mayousse, S. Arrii-Clacens, T. W. Napporn, K. Servat, N. Guillet and K. B. Kokoh, *Appl. Catal. B Environ.*, 2012, **111–112**, 376-380.
499. Y. Zhao, R. Nakamura, K. Kamiya, S. Nakanishi and K. Hashimoto, *Nat Commun.*, 2013, **4**, 2390-2396.

500. M. Gao, X. Cao, Q. Gao, Y. Xu, Y. Zheng, J. Jiang and S. Yu, *ACS Nano*, 2014, **8**, 3970-3978.
501. X. Liu, Z. Chang, L. Luo, T. Xu, X. Lei, J. Liu and X. Sun, *Chem. Mater.*, 2014, **26**, 1889-1895.
502. Y. Li, P. Hasin and Y. Wu, *Adv. Mater.*, 2010, **22**, 1926-1929.
503. H. Liang, F. Meng, M. Cabán-Acevedo, L. Li, A. Forticaux, L. Xiu, Z. Wang and S. Jin, *Nano Lett.*, 2015, **15**, 1421-1427.
504. T. Y. Ma, S. Dai, M. Jaroniec and S. Z. Qiao, *J. Am. Chem. Soc.*, 2014, **136**, 13925-13931.
505. Y. Zhu, Y. Liu, T. Ren and Z. Yuan, *Adv. Funct. Mater.*, 2015, **25**, 7337-7347.
506. M. Gao, Y. Xu, J. Jiang, Y. Zheng and S. Yu, *J. Am. Chem. Soc.*, 2012, **134**, 2930-2933.
507. Y. Yang, H. Fei, G. Ruan and J. M. Tour, *Adv. Mater.*, 2015, **27**, 3175-3180.
508. H. Yu, S. Chen, X. Fan, X. Quan, H. Zhao, X. Li and Y. Zhang, *Angew. Chem. Int. Ed.*, 2010, **49**, 5106-5109.
509. W. Xu, Z. Lu, X. Lei, Y. Li and X. Sun, *Phys. Chem. Chem. Phys.*, 2014, **16**, 20402-20405.
510. I. C. Man, H. Su, F. Calle-Vallejo, H. A. Hansen, J. I. Martínez, N. G. Inoglu, J. Kitchin, T. F. Jaramillo, J. K. Nørskov and J. Rossmeisl, *ChemCatChem*, 2011, **3**, 1159-1165.
511. M. E. G. Lyons and M. P. Brandon, *J. Electroanaly. Chem.*, 2010, **641**, 119-130.
512. X. Han, F. Cheng, T. Zhang, J. Yang, Y. Hu and J. Chen, *Adv. Mater.*, 2014, **26**, 2047-2051.
513. J. Masa, W. Xia, I. Sinev, A. Zhao, Z. Sun, S. Grützke, P. Weide, M. Muhler and W. Schuhmann, *Angew. Chem. Int. Ed.*, 2014, **53**, 8508-8512.
514. J. Kibsgaard, Z. Chen, B. N. Reinecke and T. F. Jaramillo, *Nat Mater.*, 2012, **11**, 963-969.
515. Y. Zheng, Y. Jiao, Y. Zhu, L. H. Li, Y. Han, Y. Chen, A. Du, M. Jaroniec and S. Z. Qiao, *Nat Commun.*, 2014, **5**, 3783-3791.